

APPLICATION OF BAYESIAN RECURSIVE ESTIMATION
FOR SEISMIC SIGNAL PROCESSING

by

ERICK BAZIW

B.A.Sc., The University of British Columbia, 1986

M.A.Sc., The University of British Columbia, 1988

A THESIS SUBMITTED IN PARTIAL FULFILMENT OF THE REQUIREMENTS FOR
THE DEGREE OF

DOCTOR OF PHILOSOPHY

in

THE FACULTY OF GRADUATE STUDIES

(Geophysics)

THE UNIVERSITY OF BRITISH COLUMBIA

April 2007

© Erick Baziw, 2007

Abstract

Bayesian recursive estimation (BRE) requires that the posterior density function be estimated so that conditional mean estimates of desired parameters or states can be obtained. BRE has been referred to as a complete solution to the estimation problem since the posterior density function embodies all available statistical information (i.e., prior, likelihood and evidence). Until recent advances in BRE, most applications required that the system and measurement equations be linear, and that the process and measurement noise be Gaussian and white. A Kalman filter, KF, (closed form solution to the BRE) could be applied to systems that met these conditions. Previous applications of the KF to solve seismic signal processing problems (e.g., deconvolution) have had very limited success and acceptability in the geophysics signal processing community due to the restrictive nature of the KF. The recently new BRE development of sequential Monte Carlo (SMC) techniques for numerically solving non-stationary and non-linear problems has generated considerable interest and active research within the last decade. This thesis focuses upon the implementation of SMC techniques (e.g., particle filtering) for solving seismic signal processing problems. All the associated filters of BRE (hidden Markov model filter, KF, particle filter, Rao-Blackwellised particle filter, and jump Markov systems) and a new and highly robust and unique model of the seismic source wavelet are implemented in two innovative algorithms for solving the important problems of passive seismic event detection and blind seismic deconvolution. A ground-breaking concept in blind seismic deconvolution referred to as principle phase decomposition (PPD) is outlined and evaluated in this thesis. The PPD technique estimates and separates overlapping source wavelets instead of estimating high bandwidth reflection coefficients. It is shown that one can then easily generate reflection coefficients from the separated source wavelets. In this thesis many advantages of the PPD are outlined. Simulated seismogram data with low signal-to-noise ratios is blindly deconvolved where non-stationary, mixed-phase, and zero-phase source wavelets are present. I believe that there are currently no existing blind seismic deconvolution techniques which could obtain comparable performance results of the PPD technique. The work in this thesis has resulted in three IEEE publications and one peer reviewed conference publication.

Table of Contents

Abstract.....	ii
Table of Contents	iii
List of Tables.....	v
List of Figures.....	vi
List of Abbreviations.....	xii
Acknowledgments.....	xiv
Dedication.....	xv
I. Introduction.....	1
II. Bayesian Recursive Estimation and Seismic Modeling	4
III. Mathematical background	8
A. Bayesian Recursive Estimation.....	8
B. Kalman Filter and Jump Markov Linear Gaussian System	9
C. Hidden Markov Model Filter	11
D. Particle Filter and Rao-Blackwellised Particle Filter.....	13
a) Bayesian Importance Sampling	13
b) Sampling Importance Re-sampling (SIR)	17
c) Choice of Importance Function.....	20
IV. Seismic Signal Processing.....	23
A. Passive Seismic Monitoring.....	23
1) PS-SEED Filter Outline	25
a) State-Space Formulation	25
b) PS-SEED RBPF and HMM Filter Implementation	26
c) Evaluating the PS-SEED with Simulated Data	28
B. Seismic Deconvolution	32
1) Application of Kalman Filter Smoother to Seismic deconvolution.....	33
a) Kalman Filter Smoother Governing Equations	34
b) Kalman Filter Seismic Deconvolution (KFSD) Algorithm Outline.....	36
c) ARMA Parameter Estimation by the Least Squares Method	38
d) Evaluating the KFSD Algorithm with Simulated Finite Difference Data.....	41
2) Application of Particle Filtering to Blind Seismic Deconvolution.....	45
a) Amplitude Modulated Sinusoid	47
b) PPD Algorithm Outlined.....	49
c) PPD Kalman Filter and Jump Markov Linear Gaussian System Formulation....	52
d) PPD Parameter Specification and Algorithm Implementation	53
e) Evaluating the PPD Algorithm with Simulated Data.....	57
f) Proposed Methodology in Processing Seismograms with the PPD Algorithm...69	69
g) Estimation of the Dominant Frequency of the Wavelet to be extracted within the PPD-WE Algorithm.....	89
h) Utilization of the PPD-WE Algorithm within Standard Frequency Domain Deconvolution Techniques.....	104
i) Monte Carlo Simulations	111
j) Sensitivity Analysis	114
3) Implementation of the PPD-WE Algorithm on Real Data.....	118

V. Conclusions	134
References	137
Appendix	143
A. Derivation of Chapman-Kolomogorov Equation	143
B. Derivation of the BRE Update Equation	143
C. Derivation of the Recursive Weights Update Equation	144
D. Derivation of the "Likelihood" Formula	146
E. PS-SEED FSMCD and HMM Filter Implementation.....	148
F. PPD FSMCD and HMM Filter Implementation	150
G. Implementation of the Three State FSMCD within the PPD-WE Algorithm.....	152
H. PPD-WE Estimated Source and Residual Wavelets for SCPT Test Hole SC 64. ...	154
1) Estimated Source Wavelet at 3m	154
2) Estimated Source Wavelet at 4m	155
3) Estimated Source Wavelet at 5m	156
4) Estimated Source Wavelet at 6m	157
5) Estimated Source Wavelet at 7m	158
6) Estimated Source Wavelet at 8m	159
7) Estimated Source Wavelet at 9m	160
8) Etimated Source Wavelet at 10m.....	161
9) Estimated Source Wavelet at 11m:.....	162
10) Estimated Source Wavelet at 12m	163
11) Estimated Source Wavelet at 13m	164
12) Estimated Source Wavelet at 14m	165
13) Estimated Source Wavelet at 15m	166
14) Estimated Source Wavelet at 16m	167
15) Estimated Source Wavelet at 17m	168

List of Tables

Table 3.1 KF Governing Equations for JMLGS	10
Table 3.2 HMM Filtering Algorithm.....	12
Table 3.3. Typical Particle Filtering Algorithm.	16
Table 4.1 PS-Seed Filter Formulation.	27
Table 4.2 KF Fixed-Interval Smoother Governing Equations.....	35
Table 4.3 PPD Filter Formulation.	55
Table 4.4 PPD-WE Filter Formulation.....	72
Table 4.5 Interval Velocities (PPD-WE Extracted Source Wavelets) from the Crosscorrelation Technique for SCPT SC 64.....	128
Table 4.6 Interval Velocities (Processed Seismograms) from the Crosscorrelation Technique for SCPT SC 64	128
Table 4.7 Estimated Secondary Arriving Source Wavelet Time Offset for SCPT SC 64	132

List of Figures

Figure 3.1. Schematic illustrating the bootstrap re-sampling methodology.....	19
Figure 4.1. Source wavelet embedded with varying types of Gauss-Markov background noise.....	30
Figure 4.2. PS-SEED output results for estimating state \hat{x}_{2k} after processing the data shown in Fig. 4.1.	31
Figure 4.3. Estimated probability of an event for the test case shown in Fig. 4.1(b).....	32
Figure 4.4. Finite difference simulated source wavelet.	41
Figure 4.5. Estimating source wavelet in Fig. 4.4 with 5 th order ARMA model.	42
Figure 4.6. The reflection coefficients utilized to test the performance of the KFSD algorithm.....	422
Figure 4.7. the output after convolving ARMA wavelet with reflection coefficients shown in Fig. 4.6.	43
Figure 4.8. The KFSD estimated reflection coefficients.....	433
Figure 4.9. Seismic data of Fig. 4.7 with Gauss-Markov noise of $T_c = 0.02$ ms and $s = 0.08$ added.....	44
Figure 4.10. The KFSD estimated reflection coefficients for data shown in Fig. 4.9.	45
Figure 4.11. A zero-phase Ricker wavelet with superimposed 50 Hz sinusoid with phase of 96°	48
Figure 4.12. Amplitude modulating term for estimating Ricker wavelet of Fig. 4.14.....	48
Figure 4.13. Reconstructed Ricker wavelet superimposed upon actual Ricker wavelet of Fig. 4.11.	49
Figure 4.14. Illustration of the convolution operation as the summation of AMS source wavelets	50
Figure 4.15. A mixed phased Berlage wavelet.....	57
Figure 4.16. Reflection coefficients convolved with Berlage wavelet shown in Fig. 4.15	58
Figure 4.17. The output after convolving Berlage wavelet with reflection coefficients illustrated in Fig. 4.16 and adding measurement noise.	58
Figure 4.18. Estimating dominant frequency and initial phase component interactively.....	59
Figure 4.19. The addition of a 50 Hz sinusoid with phase of 100° at time of 104 ms.	60
Figure 4.20. The output of PPD algorithm where the Berlage wavelets have been separate.	61
Figure 4.21. The error residual which is defined to be the difference between the filtered seismogram of Fig. 4.17 and the estimated Berlage wavelets of Fig. 4.20.	61
Figure 4.22. The dipole reflection coefficients convolved with Berlage wavelet shown in Fig. 4.15.	62
Figure 4.23. The output after convolving Berlage wavelet with reflection coefficients illustrated in Fig. 4.22 and adding Gauss-Markov measurement noise.	62
Figure 4.24. The output of PPD algorithm where the algorithm did an impressive job in extracting the dipole Berlage source wavelets.....	63
Figure 4.25. The error residual which is defined to be the difference between the filtered seismogram of Fig. 4.23 and the estimated Berlage wavelets of Fig. 4.24.	63

Figure 4.26. The output after superimposing Berlage wavelet with arrival time of 99 ms and zero-phase Ricker wavelet of Fig. 4.11.....	64
Figure 4.27. The output of PPD algorithm where the algorithm did an impressive job in extracting the Berlage source wavelet from the overlapping zero-phase Ricker wavelet.	65
Figure 4.28. The error residual which is defined to be the difference between the filtered seismogram of Fig. 4.26 and the estimated source wavelets of Fig. 4.27.	65
Figure 4.29. Mixed phased Berlage wavelet with $f = 40 \text{ Hz}$, $n = 2$, $a = 100$, and $\phi = 10^\circ$...	66
Figure 4.30. Output after superimposing the time-variant Berlage source wavelets with additive measurement noise (variance = 50 units ² and time constant = 0.001 ms)..	67
Figure 4.31. The addition of a 40 Hz sinusoid with phase of 100° at time of 104 ms to the sinusoid shown in Fig. 4.18.....	67
Figure 4.32. The output of PPD algorithm where the algorithm did an impressive job in extracting the non-stationary Berlage source wavelets.	68
Figure 4.33. The error residual which is defined to be the difference between the filtered seismogram of Fig. 4.30 and the estimated source wavelets of Fig. 4.32.	68
Figure 4.34. The output after convolving Berlage wavelet of Fig 4.15 with reflection coefficients illustrated in Fig. 4.16 and adding Gauss-Markov measurement noise with a variance of 400 units ² and a time constant of 0.01 ms.	74
Figure 4.35. The output after applying a 100 Hz, eighth order, zero-phase shift, low-pass Butterworth frequency filter to the synthetic seismogram shown in Fig. 4.34.....	75
Figure 4.36. The initial HMM f_{3k} phase estimates for first pass of PPD-WE algorithm on data shown in Fig. 4.35.....	75
Figure 4.37. The estimated and true Berlage source wavelets for the first reflection coefficient illustrated in Fig 4.16.	77
Figure 4.38. The estimated and true Berlage source wavelets for the second reflection coefficient illustrated in Fig 4.16.	77
Figure 4.39. The AMTs for the two estimated AMSs shown in Figs. 4.37 and 4.38	78
Figure 4.40. The normalized cross-correlation function for estimated source wavelets illustrated in Figs. 4.37 and 4.38. Peak value occurs at 4.7 ms.	78
Figure 4.41. The estimated and true Reflection coefficients for synthetic seismogram illustrated in Fig. 4.34.....	79
Figure 4.42. Three state FSMCD realization for time $t = 40 \text{ ms}$	79
Figure 4.43. The reflection coefficients convolved with Berlage wavelet shown in Fig. 4.15.	80
Figure 4.44. The output after convolving Berlage wavelet of Fig 4.15 with reflection coefficients illustrated in Fig. 4.43 and adding Gauss-Markov measurement noise with a variance of 400 units ² and a time constant of 0.01 ms.	80
Figure 4.45. The output after applying a 100 Hz, eighth order, zero-phase shift, low-pass Butterworth frequency filter to the synthetic seismogram shown in Fig. 4.44	81
Figure 4.46. The initial HMM f_{3k} phase estimates for first pass of PPD-WE algorithm on data shown in Fig. 4.44..	82

Figure 4.47. Estimated and true Berlage source wavelets for the first reflection coefficient illustrated in Fig 4.44.....	83
Figure 4.48. Estimated and true time series residual for the last two reflection coefficients illustrated in Fig 4.43 convolved with the Berlage source wavelet of Fig. 4.15.....	83
Figure 4.49. The AMTs for the two estimated AMSs shown in Figs. 4.47 and 4.48..	84
Figure 4.50. The estimated time series residual of Fig. 4.48 with AMS-E sinusoid with phase of 44° superimposed.....	84
Figure 4.51. The initial HMM $f 3_k$ phase estimates for first pass of PPD-WE algorithm on data shown in Fig. 4.50.....	85
Figure 4.52. The estimated and true Berlage source wavelets for the first second coefficient illustrated in Fig 4.44.....	86
Figure 4.53. The estimated and true Berlage source wavelets for the third reflection coefficient illustrated in Fig 4.44.....	86
Figure 4.54. The AMTs for the two estimated AMSs shown in Figs. 4.52 and 4.53	87
Figure 4.55. The normalized cross-correlation function for the first and estimated second arriving Berlage source wavelet shown in Fig. 4.52. Peak value occurs at 4.5 ms..	87
Figure 4.56. The normalized cross-correlation function for the first and estimated third arriving Berlage source wavelet shown in Fig. 4.54. Peak value occurs at 8.9 ms..	88
Figure 4.57. The estimated and true reflection coefficients for synthetic seismogram illustrated in Fig. 4.44	88
Figure 4.58. Illustration of the filtered synthetic seismogram of Fig. 4.44 with the AMS-E sinusoid and corresponding initial zero crossing of 4.2 ms shown	90
Figure 4.59. Illustration of the output of the HMM-FE filter after processing the synthetic seismogram shown in Fig. 4.44.....	91
Figure 4.60. Illustration of BSW1 with parameters $f = 55 \text{ Hz}$, $n = 2$, $a = 170$ and $\phi = 60^\circ$ specified.....	92
Figure 4.61. Illustration of BSW2 with parameters $f = 50 \text{ Hz}$, $n = 2$, $a = 170$ and $\phi = 60^\circ$ specified.....	93
Figure 4.62. Illustration of BSW3 with parameters $f = 45 \text{ Hz}$, $n = 2$, $a = 170$ and $\phi = 60^\circ$ specified.....	93
Figure 4.63. Illustration of BSW4 with parameters $f = 40 \text{ Hz}$, $n = 2$, $a = 170$ and $\phi = 60^\circ$ specified.....	94
Figure 4.64. Synthetic seismogram generated by summing time variant source wavelets BSW1, BSW2, BSW3, and BSW4	94
Figure 4.65. The reflection coefficients utilized to generated synthetic seismogram illustrated in Fig. 4.64.....	95
Figure 4.66. The output after convolving BSW1, BSW2, BSW3, and BSW4 with the first, second, third, and fourth reflection coefficients, respectively, shown in Fig. 4.65 ..	95
Figure 4.67. The output after applying a 100 Hz, eighth order, zero-phase shift, low-pass Butterworth frequency filter to the synthetic seismogram shown in Fig. 4.64.....	96

Figure 4.68. Illustration of the output of the HMM-FE filter after processing the synthetic seismogram shown in Fig. 4.64.....	97
Figure 4.69. The estimated and true BSW1 source wavelets	97
Figure 4.70. The estimated residual wavelet and the actual residual wavelet (i.e., BSW1+BSW3+BSW4).....	98
Figure 4.71. The estimated time series residual of Fig. 4.70 with the time parameters t^* and t' set to 11 ms and 8.96 ms, respectively.....	99
Figure 4.72. Illustration of the output of the HMM-FE filter after processing the synthetic seismogram shown in Fig. 4.71.....	99
Figure 4.73. The estimated and true BSW2 source wavelets	100
Figure 4.74. The estimated residual wavelet and the actual residual wavelet (i.e., BSW3+BSW4)	100
Figure 4.75. The estimated time series residual of Fig. 4.74 with the time parameters t^* and t' set to 17 ms and 15 ms, respectively.....	101
Figure 4.76. Illustration of the output of the HMM-FE filter after processing the synthetic seismogram shown in Fig. 4.75.....	102
Figure 4.77. The estimated and true BSW3 source wavelets	103
Figure 4.78. The estimated and true BSW4 source wavelets	103
Figure 4.79. Typical synthetic seismogram.....	105
Figure 4.80. The amplitude spectrum of seismogram illustrated in Fig. 4.79.....	105
Figure 4.81. Superposition of filtered seismogram onto seismogram shown in Fig. 4.79	106
Figure 4.82. Illustration of the output of the HMM-FE filter after processing the synthetic seismogram shown in Fig. 4.81.....	107
Figure 4.83. The estimated (solid black line) and true (dotted line) first arriving source wavelet	108
Figure 4.84. The estimated (solid black line) first arriving source wavelet of Fig. 4.83 with the time series beyond 105 ms set to zero.....	109
Figure 4.85. The superposition of the true reflection series (black line) onto the estimated reflection series (dotted line).....	110
Figure 4.86. Ten PPD-WE estimates for noisy synthetic seismogram shown in Fig. 4.79. The estimate illustrated by the dotted line differs from the nine other approximations. The bold light grey line identifies the true source wavelet.....	111
Figure 4.87. Synthetic seismogram where the noise free seismogram of Fig. 4.79 has additive Gauss-Markov noise with a time constant of 0.001 ms and a variance of 0.005 units ²	112
Figure 4.88. The PPD-WE source wavelet estimates for ten additive Gauss-Markov noise (time constant of 0.001 ms and a variance of 0.005 units ²) realizations. The bold light grey line identifies the true source wavelet	113
Figure 4.89. The output after overlapping two Berlage source wavelets with additive measurement noise. These two source wavelets have a phase difference of 170°.	114
Figure 4.90. The output of the PPD algorithm where the algorithm was able to separate the two source wavelets, but has some difficulty in estimating the modulating amplitude term.	115

Figure 4.91. The error residual between the estimated PPD Berlage wavelet and the true Berlage wavelet with arrival time of 99 ms.	115
Figure 4.92. The error residual between the estimated PPD Berlage wavelet and the true Berlage wavelet with arrival time of 108 ms.	116
Figure 4.93. Illustration of the null spaces with a 50 Hz (T = 20 ms) source wavelet. Overlapping wavelets which arrive within the null spaces cannot be separated from the source wavelet to be extracted.....	117
Figure 4.94. Typical SCPT configuration.	120
Figure 4.95. Raw X axis VSP from SCPT hole SC 64	121
Figure 4.96. Raw Y axis VSP from SCPT hole SC 64	122
Figure 4.97. VSP for the processed seismic data captured at test site SC 64 for depths 2 m to 17 m. There is clear evidence of overlapping source wavelets.....	123
Figure 4.98. The amplitude spectrum of the seismogram captured at 2 m	125
Figure 4.99. Estimating t'_{min} for the seismogram acquired at 12 m	125
Figure 4.100. Extracted (utilizing PPD-WE technique) primary source wavelets VSP for depths 2 m to 17 m of SCPT hole SC 64	127
Figure 4.101. Residual wavelets VSP for depths 3 m to 17 m of SCPT hole SC 64	129
Figure 4.102. Estimated reflection coefficients for depth 16 m utilizing the WLT	130
Figure 4.103. Estimated reflection coefficients for depth 17 m utilizing the WLT	130
Figure 4.104. Superposition of estimated primary source wavelets for depths 4m to 17m...	131
Figure 4.105. Estimated source wavelet (black line) obtained by averaging estimated PPD-WE source wavelets shown in Fig. 4.104. The light grey lines signify the maximum and minimum bounds based upon the response outlined in Fig. 4.104	131
Figure H.1. Thirty five PPD-WE primary source wavelet estimations at depth of 3.0 m	154
Figure H.2. The Averaged Estimated First Arriving Source Wavelet at 3.0m	154
Figure H.3. The estimated first arriving source wavelet superimposed upon residual wavelet at 3.0 m.....	154
Figure H.4. Thirty five PPD-WE primary source wavelet estimations at depth of 4.0 m	155
Figure H.5. The Averaged Estimated First Arriving Source Wavelet at 4.0m	155
Figure H.6. The estimated first arriving source wavelet superimposed upon residual wavelet. One can have high confidence in the results due to the fact that the Primary and Secondary source wavelets are very similar in form.....	155
Figure H.7. Thirty five PPD-WE primary source wavelet estimations at depth of 5.0 m	156
Figure H.8. The Averaged Estimated First Arriving Source Wavelet at 5.0m	156
Figure H.9. The estimated first arriving source wavelet superimposed upon residual wavelet at 5.0 m.....	156
Figure H.10. Thirty five PPD-WE primary source wavelet estimations at depth of 6.0 m ...	157
Figure H.11. The Averaged Estimated First Arriving Source Wavelet at 6.0m	157
Figure H.12. The estimated first arriving source wavelet superimposed upon residual wavelet at 6.0 m.....	157
Figure H.13. Thirty five PPD-WE primary source wavelet estimations at depth of 7.0 m ...	158
Figure H.14. The Averaged Estimated First Arriving Source Wavelet at 7.0m	158

Figure H.15. The estimated first arriving source wavelet superimposed upon residual wavelet at 7.0 m	158
Figure H.16. Thirty five PPD-WE primary source wavelet estimations at depth of 8.0 m ...	159
Figure H.17. The Averaged Estimated First Arriving Source Wavelet at 8.0m	159
Figure H.18. The estimated first arriving source wavelet superimposed upon residual wavelet at 8.0 m	159
Figure H.19. Thirty five PPD-WE primary source wavelet estimations at depth of 9.0 m ...	160
Figure H.20. The Averaged Estimated First Arriving Source Wavelet at 9.0m	160
Figure H.21. The estimated first arriving source wavelet superimposed upon residual wavelet at 9.0 m	160
Figure H.22. Thirty five PPD-WE primary source wavelet estimations at depth of 10.0 m .	161
Figure H.23. The Averaged Estimated First Arriving Source Wavelet at 10.0m	161
Figure H.24. The estimated first arriving source wavelet superimposed upon residual wavelet at 10.0 m1	161
Figure H.25. Thirty five PPD-WE primary source wavelet estimations at depth of 11.0 m .	162
Figure H.26. The Averaged Estimated First Arriving Source Wavelet at 11.0m	162
Figure H.27. The estimated first arriving source wavelet superimposed upon residual wavelet at 11.0 m	162
Figure H.28. Thirty five PPD-WE primary source wavelet estimations at depth of 12.0 m .	163
Figure H.29. The Averaged Estimated First Arriving Source Wavelet at 12.0m	163
Figure H.30. The estimated first arriving source wavelet superimposed upon residual wavelet at 12.0 m	163
Figure H.31. Thirty five PPD-WE primary source wavelet estimations at depth of 13.0 m .	164
Figure H.32. The Averaged Estimated First Arriving Source Wavelet at 13.0m	164
Figure H.33. The estimated first arriving source wavelet superimposed upon residual wavelet at 13.0 m	164
Figure H.34. Thirty five PPD-WE primary source wavelet estimations at depth of 14.0 m .	165
Figure H.35. The Averaged Estimated First Arriving Source Wavelet at 14.0m	165
Figure H.36. The estimated first arriving source wavelet superimposed upon residual wavelet at 14.0 m	165
Figure H.37. Thirty five PPD-WE primary source wavelet estimations at depth of 15.0 m .	166
Figure H.38. The Averaged Estimated First Arriving Source Wavelet at 15.0m	166
Figure H.39. The estimated first arriving source wavelet superimposed upon residual wavelet at 15.0 m	166
Figure H.40. Thirty five PPD-WE primary source wavelet estimations at depth of 16.0 m .	167
Figure H.41. The Averaged Estimated First Arriving Source Wavelet at 16.0m	167
Figure H.42. The estimated first arriving source wavelet superimposed upon residual wavelet at 16.0 m	167
Figure H.43. Thirty five PPD-WE primary source wavelet estimations at depth of 17.0 m .	168
Figure H.44. The Averaged Estimated First Arriving Source Wavelet at 17.0m	168
Figure H.45. The estimated first arriving source wavelet superimposed upon residual wavelet at 17.0 m	168

List of Abbreviations

Abbrev.	Meaning
A	
AMS	amplitude modulated sinusoid
AMT	amplitude modulating term
AMS-E	AMS source wavelet to be extracted
ARMA	autoregressive moving average
B	
BRE	Bayesian recursive estimation
BSW	Berlage source wavelet
BSD	blind seismic deconvolution
BIS	Bayesian importance sampling
D	
DF	dominant frequency
F	
FSMCD	finite state Markov chain distribution
FMDSM	Forward Modeling / Downhill Simplex Method
H	
HMM	hidden Markov model
HMM-FE	HMM frequency estimation
J	
JMLGS	jump Markov linear Gaussian systems
K	
KF	Kalman filter
KFSD	Kalman filter seismic deconvolution

P	
PF	particle filters
PDF	probability distribution function
PSM	passive seismic monitoring
PS-SEED	passive seismic signal enhancement and event detection
PPD	principle phase decomposition
PPD-WE	PPD filter wavelet extraction
PPD-WEMC	PPD filter wavelet extraction Monte Carlo
R	
RBPF	Rao-Blackwellised particle filter
S	
S/N	signal to noise ratio
SMC	sequential Monte Carlo
SIR	sampling importance re-sampling
STA/LTA	short term averaging / long term averaging
SWE	source wavelet to be extracted
SC	seismic cone
SCPT	seismic cone penetration test
V	
VSP	vertical seismic profiling
V _p	P-wave velocity
V _s	S-waves velocities
W	
WLT	water level technique

Acknowledgments

The work outlined in this thesis would not have been possible without the guidance of Dr. Tadeusz Ulrych. Dr. Ulrych's openness to exploring new ideas in seismic signal processing, and his strong background in this area, facilitated the advancement of my research interests. Dr. Vikram Krishnamurthy, of the University of British Columbia's Electrical and Computer Engineering Department, is an expert in the design and implementation of Bayesian recursive estimation filters, and I greatly appreciate his agreement to act as one of my committee members. Dr. Krishnamurthy is responsible for introducing me to the relatively new and exciting technique of sequential Monte Carlo filtering or more commonly known as particle filtering. Dr. Michael Bostock's expertise in seismology was fundamental for a thorough review of my work. In addition, Dr. Bostock's assistance proved essential in the completion of my thesis and its subsequent submission to the university's Department of Graduate Studies.

Dedication

This thesis is dedicated to my beautiful and loving wife, Colleen: without her support, this work would not have been possible.

Application of Bayesian Recursive Estimation for Seismic Signal Processing

I. Introduction

There is considerable interest in the engineering community in the relatively new implementation of sequential Monte Carlo (SMC) methods [3], [26], [27], [35] to solve optimal estimation problems where the physical system is non-stationary and non-linear. In addition, SMC techniques are ideally suited for real-time optimal estimation. SMC filters are a form of Bayesian recursive estimation (BRE) and they are most commonly referred to as particle filters (PF). In SMC filtering, the required posterior density function is represented by a set of random samples with associated weights where state estimates are computed based on these samples and weights. To the best of my knowledge, there currently is little published work with regard to the implementation of PF and its variants for solving seismic signal processing problems. Section III of this thesis outlines the mathematical background of BRE where the requirement of modeling the physical problem in a state-space formulation is addressed and the fundamental Chapman-Komolgorov equation is outlined. Additional topics covered include the Kalman filter formulation, jump Markov linear Gaussian systems, hidden Markov model filter, particle filtering, and Rao-Blackwellised particle filtering.

Crump [22] and Bayless and Brigham [6] were among the first researchers to fit geophysical problems into a BRE formulation. Mendel and his colleagues [41], [42] carried out work in implementing BRE techniques for solving the seismic deconvolution problem. In Mendel's work, the basic seismogram was modeled as an ARMA process. In the work of Bayless, Brigham, Crump, and Mendel the Kalman filter (KF) set of equations were utilized. Kalman filtering is a particular restrictive form of BRE where certain conditions are required. These special conditions consist of the case where the measurement and process noise are zero mean independent Gaussian white noise processes, the system equation is a linear function of the state vector and process noise, the measurement is a linear function of the state vector and measurement noise, and the initial estimate of state vector has a Gaussian distribution. The focus of my research has been to structure geophysical optimal estimation problems

into BRE formulations, so that the relatively new and powerful PF technique and its variants could be utilized. Two specific seismic signal processing problems I address are real-time, non-linear, non-stationary passive seismic event detection and blind seismic deconvolution (BSD).

A passive seismic monitoring (PSM) system is an assembly of hardware and software components designed to acquire and analyze, in real time, the acoustic signals collected by an array of appropriate seismic transducers. Section III(A) outlines a novel, unique and robust algorithm for identifying seismic events within low signal-to-noise ratio (S/N) passive seismic data in real-time. This algorithm is referred as the passive seismic signal enhancement and event detection (PS-SEED) filter. Since the event detection problem is a continuous, real-time process that has non-linear mathematical representations, a Rao-Blackwellised particle filter is utilized. In this algorithm, a jump Markov linear Gaussian system (JMLGS) is defined where changes (i.e., jumps) in the state-space system and measurement equations are due to the occurrences and losses of events within the measurement noise. The Rao-Blackwellised particle filter (RBPF) obtains optimal estimates of the possible seismic events by individually weighting and subsequently summing a bank of Kalman filters. These Kalman filters are specified and updated by samples drawn from a Markov chain distribution that defines the probabilities and transitional probabilities of the individual dynamical systems which compose the JMLGS. In addition, a hidden Markov model filter is utilized within the RBPF filter formulation so that real-time estimates of the phase of the seismic event can be obtained. The PS-SEED filter is demonstrated to provide up to an 80-fold improvement in the S/N when processing simulated seismic data with highly variable Gauss-Markov measurement noise.

Seismic deconvolution is a very widely utilized signal enhancement technique in seismic signal processing. Ideally, by deconvolving the source wavelet from the recorded time series data, only the reflection coefficients remain. The reflection coefficients identify the impedance mismatches between different stratigraphic layers. BRE is ideally suited for seismic deconvolution, due to the fact that one easily accounts for non-stationarity of the source wavelet and a wide variety of additive measurement noise models can readily be incorporated into the model. There are two types of seismic deconvolution problems. The first consist of the typical case where the source wavelet is assumed known and the

reflection coefficients are unknown. The second problem is referred to as blind deconvolution. In this case, both the source wavelet and reflection coefficients are assumed unknown. Section IV(B)-1 outlines a KF algorithm for carrying out seismic deconvolution on simulated data where the source wavelet is known and the seismogram is modeled as an ARMA process (where the reflection coefficients are assumed Gaussian and white).

Section IV(B)-2 outlines an innovative and powerful RBPF algorithm for solving the BSD problem. This algorithm is referred to as principle phase decomposition (PPD) and it incorporates a ground-breaking concept when carrying out BSD. The PPD algorithm is shown to have many advantages such as simple filter formulation with minimal parameter specification, conducive to blind seismic deconvolution, assumption of minimum phase source wavelet is not required, ability to apply frequency filters so that high frequency measurement noise is readily removed, avoids problems associated with band-limited source wavelets when carrying out frequency domain deconvolution, easily handles non-stationary source wavelets, provides for time-variant estimations of the source wavelet, relatively low associated computer processing cost, reflection coefficients are not required to be represented by discrete state levels, and a whiteness assumption governing the reflection coefficient series is not required.

In both the PS-SEED and PPD formulations, an innovative model of the source wavelet is outlined and utilized. This source wavelet model is referred to as the amplitude modulated sinusoid (AMS). The AMS representation of the source wavelet is a highly robust and accurate (with only two defining parameters) model which allows for time variance. The AMS is demonstrated to be a highly accurate approximation for many analytical representations of seismic source wavelets such as the exponentially decaying cyclic waveform, mixed-phase Berlage wavelet, zero-phase Ricker wavelet, and zero-phase Klaunder wavelet. In addition, the AMS wavelet has proven very accurate in modeling seismic data acquired during passive seismic monitoring and vertical seismic profiling. In both the PS-SEED and PPD formulations, all the associated filters of BRE (hidden Markov model filter, KF, particle filter, Rao-Blackwellised particle filter, and jump Markov systems) are implemented.

II. Bayesian Recursive Estimation and Seismic Modeling

Bayesian recursive estimation is an optimal filtering technique that is based on state-space, time-domain formulations of physical problems. Application of this type of filter requires that the dynamics of the system and measurement model that relates the noisy measurements to the system state equations be describable in a mathematical representation and probabilistic form which, with initial conditions, uniquely defines the system behaviour. The potentially non-linear discrete stochastic equation describing the system dynamics is defined as follows:

$$\mathbf{x}_k = \mathbf{f}_{k-1}(\mathbf{x}_{k-1}, \mathbf{u}_{k-1}) \leftrightarrow p(\mathbf{x}_k | \mathbf{x}_{k-1}) \quad (1)$$

In (1), the vector \mathbf{f}_k is a non-linear function of the state vector \mathbf{x}_k and the process or system noise \mathbf{u}_k . (1) describes a Markov process of order one. The sampled, potentially non-linear, measurement equation is given as follows:

$$z_k = \mathbf{h}_k(\mathbf{x}_k, \mathbf{v}_k) \leftrightarrow p(z_k | \mathbf{x}_k) \quad (2)$$

In (2), \mathbf{h}_k depends on the index k , the state \mathbf{x}_k , and the measurement noise \mathbf{v}_k at each sampling time. The probabilistic state-space formulation described by (1) and the requirement for updating the state vector estimate based upon the newly available measurements described by (2) are ideally suited for the Bayesian approach to optimal estimation.

The main advantages of utilizing a state-space formulation in describing physical problems is three-fold. 1) Time variance of the system and measurement dynamics and statistics can readily be accounted for. 2) Complicated time variant measurement noise models can easily be incorporated into the measurement equations. 3) The ability to utilize process or system noise to compensate for errors in the mathematical model of the system dynamics. If the seismic signal processing problem can be cast into state-space form, then the previously described benefits can be used to obtain an optimal solution.

The most important seismic model is, in general, written as [51]

$$z(t) = S(t) * \mu(t) + v(t) \quad (3)$$

where

$z(t)$: is the measured seismogram.

$S(t)$: is the seismic wavelet which is a superposition of earth and instrument responses.

$\mu(t)$: is the reflectivity of the earth which consists of all primary reflections as well as all surface and internal multiples.

$v(t)$: is the additive noise, generally taken to be white with a Gaussian pdf.

$*$: denotes the convolution operation.

A fundamental task for the seismologist is to estimate the impedance at depth from the recorded seismogram. A commonly adopted simple model, referred to as the Goupillaud layered medium [51], in applied seismology is that of a horizontally layered, one dimensional earth. The impedance of the k th layer of the pancake earth model is defined as

$$\varepsilon_k = \rho_k V_k \quad (4)$$

where ρ_k and V_k are, respectively, the density and velocity in the k th layer. The relationship between ε_k and μ_k , the reflection coefficient (assuming only primary reflection) of the k th layer, is

$$\mu_k = \frac{\varepsilon_{k+1} - \varepsilon_k}{\varepsilon_{k+1} + \varepsilon_k} \quad (5)$$

Rearranging (5) gives

$$\varepsilon_{k+1} = \varepsilon_k \left(\frac{1 + \mu_k}{1 - \mu_k} \right) = \varepsilon_1 \prod_{j=1}^k \left(\frac{1 + \mu_j}{1 - \mu_j} \right) \quad (6)$$

Therefore, it is required to estimate the reflection series, μ_k , in order to determine ε_k . In extracting the reflection series, the source wavelet must first be estimated and then deconvolved from the recorded seismogram.

If the measurement noise term in (3) is ignored, then the Z transform of (3) is given as

$$z(t) = S(t) * \mu(t) \Leftrightarrow Z(z) = S(z)\Psi(z) \quad (7)$$

where $\Psi(z)$ denotes the Z transform of the reflection series $\mu(t)$. Ulrych and Sacchi [51] eloquently illustrate that the seismogram given in (7) defines a autoregressive moving average (ARMA) process if it is assumed that the reflection series are Gaussian and white. A process is AR if it is assumed that the present observation is a linear combination of past observations plus a Gaussian random variable. For stability, the AR process is required to be minimum phase (i.e., zeros outside the unit circle (geophysical convention)). A time series is defined to be a MA process if it is assumed to be generated by a finite linear combination of past and present inputs only where the input is defined to be white. As expected, an ARMA time series is generated by the combination of an AR and MA process.

As outlined in Section IV(B), Mendel [42] fitted the ARMA representation of the basic seismogram into a linear state-space formulation. Mendel then applied a linear Kalman filter smoother (a particularly restrictive form of BRE) to solve the deconvolution problem. As pointed out in Section IV(B), the main disadvantages of utilizing a KFS is that it is very difficult to model seismograms by low order ARMA representations when the source wavelet is mixed or zero phase. The ARMA model is highly susceptible to sampling rates where higher rates typically require a higher order for the ARMA model. Most importantly,

the KFS algorithm is poorly suited for deconvolving seismograms with non-stationary source wavelets and for addressing the blind deconvolution problem.

Another important problem in seismic signal processing is the real-time detection of acoustic events during passive seismic monitoring. The solution to this problem also requires a non-linear approach. In order to address the issues of blind seismic deconvolution and passive seismic event detection within the state-space and BRE contexts, the relatively new techniques of sequential Monte Carlo (SMC) filtering are both reviewed and adapted in this thesis. In general terms, SMC filters are a form of Bayesian recursive estimation (BRE) where a set of particles define the possible values of a variable (in the one dimensional case) that one is interested in. These particles are propagated according to the system dynamics, (1), and they are subsequently weighted in a maximum-likelihood sense by using the measurement equations, (2). The set of particles and their corresponding weights allows one to numerically calculate the posterior density function and subsequently derive a conditional mean estimate of the variable of interest.

III. Mathematical background

A. Bayesian Recursive Estimation

In the Bayesian approach to optimal estimation, it is attempted to construct the posterior estimate of the state given all available measurements [3]. In general terms, it is desired to obtain estimates of the discretized system equation states \mathbf{x}_k based on all available measurements up to time k (denoted as $\mathbf{z}_{1:k}$) by constructing the posterior $p(\mathbf{x}_k | \mathbf{z}_{1:k})$ and having the initial (prior) pdf of the state $p(\mathbf{x}_0)$ specified as an initial condition. The posterior pdf allows one to calculate the conditional mean estimate of the state ($E[\mathbf{x}_k | \mathbf{z}_{1:k}]$).

BRE is a two-step process consisting of prediction and update [3]. The prediction step involves using the system equation defined by (1) to obtain the prior pdf of the state at time k via the Chapman-Kolmogorov equation that is given as follows:

$$p(\mathbf{x}_k | \mathbf{z}_{1:k-1}) = \int p(\mathbf{x}_k | \mathbf{x}_{k-1}) p(\mathbf{x}_{k-1} | \mathbf{z}_{1:k-1}) d\mathbf{x}_{k-1} \quad (8)$$

The Chapman-Kolmogorov equation is derived based upon the transitional densities of a Markov sequence. The derivation of the Chapman-Kolmogorov equation is outlined in Appendix A. The prediction step generally deforms, translates, and spreads the state pdf due to the system equations and process noise. The update step computes the posterior pdf from the predicted prior pdf and a newly available measurement. The posterior pdf is updated via Bayes' rule as follows:

$$p(\mathbf{x}_k | \mathbf{z}_{1:k}) = \frac{p(\mathbf{z}_k | \mathbf{x}_k) p(\mathbf{x}_k | \mathbf{z}_{1:k-1})}{p(\mathbf{z}_k | \mathbf{z}_{1:k-1})} \quad (9)$$

where the normalizing constant is given as follows:

$$p(\mathbf{z}_k | \mathbf{z}_{1:k-1}) = \int p(\mathbf{z}_k | \mathbf{x}_k) p(\mathbf{x}_k | \mathbf{z}_{1:k-1}) d\mathbf{x}_k$$

Equation (4) can also be represented as follows:

$$posterior = \frac{likelihood \cdot prior}{evidence}$$

where the prior is given by the system equation, the likelihood is given by the measurement equation, and the evidence is the normalizing constant in the denominator. The update step usually concentrates the state pdf by the action of combining the likelihood of the current measurement with the predicted state [43]. Appendix B outlines the derivation of the BRE update equation and the derivation of the “likelihood” formula is given in Appendix D. The recurrence equations defined by (8) and (9) form the basis for the optimal Bayesian solution. The BRE of the posterior density can be solved optimally (exact solution) when the state-space equations fit into a Kalman filter formulation or a Hidden Markov Model [3]. Otherwise, BRE requires an asymptotically optimal numerical estimation approach when deriving the posterior pdf.

B. Kalman Filter and Jump Markov Linear Gaussian System

As previously stated, the standard set of KF equations can be implemented as an optimal solution to the BRE when certain conditions are met. These special conditions consist of the case where \mathbf{u}_k and \mathbf{v}_k are zero mean independent, Gaussian white noise processes, \mathbf{f}_k is a linear function of the state vector and process noise, \mathbf{h}_k is a linear function of the state vector and measurement noise, and the initial estimate of \mathbf{x}_0 has a Gaussian distribution [33].

Similar to the KF, a JMLGS is also defined as a linear Gaussian system, but in this case the system and/or measurement equations (\mathbf{f}_k and \mathbf{h}_k) evolve with time according to a finite state Markov chain [24], [28], [29]. Table 3.1 outlines the KF governing equations for a JMLGS [24]. The index, i , denoted in Table 3.1, facilitates the implementation of a bank of Kalman filters when implementing a RBPF (subsequently outlined).

TABLE 3.1
KF GOVERNING EQUATIONS FOR JMLGS

Eq.	Description	Mathematical Representation
10	Finite state Markov chain.	$y_k^i \sim P(y_k^i y_{k-1}^j)$
11	System equation.	$\mathbf{x}_k^i = \mathbf{F}(y_k^i) \mathbf{x}_{k-1}^i + \mathbf{G}(y_k^i) \mathbf{u}_{k-1}^i$
12	Measurement equation.	$\mathbf{z}_k^i = \mathbf{H}(y_k^i) \mathbf{x}_k^i + \mathbf{v}_k^i$
13	State estimate extrapolation.	$\hat{\mathbf{x}}_{k k-1}^i = \mathbf{F}(y_k^i) \hat{\mathbf{x}}_{k-1 k-1}^i$
14	Error covariance extrapolation.	$\mathbf{P}_{k k-1}^i = \mathbf{F}(y_k^i) \mathbf{P}_{k-1 k-1}^i \mathbf{F}(y_k^i)^T + \mathbf{G}(y_k^i) \mathbf{Q}_{k-1 k-1}^i \mathbf{G}(y_k^i)^T$
15	Measurement extrapolation.	$\hat{\mathbf{z}}_k^i = \mathbf{H}(y_k^i) \hat{\mathbf{x}}_{k k-1}^i$
16	Innovation.	$\mathbf{v}_k^i = \mathbf{z}_k^i - \hat{\mathbf{z}}_k^i$
17	Variance of innovation.	$\mathbf{S}_k^i = \mathbf{H}(y_k^i) \mathbf{P}_{k k-1}^i \mathbf{H}(y_k^i)^T + \mathbf{R}_k^i$
18	Kalman gain matrix.	$\mathbf{K}_k^i = \mathbf{P}_{k k-1}^i \mathbf{H}(y_k^i)^T (\mathbf{S}_k^i)^{-1}$
19	State estimate update.	$\hat{\mathbf{x}}_{k k}^i = \hat{\mathbf{x}}_{k k-1}^i + \mathbf{K}_k^i \Delta_k^i$
20	Error covariance update.	$\mathbf{P}_{k k}^i = [\mathbf{I} - \mathbf{K}_k^i \mathbf{H}(y_k^i)] \mathbf{P}_{k k-1}^i$

In (11) and (12) \mathbf{v}_k and \mathbf{u}_k are mutually uncorrelated *i.i.d* Gaussian zero mean white noise processes with variances of \mathbf{Q}_k and \mathbf{R}_k , respectively (i.e., $\mathbf{v}_k \sim N(0, \mathbf{R}_k)$ and $\mathbf{u}_k \sim N(0, \mathbf{Q}_k)$). Matrices \mathbf{F} and \mathbf{G} define the recursive nature of the system and process noise, respectively. Matrix \mathbf{H} defines the relationship between the system states and the available measurements.

In terms of the BRE, the Kalman Filter can be viewed as the following recursive relationship:

$$p(\mathbf{x}_{k-1} | \mathbf{z}_{1:k-1}) = N(\mathbf{x}_{k-1}; \hat{\mathbf{x}}_{k-1|k-1}, \mathbf{P}_{k-1|k-1}) \quad (21a)$$

$$p(\mathbf{x}_k | \mathbf{z}_{1:k-1}) = N(\mathbf{x}_k; \hat{\mathbf{x}}_{k|k-1}, \mathbf{P}_{k|k-1}) \quad (21b)$$

$$p(\mathbf{x}_k | \mathbf{z}_{1:k}) = N(\mathbf{x}_k; \hat{\mathbf{x}}_{k|k}, \mathbf{P}_{k|k}) \quad (21c)$$

The KF has the sufficient finite dimensional statistics of mean and error covariance.

C. Hidden Markov Model Filter

The HMM filter (also termed a grid-based filter) has a discrete state-space representation and has a finite number of states. In the HMM filter the posterior pdf is represented by the delta function approximation as follows:

$$p(\mathbf{x}_{k-1} | \mathbf{z}_{1:k-1}) = \sum_{i=1}^{N_s} \mathbf{w}_{k-1|k-1}^i \delta(\mathbf{x}_{k-1} - \mathbf{x}_{k-1}^i) \quad (22)$$

where \mathbf{x}_{k-1}^i and $\mathbf{w}_{k-1|k-1}^i$, $i = 1, \dots, N_s$, represent the fixed discrete states and associated conditional probabilities, respectively, at time index $k-1$.

The governing equations for the HMM filter are derived by substituting (22) into the Chapman-Kolmogorov equation (8) and the posterior pdf update equation (9). This substitution results in the HMM prediction and update equations which are outlined in Table 3.2 [3].

TABLE 3.2
HMM FILTERING ALGORITHM

Step	Description	Mathematical Representation
1	Initialization (k=0) – initialize particle weights.	e.g., $w_k^i \sim 1/N_s, i = 1, \dots, N_s$.
2	Prediction - predict the weights.	$w_{k k-1}^i = \sum_{j=1}^{N_s} w_{k-1 k-1}^j p(x_k^i x_{k-1}^j)$
3	Update - update the weights.	$w_{k k}^i = \frac{w_{k k-1}^i p(z_k x_k^i)}{\sum_{j=1}^{N_s} w_{k k-1}^j p(z_k x_k^j)}$
4	Obtain optimal minimum variance estimate of the state vector and corresponding error covariance.	$\hat{x}_k \approx \sum_{i=1}^{N_s} w_{k k}^i x_k^i \quad \&$ $P_{\hat{x}_k} \approx \sum_{i=1}^{N_s} w_{k k}^i (x_k^i - \hat{x}_k)(x_k^i - \hat{x}_k)^T$
5	Let $k = k+1$ & iterate to step 2.	

In the above equations it is required that the likelihood pdf $p(z_k | x_k^i)$ and the transitional probabilities $p(x_k^i | x_{k-1}^j)$ be known and specified.

D. Particle Filter and Rao-Blackwellised Particle Filter

1) *Particle Filter*: As stated previously, the recurrence equations defined by (8) and (9) form the basis for the optimal Bayesian solution, and, except for the KF and HMM exact solutions, the BRE requires an asymptotically optimal numerical estimation approach. To solve the BRE numerically, a new family of filters that rely upon sequential Monte Carlo (SMC) methods have been made popular within the last decade. This family of new filters are most commonly referred to as particle filters.

Similar to the HMM filter, the particle filter (PF) represents the posterior pdf by the delta function approximation, but in this case a randomized grid is utilized for the estimation of the posterior pdf. If there was perfect Monte Carlo sampling ($\mathbf{x}_k^i \sim p(\mathbf{x}_k | \mathbf{z}_{1:k})$) then:

$$\lim_{N_s \rightarrow \infty} \left(\frac{1}{N_s} \sum_{i=1}^{N_s} \mathbf{x}_k^i \right) = E[\mathbf{x}_k | \mathbf{z}_{1:k}]$$

according to the strong law of large numbers. For non-linear, asymptotically optimal estimation problems, it is nearly impossible to sample from $p(\mathbf{x}_k | \mathbf{z}_{1:k})$; therefore, the weights in (22) are obtained using Bayesian importance sampling (BIS) [3].

a) Bayesian Importance Sampling

The basic idea in BIS is to represent the posterior density by a set of samples and corresponding weights utilizing an importance density. Suppose $p(x)$ is the desired probability density function which is to be estimated, where the weighted grid estimate of $p(x)$ is defined as follows:

$$p(x) = \frac{p^*(x)}{Y} \approx \sum_{i=1}^{N_s} w^i \delta(x - x^i) \quad (23)$$

In (23), it is assumed that the pdf $p(x)$ is related to pdf $p^*(x)$ via constant of proportionality Y . A proposal *importance density distribution* where samples x^i can easily be obtained¹ is then defined as follows:

$$q(x) = \frac{1}{N_s} \sum_{i=1}^{N_s} \delta(x - x^i) \quad (24)$$

The numerator and denominator of (23) are multiplied by $q(x)$ to give the following:

$$p(x) = \frac{1}{Y} \frac{p^*(x)}{q(x)} q(x) \approx \frac{1}{Y} \frac{p^*(x)}{q(x)} \frac{1}{N_s} \sum_{i=1}^{N_s} \delta(x - x^i) \quad (25)$$

Based upon the results of (25) it is clear that the constant Y must be given as² shown:

$$Y \approx \frac{1}{N_s} \sum_{i=1}^{N_s} \frac{p^*(x^i)}{q(x^i)} \quad (26)$$

Substituting (26) into (25) gives the following:

$$p(x) \approx \frac{\frac{p^*(x)}{q(x)} \sum_{i=1}^{N_s} \delta(x - x^i)}{\sum_{i=1}^{N_s} \frac{p^*(x^i)}{q(x^i)}} \quad (27)$$

Comparing (27) with (23) we see that the normalized weights for estimating pdf $p(x)$ are defined as shown:

¹ Thus $q(x)$ can be estimated numerically via realizations of x^i .

² The normalization requirement for the probability density function.

$$w^i = \frac{\frac{p^*(x^i)}{q(x^i)}}{\sum_{i=1}^{N_s} \frac{p^*(x^i)}{q(x^i)}} = \frac{\tilde{w}^i}{\sum_{i=1}^{N_s} \tilde{w}^i}, \quad \text{where } \tilde{w}^i = \frac{p^*(x^i)}{q(x^i)} \quad (28)$$

If it desired to obtain samples from the posterior density $p(x|z) \propto p(z|x)p(x)$, one could assign the prior as the proposal (i.e., $q(x) = p(x)$) to give the following weight:

$$\tilde{w}^i = \frac{p(z|x^i)p(x^i)}{q(x^i)} = \frac{p(z|x^i)p(x^i)}{p(x^i)} = p(z|x^i) \quad (29)$$

For the PF set of equations, it can be shown as outlined in Appendix C that the following recursive relationship holds for the importance weights as shown:

$$\tilde{w}_k^i = \tilde{w}_{k-1}^i \frac{p(z_k | \mathbf{x}_k^i) p(\mathbf{x}_k^i | \mathbf{x}_{k-1}^i)}{q(\mathbf{x}_k^i | \mathbf{x}_{k-1}^i, z_k)} \quad (30)$$

The posterior density function is then approximated as follows:

$$p(\mathbf{x}_k | z_{1:k}) = \frac{\sum_{i=1}^{N_s} \tilde{w}_k^i \delta(\mathbf{x}_k - \mathbf{x}_k^i)}{\sum_{i=1}^{N_s} \tilde{w}_k^i} \quad (31)$$

A typical particle filtering algorithm is outlined in Table 3.3 [3]. In the algorithm outlined in Table 3.3, the Bayesian *importance density* is defined to be the prior ($p(\mathbf{x}_k^i)$). In addition, a particle degeneracy check is made as indicated in Step 4.

TABLE 3.3
TYPICAL PARTICLE FILTERING ALGORITHM

Step	Description	Mathematical Representation
1	Initialization (k=0) - generate sample particles and set corresponding weights.	$\mathbf{x}_k^i \sim p_{x_0}$ & $w_k^i \sim 1/N_s, i = 1, \dots, N_s.$
2	Update the weights by the likelihood function and then normalize.	$\tilde{w}_k^i = w_{k-1}^i p(z_k \mathbf{x}_k^i)$ & $w_k^i = \tilde{w}_k^i / \sum_{i=1}^{N_s} \tilde{w}_k^i$
3	Obtain asymptotically optimal minimum variance estimate of the state vector and corresponding error covariance.	$\hat{\mathbf{x}}_k \approx \sum_{i=1}^{N_s} w_k^i \mathbf{x}_k^i$ & $\mathbf{P}_{\hat{\mathbf{x}}_k} \approx \sum_{i=1}^{N_s} w_k^i (\mathbf{x}_k^i - \hat{\mathbf{x}}_k)(\mathbf{x}_k^i - \hat{\mathbf{x}}_k)^T$
4	Sampling Importance Re-sampling (SIR). Re-sample if $\hat{N}_{eff} < N_T$	$\hat{N}_{eff} = \frac{1}{\sum_{i=1}^{N_s} (w_k^i)^2} < N_T$
5	Prediction: take $u_k^i \sim p_{u_k}$ & propagate the state particles.	$\mathbf{x}_{k+1}^i = \mathbf{A}\mathbf{x}_k^i + \mathbf{B}u_k^i, i = 1, \dots, N_s.$
6	Let k = k+1 & iterate to step 2.	

b) Sampling Importance Re-sampling (SIR)

A common problem with the SIS approach is that after a few iterations, most particles have a negligible weight (the weight is concentrated on a few particles only). This phenomenon is referred to as the “degeneracy problem”, and it is due to the fact that the variance of the importance weights increase over time. A simple statistic to monitor that gives an indication of the degeneracy is the effective sample size N_{eff} . An approximation to N_{eff} is given in Step 4 of Table 3.3, where N_s defines the number of particles utilized and N_T is a user specified threshold (e.g., $N_T = (0.6 \text{ to } 0.8) N_s$). A small value of N_{eff} indicates severe degeneracy. The standard technique to counter the degeneracy problem is to re-sample the particles utilizing a Bayesian bootstrap technique [3] if the effective number of particles is less than N_T .

The SIR methodology implemented is a Bayesian bootstrap technique. The Bayesian bootstrap technique maps the weighted random measure $\{\mathbf{x}_k^i, \mathbf{w}_k^i\}$ on to the equally weighted random measure $\{\mathbf{x}_k^j, N_s^{-1}\}$ by sampling uniformly with replacement from $\{\mathbf{x}_k^i\}_{i=1}^{N_s}$ with probabilities $\{\mathbf{w}_k^i\}_{i=1}^{N_s}$. Fig. 3.1 [43] outlines the general idea behind SIR. Fig. 3.1 illustrates the initial particles with uniform weight. After a pass of the SIS algorithm a degeneracy check is made. If $N_{eff} < N_T$, then a re-sampling type algorithm is implemented. In the qualitative example shown in Fig 3.1, N_c particles are generated (with weight N_s^{-1}) from the weighted random measure $\{\mathbf{x}_k^i, \mathbf{w}_k^i\}$. N_c is approximately equal to the number of uniform weights contained within \mathbf{w}_k^i (i.e., $N_c \approx \mathbf{w}_k^i / N_s^{-1}$ and $N_c \geq 1$). The newly created and uniformly distributed particles are then propagated through the system equations and the SIR cycle is repeated.

A SIR algorithm similar to that described in Fig 3.1 is outlined as follows [3]:

SIR Algorithm:

- Initialize the CDF: $c_1 = w_k^1$
- For $i = 2: N_s$
 - Construct CDF: $c_i = c_{i-1} + w_k^i$
- End For
- Start at the bottom of the CDF: $i=1$
- Draw a starting point from the uniform distribution: $u_1 \sim U(0, N_s^1)$
- For $j = 1: N_s$
 - Move along the CDF: $u_j = u_1 + N_s^{-1}(j-1)$
 - While $u_j > c_i$
 - $i = i+1$
 - End While
 - Assign sample: $x_k^j = x_k^i$
 - Assign weight: $w_k^j = N_s^{-1}$
- End For

In summary, the SIR technique generates N_i children such that $\sum_{i=1}^{N_s} N_i = N_s$ with $E[N_i] = N_s w_k^i$ and $\text{var}[N_i] = N_s w_k^i (1 - w_k^i)$.

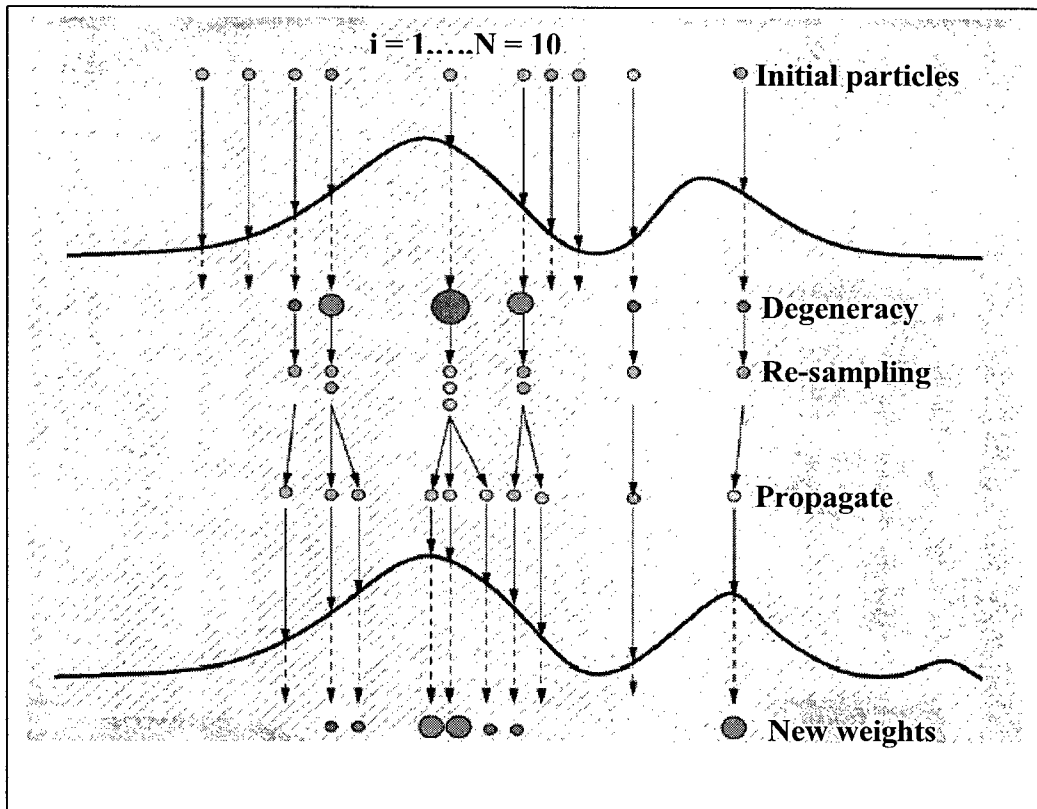


Figure 3.1 Schematic illustrating the bootstrap re-sampling methodology (after, Mühlich [43]).

c) Choice of Importance Function

The degeneracy problem can be minimized by selecting an importance density that minimizes the variance of the importance weights so that N_{eff} is maximized. Consider the following points on importance sampling:

- If $q(x) = p^*(x)$, (27) reduces to simple Monte Carlo estimation.
- Importance sampling is effective when $q(x)$ approximates $p(x)$ over most of the domain.
- There are no absolute requirements for how well $q(x)$ approximates $p(x)$, except that $q(x)$ must not be zero anywhere $p(x)$ is non-zero. In general, all importance functions give correct answers but some require larger N_s values.
- It fails when $q(x)$ misses high probability regions of $p(x)$ and systematically yields samples with small weights.
- To overcome this problem, it is critical to obtain data points from importance regions of $p(x)$ by explicitly searching for significant regions in the target distribution.

The optimal choice of the importance density that minimizes the variance of the importance weights is defined to be as follows [3]:

$$q(\mathbf{x}_k^i | \mathbf{x}_{k-1}^i, \mathbf{z}_k)_{op} = p(\mathbf{x}_k^i | \mathbf{x}_{k-1}^i, \mathbf{z}_k) \quad (32)$$

Substitution of (32) into (30) gives the following result:

$$\tilde{\mathbf{w}}_k^i = \tilde{\mathbf{w}}_{k-1}^i p(\mathbf{z}_k | \mathbf{x}_{k-1}^i) = \tilde{\mathbf{w}}_{k-1}^i \int p(\mathbf{z}_k | \mathbf{x}'_k) p(\mathbf{x}'_k | \mathbf{x}_{k-1}^i) d\mathbf{x}'_k \quad (33)$$

Equation (33) is the optimal importance density because for a given \mathbf{x}_k^i , \mathbf{w}_k^i takes the same value independent from the sample drawn from $q(\mathbf{x}_k | \mathbf{x}_{k-1}, \mathbf{z}_k)_{op}$. Therefore,

conditional on \mathbf{x}_{k-1}^i , the variance of different w_k^i resulting from different sampled \mathbf{x}_k^i is zero (i.e., $\text{var}[w_k^{*i}] = 0$). The optimal importance density is advantageous because one can compute the importance weights w_k^i and sample \mathbf{x}_k^i in parallel, since w_k^i is independent of \mathbf{x}_k^i . Two major drawbacks of the optimal importance density function are as follows:

- The need to be able to sample from $p(\mathbf{x}_k^i | \mathbf{x}_{k-1}^i, z_k)$.
- The need to compute the integral defined by (33) in closed form.

The two cases in which the optimal importance can be used are firstly when \mathbf{x}_k is a member of a finite set. In this case the integral in (33) becomes a sum and it is subsequently possible to sample from $p(\mathbf{x}_k^i | \mathbf{x}_{k-1}^i, z_k)$. The second case in which the optimal importance can be used is when there are non-linear system dynamics, linear measurement equations, and white Gaussian process and measurement noise [3]. In this case the density defined by (32) is Gaussian [25].

For problems which do not meet the previously defined two conditions, a popular choice of the importance density is defined as (i.e., the prior) [3],[43]:

$$q(\mathbf{x}_k^i | \mathbf{x}_{k-1}^i, z_k) = p(\mathbf{x}_k^i | \mathbf{x}_{k-1}^i) \quad (34)$$

Substitution of (34) into (30) gives:

$$\tilde{w}_k^i = \tilde{w}_{k-1}^i p(z_k | \mathbf{x}_k^i) \quad (35)$$

The prior importance density function is easy to implement, and it tends to move samples towards the region of high likelihood. Two drawbacks to the prior importance density function are that it does not take measurements into account and that it is sensitive to outliers.

The Rao-Blackwellised particle filter (RBPF) allows for the reduction in the number of particles when implementing BRE on non-linear systems. This is highly advantageous because, even though there is a theoretical independence of accuracy on the particle dimension, practice has shown that the number of particles needs to be quite high for high dimensional systems [35]. The RBPF combines a bank of KFs with a PF. In this case, the KFs are utilized for generating a set of particles, where the weights of the particles are calculated with a PF [24]. In essence, the posterior pdf is approximated with a recursive, stochastic mixture of Gaussians [4], [24], [26]. This type of particle filtering algorithm is referred to as Rao-Blackwellisation because it is related to the Rao-Blackwell theorem. The Rao-Blackwell theorem is named after Calyampudi Radhakrishna Rao and David Blackwell and it describes a technique that transform a crude estimator into an estimator that is optimal by typically the mean-squared-error criterion [21]. In the RBPFs implemented for the subsequently outlined algorithms, a set of particles are generated by firstly computing the finite state Markov chain distribution, which is denoted as $P(y_k^i | y_{k-1}^i)$ in Table 3.1. Secondly, based upon the samples drawn from $P(y_k^i | y_{k-1}^i)$, a bank of Kalman filters (as outlined in Table 3.1) is utilized to compute a set of particles. The posterior pdf of the state vector is then calculated and subsequent asymptotically optimal estimates are obtained [24].

IV. Seismic Signal Processing

A. Passive Seismic Monitoring

There is considerable interest in the engineering community in the real-time identification of “events” within time series data with low S/N. This is especially true for acoustic emission analysis that is utilized for monitoring and inspecting the integrity and safety of many structures, such as metal and concrete bridges, gas and oil pipe lines, large storage tanks and aerospace vehicles. A particularly important application of acoustics emission analysis is within the field of passive seismology.

A passive seismic monitoring (PSM) system is designed to acquire and analyze, in real time, the acoustic signals collected by an array of appropriate seismic transducers. Seismic activity is often observed in the vicinity of underground excavations, deep open pits and quarries, around and below large reservoirs where fluids are being injected into, or removed from, permeable subsurface formations, and adjacent to the sites of large underground explosions [34].

Extreme examples of energy release can cause violent “rockbursts”, resulting in fatalities and injuries among underground personnel and damage to mine structures (e.g., drifts, stopes, shafts, etc.). Passive seismic systems are capable of detecting rock failures in the vicinity of underground excavations caused by the sudden release of strain energy resulting from the redistribution of stresses around openings.

Various hydrocarbon production sites also benefit from seismic monitoring systems during certain phases of production. Primary or secondary extraction or the injection of material into the reservoir to enhance production can cause significant stress changes. These stress changes can result in failures of the overlying strata and the migration of hydrocarbons to aquifers or to the ground surface. Thus, PSM can be used to satisfy environmental concerns, meet regulatory requirements and assess the development of induced fracturing within the reservoir. In addition, the passive seismic monitoring systems have been successful in identifying and locating casing failures due to steam stimulation in oil sands [49].

During filling of hydroelectric or large irrigation reservoirs, changes in regional loading and pore pressures cause significant stress variations within the surrounding rock mass. These can induce a wide range of micro and macro-seismic events, some of which are capable of causing damage to adjacent structures or to the dam itself. PSM can locate and characterize these potentially hazardous, induced events.

Irrespective of the cause of seismic events, their reliable detection and placement on a common time base is of critical importance. This is because the arrival times and phase identification of the source wavelets (P- and S-wave) at various detector packages, within a three-dimensional array, provide the basis for the calculation of the location of the seismic event. Imprecision or uncertainty in arrival time and phase determination reduces the precision of the source location operation. For example, in many passive seismic monitoring situations where there is interest in the behaviour of specific geological features, or where events must be related to specific structures in a mining or hydrocarbon extraction environment, the accurate determination of event arrival times is the primary rationale for the installation of the system. In regions where the level of induced seismicity is high, and it is accompanied by significant ambient noise, it is essential that the passive seismic monitoring systems possess the capability of automatically identifying the P- and S-waves generated by seismic events within the noise contaminated seismic time series.

Reliable automated identification allows for the timely analysis of a large volume of data, and the delivery of results to the end user in a useful manner. The ability to locate seismic events accurately is directly dependent upon the ability to identify the P-wave, SV-wave and SH-wave responses (phase association) and to determine subsequent arrival times (phase picking) [32]. In addition, the derivation of important source parameters, such as attenuation, seismic moment, source radius, static stress drop, peak particle velocity, seismic energy and failure mechanism (eg., shear, tensile and casing failure) is directly related to the ability to carry out phase association and identification [50].

Since the monitoring of seismic acoustic emissions is a continuous, real-time process that typically runs twenty-four hours a day, seven days a week, it requires the incorporation of real-time, passive seismic signal enhancement and event detection (PS-SEED) digital filters. These digital filters should also provide for non-stationary and non-linear optimal estimation

capabilities. To meet these requirements, an algorithm based upon Bayesian recursive estimation (BRE) is implemented.

The innovative PS-SEED filter outlined in this section substantially builds upon previous original designs [10], [11] in fitting the PSM event detection filter into a Kalman and particle filter formulation. I also believe that the algorithms outlined in [10], [11] are the first published works that attempt to solve the PSM event detection problem utilizing BRE techniques. In the PS-SEED algorithm, a novel and unique model of the seismic event is implemented. This robust source wavelet model is an amplitude modulated sinusoid (AMS). As outlined in this section, the major improvements to the PS-SEED algorithm consist of utilizing a RBPF, which individually weights and subsequently sums a bank of linear Kalman filters with JMLGS characteristics. The JMLGS describes linear system and measurement equations that can change (“jump”) with time. In the PS-SEED filter, a HMM filter is also applied, which allows for the determination of time variant phase estimates if a seismic event is present.

1) PS-SEED Filter Outline

The PS-SEED filter is based upon the standard short term averaging / long term averaging (STA/LTA) technique, where an event is declared within the filtered time series, when the STA/LTA ratio exceeds a predefined threshold [2]. In the PS-SEED digital filter, the seismic event is modeled as an AMS, which is contained within measurement noise [7], [8], [10], [11], [12]. The rationale for modeling the seismic event as an AMS is due to the difficulty in characterizing time variant, passive seismic source wavelets (e.g., ARMA model [25]) and for added robustness, so that the filter can be applied in varied site conditions with minimal modifications.

a) State-Space Formulation

As outlined in [10], [11], [12] the measurement noise is modeled as a Gauss-Markov process with defining parameters of variance and time constant. This does not preclude any other types of ambient noise models, but it is required that the measurement noise be specified

within a state-space formulation. As previously stated, the seismic event is modeled as an AMS as follows (continuous form):

$$x_1(t) = x_2(t) \sin[\omega t + \varphi(t)] \quad (36)$$

where $x_1(t)$ is an approximation to the P-wave or S-wave seismic wavelet (the frequency anomaly), $x_2(t)$ is the seismic wavelet's amplitude modulating term, ω is the dominant frequency of the wavelet, and $\varphi(t)$ is the corresponding phase.

In [10], [11], state $x_2(t)$ was approximated as a random walk process, ω was assumed constant, and $\varphi(t)$ was derived in an *ad hoc* manner. To allow for greater flexibility, the PS-SEED models state $x_2(t)$ as a Gauss-Markov process similar to that outlined for the ambient noise model. More sophisticated amplitude models can be implemented, such as the formulation of a Taylor series on the amplitude dynamics carried out to a third term. The third term (acceleration) is then modeled as a Gauss-Markov process. In the PS-SEED formulation outlined in this section, it is again assumed that ω is constant (i.e., the investigator is looking for a dominant frequency that represents the P-wave or S-wave), while $\varphi(t)$ is derived by implementing a HMM filter.

b) PS-SEED RBPF and HMM Filter Implementation

In general terms, the PS-SEED obtains estimates of the possible seismic events by utilizing a RBPF, which individually weights and subsequently sums a bank of Kalman filters that describe the physics of the ambient noise and seismic event. These Kalman filters are specified and updated by samples drawn from a Markov chain distribution that defines the probability of the individual dynamical systems that compose the JMLGS [8], [24]. In addition, a HMM filter is applied, which determines optimal $\varphi(t)$ values if a seismic event is present. Table 4.1 outlines the PS-SEED filter formulation where Parameters $a(1-2)_k$ and $b(1-2)_k$ define the Gauss-Markov processes and Δ is the sampling rate. Ambient noise parameters $a1_k$ and $b1_k$ are adaptively derived from the autocorrelation of the noise portion of the recorded time series. Parameters $a2_k$ and $b2_k$ are set by specifying 1/3 of the expected maximum possible variance of the amplitude of the seismic event and the corresponding time constant (i.e., correlation between samples) [11]. Appendix E provides for more detail on the implementation of the PS-SEED algorithm.

TABLE 4.1
PS-SEED FILTER FORMULATION

Step	Description	Mathematical Representation
1	<p>Specify and initialize JMLGS system equations and N_s.</p> <p>Note: The measurement noise (v_k) variance R_k is set to $aI_k \times (s_k)^2$, where $(s_k)^2$ is the variance of the Gauss-Markov noise. This allows the filter to put more weight on the prior when the Gauss-Markov noise becomes more correlated from sample to sample.</p>	<p><u>System Dynamics</u></p> $\mathbf{x}_k^2 = \begin{bmatrix} x1_k \\ x2_k \end{bmatrix} = \begin{bmatrix} a1_{k-1} & 0 \\ 0 & a2_{k-1} \end{bmatrix} \begin{bmatrix} x1_{k-1} \\ x2_{k-1} \end{bmatrix} + \begin{bmatrix} b1_{k-1} & 0 \\ 0 & b2_{k-1} \end{bmatrix} \begin{bmatrix} u1_{k-1} \\ u2_{k-1} \end{bmatrix}$ <p><u>Measurement Equations</u> Case 1 ($y1_k$ - ambient noise):</p> $z_k^1 = x1_k + v_k$ <p>Case 2 ($y2_k$ - ambient noise + event):</p> $z_k^2 = x1_k + x2_k \sin(\omega k \Delta + \varphi_k) + v_k$ <p>$p(y_0^1), p(y_0^2), \& p(y_k^i y_{k-1}^j),$ $i, j = 1, 2$</p> <p>$p(\varphi^i) \& p(\varphi^i \varphi^j), i, j = 1, \dots, N_p.$ $N_p = \text{number of fixed-grid values.}$</p> <p>$y_k^i \sim P(y_k^i y_{k-1}^j)$</p> <p>$\text{Sinusoid}(t) = \sin(\omega t + \varphi_k)$</p>
2	Initialize the prior and transitional pdf for the JMLGS.	
3	Initialize the prior and transitional pdf for the fixed-grid phase.	
4	Draw samples for finite state Markov chain.	
5	Propagate sinusoids based current time index ($t = k$?) and phase estimates.	
6	Utilizing (13)-(17) outlined in Table 2.1 and updated sinusoids of Step 5, propagate the system and measurement equations, calculate importance weights for particles and then update and normalize the weights.	$\tilde{w}_k^i = w_{k-1}^i N(z_k \hat{z}_k^i, \mathbf{S}_k^i),, i = 1, \dots, N_s.$ $w_k^i = \tilde{w}_k^i / \sum_{i=1}^{N_s} \tilde{w}_k^i$
7	Obtain asymptotically optimal estimate of the state vector.	$\hat{\mathbf{x}}_k \approx \sum_{i=1}^{N_s} w_k^i \mathbf{x}_k^i$
8	Sampling Importance Re-sampling (SIR). Re-sample if $\hat{N}_{eff} < N_T$	$\hat{N}_{eff} = \frac{1}{\sum_{i=1}^{N_s} (w_k^i)^2}$
9	Use $\hat{\mathbf{x}}_k$ and HMM filter equations (Table 2.2) to estimate φ_k^i if $y_k^i = y2_k$.	
10	Utilize (18)-(20) to update the bank of KFs	
11	Let $k = k+1$ & iterate to step 4.	
1) de Freitas [23] demonstrates that the importance weights for y_k^i are given by the predictive density		
$p(z_k z_{1:k-1}, y_{1:k}^i) = N(z_k, \hat{z}_k^i, \mathbf{S}_k^i)$, where N denotes a Gaussian distribution.		

c) Evaluating the PS-SEED with Simulated Data

This section outlines the performance of the PS-SEED for the specific case of a periodic exponentially decaying source wavelet embedded within Gauss-Markov noise, with widely varying time constants and high variances. The seismic event is modeled with defining parameters of initial amplitude, damping factor and dominant angular frequency [11]. The simulated seismic event had a frequency of 200 Hz, initial amplitude of 160 mm/s² and damping factor of 79/s specified. The sampling rate was set at 0.05ms, and a total sampling time of 300 ms was specified. Fig. 4.1(a) illustrates the source wavelet generated with the previously specified parameters.

Figs. 4.2(b)-(g) show the simulated source wavelet with additive Gauss-Markov noise, with variances and time constants specified as (1000 mm²/s⁴, 0.0001 ms), (1000 mm²/s⁴, 0.0001 ms), (4000 mm²/s⁴, 0.0001 ms), (1000 mm²/s⁴, 0.1 ms), (1000 mm²/s⁴, 1.0 ms) and (2000 mm²/s⁴, 10 ms), respectively. The source wavelet had an arrival time of 150 ms ($f = 0^\circ$ in (31)) specified for the simulated traces illustrated in Figs. 4.1(b), (d) and (f). In Figs. 4.1(c), (e) and (g), the source wavelet had arrival times of 133 ms ($f = 140^\circ$), 138.7 ms ($f = 90^\circ$) and 164.4 ms ($f = 45^\circ$) specified, respectively. In Fig. 4.1, the units of the amplitudes of the time series data are not displayed in order to reduce clutter, and due to the fact that the STA/LTA event detection technique is only dependent upon relative amplitudes.

The initialization of the JMLGS system equations (Case 1 and 2 of Step 1 in Table 4.1) was carried out similarly to that outlined in [11]. The initialization of the finite state Markov chain probabilities are based upon the likelihood of an event occurring, and the transitional probability of moving from a non-event to an event. For the simulations presented here, the pdfs and the transitional pdfs were set to $p(y_0^1) = 0.9$, $p(y_0^2) = 0.1$, $p(y_k^1 | y_{k-1}^1) = 0.8$, $p(y_k^1 | y_{k-1}^2) = 0.8$, $p(y_k^2 | y_{k-1}^2) = 0.2$, and $p(y_k^2 | y_{k-1}^1) = 0.2$, respectively. In general terms, the probability of an event is about 20 percent. The initialization of the pdf of the time variant phase was set to the uniform distribution, while the fixed-grid transitional pdf $p(\varphi_k^i | \varphi_{k-1}^i)$ was set quite high (e.g., 0.996) and the remaining values were set to have a uniform distribution. There were 90 (N_p) phases specified to reflect the possible phase

shifts of 0° to 180° in 2° increments. The number of particles (N_s) specified for the PS-SEED filter was 100. Degeneracy threshold parameter N_T was set to $0.8 N_s$.

The PS-SEED filter was implemented on the simulated data illustrated in Fig. 4.1, with the output for state \hat{x}_{2k} (amplitude component of AMS model) illustrated in Figs. 4.2(b)-(g). Fig. 4.2(a) shows the actual modulating amplitude component of the simulated wavelets. As is illustrated in Figs. 4.2(b)-(g), there is a very impressive real-time S/N improvement after implementation of the PS-SEED algorithm. In these test cases, the S/N is defined as the ratio of the average maximum amplitude of the signal to the maximum average amplitude of the noise. The PS-SEED was able to increase the S/N by approximately 80-fold, 80-fold, 30-fold, 10-fold, 9-fold and 11-fold for the Gauss-Markov additive noise illustrated in Figs. 4.1(b) - (g), respectively. The lower S/N is due to the noise characteristics more closely matching those of the source wavelet, making real-time noise/signal separation more difficult. The HMM filter portion of the PS-SEED algorithm also did a good job of estimating the phase shifts for the source wavelets illustrated in Fig. 4.1 as indicated by the responses shown in Fig. 4.2. Fig. 4.3 illustrates the estimated probability of an event ($P(y_{2k} | z_{1:k})$) for the test case shown in Fig. 4.1(b). As expected, the probability of an event increases along with the seismic amplitude estimate illustrated in Fig. 4.2(b).

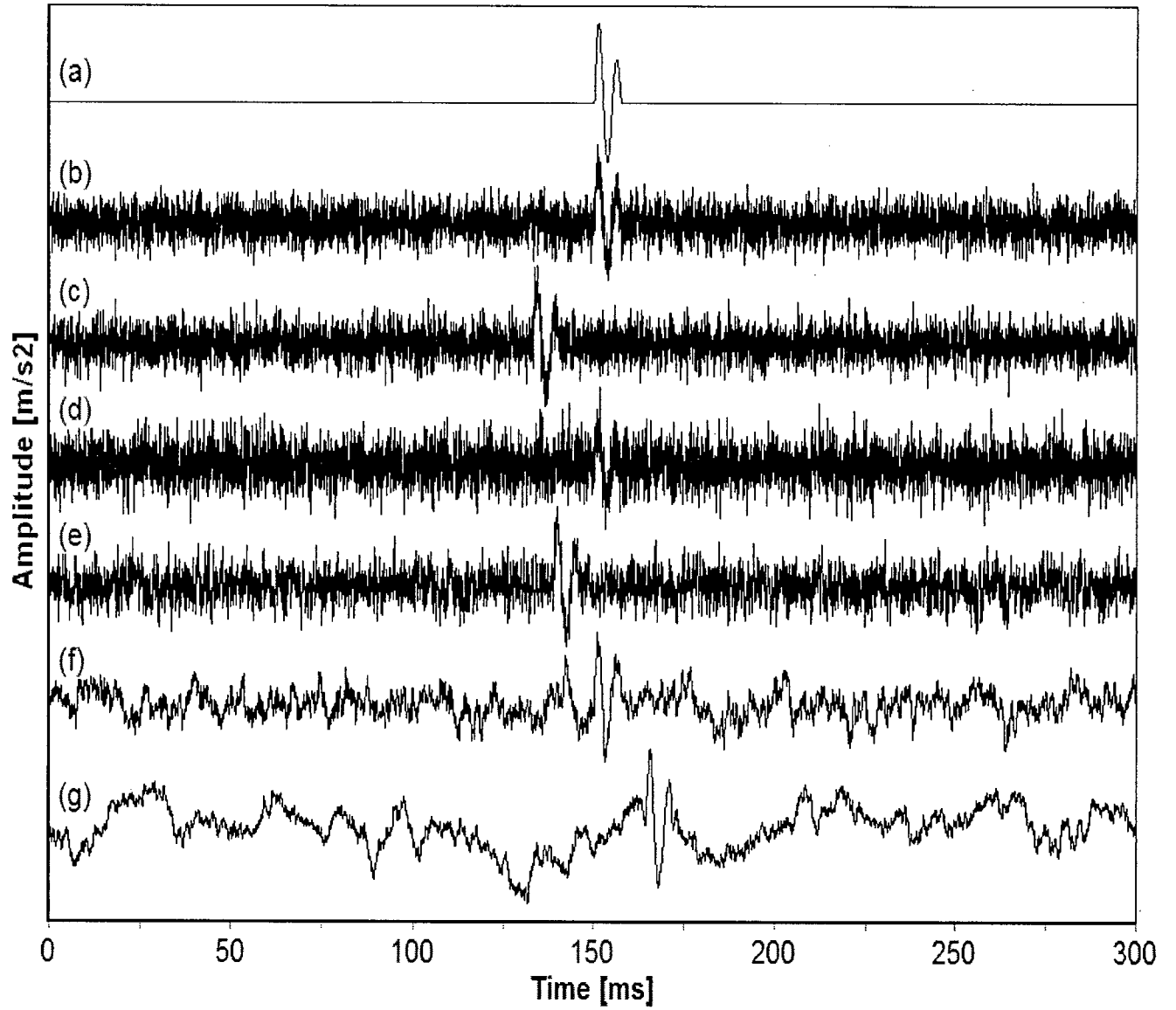


Figure 4.1. Source wavelet embedded with varying types of Gauss-Markov background noise.

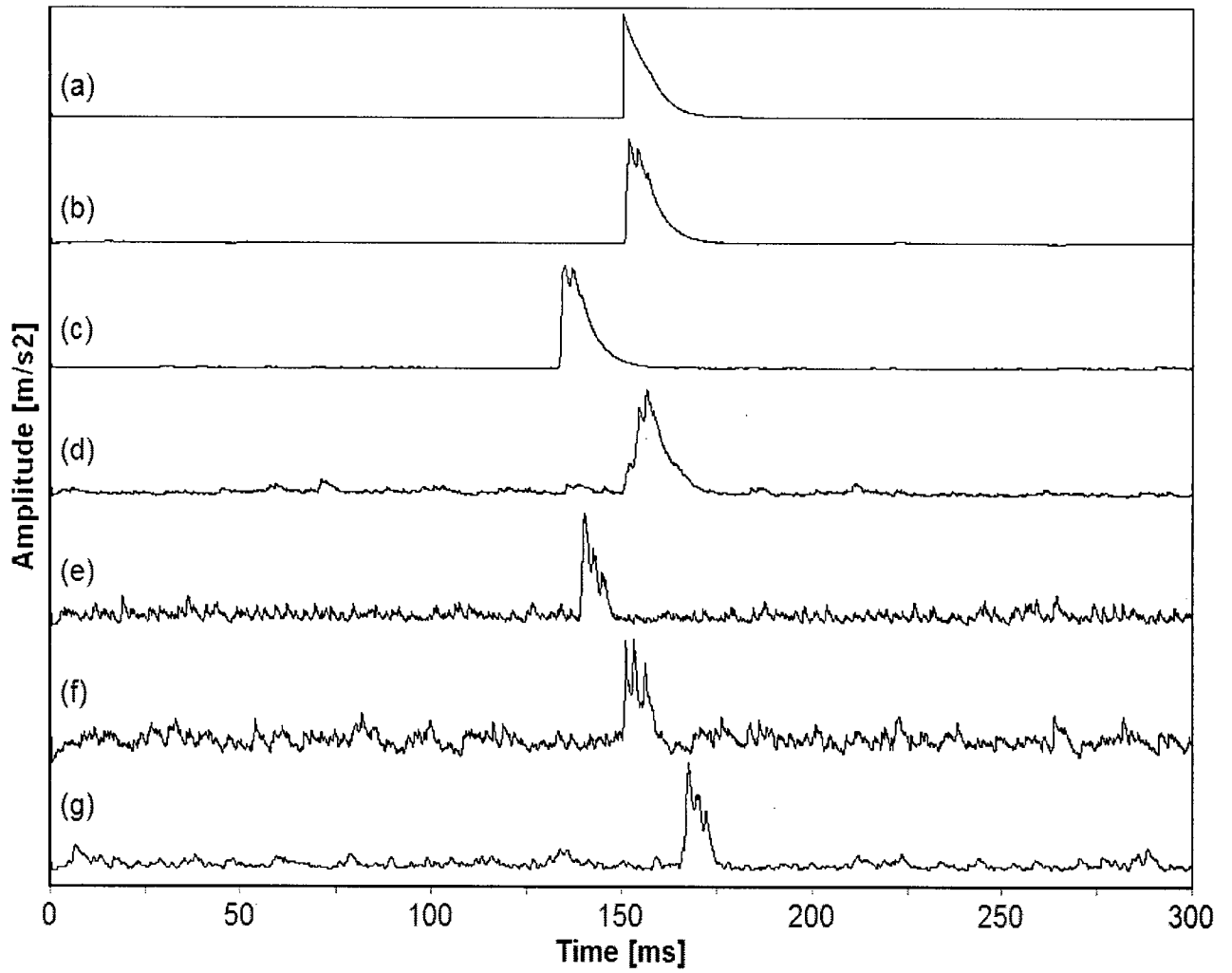


Figure 4.2. PS-SEED output results for estimating state \hat{x}_{2_k} after processing Fig. 4.1 data.

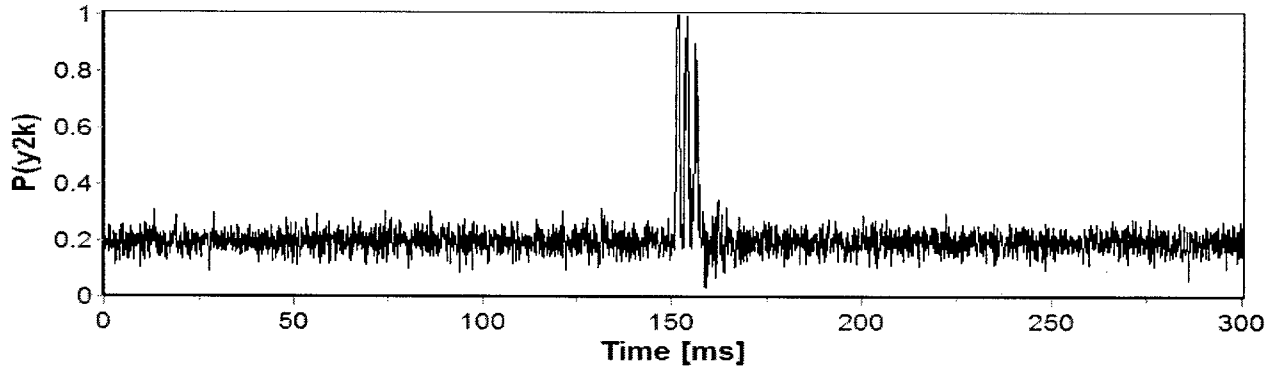


Figure 4.3. Estimated probability of an event for the test case shown in Fig. 4.1(b).

B. Seismic Deconvolution

Seismic deconvolution is one of the most widely researched and implemented seismic signal processing tools. The primary goal of seismic deconvolution is to remove the characteristics of the source wavelet from the recorded seismic time series, so that one is ideally left with only the reflection coefficients. The reflection coefficients identify and quantify the impedance mismatches between different geological layers that are of great interest to the geophysicist.

In seismology, the recorded time series, $z(t)$, is defined to be the linear convolution of the source wavelet, $S(t)$, with the earth's reflection coefficients, $\mu(t)$, with additive measurement noise, $v(t)$. The mathematical representation of this relationship is given as shown:

$$z(t) = \int_0^t \mu(\tau) S(t - \tau) d\tau + v(t) \quad (37)$$

The discrete representation of (38) is given as follows:

$$z(k) = \sum_{i=1}^k \mu(i) S(k - (i - 1)) + v(k), \quad k = 1, 2 \dots N \quad (38)$$

There are many techniques of seismic deconvolution that can be implemented so that an optimal estimate is made of the earth model. A majority of the standard seismic

deconvolution methods utilize the steady state Wiener digital filter that assumes a minimum phase source wavelet [48]. Other techniques implement inverse theory, minimum entropy deconvolution, adaptive deconvolution, complex cepstrum deconvolution and independent component analysis. Many of these deconvolution techniques are ad hoc in nature [42], they are effected by the band-limited nature of the source wavelet, they are highly susceptible to additive measurement noise, and they assume that the source wavelet is stationary. However, it is readily known that the higher frequencies are attenuated more rapidly than lower frequencies, resulting in significant variation in the source signal as it travels through the earth. A more effective deconvolution technique would be one that potentially allows for time variation of the source wavelet and it should be able to handle diverse additive measurement noise [9]. In addition, the case where one attempts to deconvolve an unknown source wavelet from an unknown reflection sequence (blind deconvolution) is also of great interest. PF is an ideal tool to assess with regards to carrying out blind seismic deconvolution, due to the fact that the solution is non-linear.

1) Application of Kalman Filter Smoother to Seismic deconvolution

Mendel [42] is one of the original researchers to carry out work in fitting the seismic convolution model into a state-space representation for the purpose of minimum variance seismic deconvolution. In Mendel's approach to minimum variance state-space seismic deconvolution the basic seismogram is represented as an autoregressive moving average process (ARMA) [9], [42]. The ARMA model is a combination of both an autoregressive (AR) process and a moving average (MA) process [19]. An AR time series process is generated by a linear combination of past observations plus a Gaussian random variable. The MA process is generated by a finite linear combination of past and present inputs only. In the Kalman filter seismic deconvolution (KFSD) algorithm, the recorded seismogram is modeled as an ARMA process, which is driven by a forcing function defined as the in-situ reflection coefficients.

a) Kalman Filter Smoother Governing Equations

Smoothing is an off-line data processing procedure that uses all measurements between 0 and T to estimate a state at a time t where $0 < t < T$ [33]. The smoothed estimate of $x(t)$, based on all the measurements between 0 and T, is identified as $\hat{x}(t|T)$. There are three types of Kalman Filter smoothers, which are identified as follows:

1. *Fixed-interval smoothing*: the time interval of measurements (i.e., the data span) is fixed, and we seek optimal estimates at some, or perhaps all, interior points.

2. *Fixed-point smoothing*: an estimate at a single fixed point in time is obtained, and the data span time, T, is assumed to increase indefinitely.

4. *Fixed-lag smoothing*: it is again assumed that T increases indefinitely, but in this case we are interested in an optimal estimate of the state at a fixed length of time in the past (i.e., $\hat{x}(t - \delta | T)$, with δ held fixed).

In the KFSD algorithm, a Fixed-Interval Smoother is applied. The discrete optimal fixed-interval smoothed estimate $\hat{x}(k | N)$ (where $N = T/\Delta$ and Δ is the sampling rate) is defined in Table 4.2 [33].

The computational sequence for the discrete fixed-interval Kalman Filter smoother can be thought of as a two pass process. In the first pass, optimal real-time state estimates are obtained by implementation of equations (9)-(20) outlined in Table 3.1. In the second pass, results from the first-pass estimates (i.e., \hat{x} and P) are reprocessed starting from time index N and utilizing equations (39) to (43). Gelb [33] defines a state to be smoothable (**Smoothability Condition**) if an optimal smoother provides a state estimate with lower error covariance values compared to the real-time filtered estimate. Only those states, such as randomly time-varying states, which are controllable by the noise driving the system state vector are smoothable. Therefore, constant states are not smoothable.

TABLE 4.2
KF FIXED-INTERVAL SMOOTHER GOVERNING EQUATIONS

Eq.	Description	Mathematical Representation
39	State smoother estimate.	$\hat{\mathbf{x}}_{k N} = \hat{\mathbf{x}}_{k k-1} + \mathbf{P}_{k k-1} \mathbf{r}_{k N}$
40	Backward recursive equation.	$\mathbf{r}_{j N} = \mathbf{F}_{j+1}^{p'} \mathbf{r}_{j+1 N} + \mathbf{H}'_j \left[\mathbf{H}_j \mathbf{P}_{j j-1} \mathbf{H}'_j + \mathbf{R}_j \right]^{-1} \left[z_j - \mathbf{H}_j \hat{\mathbf{x}}_{j j-1} \right]$
41	Smoothing state transition matrix.	$\mathbf{F}_{k+1}^p = \mathbf{F}_{k+1} \left[\mathbf{I} - \mathbf{K}_k \mathbf{H}_k \right]$
42	Smoothing error covariance matrix	$\mathbf{P}_{k N} = \mathbf{P}_{k k-1} - \mathbf{P}_{k k-1} \mathbf{S}_{k N} \mathbf{P}_{k k-1}$
43	Covariance matrix of $\mathbf{r}_{j N}$.	$\mathbf{S}_{j N} = \mathbf{F}_{j+1}^{p'} \mathbf{S}_{j+1 N} \mathbf{F}_{j+1}^p + \mathbf{H}'_j \left[\mathbf{H}_j \mathbf{P}_{j j-1} \mathbf{H}'_j + \mathbf{R}_j \right]^{-1} \mathbf{H}_j$

In (39) $k = N-1, N-2, \dots, 1$ and $n \times 1$ vector \mathbf{r} is a $n \times 1$ vector.

In (40) $j = N, N-1, \dots, 1$ and $\mathbf{r}_{(N+1|N)} = 0$.

In (42) $k = N-1, N-2, \dots, 1$.

In (43) $j = N, N-1, \dots, 1$ and $\mathbf{S}_{(N+1|N)} = 0$.

b) Kalman Filter Seismic Deconvolution (KFSD) Algorithm Outline

The first step in the KFSD algorithm is for the user to specify the order of the ARMA process. For example, the Z transform for a fourth order ARMA model is given as follows:

$$V(z) = \frac{b_1 z^4 + b_2 z^3 + b_3 z^2 + b_4 z^1}{z^4 + a_1 z^3 + a_2 z^2 + a_3 z^1 + a_4} = \frac{X(z)}{U(z)} \quad (44)$$

where the parameters, b_1 , b_2 , b_3 , and b_4 , define the MA process coefficients, while the parameters, a_1 , a_2 , a_3 , and a_4 define the AR process coefficients. $V(z)$ is the Z transform of the source wavelet, $X(z)$ is the Z transform of the seismogram, and $U(z)$ is the Z transform of the in-situ reflection coefficients.

In (44), the output x_{k+4} is estimated on the basis of x_{k+3} , x_{k+2} , x_{k+1} , x_k , μ_{k+4} , μ_{k+3} , μ_{k+2} , and μ_{k+1} according to the following equation:

$$x_{k+4} + a_1 x_{k+3} + a_2 x_{k+2} + a_3 x_{k+1} + a_4 x_k = b_1 \mu_{k+4} + b_2 \mu_{k+3} + b_3 \mu_{k+2} + b_4 \mu_{k+1} \quad (45)$$

For the 4th order case³, the KFSD state-space formulation is derived by introducing variable $Y1(z)$ into (44) [42] outlined as follows:

$$V(z) = \frac{b_1 z^4 + b_2 z^3 + b_3 z^2 + b_4 z^1}{z^4 + a_1 z^3 + a_2 z^2 + a_3 z^1 + a_4} \frac{Y1(z)}{Y1(z)} = \frac{X(z)}{U(z)} \quad (46)$$

Equating numerator and denominator terms in (46) results in the following two expressions:

$$x_k = b_1 y1_{k+4} + b_2 y1_{k+3} + b_3 y1_{k+2} + b_4 y1_{k+1} \quad (47a)$$

³Can be generalized to an ARMA model of any order.

$$\mu_k = y1_{k+4} + a_1 y1_{k+3} + a_2 y1_{k+2} + a_3 y1_{k+1} + a_4 y1_k \quad (47b)$$

By choosing $x1_k = y1_k$, $x2_k = y1_{k+1}$, $x3_k = y1_{k+2}$, and $x4_k = y1_{k+3}$, (47a) and (47b) can be written as into a state-space formulation as follows:

$$\begin{bmatrix} x1_{k+1} \\ x2_{k+1} \\ x3_{k+1} \\ x4_{k+1} \end{bmatrix} = \begin{bmatrix} 0 & 1 & 0 & 0 \\ 0 & 0 & 1 & 0 \\ 0 & 0 & 0 & 1 \\ -a_4 & -a_3 & -a_2 & -a_1 \end{bmatrix} \begin{bmatrix} x1_k \\ x2_k \\ x3_k \\ x4_k \end{bmatrix} + \begin{bmatrix} 0 \\ 0 \\ 0 \\ 1 \end{bmatrix} \mu_k \quad (48)$$

where the impedance structure μ_k is defined as $E[\mu_k \mu_\tau] = Q_k \delta(k - \tau)$. μ_k is a Gaussian white noise process with mean zero and variance Q_k .

The discrete measurement equation is given as follows:

$$z_k = \begin{bmatrix} b_4 & b_3 & b_2 & b_1 \end{bmatrix} \begin{bmatrix} x1_k \\ x2_k \\ x3_k \\ x4_k \end{bmatrix} \quad (49)$$

The computational sequence for the discrete KFSD algorithm is outlined as follows:

1. Specify the order of the ARMA process and derive coefficients (e.g., $a_1, a_2, a_3, a_4, b_1, b_2, b_3$, and b_4) (subsequently addressed).
2. Define the state-space matrix equation (48) and measurement equation (49).
4. Obtain the filtered estimates (e.g., $\hat{x}_{k|k}, P_{k|k}, K_k$) by implementation of equations (9)-(20) outlined in Table 3.1.
4. Obtain smoothed estimates (e.g., $\hat{x}_{k|N}, r_{k|N}, P_{k|N}, F_k^P$) by utilizing the values derived in step 3 and subsequently implementing equations (39) to (43) outlined in Table 4.2.
5. Derive reflection coefficients or in-situ impedance structure by implementing [42]

$$\hat{\mu}_{k|N} = \mathcal{Q}_k \mathbf{G}_k' \mathbf{r}_{k+1|N} \quad (50)$$

As previously stated, the first step in the KFSD algorithm is for the user to determine the order of the ARMA process and subsequently derive the necessary model parameters. This portion of the KFSD analysis is referred to as *system identification*. The maximum-likelihood of approximating the true source wavelet with an ARMA model increases monotonically with increasing system order, while the computational cost of increasing the system order is proportional to n^3 where n is the ARMA model order [42]. In general terms, the process of determining the ARMA model order is a trial and error approach. In this analysis, the investigator chooses a model that has the smallest number of parameters while meeting a performance index requirement that measures how well the ARMA model fits the actual in-situ model. The technique that I utilized to derive the ARMA model parameters is based upon the work of Ogata [44]. In this approach to *system identification*, a least squares cost function that is defined as the difference between the ARMA model response, and the corresponding experimental response, is minimized.

c) ARMA Parameter Estimation by the Least Squares Method

The derivation of the ARMA model parameters by utilizing a least squares method is demonstrated by again considering the 4th order (i.e., $n = 4$) ARMA model given in (44). If the numerator and denominator of (44) are multiplied by z^{-4} , we obtain the following:

$$\frac{X(z)}{U(z)} = \frac{b_1 + b_2 z^{-1} + b_3 z^{-2} + b_4 z^{-3}}{1 + a_1 z^{-1} + a_2 z^{-2} + a_3 z^{-3} + a_4 z^{-4}} \quad (51)$$

In (51), the output x_k is estimated on the basis of x_{k-1} , x_{k-2} , x_{k-3} , x_{k-4} , μ_k , μ_{k-1} , μ_{k-2} , and μ_{k-3} according to the following equation:

$$\hat{x}_k = -a_1 x_{k-1} - a_2 x_{k-2} - a_3 x_{k-3} - a_4 x_{k-4} + b_1 \mu_k + b_2 \mu_{k-1} + b_3 \mu_{k-2} + b_4 \mu_{k-3} \quad (52)$$

where \hat{x}_k is the estimated value of x_k .

The error between the estimated output value and actual output value is defined as follows:

$$\varepsilon_k = x_k - \hat{x}_k \quad (53)$$

Since x_k depends on past data up to n sampling periods earlier, the error e_k is defined only for $k \geq n$. By substituting (52) and $k = n, n+1, \dots, N$ into (53) and combining the resulting $N-n+1$ equations into a vector-matrix equation, we obtain the following:

$$\mathbf{x}_N = \mathbf{C}_N \mathbf{q}_N + \mathbf{e}_N \quad (54)$$

where $\mathbf{x}_N = [x_4 \ x_5 \ \dots \ x_N]$, $\mathbf{q}_N = [-a_1, -a_2, -a_3, -a_4, b_1, b_2, b_3, b_4]$, $\mathbf{e}_N = [e_4 \ e_5 \ \dots \ e_N]$, and \mathbf{C}_N is defined as

$$\mathbf{C}_N = \begin{bmatrix} x_3 & x_2 & x_1 & x_0 & \mu_4 & \mu_3 & \mu_2 & \mu_1 \\ x_4 & x_3 & x_2 & x_1 & \mu_5 & \mu_4 & \mu_3 & \mu_2 \\ \cdot & \cdot \\ \cdot & \cdot \\ \cdot & \cdot \\ x_{N-1} & x_{N-2} & x_{N-3} & x_{N-4} & \mu_N & \mu_{N-1} & \mu_{N-2} & \mu_{N-3} \end{bmatrix} \quad (55)$$

The least squares performance index is defined as follows:

$$J_N = \frac{1}{2} \sum_{k=4}^N \varepsilon_k^2 = \frac{1}{2} \varepsilon_N' \varepsilon_N \quad (56)$$

The least squares method involves minimizing (56), such that the ARMA parameter values will best fit the observed data. In Ogata's [36] formulation, it is assumed that the input sequence $\{\mu_k\}$ is such that for $N > 4$, $\mathbf{C}_N' \mathbf{C}_N$ is nonsingular. Ogata shows that the optimal

estimate of \hat{q}_N is given as shown:

$$\hat{q}_N = [C'_N C_N]^{-1} C'_N y_N \quad (57)$$

In (57) it is required that $\{\mu_k\}$ is sufficiently time-varying, so that $C'_N C_N$ is non-singular.

Equation (57) is a first best estimate (in a least squares sense) of the ARMA parameters. Ogata presents a subsequent recursive formulation for the estimate of ARMA parameters, utilizing (57) as an initial estimate. The recursive least square estimation is defined as follows:

$$\hat{q}_{N+1} = \hat{q}_N + K_{N+1} [y_{N+1} - c_{N+1} \hat{x}_N] \quad (58)$$

where

$$K_{N+1} = \frac{[C'_N C_N]^{-1} c'_{N+1}}{1 + c_{N+1} [C'_N C_N]^{-1} c'_{N+1}} \quad (59)$$

and

$$c_{N+1} = [y_N : y_{N-1} : y_{N-2} : y_{N-3} : \mu_{N+1} : \mu_N : \mu_{N-1} : \mu_{N-2}] \quad (60)$$

The method that I utilize for determining the ARMA parameters for the source wavelet is to firstly convolve the isolated wavelet with a highly variable and known noise process with mean zero and unit variance. This insures that $\{\mu_k\}$ is sufficiently time-varying so that $C'_N C_N$ is non-singular. Initial estimates of the ARMA parameters are obtained by implementation of (57), known μ_k , and the convolved output sequence y_k . The initial estimates of \hat{q}_N are then fed into the recursive estimation equation, defined by (58), until the performance index (56) reaches a predefined minimum.

d) Evaluating the KFSD Algorithm with Simulated Finite Difference Data

This section presents test test-bed simulation results when implementing the KFSD algorithm previously outlined. The first step in the simulation was to define a seismic source wavelet. Amini and Howie utilized the finite difference program FLAC to model seismic source wavelets [9], [36]. Fig. 4.4 illustrates the simulated source wavelet generated by Amini and Howie and obtained by personal communication [36]. The wavelet shown in Fig. 4.4 was generated by assuming a uniform half-space, with an in-situ shear wave velocity of 180 m/s, and a sampling rate of 0.02 ms.

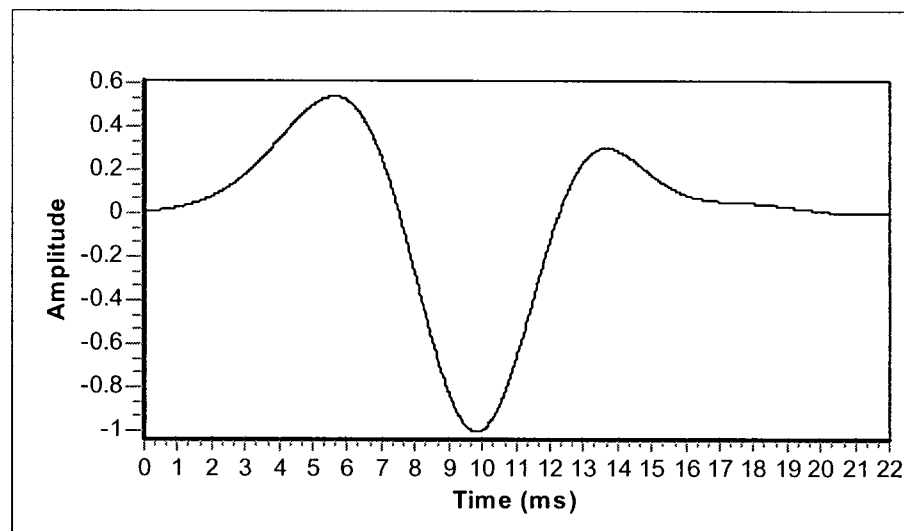


Figure 4.4. The finite difference simulated source wavelet.

The KFSD algorithm was then implemented on the data illustrated in Fig. 4.4. In deriving the necessary ARMA parameters, a 5th order AR and MA was utilized with a data compression ratio of 16 to 1, so that the sampling rate became 0.32 ms. In addition, it was found that the ARMA model estimation algorithm worked best when the source wavelet was time reversed. The only impact that time reversing the source wavelet has on the KFSD algorithm is that the recorded seismic time series must be time reversed when processing. Fig. 4.5 illustrates the results of the ARMA estimation of the time reversed source wavelet shown in Fig. 4.4

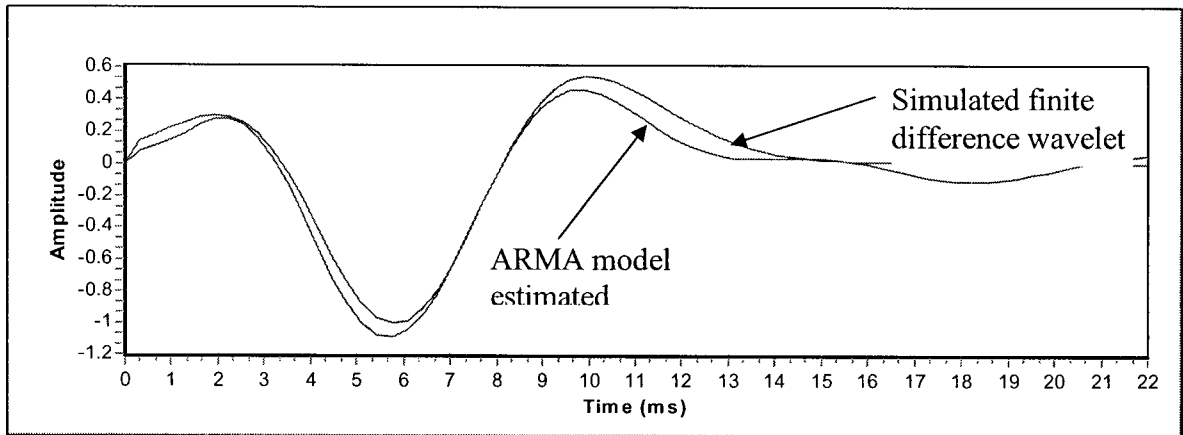


Figure 4.5. Estimating the source wavelet in Fig. 4.4 with the 5th order ARMA model.

The estimated ARMA model is then convolved with the impedance structure illustrated in Fig. 4.6 to give the output shown in Fig. 4.7. If the KFSD algorithm is applied to the seismic data shown in Fig. 4.7, the reflection coefficients illustrated in Fig. 4.6 are recovered exactly.

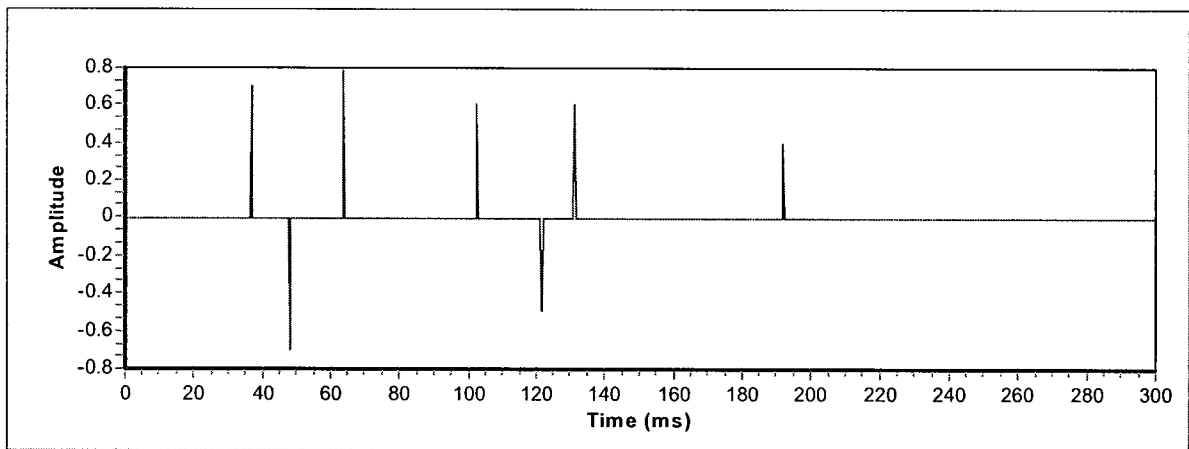


Figure 4.6. The reflection coefficients utilized to test the performance of the KFSD algorithm.

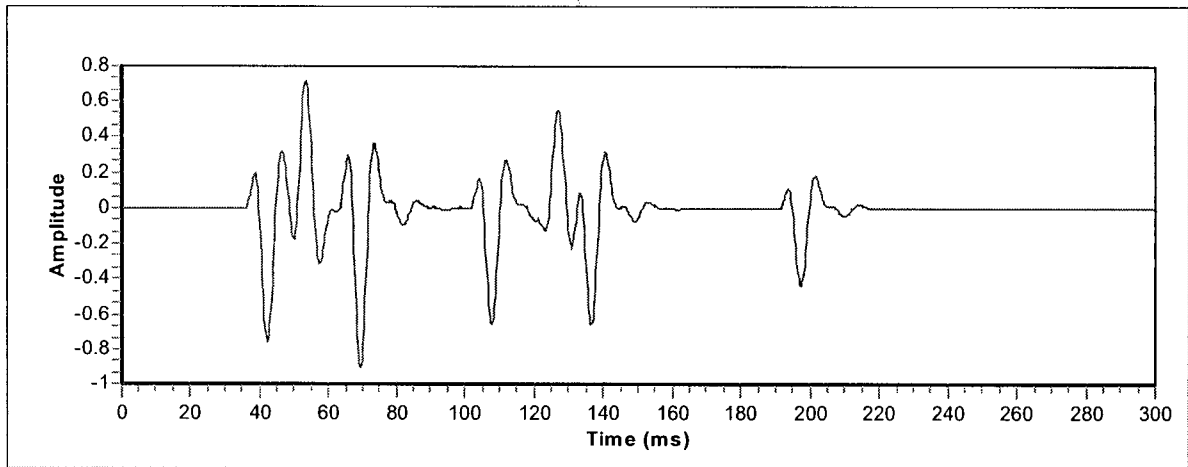


Figure 4.7. The output after convolving the ARMA wavelet with the reflection coefficients shown in Fig. 4.6.

Gauss-Markov noise is then added to the synthetic seismogram shown in Fig. 4.7, where a time constant of $T_c = 0.02$ ms and standard deviation of $s = 0.002$ was specified. The KFSD algorithm derived the output shown in Fig. 4.8. As is illustrated in Fig. 4.8, the arrival time locations of the reflection coefficients is recovered exactly, but there is some degradation in the estimation of the amplitudes. The KFSD algorithm gives accurate estimates of the relative amplitudes of the reflection coefficients.

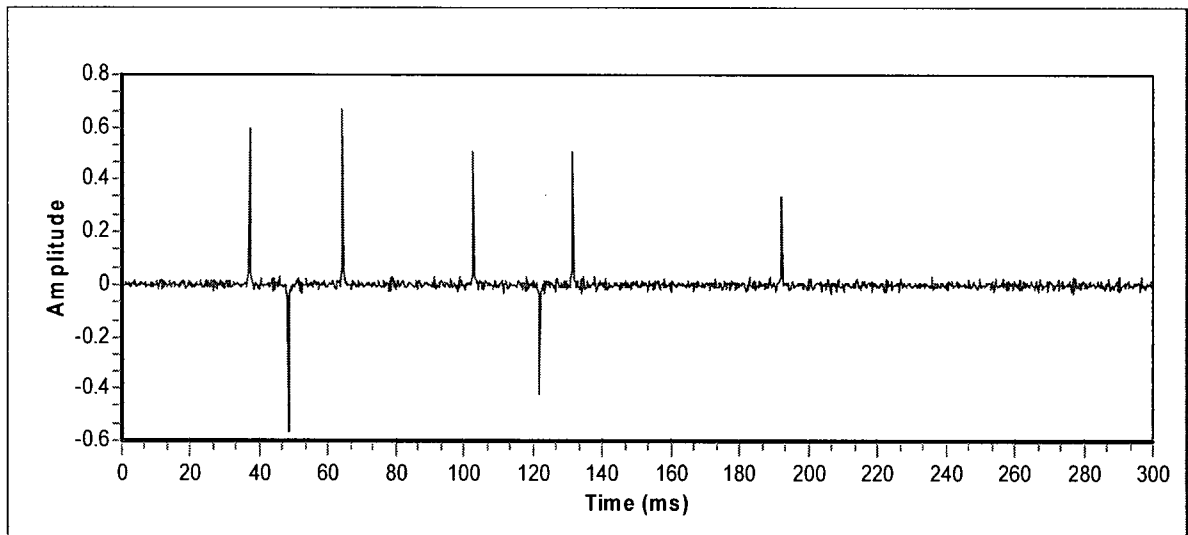


Figure 4.8. The KFSD estimated reflection coefficients.

The KFSD algorithm was next tested for its ability to derive the reflection coefficients within a high noise environment. Fig. 4.9 shows the seismic data of Fig. 4.7 with Gauss-Markov noise of $T_c = 0.02$ ms and $s = 0.08$ added. The KFSD algorithm derived the estimates illustrated in Fig. 4.10. As is shown in Fig. 4.10, the arrival time locations of the reflection coefficients are recovered exactly, but the algorithm fails to determine the amplitudes. The KFSD algorithm gives accurate estimates of the relative amplitudes of the reflection coefficients which facilitates the investigator to recover the true amplitudes. Mendel [42] outlines a fixed-point smoother which can be utilized to estimate the reflection coefficient amplitudes once the corresponding time locations are known.

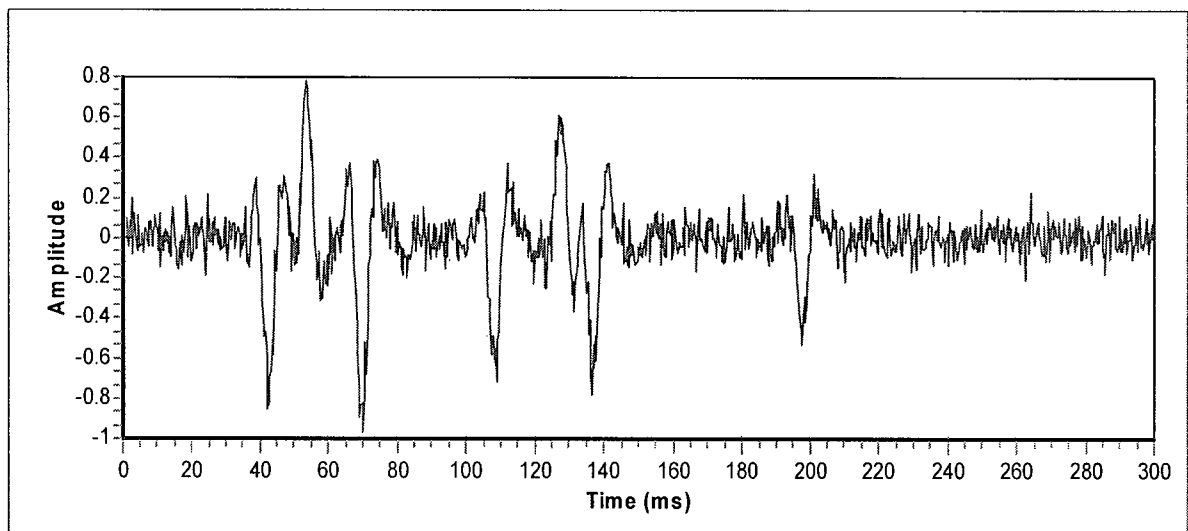


Figure 4.9. Seismic data of Fig. 4.7 with Gauss-Markov noise of $T_c = 0.02$ ms and $s = 0.08$ added.

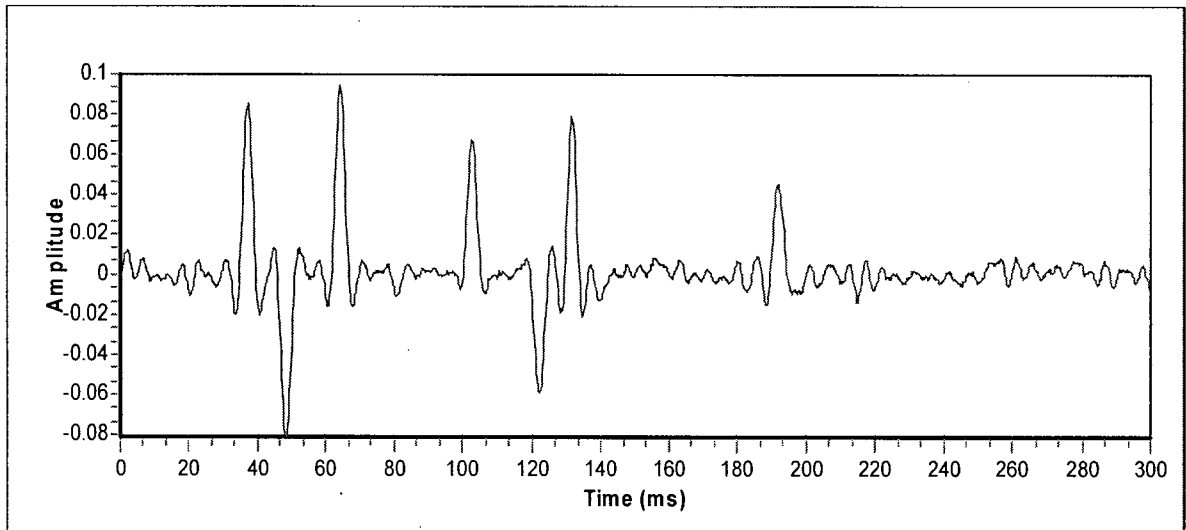


Figure 4.10. The KFSD estimated reflection coefficients for data shown in Fig. 4.9.

Fig. 4.11 shows the KFSD output for the data derived when the true time reversed wavelet of Fig. 4.4 is convolved with the reflection coefficients in Fig. 4.6 and Gauss-Markov noise of $T_c = 0.02 \text{ ms}$ and $s = 0.08$ is added. The KFSD algorithm provided very similar results to those illustrated in Fig. 4.10.

The main disadvantage of utilizing the previously described KFSD algorithm is that it is very difficult to model seismograms as ARMA models when the source wavelet is mixed or zero phased [37]. In addition, the ARMA model is highly susceptible to sampling rates where higher sampling rates typically require a higher order for the ARMA model, the KFSD makes the assumption that the reflection coefficients are Gaussian and white, and the KFSD algorithm is poorly suited for deconvolving seismograms with non-stationary source wavelets and for addressing the blind deconvolution problem

2) Application of Particle Filtering to Blind Seismic Deconvolution

Liu and Chen [40] were one of the first researchers to address the blind deconvolution problem utilizing SMC techniques. Their work predominantly focused upon deconvolving signals within the digital communications field. In this case, the source wavelet, ($S(k)$) in

(38) is referred to as the blurring mechanism, and the reflection coefficients ($\mu(i)$) are the unobserved input signal, which is assumed to have discrete values with known state levels s_1, \dots, s_m (similar to a finite state Markov chain). Fortunately for digital communication problems, the blurring function (i.e., source wavelet) has very few coefficients and there are typically a very limited number of state levels describing the input signal. For example, in the simulated results given by Liu and Chen [40], the number of blurring coefficients was three, with 16 possible state levels for the input signal. This system configuration results in a total of $16^3 = 4,096$ possible combinations. Unfortunately, a typical seismic source wavelet has a minimum of 30 coefficients, and the reflections coefficients would require a minimum of 40 state levels⁴. This system configuration results in a total of $40^{30} = 10^{48}$ combinations. In addition, the input data communication signals are characteristically highly variable, unlike the sparse reflection coefficients typically encountered in seismology.

The number of combinations is indicative of the required particles for solving the blind deconvolution problem, and 10^{48} is not a feasible number. For these reason, a new approach in carrying out blind seismic deconvolution, which relies upon the unique AMS model of the source wavelet, is outlined in this section. Similar to the PS-SEED algorithm, the source wavelet is modeled as an amplitude modulated sinusoid and the blind deconvolution is carried out by initially determining the seismogram's principle phases. Once the principle phases are determined, a RBPF algorithm is utilized to separate the corresponding overlapping source wavelets. The subsequently outlined techniques are referred to as the principle phase decomposition (PPD) and principle phase decomposition wavelet extraction (PPD-WE) algorithms. The PPD and PPD-WE techniques makes use of the fact that the discrete convolution operation outlined by (38) can also be represented as the summation of several source wavelets of differing arrival times.

⁴ Range of values of +0.2 to -0.2 in steps of 0.01.

a) Amplitude Modulated Sinusoid

Similar to the PS-SEED algorithm, a fundamental and unique component of the PPD and PPD-WE algorithms is that the seismic source wavelet is modeled as an amplitude modulated sinusoid. The AMS representation of the source wavelet has proven to be highly robust and accurate in the case of passive event detection, where it is desired to identify non-stationary source wavelets within complicated measurement noise in real-time [10], [11]. In addition, a source wavelet generated from vertical seismic profiling can be modeled as an AMS [9]. The AMS has also proven to be a good approximation for many analytical representations of seismic source wavelets, such as the exponentially decaying cyclic waveform [47], mixed-phase Berlage wavelet [1], zero-phase Klauder wavelet [38], and zero-phase Ricker wavelet [47].

The following example demonstrates the robustness of the AMS model. The Ricker wavelet is mathematical represented in the time-domain as [47]:

$$f(t) = A_0 \left(1 - 2\pi^2 v_M^2 (t - t_0)^2 \right) \exp^{-\pi^2 v_M^2 (t - t_0)^2}, \quad t \geq t_0 \quad (61)$$

where $A_0 \equiv$ wavelet maximum amplitude (centered between two flanking lobes), $v_M \equiv$ dominant or peak frequency of the Ricker wavelet, and $t_0 \equiv$ wavelet arrival time of maximum amplitude.

Fig. 4.11 illustrates a zero-phase Ricker wavelet, with the following parameters specified, $A_0 = 160$ units, $v_M = 50$ Hz, and $t_0 = 120$. Superimposed upon the Ricker wavelet is a scaled 50 Hz sinusoid with a phase of 96° . If the sinusoid shown in Fig. 4.11 (unscaled) is multiplied by the PS-SEED numerically estimated amplitude modulating term shown in Fig. 4.12, then the source wavelet illustrated in Fig. 4.13 is obtained (superimposed upon the true Ricker wavelet of Fig. 4.11). Although the Ricker wavelet has a peak frequency, it doesn't have a specific sinusoidal term, and one is still able to reconstruct the desired wavelet by applying an appropriate amplitude modulating term.

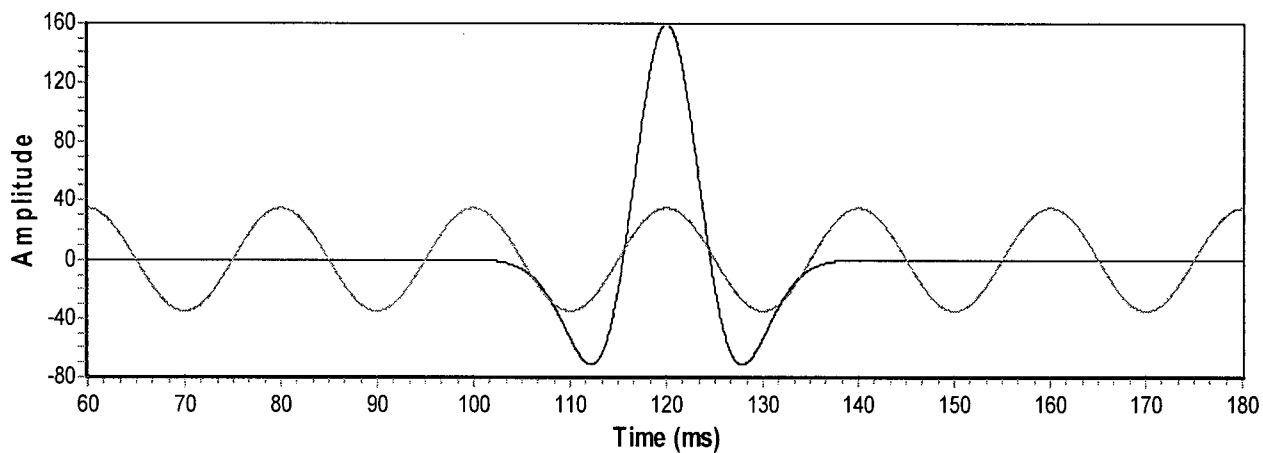


Figure 4.11. A zero-phase Ricker wavelet with superimposed 50 Hz sinusoid with a phase of 96° .

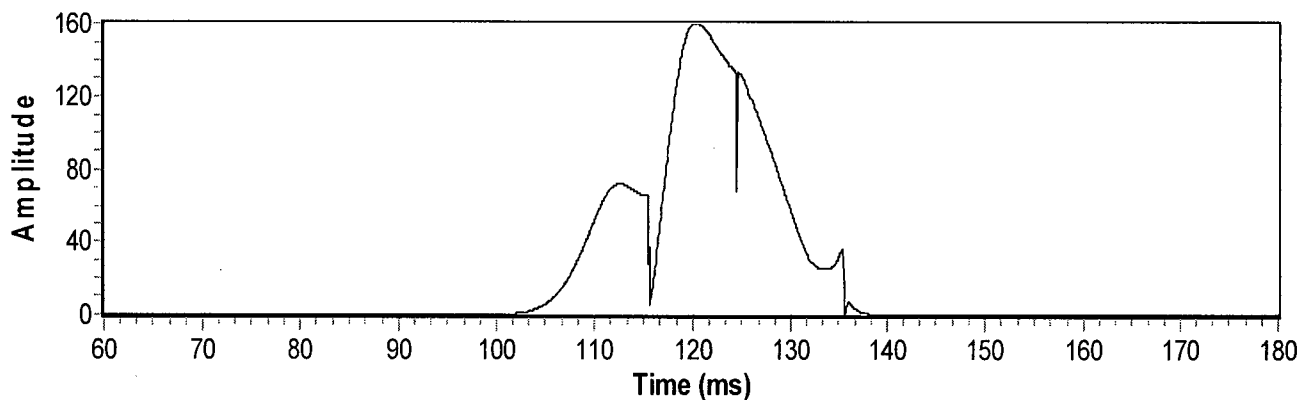


Figure 4.12. Amplitude modulating term for estimating the Ricker wavelet of Fig. 4.11.

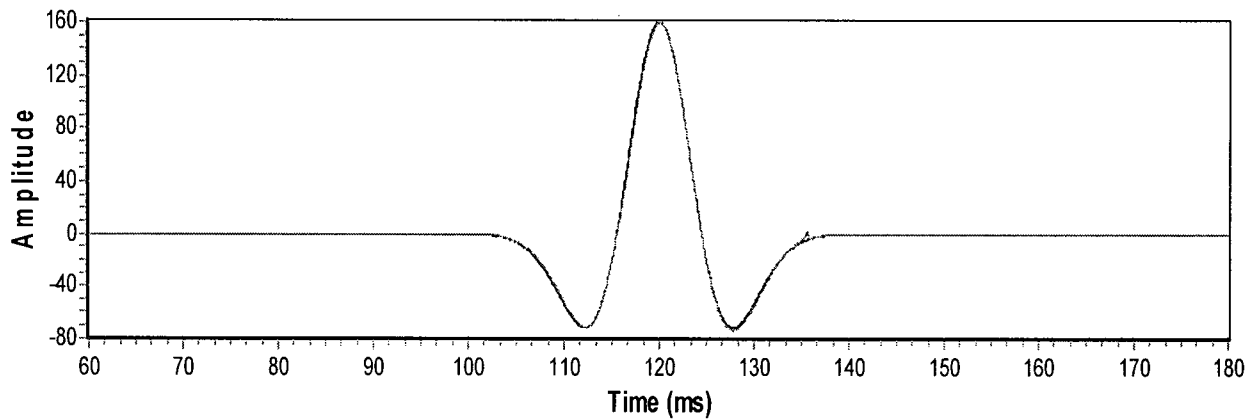


Figure 4.13. Reconstructed Ricker wavelet superimposed upon actual Ricker wavelet of Fig. 4.11.

b) PPD Algorithm Outlined.

The formulation of the PPD algorithm has similarities to the passive seismic signal enhancement and event detection (PS-SEED) filter previously outlined, with the added complexity of modeling and reconstructing several overlapping source wavelets, as opposed to identifying a single source wavelet (“event”) in real-time. In the PPD algorithm, the only prior requirement is that the source wavelet be modeled as an AMS. As opposed to standard seismic deconvolution techniques that attempt to derive reflection coefficients, the PPD algorithm decomposes the seismogram into its associated overlapping source wavelets. This mitigates the problem associated with obtaining high bandwidth reflection coefficients from band-limited source wavelets. If desired, reflection coefficients can be readily constructed from the derived overlapping source wavelets. The PPD algorithm also provides for time-variant estimations of the source wavelet. This information could be utilized within non-blind (known source wavelet) deconvolution techniques.

The concept of decomposing a seismogram into overlapping AMS source wavelets, based upon inherent phase differences, is illustrated in Fig. 4.14. Fig. 4.14 shows three sinusoidal wavelets that have an identical dominant frequency and varying phase components of

0°, 110°, and 250°. Three source wavelets are generated by modulating the amplitudes of the sinusoidal wavelets (outlined in bold), as is shown in Fig 4.14. The seismogram can be generated and decomposed by superimposing the AMS source wavelets and separating the AMS wavelets, respectively.

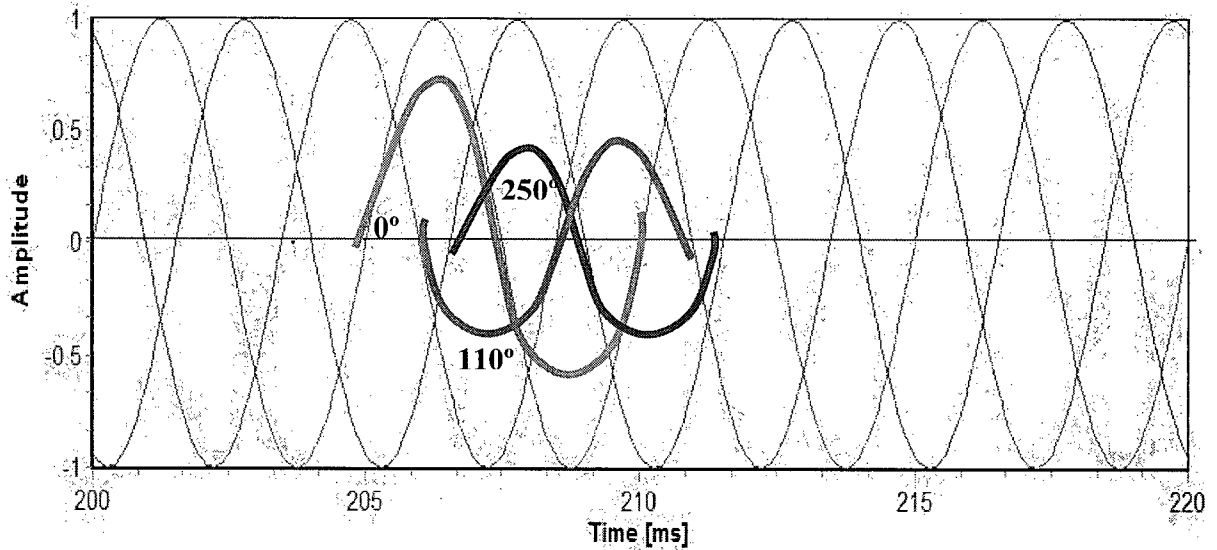


Figure 4.14. An illustration of the convolution operation as the summation of AMS source wavelets.

Similar to the PS-SEED filter, the PPD algorithm implements a RBKF that individually weights and subsequently sums a bank of linear Kalman filters with JMLGS. The KFs define the system and measurement dynamics for event and non-event conditions. The event condition is associated with the case of a source wavelet or overlapping source wavelets being present within the recorded time series at time index, k . The non-event condition represents the case when only measurement noise is present. As shown in Table 3.1, the Kalman filters are specified and updated by samples drawn from a finite state Markov chain distribution (FSMCD). The FSMCD defines the probability and transitional probabilities of the event and non-event conditions.

In the PPD algorithm, there is the added complexity that more than one source wavelet can be present at time index, k . The number of Kalman filters required and the associated definition of the system and measurement equations must reflect that possibility of

overlapping source wavelets. In shallow and deep reflection seismology, it is reasonable to assume there will be a maximum of three to four overlapping source wavelets recorded within the seismogram. For example, Sheriff and Geldart [47] demonstrate that the expected vertical resolution of a noise free reflection seismic survey is $\lambda/4$, where λ defines the wavelength of the source wavelet. For shallow investigations (20 m to 100 m), it is feasible to assume a dominant compression source wave frequency (f) of approximately 100 Hz ($T = 1/f = 10$ ms) and a corresponding velocity (V_p) of 1500 m/s. Based upon these parameters, the calculated vertical resolution is 4.75 m (note: $\lambda = V/f$). The associated two way travel time (Δt) of the source wavelet for a vertical resolution of 4.75 m is 5 ms (i.e., $\Delta t = 2*4.75/V$). If the period (10 ms) of the source wavelet is divided by the two way travel time, a ratio of two is obtained. This implies that for this particular configuration, one would not expect more than three overlapping source wavelets. This assumes that the duration of the source wavelet is equal to its period. A similar calculation can be made for a deep reflection (500 m to 5 Km) survey, where $V_p \approx 3000$ m/s to 5000 m/s and $f \approx 50$ Hz.

If it is assumed that there is a maximum of three overlapping source wavelets for an event condition, then there are a total of seven overlapping source wavelet combinations. These combinations are outlined as follows:

- Only one source wavelet present resulting in three possible configurations ((1,0,0), (0,1,0), and (0,0,1));
- Two overlapping source wavelets present, resulting in three possible configurations (1,1,0), (1,0,1), and (0,1,1);
- Three overlapping source wavelets present (1,1,1).

If one assigns a total of 200 event/no-event KFs (particles) for each time increment, and it is assumed that there is a 40 percent chance of an event, then the total number of required Kfs (particles) is $200*0.4*7$ (event) + $200*0.6$ (no-event) = $560+120 = 680$. This is a dramatically lower number than the previously outlined value of 10^{48} without the requirement of modeling the reflection coefficients as discrete state levels.

In addition to utilizing a RBPF, and similar to the PS-SEED algorithm, the PPD algorithm implements a set of HMM filters in order to refine the initially specified phase components of the AMS source wavelets. For example, if an approximate phase of 100° is specified with a fixed-grid phase interval resolution of $\pm 15^\circ$, then the HMM filter will adjust the 100° phase within the -85° to 115° phase interval window to give an optimal estimate.

c) PPD Kalman Filter and Jump Markov Linear Gaussian System Formulation

The PPD algorithm models the amplitude modulating term of the AMS source wavelet as a slowly varying (high time constant) Gauss-Markov process. When specifying the KF system equation, the user must take into account the maximum number of possible overlapping source wavelets. For example, (62) illustrates the required KF system equation for the case of a maximum of three overlapping source wavelets. The state vector represents the amplitude component of the three source wavelets and the additive background noise (state x_{4k}) that is modeled as a Gauss-Markov process with defining parameters of variance and time constant. As previously stated for the PS-SEED algorithm, this does not preclude any other types of ambient-noise models, but it is required that the measurement noise be specified within a state-space formulation.

The PPD measurement equation incorporates the JMLGS dynamics of the SBD problem, where the measurement equation can change (“jump”) based upon the event and no-event conditions. An event condition signifies that source wavelets are present. The PPD algorithm must take into account the possibility that only one source wavelet or several overlapping source wavelets are present when an event condition occurs. Equation (63) outlines the PPD measurement equation for the BSD problem when it is assumed that a maximum of three source wavelets are overlapped at time index, k , for the event condition.

$$\begin{bmatrix} x1_{k+1} \\ x2_{k+1} \\ x3_{k+1} \\ x4_{k+1} \end{bmatrix} = \begin{bmatrix} a_1 & 0 & 0 & 0 \\ 0 & a_2 & 0 & 0 \\ 0 & 0 & a_3 & 0 \\ 0 & 0 & 0 & a_n \end{bmatrix} \begin{bmatrix} x1_k \\ x2_k \\ x3_k \\ x4_k \end{bmatrix} + \begin{bmatrix} b_1 & 0 & 0 & 0 \\ 0 & b_2 & 0 & 0 \\ 0 & 0 & b_3 & 0 \\ 0 & 0 & 0 & b_n \end{bmatrix} \begin{bmatrix} u1_k \\ u2_k \\ u3_k \\ u4_k \end{bmatrix} \quad (62)$$

$$z_k = x1_k \sin(\omega k \Delta + \varphi1_k) + x2_k \sin(\omega k \Delta + \varphi2_k) + x3_k \sin(\omega k \Delta + \varphi3_k) + x4_k \quad (63)$$

In (63), ω represents the dominant frequency of the source wavelet and $f(1..3)_k$ are the HMM filter phase estimates at time index, k , for source wavelets 1 to 3, respectively. As previously outlined, for each event condition there are seven possible combinations ((1,0,0), (0,1,0), (0,0,1), (1,1,0), (1,0,1), (0,1,1) and (1,1,1)) for the case of three source wavelets. The PPD algorithm also synthesizes measurements for the no-event condition. In these cases, synthetic measurements of very low value are assigned to the respective source wavelets. This removes the residual influence of source wavelets that do not contribute to the estimated measurement equation described by (68).

d) PPD Parameter Specification and Algorithm Implementation

The first step in formulating the PPD algorithm consists of specifying the maximum number of possible overlapping source wavelets and outlining the corresponding KF system and measurement equations. Subsequent to this, the dominant frequency and approximate values of the AMS source wavelets' initial phase estimates and corresponding fixed-grid phase interval resolutions are specified. This information is readily available from the seismogram under investigation. Section IV.B.2.g outlines an algorithm utilized for estimating the source wavelet's dominant frequency. After the dominant frequency and approximate phase of the first source wavelet is estimated, approximate values of the remaining AMS source wavelet phases and corresponding phase resolutions are specified. This can be carried out

utilizing a parameter estimation program, such as the simplex method. It is also possible to implement the PPD filter without the requirement of specifying all the initial phase estimates. This PPD algorithm configuration is outlined in Section IV.B.2.f. In this case, the overlapping source wavelets are extracted sequentially and chronologically from the seismogram. The only phase which is required to be specified is that of the current source wavelet to be extracted.

The final important parameter to specify within the PPD algorithm is the number of Kalman filters or particles required. As previously outlined, in the RBPF implemented for the PPD algorithm, a set of particles (N'_S) that define the event/no-event⁵ condition are initially generated by computing a FSMCD. If an event has occurred, then a set of additional KFs or particles are generated, equal to the total number of overlapping source wavelet combinations, which is calculated as follows:

$$N_{OSC} = N_{SW} + 1 + \sum_{i=2}^{N_{SW}-1} \frac{N_{SW}!}{i!(N_{SW}-i)!} \quad (64)$$

In (64), N_{OSC} = the number of overlapping source wavelet combinations and N_{SW} = the number of source wavelets. The total number of particles (N_S) and corresponding Kalman filters for the PPD algorithm is calculated as follows:

$$N_S = N_{OSC} \times PE \times N'_S + (1 - PE) \times N'_S \quad (65)$$

In (65), PE = the probability of an event. Table 4.3 outlines the PPD filter formulation. Appendix F provides for more detail on the utilization of the FSMCD and the corresponding implementation of the HMM filter within the PPD algorithm.

⁵ Source wavelet present/not-present condition for each time increment.

TABLE 4.3
PPD FILTER FORMULATION

Step	Description	Mathematical Representation
1	Specify the number of source wavelets (N_{SW}) and their corresponding phases and phase intervals, respectively. Specify the measurement-noise variance and time constant. Based upon these parameter formulate the JMLGS system and measurement equations.	<p><u>System Dynamics</u></p> <p>See (57) for the case of 3 source wavelets</p> <p><u>Measurement Equations</u></p> <p>See (58) for the case of 3 overlapping source wavelets.</p>
2	Calculate N_S and initialize the prior and transitional pdf for the event/no-event JMLGS.	$p(y_0^1), p(y_0^2), \& p(y_k^i y_{k-1}^j),$ $i, j = 1, 2$
3	For each phase interval, initialize the prior and transitional pdf for the fixed-grid phases.	$p(\varphi_l^i) \& p(\varphi_l^i \varphi_l^j), i = 1, \dots, N_{SW}, \text{ and } j = 1, \dots, N_{PI},$ <p>where N_{PI} = number of fixed-grid value (i.e., phase interval resolution).</p>
4	At each time index, draw samples for finite state Markov chain for the event/no-event conditions. If event is present (i.e., $y_k^i = y_{2k}$) generate additional particles (i.e., Kalman filters) based upon the calculated combinations.	$y_k^i \sim P(y_k^i y_{k-1}^j)$
5	Propagate sinusoids based current time index ($t = k?$) and phase estimates.	$\text{Sinusoid}(1..3) = \sin(\omega t + f(1..3)_k)$

TABLE 4.3 (CONTINUED)
PPD FILTER FORMULATION

Step	Description	Mathematical Representation
6	Utilizing (13)-(17) outlined in Table 3.1 and updated sinusoids of Step 5, propagate the system and measurement equations, calculate importance weights ¹ for particles and then update and normalize the weights.	$\tilde{w}_k^i = w_{k-1}^i N(z_k \hat{z}_k^i, \mathbf{S}_k^i),, i = 1, \dots, N_s.$ $w_k^i = \tilde{w}_k^i / \sum_{i=1}^{N_s} \tilde{w}_k^i$
7	Obtain asymptotically optimal estimate of the state vector (i.e., estimate source wavelet responses for the three specified overlapping wavelets).	$\hat{\mathbf{x}}_k \approx \sum_{i=1}^{N_s} w_k^i \mathbf{x}_k^i$
8	Sampling Importance Re-sampling (SIR). Re-sample if $\hat{N}_{eff} < N_T$	$\hat{N}_{eff} = \frac{1}{\sum_{i=1}^{N_s} (w_k^i)^2}$
9	Use $\hat{\mathbf{x}}_k$ and HMM filter equations (Table 3.2) to estimate $f(1..3)_k$.	
10	Utilize (18)-(20) to update the bank of KFs	
11	Let $k = k+1$ & iterate to step 4.	

1) de Freitas [23] demonstrates that the importance weights for y_k^i are given by the predictive density $p(z_k | z_{1:k-1}, y_{1:k}^i) = N(z_k; \hat{z}_k^i, \mathbf{S}_k^i)$, where N denotes a Gaussian

e) Evaluating the PPD Algorithm with Simulated Data

The deconvolution of minimum phase wavelets is a standard procedure, and the Wiener filter has been used extensively for this purpose [48]. The real challenge for seismic signal processors is to deconvolve mixed phased wavelets. For this reason, the performance of the PPD was assessed by deconvolving seismograms that contained mixed phased Berlage wavelets [1]. The Berlage wavelet is defined as follows:

$$w(t) = AH(t)t^n e^{-\alpha t} \cos(2\pi ft + \phi), \quad (66)$$

where $H(t)$ is the Heaviside unit step function [$H(t) = 0$ for $t = 0$ and $H(t) = 1$ for $t > 0$]. The amplitude modulation component is controlled by two factors: the exponential decay term, α , and the time exponent, n . These parameters are considered to be non-negative, real constants. Figure 4.15 illustrates a mixed phased Berlage wavelet, with $f = 50$ Hz, $n = 2$, $\alpha = 100$ and $\phi = 10^\circ$. The parameter, A , was set to give a maximum amplitude of approximately 80 units, and the sampling rate was 0.05 ms. The Berlage wavelet of Fig. 4.15 was then convolved with the closely spaced reflection coefficients shown in Fig. 4.16 to give the output illustrated in Fig. 4.17. The synthetic seismogram shown in Fig. 4.17 and all subsequently illustrated synthetic seismograms in Section IV.B.2.e have additive Gauss-Markov noise with a variance of 50 units² and a time constant of 0.001 ms.

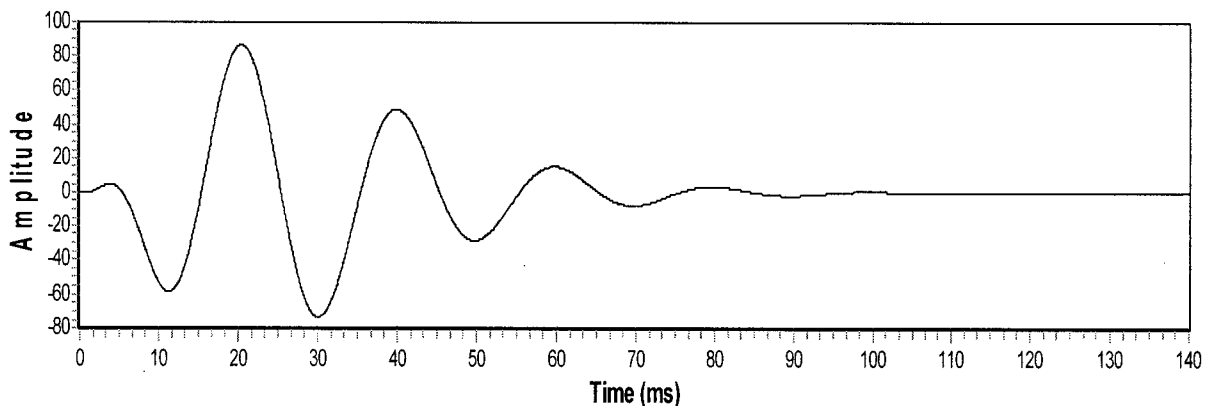


Figure 4.15. A mixed phased Berlage wavelet.

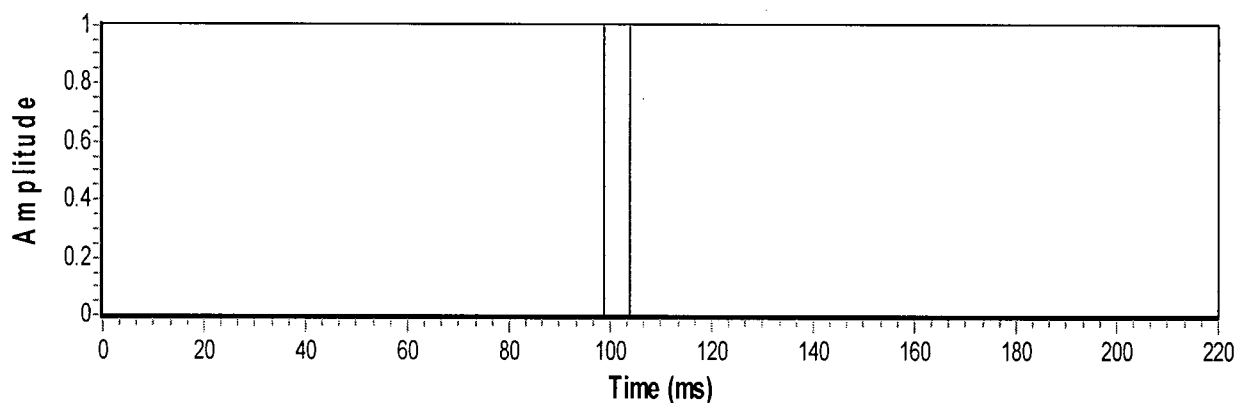


Figure 4.16. Reflection coefficients convolved with Berlage wavelet shown in Fig. 4.15.

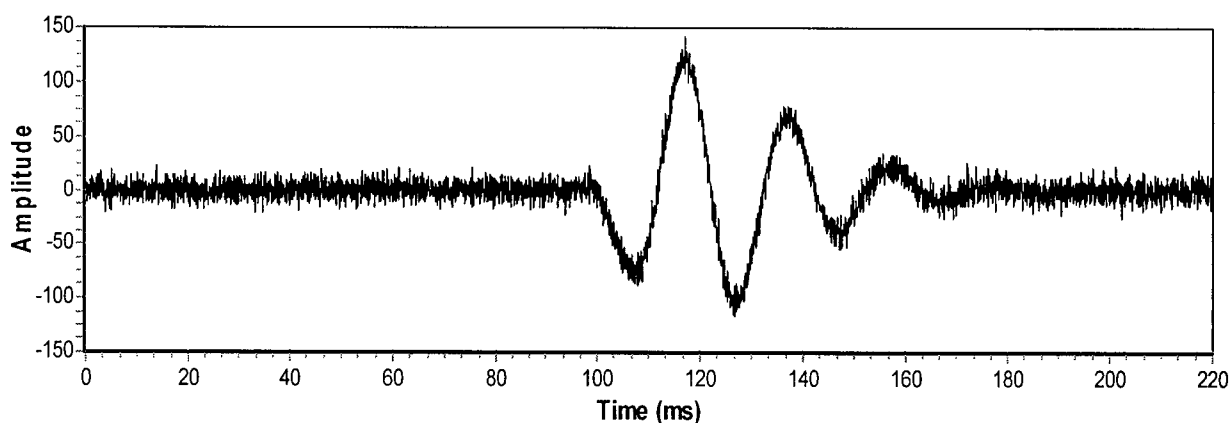


Figure 4.17. The output after convolving Berlage wavelet with reflection coefficients illustrated in Fig. 4.16 and adding measurement noise.

In all subsequent post analysis, a 200 Hz, eighth order, zero-phase shift, low-pass Butterworth frequency filter [31] is applied so that the signal-to-noise ratio of the synthetic seismogram is significantly increased. This is due to the fact the PPD algorithm is separating overlapping source wavelets and not estimating high bandwidth reflection coefficients as in the case of standard seismic deconvolution algorithms. For example, a major concern in frequency domain deconvolution is that one is working with bandlimited source wavelets and any high frequency measurement noise will significantly degrade the ability to estimate the reflection coefficients. In this case, one cannot simply apply a low-pass frequency filter because this will remove information associated with the high bandwidth

reflection coefficients. In the KFSD algorithm, it would be required to incorporate the applied low-pass frequency filter within the state-space formulation [42]. This would result in a relatively complicated filter formulation becoming more complicated and unstable.

In order to demonstrate the general concept of the PPD algorithm, the dominant frequency and associated phases were determined interactively as opposed to utilizing a parameter estimation algorithm. For example, Fig. 4.18 illustrates the seismogram of Fig. 4.17 after the 200 Hz low-pass frequency filter was applied. Superimposed on this seismogram is a scaled sinusoid with dominant frequency of 50 Hz and corresponding phase of 190° . As is evident in Fig. 4.18, the sinusoid nearly overlaps the first portion of the filtered synthetic time series of Fig. 4.17; therefore, when implementing the PPD algorithm on the filtered seismogram of Fig. 4.17, a dominant frequency of 50 Hz is specified along with an initial phase component of 190° .

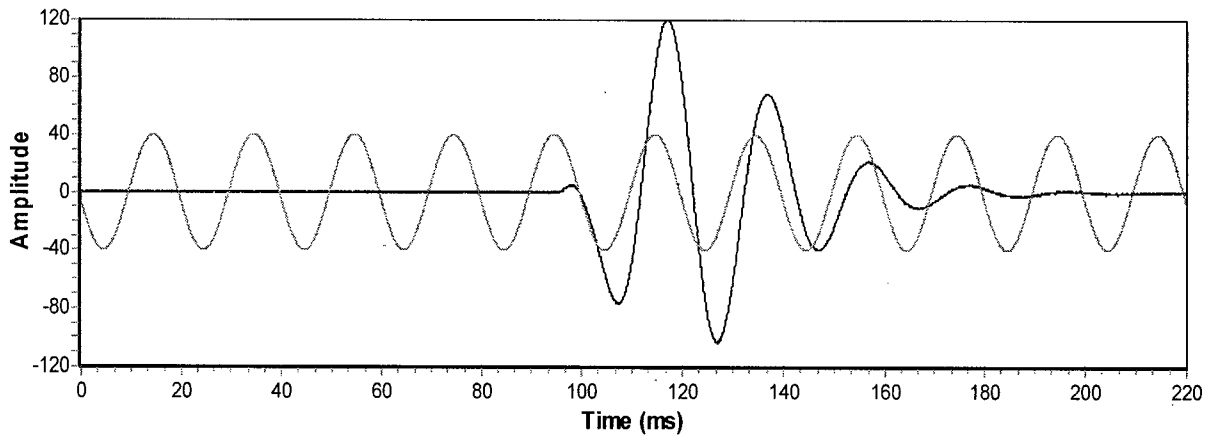


Figure 4.18. Estimating the dominant frequency and initial phase component interactively.

In Fig. 4.18, it is also apparent that another source wavelet is present around 104 ms, due to the fact that the seismogram no longer follows the sinusoid with a frequency of 50 Hz and a corresponding phase of 190° . For these reasons, an additional scaled 50 Hz sinusoid with a phase of 100° is interactively introduced and summed with the sinusoid of 190° at 104 ms. As is shown in Fig. 4.19, the two sinusoids add such that they nearly have identical oscillations as the synthetic seismogram; therefore, the PPD algorithm is initialized with a dominant frequency of 50 Hz and two phases of 190° and 100° and corresponding phase interval resolution of $\pm 3^\circ$ (i.e., 187° to 193° and 97° to 103° , respectively). Figure 4.20 illustrates the output of the PPD algorithm, where the two Berlage wavelets have been separated exactly. This is demonstrated by the error residual illustrated in Fig. 4.21. The error residual in Fig. 4.21 is defined to be the difference between the filtered seismogram of Fig. 4.17 and the estimated Berlage wavelets of Fig. 4.20.

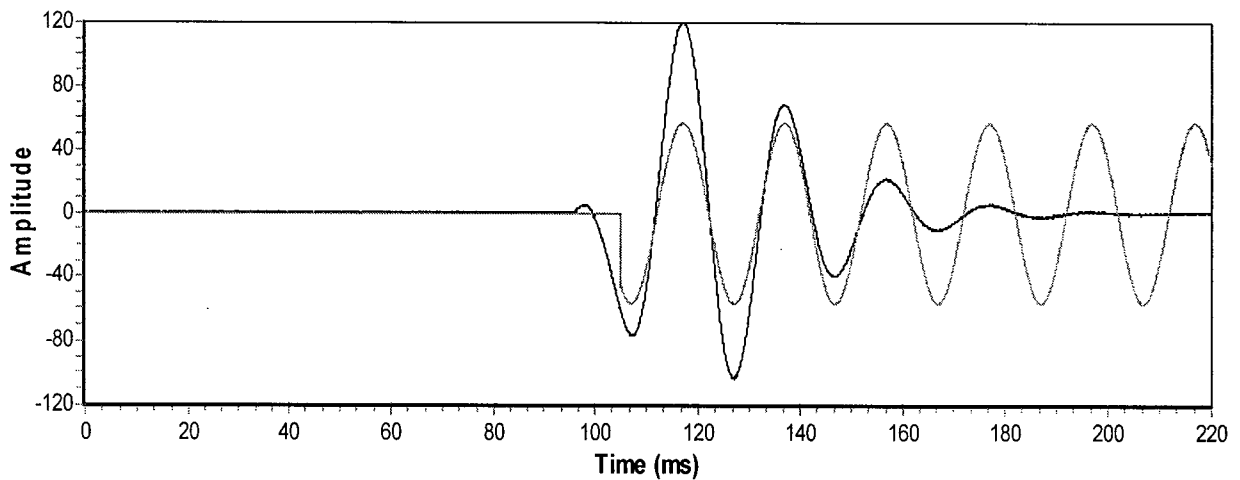


Figure 4.19. The addition of a 50 Hz sinusoid with a phase of 100° at a time of 104 ms.

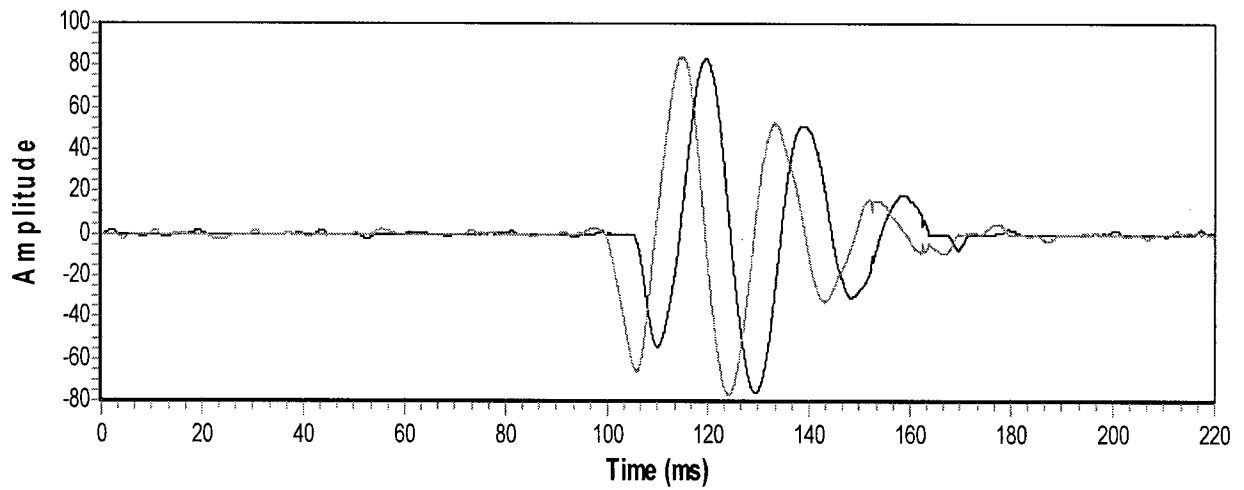


Figure 4.20. The output of the PPD algorithm, where the Berlage wavelets have been separated.

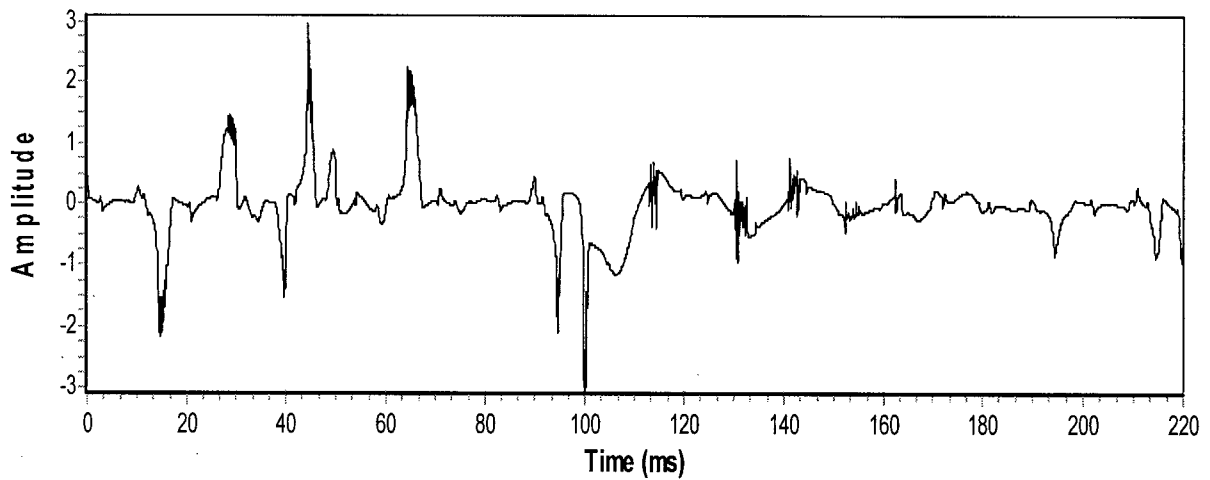


Figure 4.21 The error residual, which is defined to be the difference between the filtered seismogram of Fig. 4.17 and the estimated Berlage wavelets of Fig. 4.20.

The PPD algorithm was next tested for its ability to deconvolve a closely spaced dipole. For this test, the Berlage wavelet of Fig. 4.15 was convolved with the dipole shown in Fig. 4.22 to give the output (with additive Gauss-Markov noise) as illustrated in Fig. 4.24.

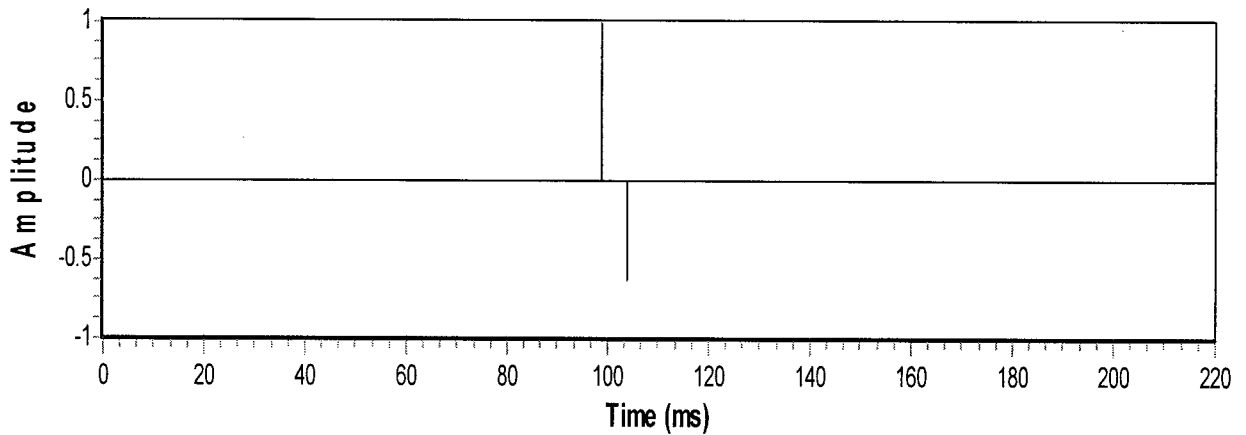


Figure 4.22. The dipole reflection coefficients convolved with the Berlage wavelet shown in Fig. 4.15.

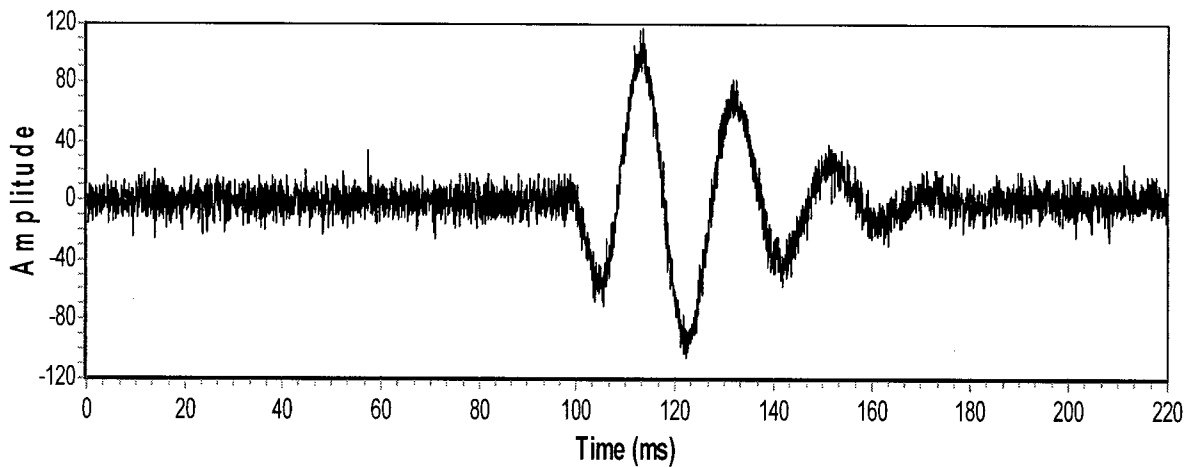


Figure 4.23. The output after convolving the Berlage wavelet of Fig. 4.15 with reflection coefficients illustrated in Fig. 4.22 and adding the Gauss-Markov measurement noise.

Figure 4.24 illustrates the output of the PPD algorithm, where the algorithm did an impressive job in extracting the dipole Berlage source wavelets. Figure 4.25 shows the error residual, which is defined to be the difference between the filtered seismogram of Fig. 4.23 and the estimated Berlage wavelets of Fig. 4.24.

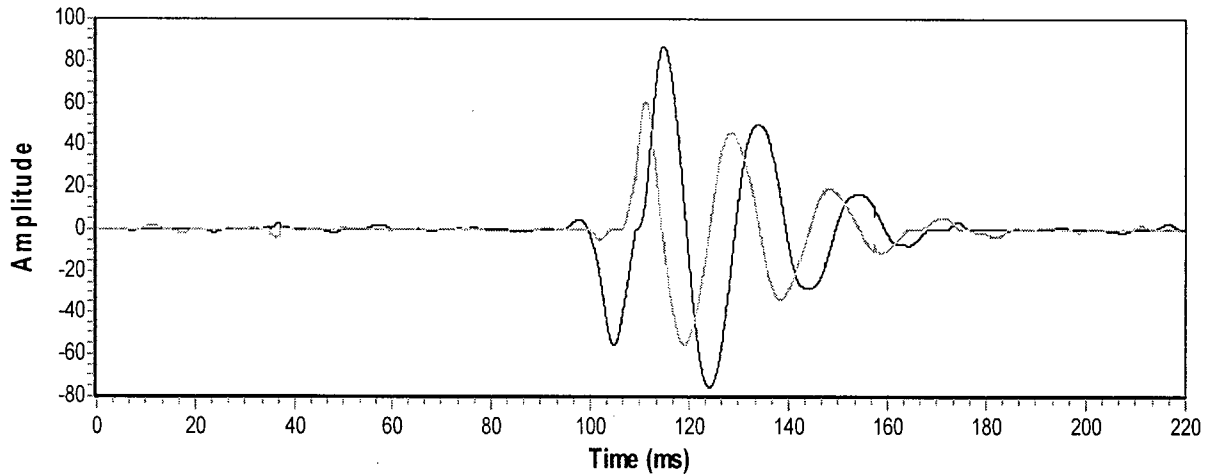


Figure 4.24. The output of the PPD algorithm, where the algorithm did an impressive job in extracting the dipole Berlage source wavelets.

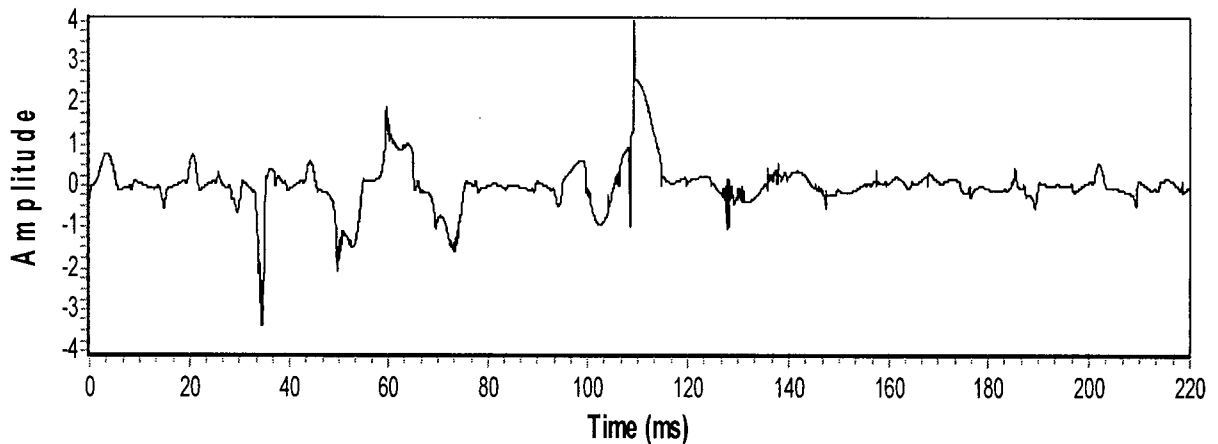


Figure 4.25. The error residual, which is defined to be the difference between the filtered seismogram of Fig. 4.23 and the estimated Berlage wavelets of Fig. 4.24.

The next two sets of synthetic seismograms were designed to test the PPD algorithm's ability to carry out blind seismic deconvolution on non-stationary source wavelets. In the first test, the zero-phase Ricker wavelet of Fig. 4.11 is superimposed upon the Berlage wavelet illustrated in Fig. 4.15 (with an arrival time of 99 ms) to give the output (with additive measurement noise) shown in Fig. 4.26. Figure 4.27 illustrates the output of the PPD algorithm, where the algorithm did an impressive job in extracting the Berlage source wavelet from the overlapping zero-phase Ricker wavelet. I believe that this is the first example where a Ricker wavelet has been separated from a mixed-phase Berlage wavelet, utilizing a blind deconvolution algorithm. Figure 4.28 shows the error residual, which is defined to be the difference between the filtered seismogram of Fig. 4.26 and the estimated wavelets of Fig. 4.27.

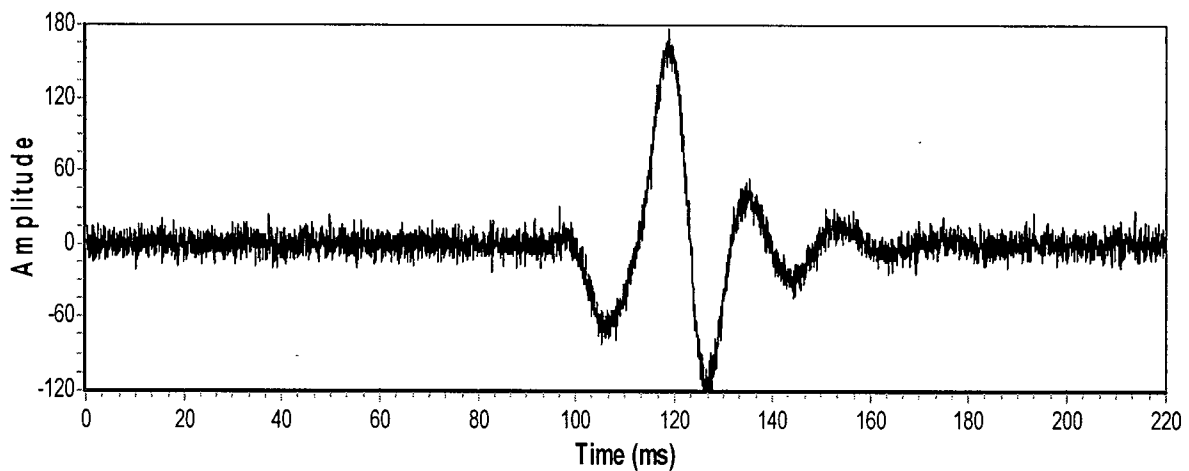


Figure 4.26. The output after superimposing a Berlage wavelet with an arrival time of 99 ms and the zero-phase Ricker wavelet of Fig. 4.11.

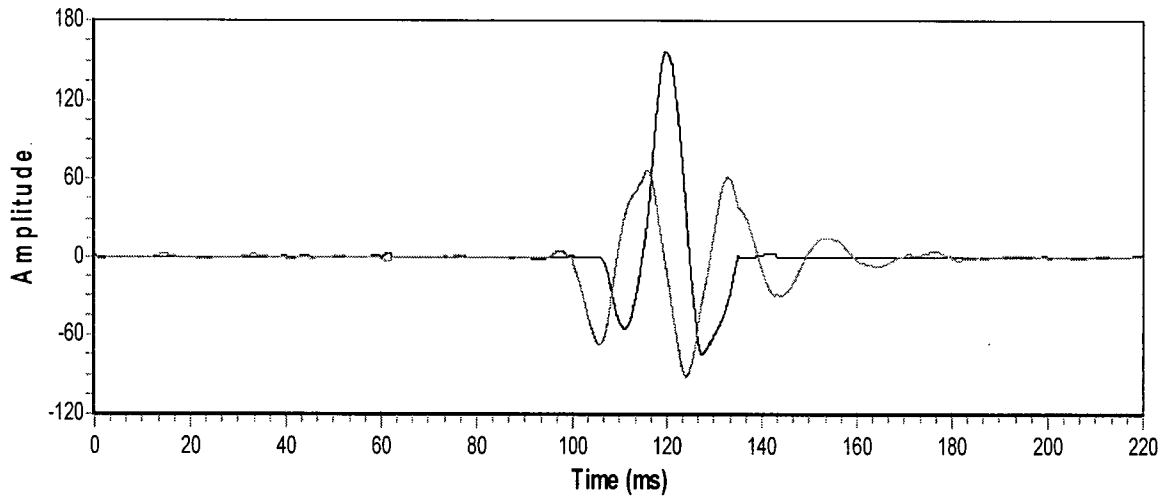


Figure 4.27. The output of the PPD algorithm, where the algorithm did an impressive job in extracting the Berlage source wavelet from the overlapping zero-phase Ricker wavelet.

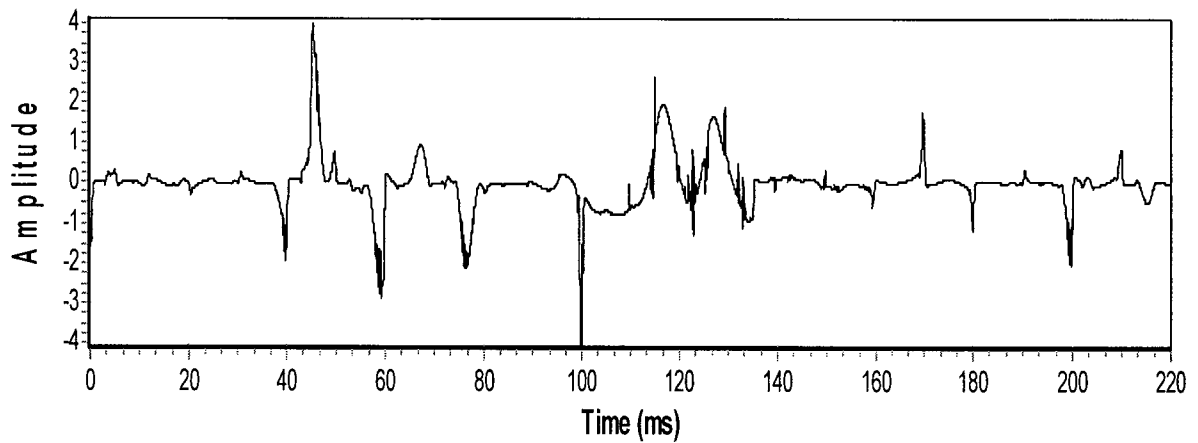


Figure 4.28. The error residual, which is defined to be the difference between the filtered seismogram of Fig. 4.26 and the estimated source wavelets of Fig. 4.27.

The next non-stationary source wavelet test demonstrates the ability of the PPD algorithms to deconvolve two Berlage wavelets, where the first wavelet has a frequency of 50 Hz and the second wavelet has a frequency of 40 Hz. This test illustrates the effects of the Q value on the source wavelet. It is readily known that the higher frequencies are attenuated more rapidly than lower frequencies as the source wavelet travels through the earth. This test attempts to replicate this attenuation. Figure 4.29 shows a mixed phased Berlage wavelet with $f = 40 \text{ Hz}$, $n = 2$, $a = 100$, $\phi = 10^\circ$, and an arrival time of 104 ms. This source wavelet was then superimposed upon the Berlage wavelet of Fig. 4.15 with arrival time of 99 ms. Figure 4.30 illustrates the result of superimposing the time-variant Berlage source wavelets with additive measurement noise.

The dominant frequencies and associated phases were again determined interactively, as was illustrated in Figs. 4.18 and 4.19. As outlined in Fig. 4.18, the first Berlage source wavelet was determined to have a dominant frequency of 50 Hz and corresponding phase of 190° . Figure 4.31 illustrates an additional scaled 40 Hz sinusoid with a phase of 100° , which is interactively introduced and summed with the 50 Hz sinusoid of phase 190° at 104 ms. As is shown in Fig. 4.31, the two sinusoids add, such that they nearly have identical oscillations as the synthetic seismogram; therefore, the PPD algorithm is initialized with two dominant frequencies of 50 Hz and 40 Hz, and two phases of 190° and 100° , respectively. Figure 4.32 illustrates the output of the PPD algorithm, where the two Berlage wavelets have been separated. The error residual is shown in Fig. 4.33.

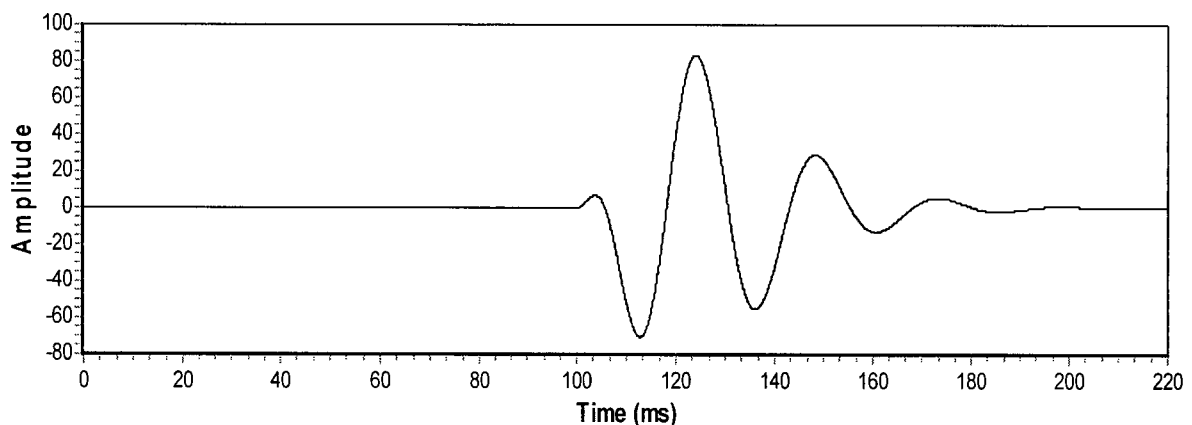


Figure 4.29. A mixed-phased Berlage wavelet with $f = 40 \text{ Hz}$, $n = 2$, $a = 100$, and $\phi = 10^\circ$.

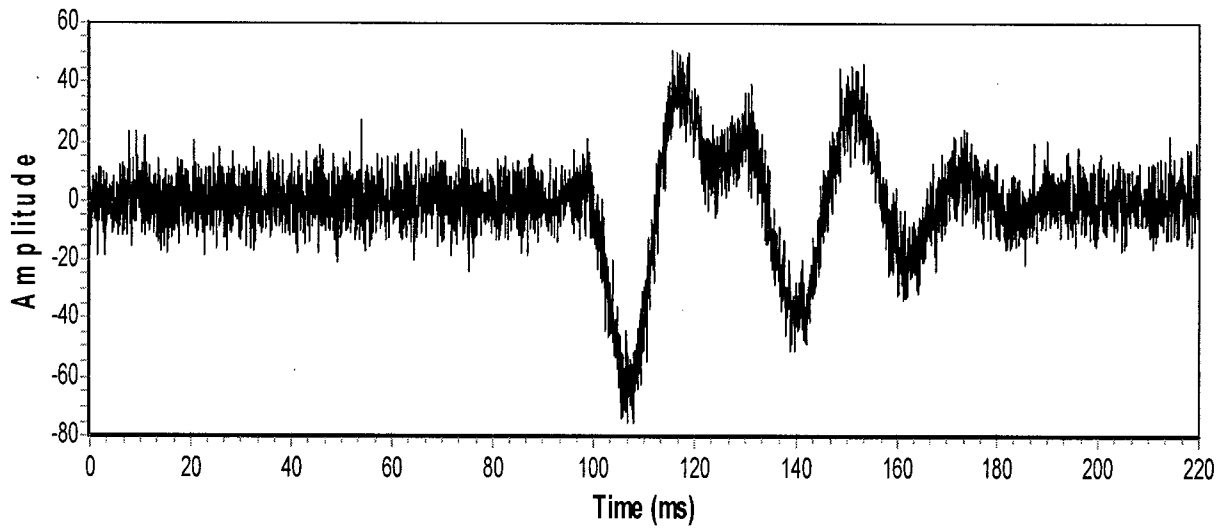


Figure 4.30. The output after superimposing the time-variant Berlage source wavelets with additive measurement noise (variance = 50 units² and time constant = 0.001 ms).

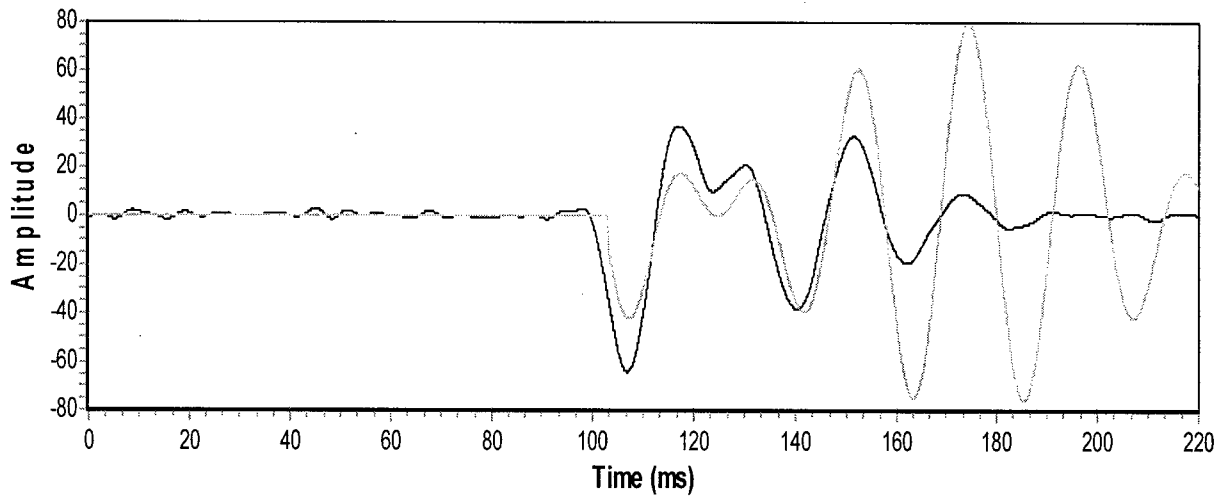


Figure 4.31. The addition of a 40 Hz sinusoid with phase of 100° at time of 104 ms to the sinusoid shown in Fig. 4.18.

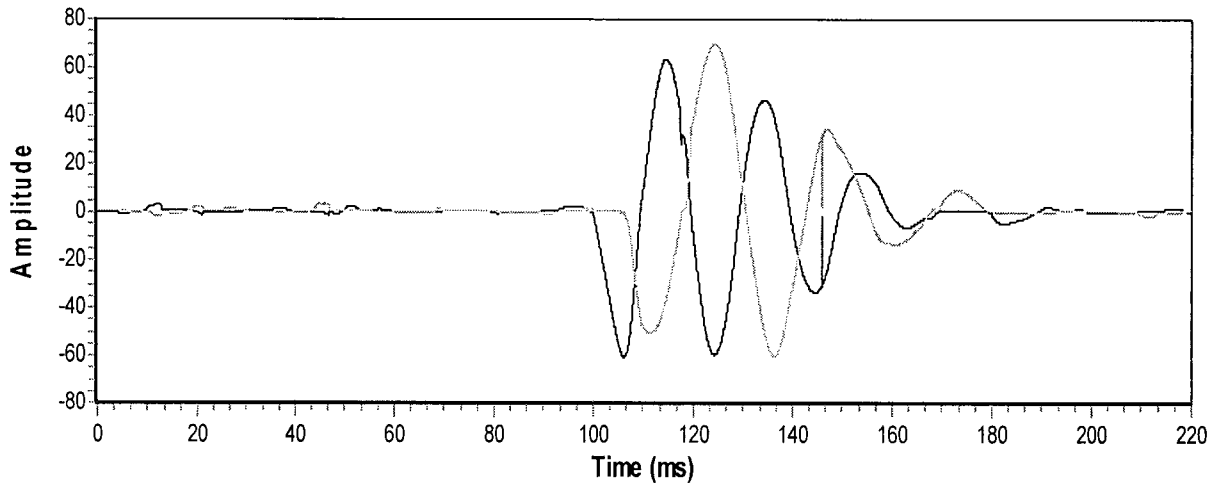


Figure 4.32. The output of the PPD algorithm, where the algorithm did an impressive job in extracting the non-stationary Berlage source wavelets.

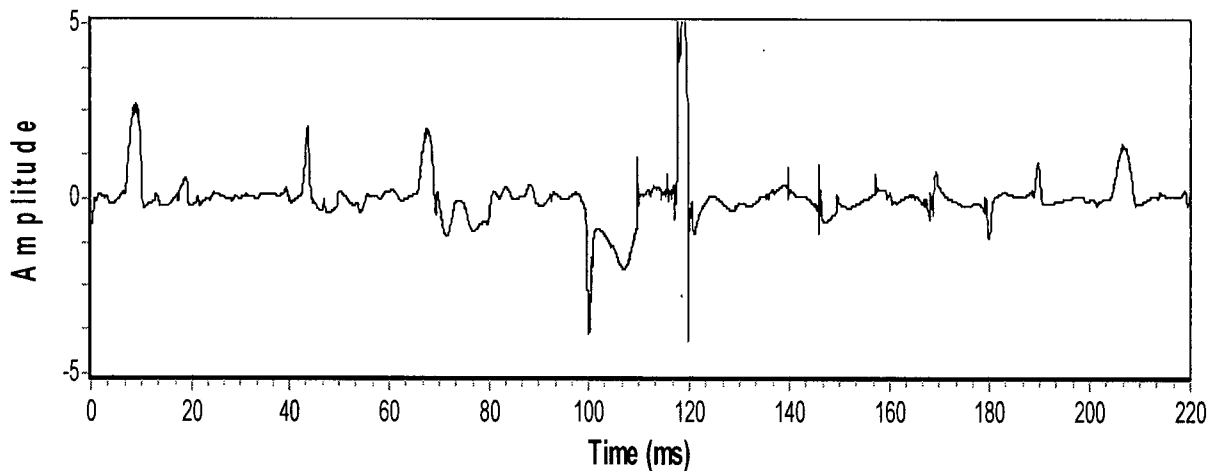


Figure 4.33 Error residual that is defined to be the difference between the filtered seismogram of Fig. 4.30 and the estimated source wavelets of Fig. 4.32.

f) **Proposed Methodology in Processing Seismograms with the PPD Algorithm**

As previously outlined, the main challenge in implementing the PPD algorithm is the specification of the principle phase components of the seismogram. For this reason, I recommend that the overlapping source wavelets be sequentially and chronologically extracted from the seismogram under analysis. This mitigates the requirement of pre-specifying the principle phase components. The only phase which is required to be specified is that of the current (in chronological order) source wavelet which is to be extracted from the seismogram. This information is readily available from the seismogram under study.

In this PPD filter wavelet extraction (PPD-WE) configuration there are only two possible overlapping source wavelets: the source wavelet to be extracted and the remaining seismogram time series data. Furthermore, for each event condition there are only two permutations. These permutations reflect the situation where only the source wavelet under study is present at time index k (i.e., (1,0)) and the case where the source wavelet under study is overlapped with other time series data at time index k (i.e., (1,1)). The two event condition allows the investigator to implement a significantly simplified PPD where only a 3 state FSMCD (i.e., noise, event condition (1,0) + noise, and event condition (1,1) + noise) is required. This avoids the requirement of calculating the total number of overlapping source wavelet combinations (i.e., (59)). Appendix G provides for more detail on the utilization of the 3 state FSMCD within the PPD-WE.

In the PPD-WE filter formulation the state equation defined by (62) is slightly modified as follows:

$$\begin{bmatrix} x1_{k+1} \\ x2_{k+1} \\ x3_{k+1} \\ x4_{k+1} \\ x5_{k+1} \end{bmatrix} = \begin{bmatrix} 1 & \Delta & 0 & 0 & 0 \\ 0 & a_2 & 0 & 0 & 0 \\ 0 & 0 & 1 & \Delta & 0 \\ 0 & 0 & 0 & a_4 & 0 \\ 0 & 0 & 0 & 0 & a_n \end{bmatrix} \begin{bmatrix} x1_k \\ x2_k \\ x3_k \\ x4_k \\ x5_k \end{bmatrix} + \begin{bmatrix} 0 & 0 & 0 & 0 & 0 \\ 0 & b_2 & 0 & 0 & 0 \\ 0 & 0 & 0 & 0 & 0 \\ 0 & 0 & 0 & b_4 & 0 \\ 0 & 0 & 0 & b_n & 0 \end{bmatrix} \begin{bmatrix} 0 \\ u2_k \\ 0 \\ u4_k \\ un_k \end{bmatrix} \quad (67)$$

The PPD-WE algorithm models the amplitude modulating terms (AMT) (states $x1_k$ and $x3_k$) of the AMS source wavelet with a first order Taylor series approximation⁶. The rate of change terms (states $x2_k$ and $x4_k$) are then approximated as Gauss-Markov processes. This allows for considerable flexibility and controllability when assigning prior to the amplitude modulating terms (e.g., smoothness). The time constant terms of states $x2_k$ and $x4_k$ are important and fundamental parameters within the PPD-WE algorithm. It is desired that states $x2_k$ and $x4_k$ result in a smooth trajectory of the amplitude modulation terms of the AMS while at the same time allow for sufficient maneuverability so that the AMS source wavelet to be extracted (AMS-E) follows the oscillations of the user specified sinusoid. The PPD-WE applies a linear range of possible time constant terms equal to the number of specified particles (i.e., Kalman Filters) for states $x2_k$ and $x4_k$. In the subsequent test bed simulations, the range of time constant terms varies from 0.6 ms (i.e., $a_1 = a_2 = 0.92$, highly maneuverable) to 6.22 ms (i.e., $a_1 = a_2 = 0.992$, sluggish). The SIR (i.e., degeneracy check) portion of the PPD-WE estimates the optimal value of the time constant for states $x2_k$ and $x4_k$ within the range specified.

Another important PPD-WE parameter to specify is the time index t^* where it is assumed that the overlapping time series data has not yet arrived (i.e., only the AMS-E exist). This value is an approximation and is readily estimated as the end time of the AMS-E initial phase estimate. Time index t^* allows the PPD-WE to initially lock onto the AMS-E. Equation (68) outlines the PPD-WE measurement equation for the BSD problem when it is assumed that a maximum of two source wavelets are overlapped at time index, k , for the event condition.

$$z_k = x1_k \sin(\omega k \Delta + \phi1_k) + x3_k \sin(\omega k \Delta + \phi3_k) + x5_k \quad (68)$$

In (68), ω again represents the dominant frequency of the source wavelet and $f1_k$ is the HMM filter phase estimate at time index, k , for the source wavelet to be extracted. The phase window resolution for the source wavelet is set quite small (e.g., $\pm 3^\circ$) because the

⁶ Please note that the amplitude modulating terms defined by (62) and (67) are forced to be positive.

phase of the source wavelet to be extracted is easily determined from the seismogram with high accuracy. The HMM filter phase estimate at time index, k , for time series data overlapping the source wavelet to be extracted is defined by parameter $f3_k$. The phase window resolution for $f3_k$ is initially set at 1° to 360° . This range of phases is generally refined based upon the initial values estimated from the first pass of data. For example, if after the first pass of processing the seismogram it is found that the HMM estimates of $f3_k$ range between 100° to 150° , then the PPD-WE is re-applied to the data set with $f3_k$ restricted to this range of phase.

Major advantages of the PPD-WE algorithm are the simplicity of implementation, minimal parameter specification and there is no theoretical limit on the number of overlapping source wavelets. Table 4.4 outlines the PPD-WE filter formulation. A disadvantage of the PPD-WE algorithm is that any errors generate during the wavelet extraction process will propagate as the seismogram is sequentially and chronologically processed.

TABLE 4.4
PPD-WE FILTER FORMULATION

Step	Description	Mathematical Representation
1	Identify the source wavelet to be extracted by specifying its corresponding dominant frequency and corresponding phase and phase resolution window. Specify the measurement-noise variance and time constant and the variance and time constant range for states $x2_k$ and $x4_k$. Based upon these parameter formulate the JMLGS system and measurement equations.	<p><u>System Dynamics</u></p> <p>See (62).</p> <p><u>Measurement Equations</u></p> <p>See (63) for the case of 3 overlapping source wavelets.</p>
2	Specify N_S and initialize the prior and transitional pdf for the 3 state FSMCD as outlined in Appendix F (e.g., (A20)).	$p(y_0^1), p(y_0^2), p(y_0^3), \& p(y_k^i y_{k-1}^j),$ $i, j = 1, 2, 3$
3	For the two phase intervals, initialize the prior and transitional pdfs for the fixed-grid phases.	$p(\phi_l^i) \& p(\phi_l^i \phi_l^j), i = 1, 2 \text{ and } j =$ $1, \dots, N_{PI}, \text{ where } N_{PI} = \text{number of}$ $\text{fixed-grid value (i.e., phase interval}$ resolution).
4	At each time index, draw N_S samples for 3 state FSMCD. Update Kalman filter measurement equations based upon y_k^i as outlined in Appendix F ((A21) and (A22)). If $y_k^i = y_k^3$, then states $x1_k$ and $x3_k$ are jittered [25] (i.e., add on $U[-1.5, +1.5]$) to facilitate a diversity of particles.	$y_k^i \sim P(y_k^i y_{k-1}^j)$
5	Propagate sinusoids based current time index ($t = k?$) and phase estimates.	$\text{Sinusoid}(1, 3) = \sin(\omega t + f(1, 3)_k)$

TABLE 4.4 (CONTINUED)
PPD-WE FILTER FORMULATION

Step	Description	Mathematical Representation
6	Utilizing (13)-(17) outlined in Table 2.1 and updated sinusoids of Step 5, propagate the system and measurement equations, calculate importance weights ¹ for particles and then update and normalize the weights.	$\tilde{w}_k^i = w_{k-1}^i N(z_k \hat{z}_k^i, \mathbf{S}_k^i), \quad i = 1, \dots, N_s.$ $w_k^i = \tilde{w}_k^i / \sum_{i=1}^{N_s} \tilde{w}_k^i$
7	Obtain asymptotically optimal estimate of the state vector (i.e., estimate source wavelet to be extracted).	$\hat{\mathbf{x}}_k \approx \sum_{i=1}^{N_s} w_k^i \mathbf{x}_k^i$
8	Sampling Importance Re-sampling (SIR). Re-sample if $\hat{N}_{eff} < N_T$	$\hat{N}_{eff} = \frac{1}{\sum_{i=1}^{N_s} (w_k^i)^2}$
9	Use $\hat{\mathbf{x}}_k$ and HMM filter equations (Table 2.2) to estimate $f(1,3)_k$.	
10	Utilize (18)-(20) to update the bank of KFs	
11	Let $k = k+1$ & iterate to step 4.	

1) de Freitas [23] demonstrates that the importance weights for y_k^i are given by the predictive density $p(z_k | z_{1:k-1}, y_{1:k}^i) = N(z_k; \hat{z}_k^i, \mathbf{S}_k^i)$, where N denotes a Gaussian

The implementation of the PPD-WE algorithm is outlined in more detail by considering the following analysis of synthetic seismograms. In the first test case, the mixed phased Berlage wavelet illustrated in Fig. 4.15 is convolved with the reflection coefficients outlined in Fig 4.16 to give the output illustrated in Fig. 4.34. The synthetic seismogram shown in Fig. 4.34 is similar to that illustrated in Fig. 4.17, but in this case the additive Gauss-Markov noise has a significantly higher variance of 400 units² and a lower time constant of 0.01 ms (i.e., significantly higher correlation in measurement noise) which results in a substantially lower signal-to-noise ratio.

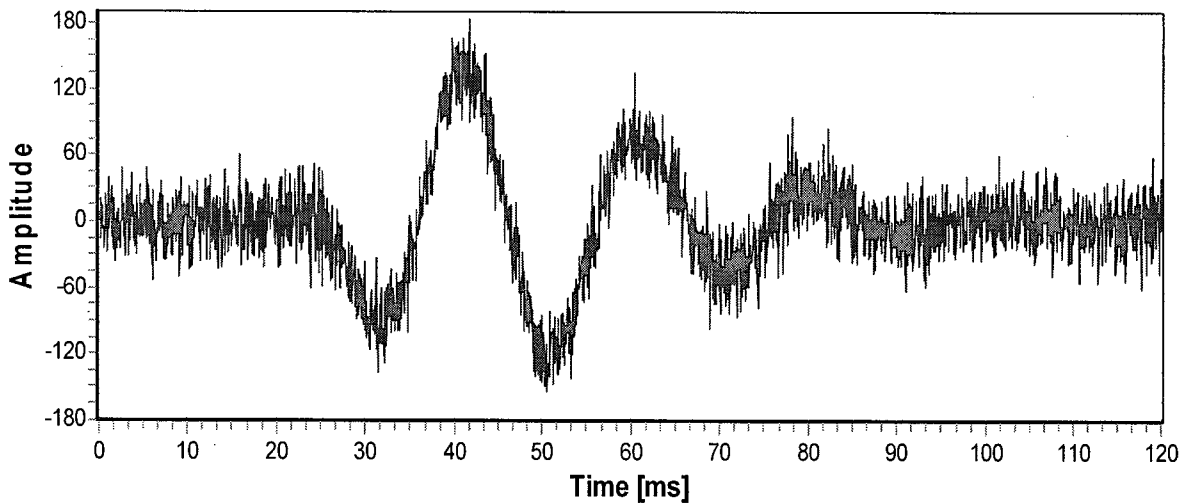


Figure 4.34. The output after convolving Berlage wavelet of Fig 4.15 with reflection coefficients illustrated in Fig. 4.16 and adding Gauss-Markov measurement noise with a variance of 400 units² and a time constant of 0.01 ms.

A 100 Hz, eighth order, zero-phase shift, low-pass Butterworth frequency filter is then applied to the synthetic seismogram shown in Fig 4.34 to give the output illustrated in Fig 4.35. Figure 4.35 shows the filtered time series data superimposed upon the raw synthetic seismogram illustrated in Fig 4.34. In Fig 4.34 the initial 20 ms of the synthetic seismogram time series data shown in Fig. 4.34 has been ignored due to the fact that there is no source wavelet information present within this time window. Figure 4.35 also illustrates the initial phase estimate of 105° ($\pm 3^\circ$) of the AMS-E source wavelet and a t^* estimate of 7 ms.

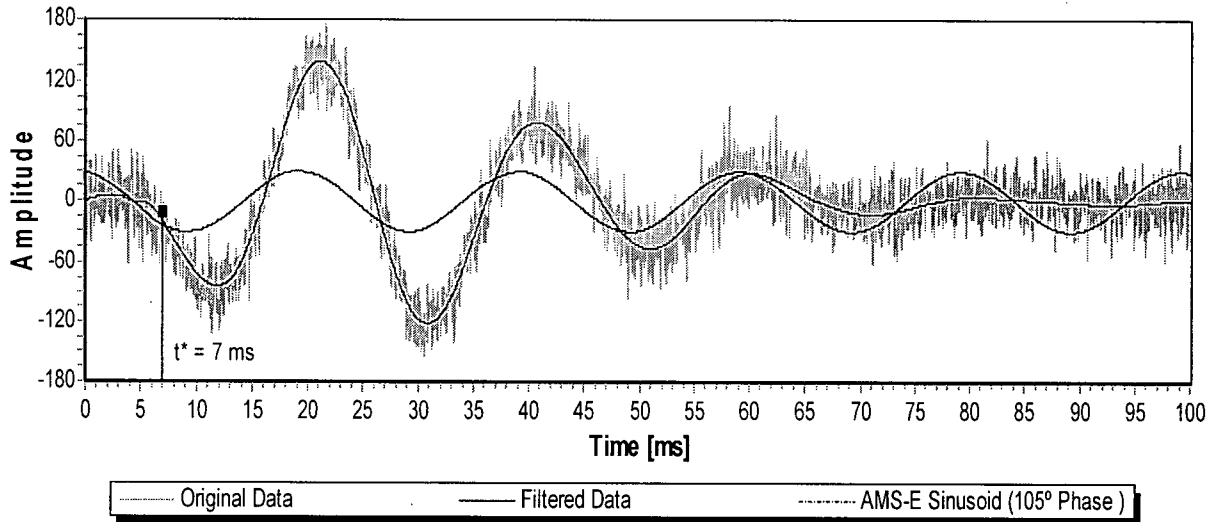


Figure 4.35. The output after applying a 100 Hz, eighth order, zero-phase shift, low-pass Butterworth frequency filter to the synthetic seismogram shown in Fig. 4.34.

The PPD-WE algorithm was then implemented on the synthetic seismogram illustrated in Fig. 4.34. The variance specified for states x_{2k} and x_{4k} was $90000 \text{ (units/s)}^2$. There were a total of $N_s = 500$ particles (Kalman filters) specified. The first pass of the PPD-WE algorithm implemented on the synthetic seismogram shown in Fig. 4.34 resulted in the initial f_{3k} phase estimates illustrated in Fig. 4.36. As is evident from Fig. 4.36, the phases 30° to 50° are dominant for f_{3k} ; therefore, the PPD-WE was re-executed with this phase restriction specified for f_{3k} .

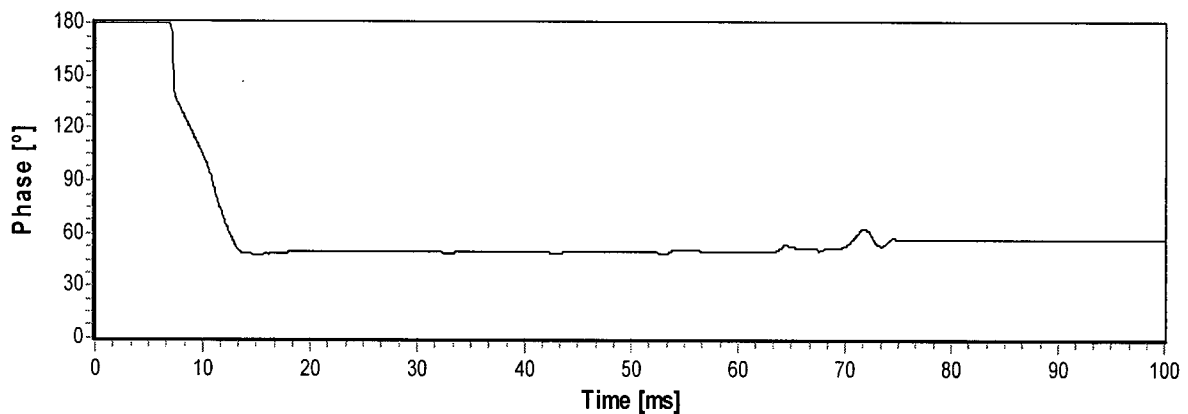


Figure 4.36. The initial HMM f_{3k} phase estimates for first pass of PPD-WE algorithm on data shown in Fig. 4.35.

The second pass of the PPD-WE algorithm provided for the AMS wavelet estimates illustrated in Figs. 4.37 and 4.38. Figure 4.37 shows the estimated and true Berlage source wavelets for the first reflection coefficient illustrated in Fig 4.16. Figure 4.38 shows the estimated and true Berlage source wavelets for the second reflection coefficient illustrated in Fig 4.16. As is evident from Figs. 4.37 and 4.38, there is very close agreement between the estimated and true mixed-phased Berlage source wavelets. Fig 4.39 illustrates the AMTs for the two estimated AMSs shown in Figs. 4.37 and 4.38. The AMTs in Fig. 4.39 have smoothed trajectories while at the same they allow for significant maneuverability of the corresponding AMSs. The PPD-WE algorithm obtained an optimal estimate time constant estimate of 0.96 ms (i.e., $a_1 = a_2 = 0.949$) for states x_{2k} and x_{4k} .

One can readily synthesize reflection coefficients from the PPD-WE estimated source wavelets. A simplistic approach consist of determining and averaging peak amplitude offsets and corresponding amplitude ratios from the estimated AMSs. If the source wavelet is stationary then the investigator can cross-correlate the estimated source wavelets and obtain relative arrival time estimates of the reflection coefficients. For example, Fig. 4.40 illustrates the normalized cross-correlation function for estimated source wavelets shown in Figs. 4.37 and 4.38. The peak value of the cross-correlation function in Fig. 4.40 occurs at 4.7 ms; therefore the second reflection coefficient is estimated to arrive 4.7 ms after the previous (sequentially) reflection coefficient. The corresponding amplitude of the reflection coefficient is estimated by averaging the dominant amplitude ratios of the two estimated AMSs. Fig 4.41 illustrates the estimated and true reflection coefficients for the synthetic seismogram illustrated in Fig. 4.34 and the PPD-WE output shown in Figs. 4.37 and 4.38.

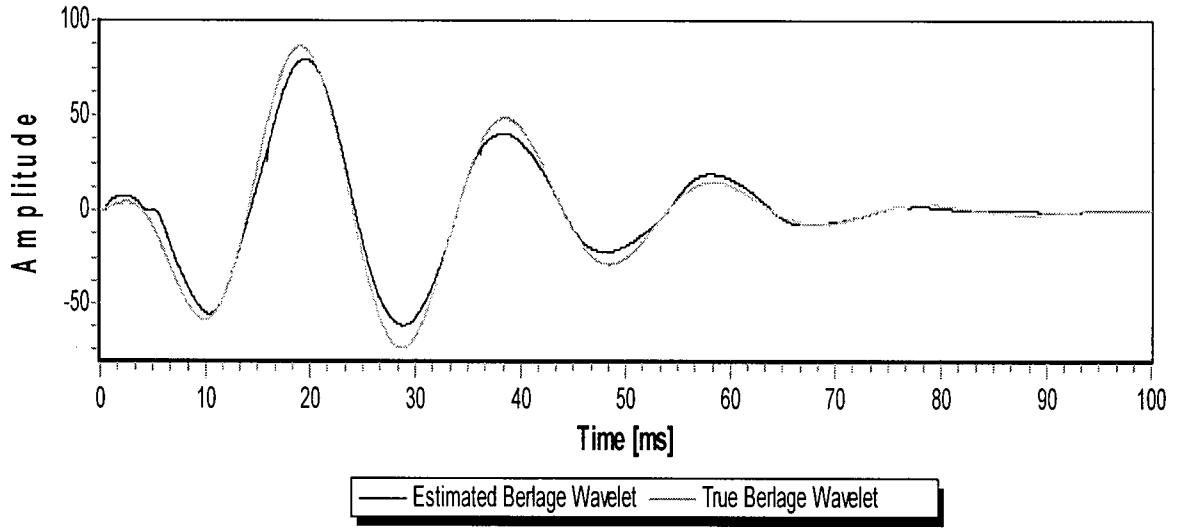


Figure 4.37. The estimated and true Berlage source wavelets for the first reflection coefficient illustrated in Fig 4.16.

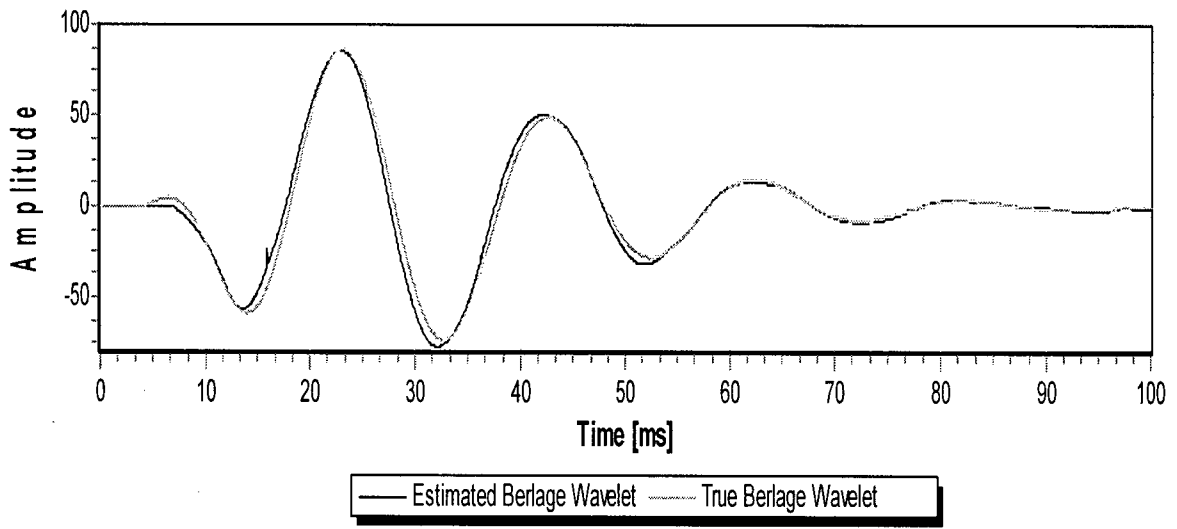


Figure 4.38. The estimated and true Berlage source wavelets for the second reflection coefficient illustrated in Fig 4.16.

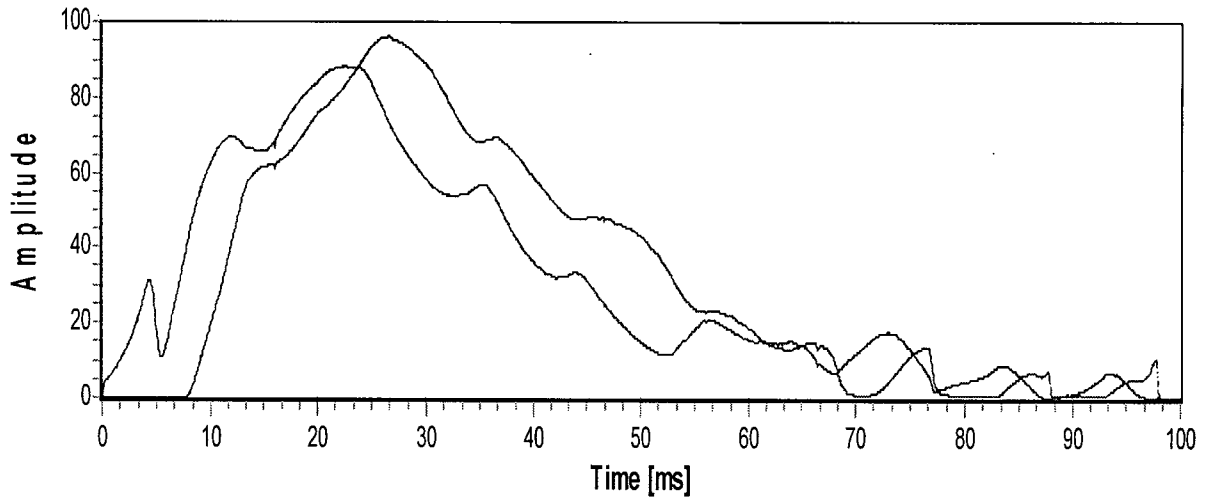


Figure 4.39. The AMTs for the two estimated AMSs shown in Figs. 4.37 and 4.38.

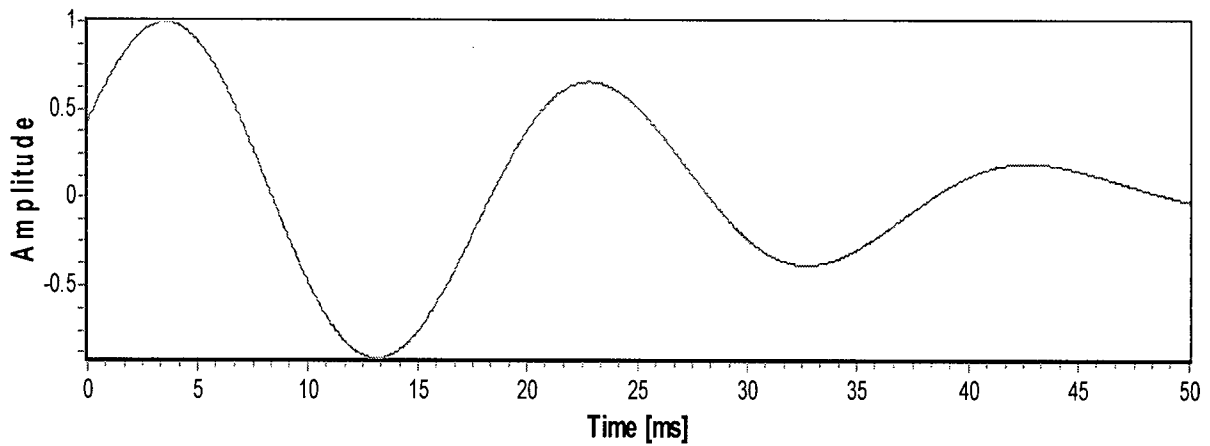


Figure 4.40. The normalized cross-correlation function for estimated source wavelets illustrated in Figs. 4.37 and 4.38. Peak value occurs at 4.7 ms.

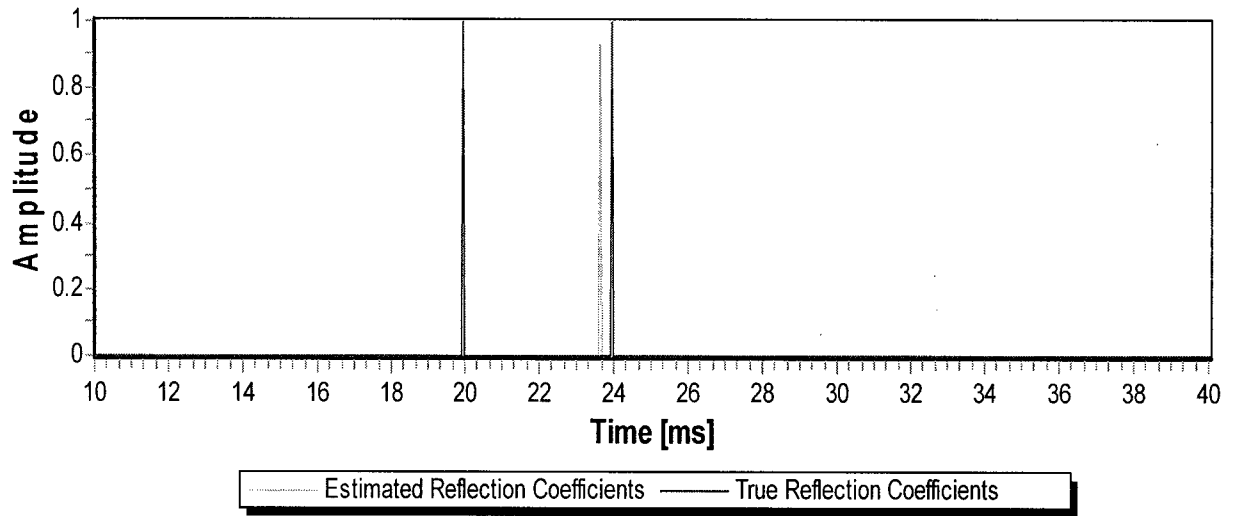


Figure 4.41. Estimated and true Reflection coefficients for synthetic seismogram illustrated in Fig. 4.34.

Fig. 4.42 shows a realization of the three state FSMCD for time $t = 40$ ms. FSMCD values of 0, 1 and 2 correspond to the cases $y_k^i = y_k^1$, $y_k^i = y_k^2$ and $y_k^i = y_k^3$, respectively, as outlined in Appendix G.

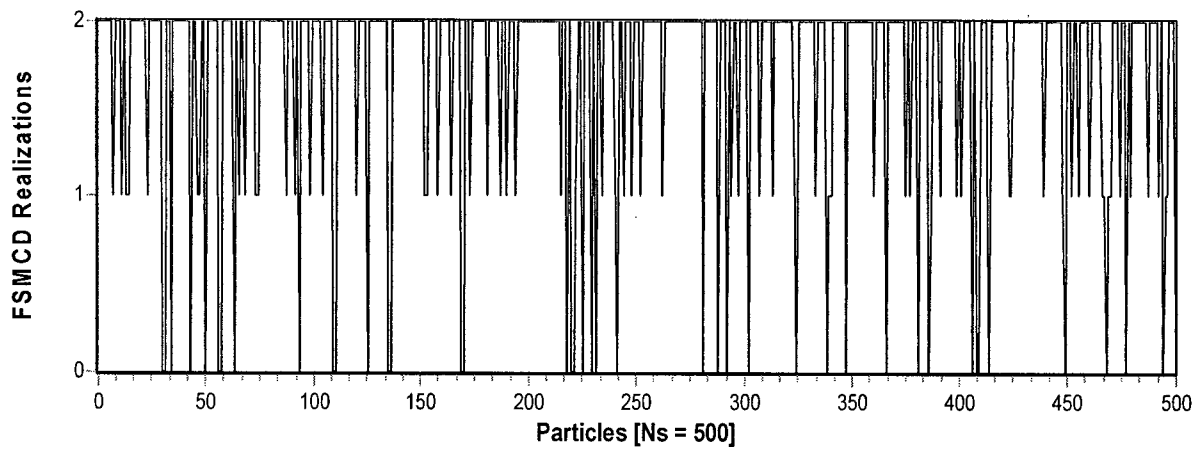


Figure 4.42. Three state FSMCD realization for time $t = 40$ ms.

In the second test bed analysis of the PPD-WE algorithm, the mixed phased Berlage wavelet illustrated in Fig. 4.15 is convolved with the reflection coefficients outlined in Fig 4.43 to give the output illustrated in Fig. 4.44. The synthetic seismogram shown in Fig. 4.44 has additive Gauss-Markov noise with a variance of 400 units^2 and a time constant of 0.01 ms .

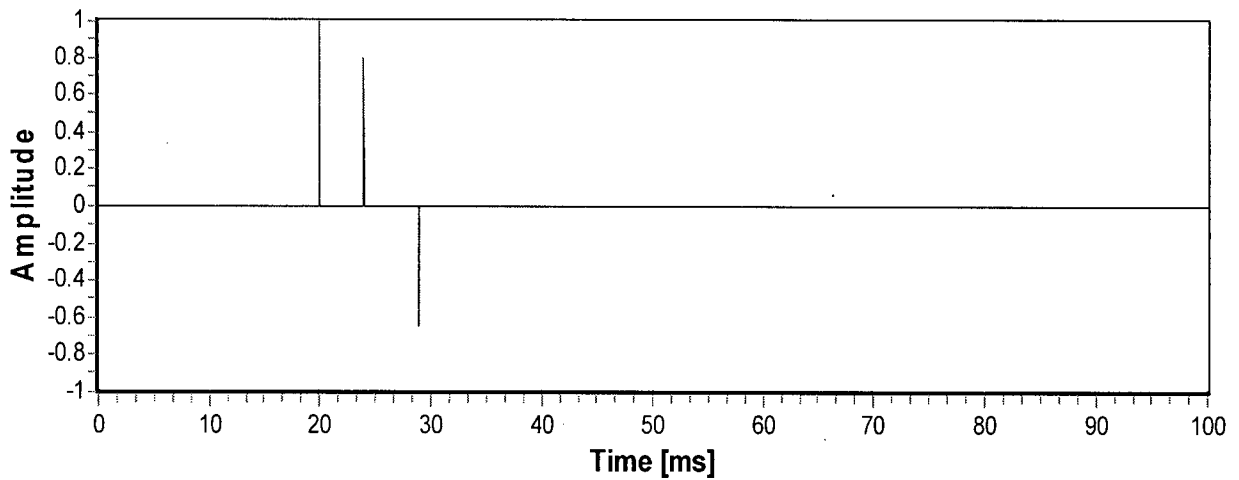


Figure 4.43 Reflection coefficients convolved with Berlage wavelet shown in Fig. 4.15.

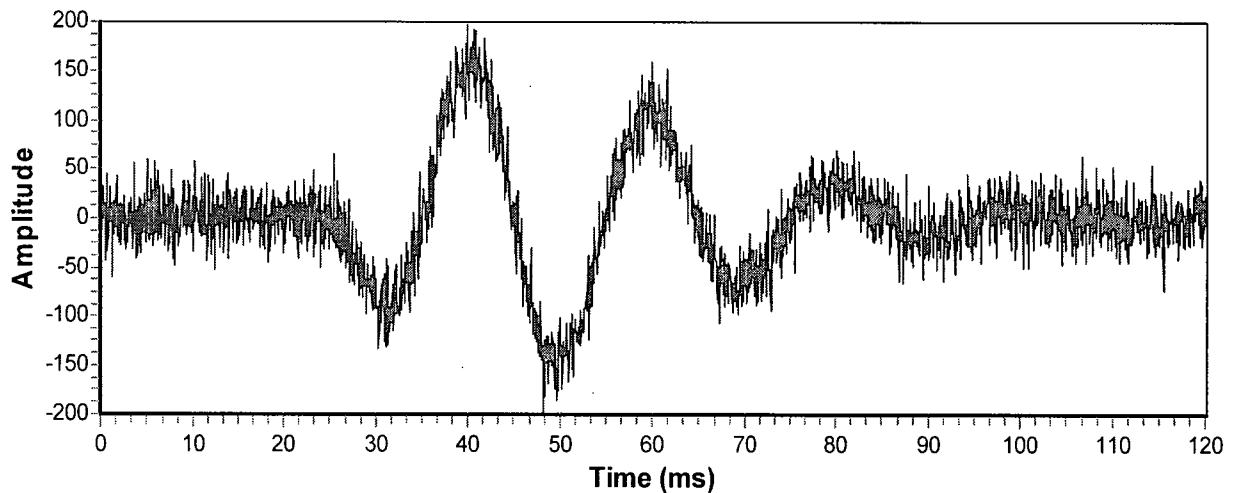


Figure 4.44. The output after convolving Berlage wavelet of Fig 4.15 with reflection coefficients illustrated in Fig. 4.43 and adding Gauss-Markov measurement noise with a variance of 400 units^2 and a time constant of 0.01 ms .

A 100 Hz, eighth order, zero-phase shift, low-pass Butterworth frequency filter is then applied to the synthetic seismogram shown in Fig 4.44 to give the output illustrated in Fig 4.45. Figure 4.45 shows the filtered time series data superimposed upon the raw synthetic seismogram illustrated in Fig 4.44. In Fig 4.45 the initial 20 ms of the synthetic seismogram time series data shown in Fig. 4.44 has again been ignored due to the fact that there is no source wavelet information present within this time window. Figure 4.44 also illustrates the initial phase estimate of $105^\circ (\pm 3^\circ)$ of the sinusoid of the source wavelet to be extracted. Time index t^* was again set to 7 ms.

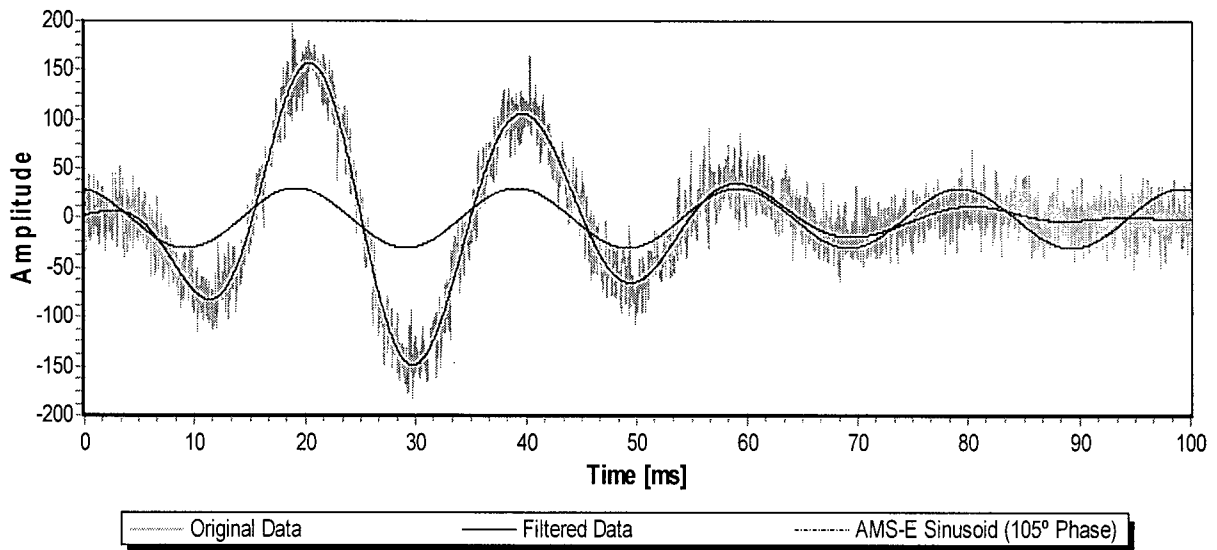


Figure 4.45. The output after applying a 100 Hz, eighth order, zero-phase shift, low-pass Butterworth frequency filter to the synthetic seismogram shown in Fig. 4.44.

The PPD-WE algorithm was then implemented on the synthetic seismogram illustrated in Fig. 4.44. There were a total of $N_s = 600$ particles (Kalman filters) specified. The first pass of the PPD-WE algorithm implemented on the synthetic seismogram shown in Fig. 4.44 resulted in the initial $f 3_k$ phase estimates illustrated in Fig. 4.46. As is evident from Fig. 4.46, the phases 50° to 80° are dominant for $f 3_k$; therefore, the PPD-WE was re-executed with this phase resolution specified for $f 3_k$.

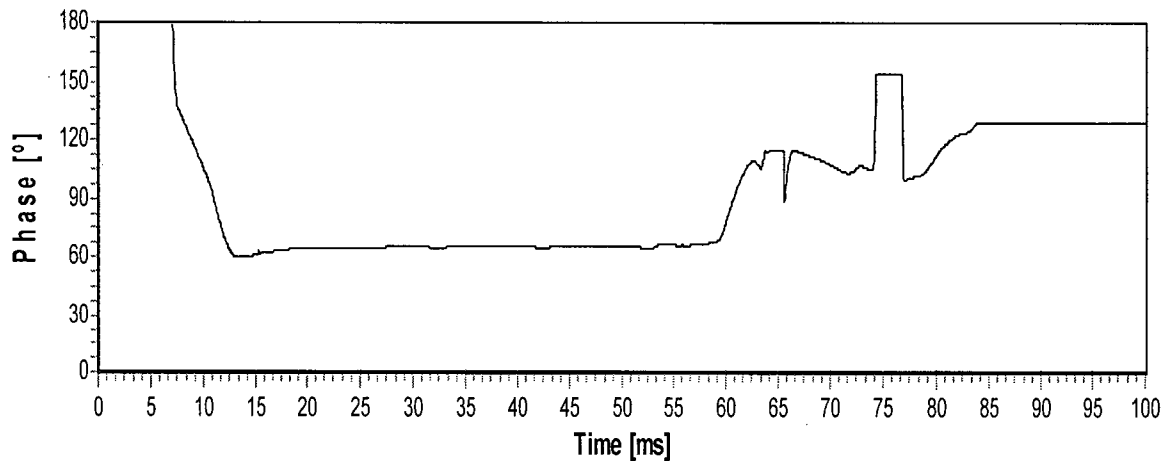


Figure 4.46. The initial HMM f_{3k} phase estimates for first pass of PPD-WE algorithm on data shown in Fig. 4.44.

The second pass of the PPD-WE algorithm provided for the AMS wavelet estimates illustrated in Figs. 4.47 and 4.48. Figure 4.47 shows the estimated and true Berlage source wavelets for the first reflection coefficient illustrated in Fig 4.43 Figure 4.48 shows the estimated residual wavelet and the actual residual wavelet generate by convolving the Berlage wavelet illustrated in Fig. 4.15 with the last two reflection coefficients illustrated in Fig 4.44. As is evident from Figs. 4.47 and 4.48, there is very close agreement between the estimated and true time series responses for time interval 0 ms to 27 ms. After time 27 ms the estimated wavelets start to slightly diverge from the true wavelets. Fig 4.49 illustrates the AMTs for the two estimated AMSs shown in Figs. 4.47 and 4.48. The PPD-WE algorithm obtained an optimal estimate time constant estimate of 1.14 ms (i.e., $a_1 = a_2 = 0.957$) for states x_{2k} and x_{4k} .

Subsequent to the extraction of the first arriving Berlage source wavelet illustrated in Fig. 4.47, the PPD-WE algorithm is then applied to the estimated residual wavelet shown in Fig. 4.48. Figure 4.50 illustrate the estimated residual wavelet shown in Fig. 4.48 with an initial phase estimate of $44^\circ (\pm 3^\circ)$ for the sinusoid of the source wavelet to be extracted and a time index t^* of 9 ms. The first pass of the PPD-WE algorithm implemented on the estimated residual wavelet shown in Fig. 4.50 resulted in the initial f_{3k} phase estimates illustrated in Fig. 4.51. As is evident from Fig. 4.51, the phases 110° to 140° are dominant for f_{3k} ; therefore, the PPD-WE was re-executed with this phase resolution specified for f_{3k} .

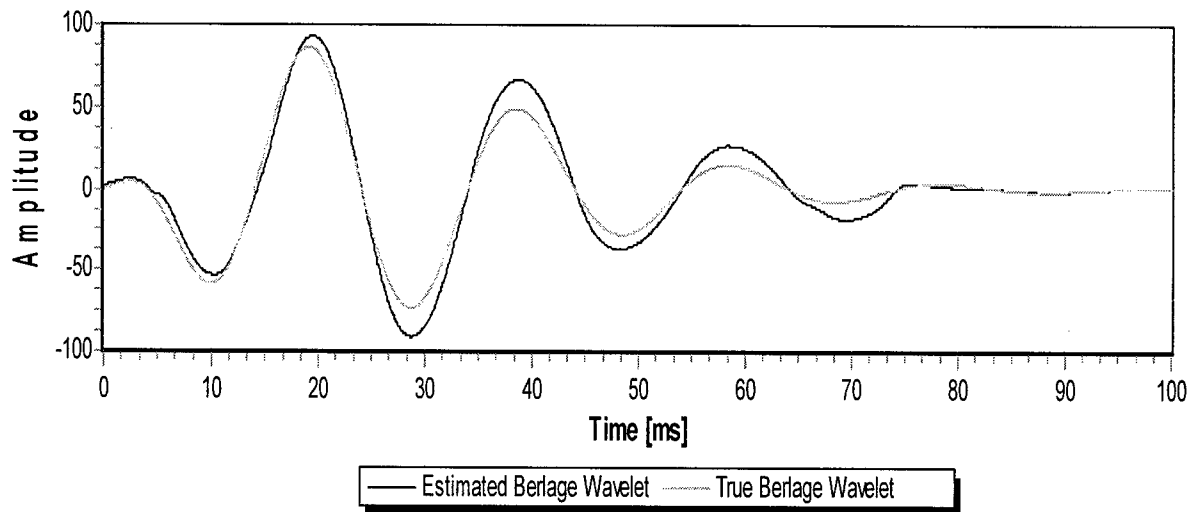


Figure 4.47. The estimated and true Berlage source wavelets for the first reflection coefficient illustrated in Fig 4.43

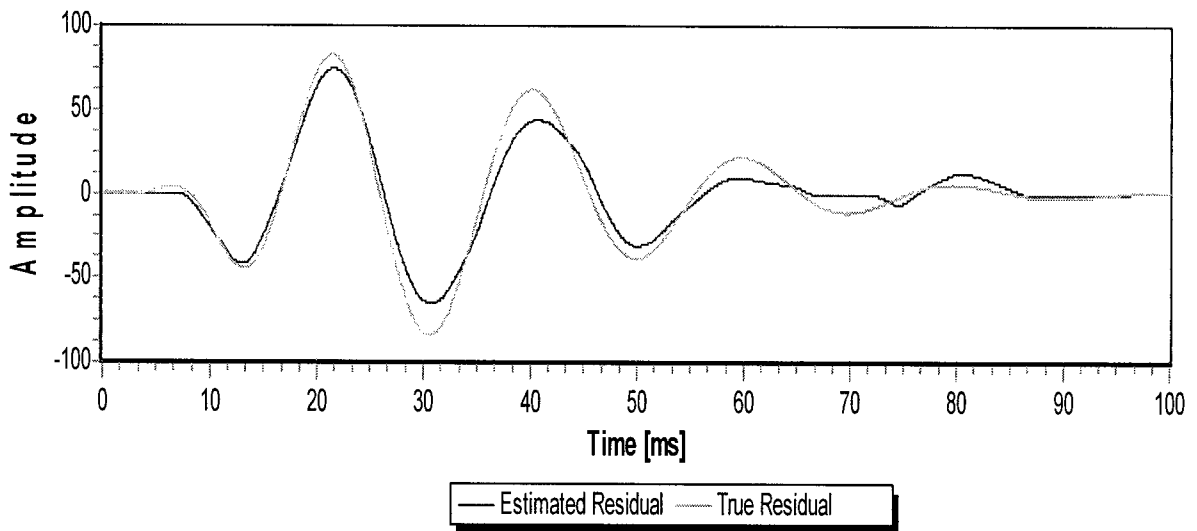


Figure 4.48. The estimated and true time series residual for the last two reflection coefficients illustrated in Fig 4.43 convolved with the Berlage source wavelet of Fig. 4.15.

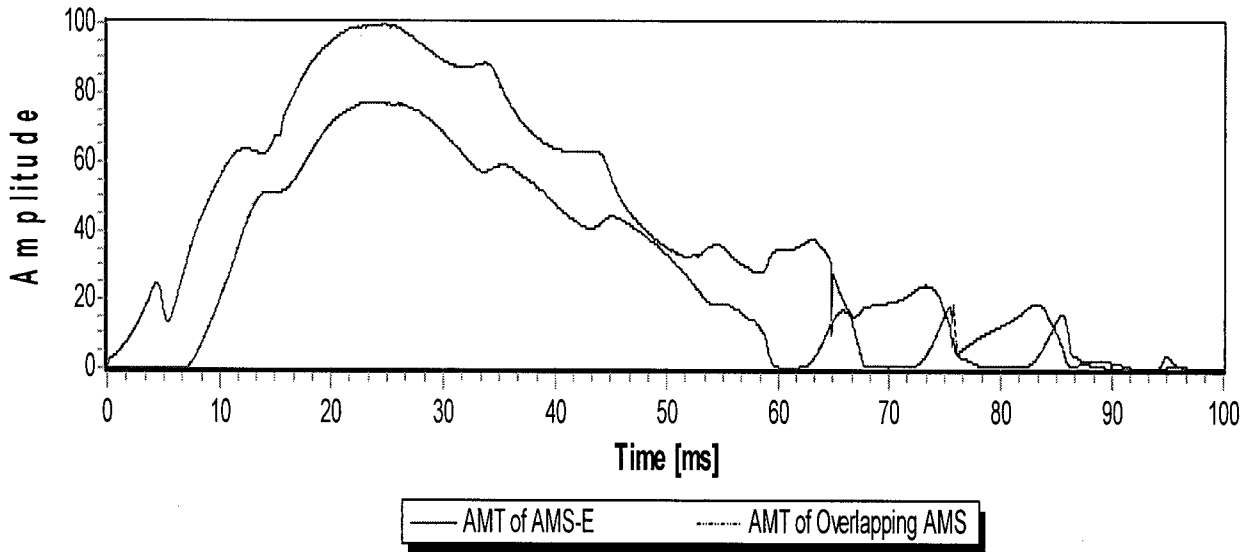


Figure 4.49. The AMTs for the two estimated AMSs shown in Figs. 4.47 and 4.48.

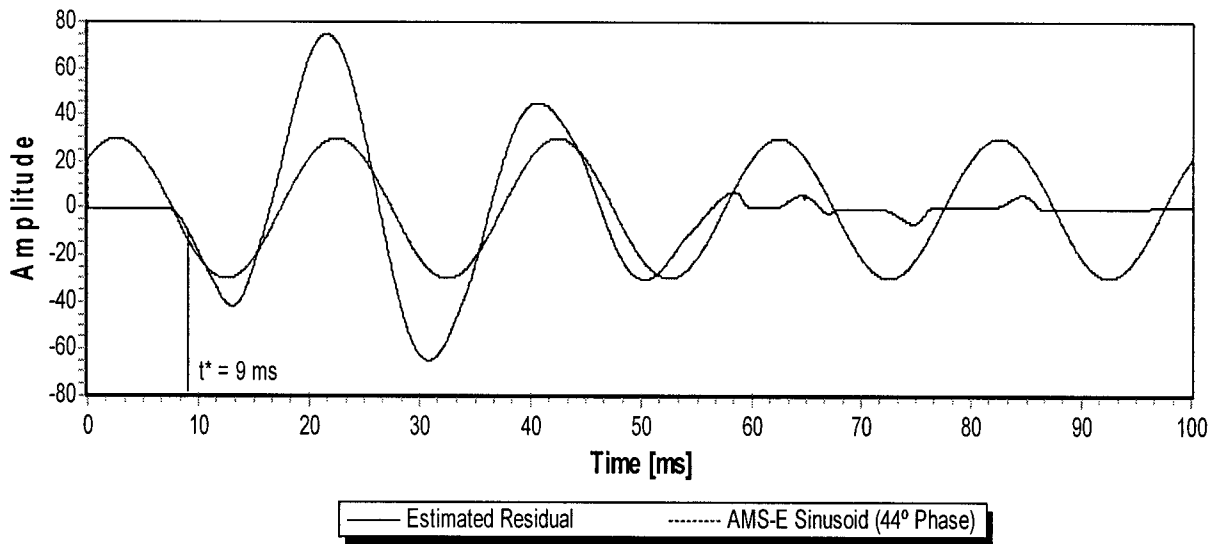


Figure 4.50. The estimated time series residual of Fig. 4.48 with AMS-E sinusoid with phase of 44° superimposed.

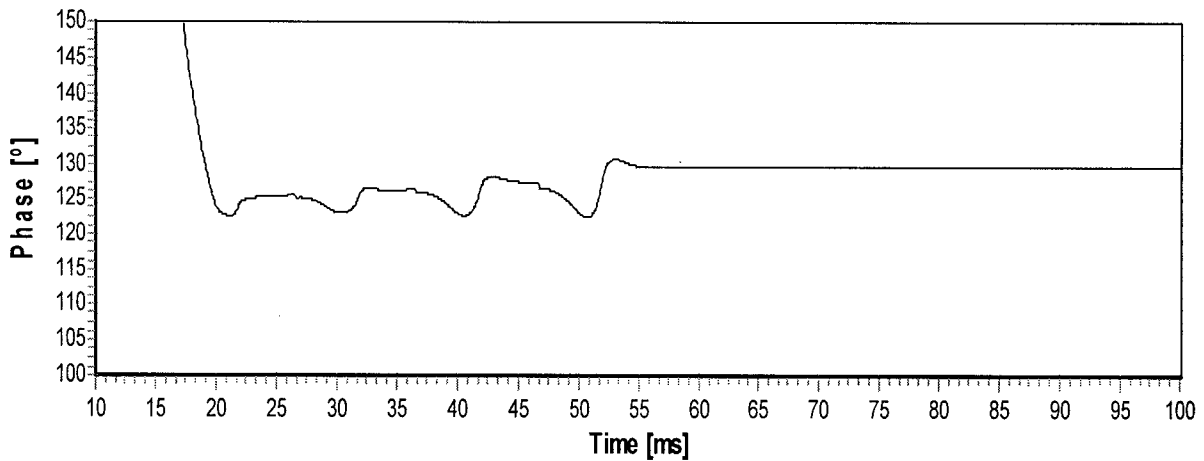


Figure 4.51. The initial HMM f_{3k} phase estimates for first pass of PPD-WE algorithm on data shown in Fig. 4.50.

The second pass of the PPD-WE algorithm provided for the AMS wavelet estimates illustrated in Figs. 4.52 and 4.54. Figure 4.52 shows the estimated and true Berlage source wavelets for the second reflection coefficient illustrated in Fig 4.43 As is evident from Fig. 4.52, there is very close agreement between the estimated and true Berlage source wavelets. Figure 4.53 shows the estimated (with 100 Hz low-pass filter applied) and true Berlage source wavelets for the third reflection coefficient illustrated in Fig 4.43 The PPD-WE algorithm did a good job in obtaining accurate amplitude oscillations but it had difficulty in obtaining the correct amplitude scaling.

This test bed outlines the current limitation of the PPD-WE algorithm in that any errors generate during the wavelet extraction process will propagate as the seismogram is sequentially and chronologically processed. Figure 4.54 illustrates the AMTs for the two estimated AMSs shown in Figs. 4.52 and 4.54. The PPD-WE algorithm obtained an optimal estimate time constant estimate of 1.14 ms (i.e., $a_1 = a_2 = 0.957$) for states x_{2k} and x_{4k} .

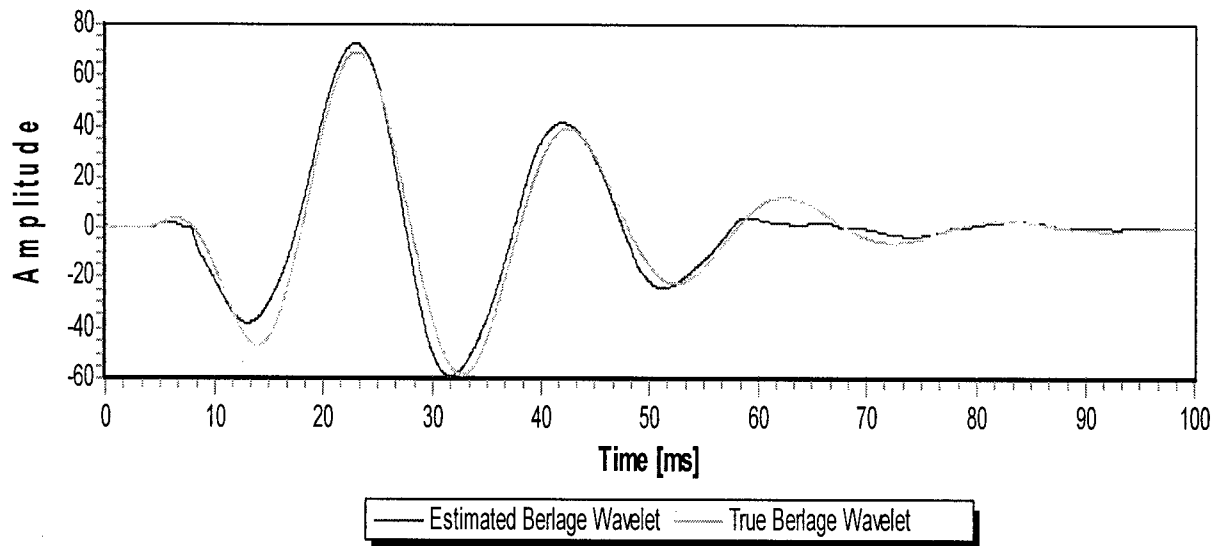


Figure 4.52. The estimated and true Berlage source wavelets for the first second coefficient illustrated in Fig 4.43

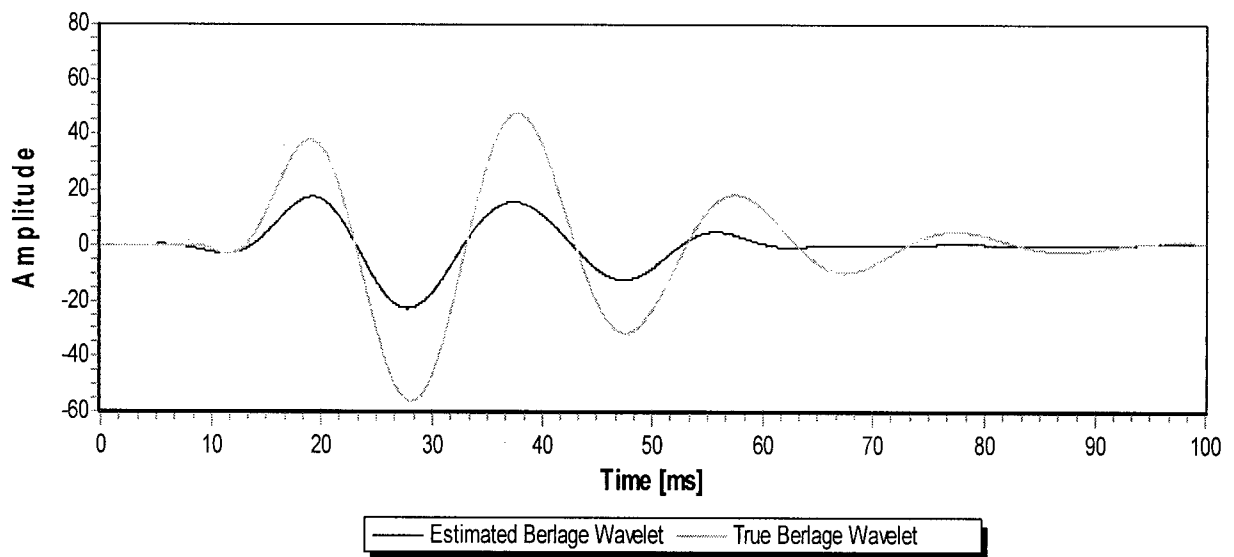


Figure 4.53. The estimated and true Berlage source wavelets for the third reflection coefficient illustrated in Fig 4.43.

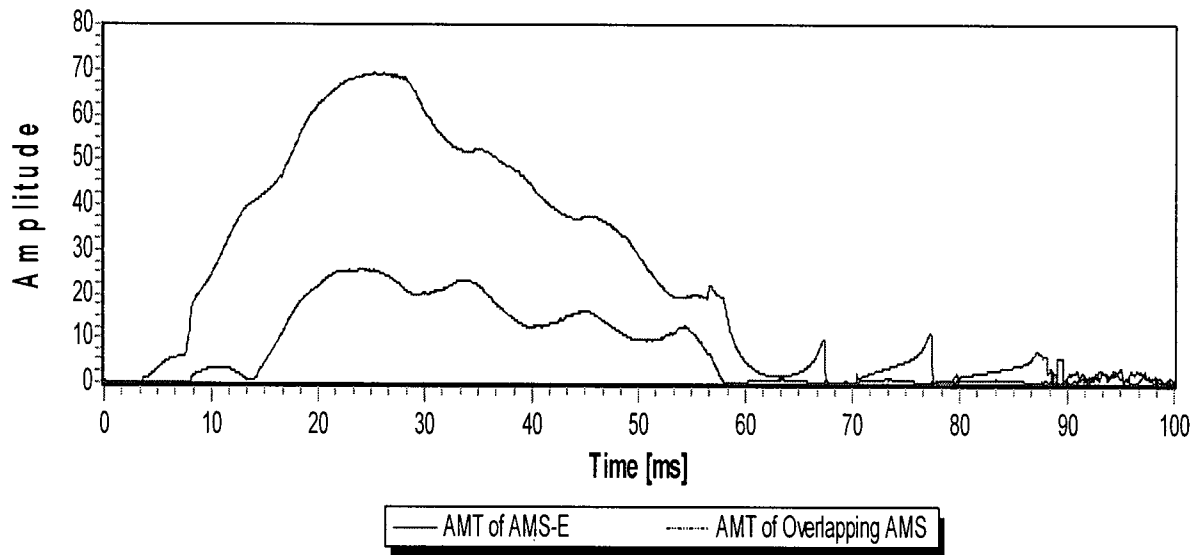


Figure 4.54. The AMTs for the two estimated AMSs shown in Figs. 4.52 and 4.53.

Figure 4.55 illustrates the normalized cross-correlation function for the first and estimated second arriving Berlage source wavelets shown in Fig. 4.52. The peak value of the cross-correlation function in Fig. 4.55 occurs at 4.5 ms; therefore the second reflection coefficient is estimated to arrive 4.5 ms after the previous (sequentially) reflection coefficient. Figure 4.56 illustrates the normalized cross-correlation function for the first and estimated third arriving Berlage source wavelets shown in Fig. 4.53. The peak value of the cross-correlation function in Fig. 4.56 occurs at 8.9 ms; therefore the third reflection coefficient is estimated to arrive 8.9 ms after the first reflection coefficient.

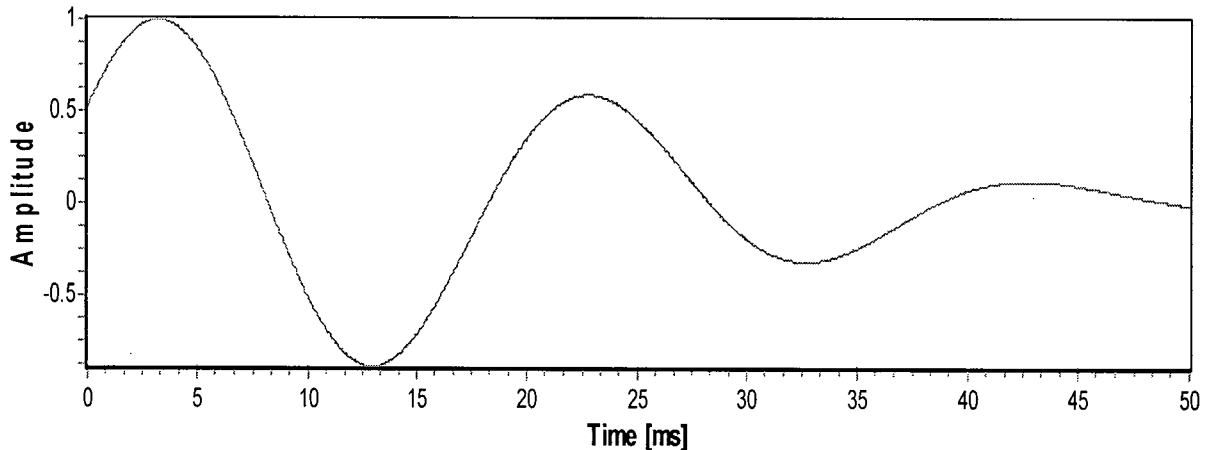


Figure 4.55. The normalized cross-correlation function for the first and estimated second arriving Berlage source wavelet shown in Fig. 4.52. Peak value occurs at 4.5 ms.

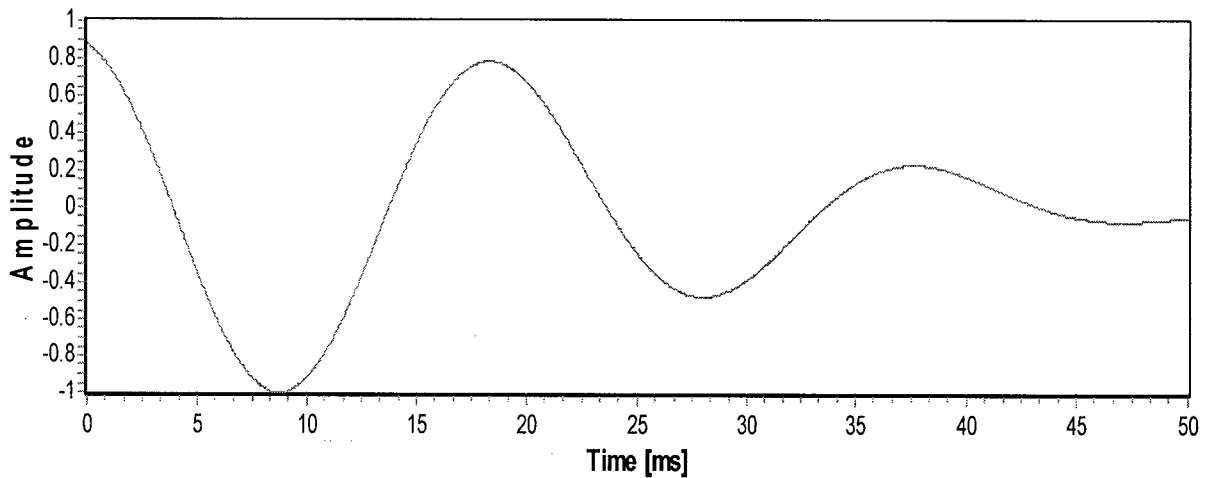


Figure 4.56. The normalized cross-correlation function for the first and estimated third arriving Berlage source wavelet shown in Fig. 4.53. Peak value occurs at 8.9 ms.

The corresponding amplitudes of the reflection coefficients are estimated by averaging the four dominant amplitude ratios of the first arriving Berlage source wavelet and the estimated overlapping source wavelets arriving at 24 ms and 25 ms, respectively. Fig 4.57 illustrates the estimated and true reflection coefficients for the synthetic seismogram illustrated in Fig. 4.44 and the PPD-WE output shown in Figs. 4.47, 4.52 and 4.53.

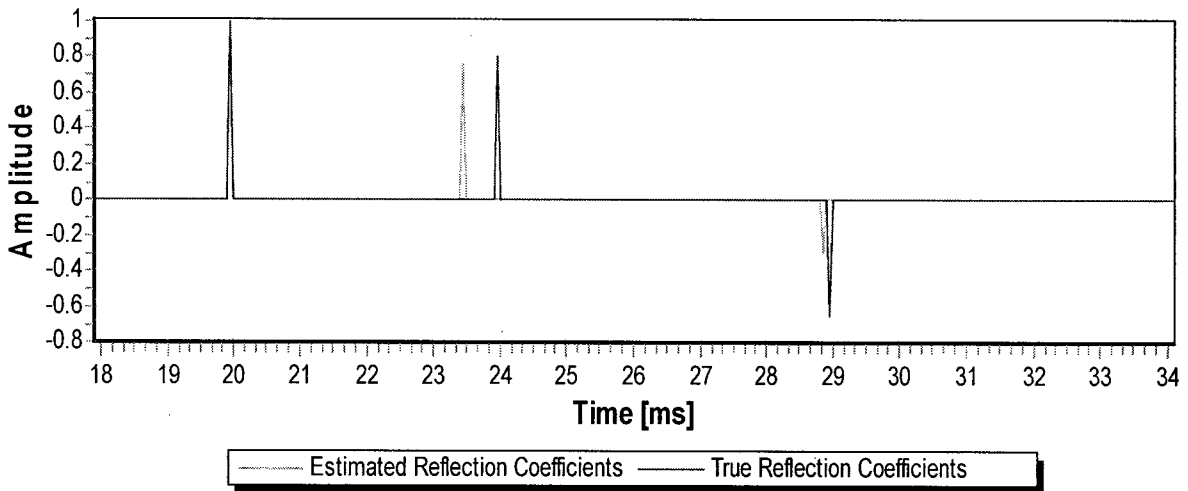


Figure 4.57. The estimated and true reflection coefficients for synthetic seismogram illustrated in Fig. 4.44.

g) Estimation of the Dominant Frequency of the Wavelet to be extracted within the PPD-WE Algorithm

In the previously outlined PPD-WE algorithm the dominant frequency (DF) of the source wavelet to be extracted (SWE) was assumed known. In order to make the PPD-WE truly blind, it is necessary to estimate the SWE's DF. The approach taken is to implement a HMM filter similar to the HMM filters utilized to estimate the AMS phases. In this PPD-WE filter formulation, a range of possible DFs (e.g., 30 Hz to 70 Hz in 1 Hz increments) and corresponding phases are pre-specified within a HMM filter formulation. As the data is processed, the HMM frequency estimation (HMM-FE) filter obtains an optimal estimate of the dominant frequency. The PPD-WE filter is re-executed with the estimate of the HMM-FE DF specified.

The PPD-WE measurement equation for the case when there is only the SWE present is given as

$$z_k = x1_k \sin(\omega t + \phi1_k), \quad \text{where } t = k\Delta \quad (69)$$

In (69), ω represents the DF of the SWE and $f1_k$ is the corresponding HMM-FE DF estimate at time index k . As previously outlined, knowing the DF one can easily obtain an initial estimate for the AMS-E sinusoid. For example, in Fig 4.35 the DF of the AMS-E sinusoid was known (i.e., 50 Hz) and the initial phase was estimated to be 105° with a corresponding initial sinusoidal zero crossing of $t' = 4.2$ ms as illustrated in Fig. 4.58.

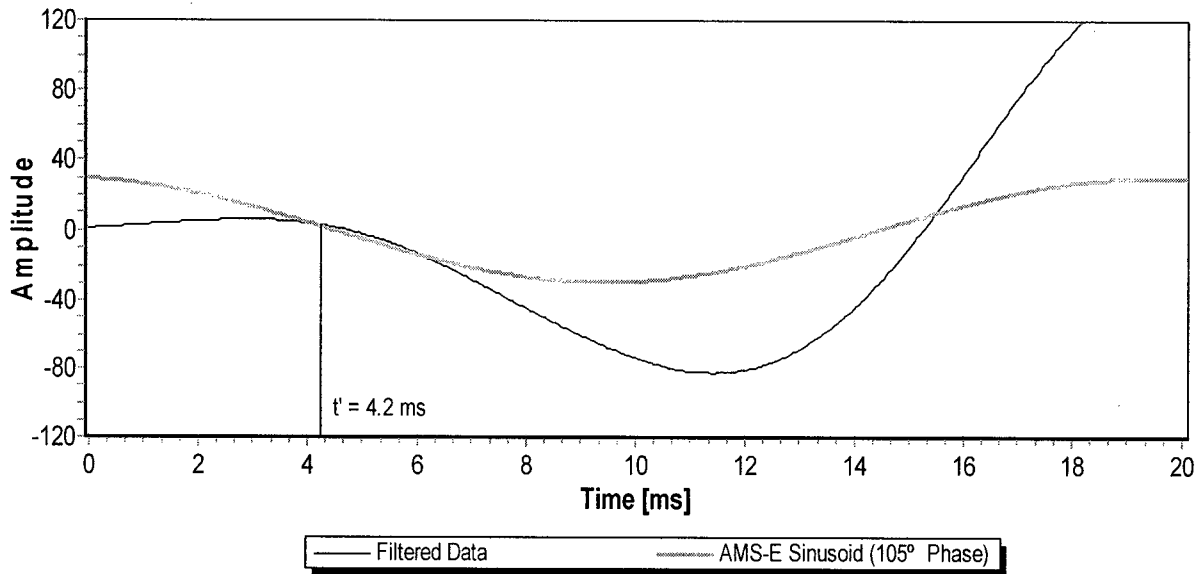


Figure 4.58. Illustration of the filtered synthetic seismogram of Fig. 4.34 with the AMS-E sinusoid and corresponding initial zero crossing of 4.2 ms shown.

At the first zero crossing of the AMS-E sinusoid, we have the following relationship (for negative amplitude first break):

$$\omega t' + \phi_1' = 180^\circ \quad (70)$$

From (70), it is clear that there is a linear relationship between the DF and the corresponding phase at the first zero crossing denoted by t' which is given as

$$\phi_1' = 180^\circ - \omega t' \quad (71)$$

By utilizing (71) one can easily calculate a corresponding phase for any DF specified. For example, in the case outlined in Fig. 4.58 a DF of 40 Hz would result in a corresponding phase of 119.5° and a DF of 70 Hz result in a corresponding phase of 74.2° .

The implementation of the HMM-FE filter within the PPD-WE is outlined by considering the synthetic seismogram illustrated in Fig. 4.34. In this case, the DF is assumed unknown and an initial frequency range of 30 Hz to 70 Hz is specified with a increment resolution of 1 Hz and (71) is utilized to calculate the corresponding phases. Figure 4.39 shows the output of the HMM-FE filter after the first pass of the HMM-FE filter and an initial value of $\omega = 35 \text{ Hz}$ is specified.

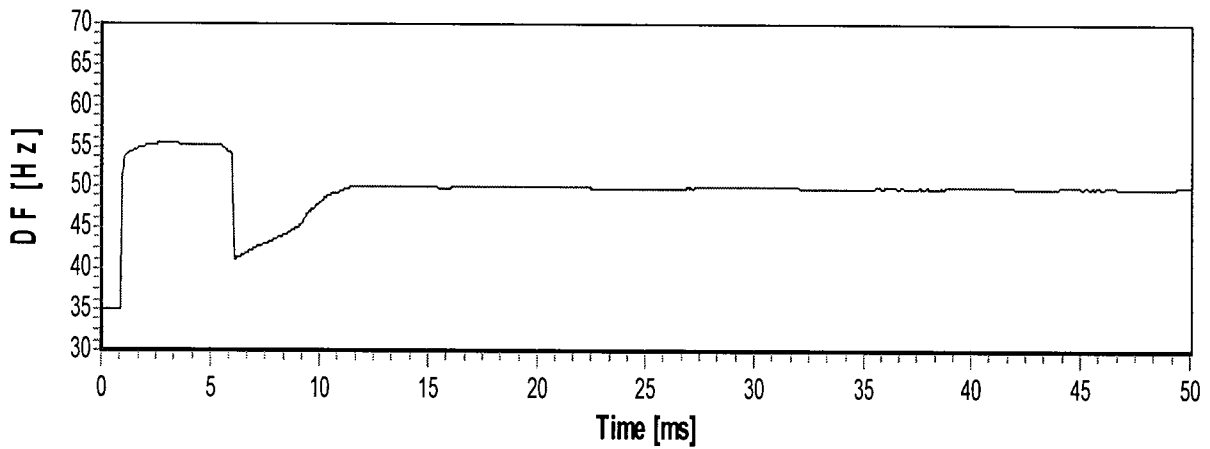


Figure 4.59. Illustration of the output of the HMM-FE filter after processing the synthetic seismogram shown in Fig. 4.44.

As is evident from Fig 4.59, the HMM-FE filter did an impressive job on locking onto the correct DF value of 50 Hz within a relatively short time frame. The DF value of 50 Hz is then specified within the PPD-WE algorithm and the synthetic seismogram illustrated in Fig. 4.34 is then reprocessed to give the output shown in Figs. 4.37 and 4.38.

In the next test bed analysis a synthetic seismogram is generated were there is time variance of the AMTs and dominant frequency components of the source wavelet. In this analysis there are four overlapping source wavelets. The four overlapping source wavelets BSW1, BSW2, BSW3, and BSW4 are Berlage wavelets with dominant frequencies of $f = 55 \text{ Hz}$, $f = 50 \text{ Hz}$, $f = 45 \text{ Hz}$ and $f = 40 \text{ Hz}$, respectively, and parameters $n = 2$, $a = 170$, $\phi = 60^\circ$ specified. Figures 4.60, 4.61, 4.62, and 4.63 illustrate Berlage source wavelets BSW1, BSW2, BSW3, and BSW4, respectively.

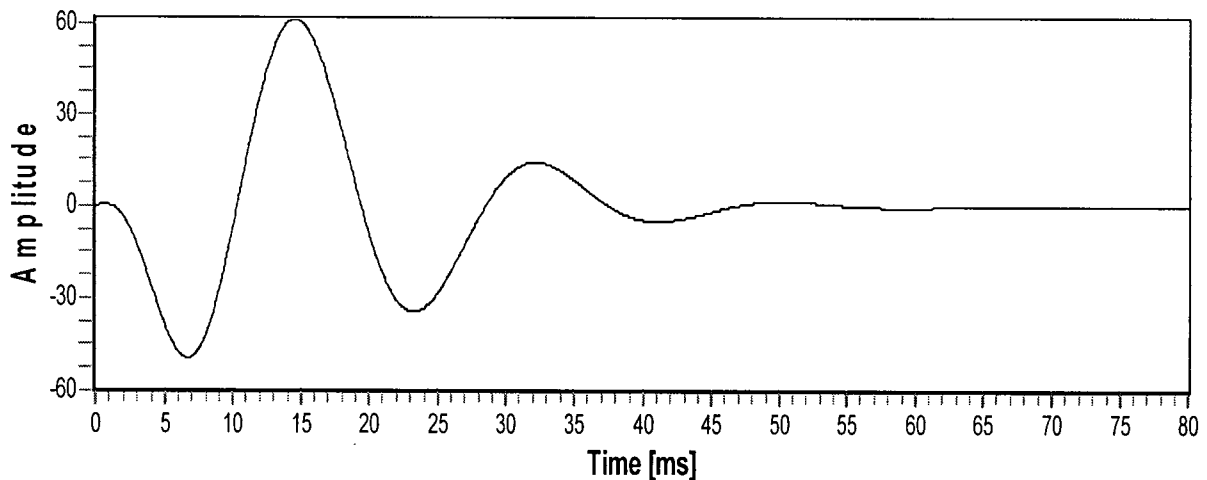


Figure 4.60. Illustration of BSW1 with parameters $f = 55 \text{ Hz}$, $n = 2$, $a = 170$ and $\phi = 60^\circ$ specified.

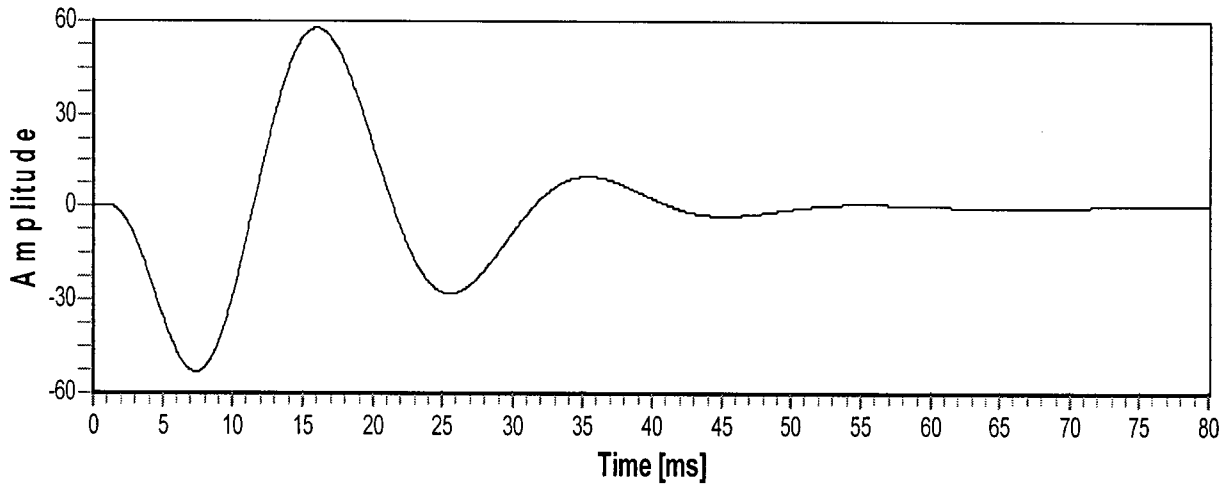


Figure 4.61. Illustration of BSW2 with parameters $f = 50 \text{ Hz}$, $n = 2$, $a = 170$ and $\phi = 60^\circ$ specified.

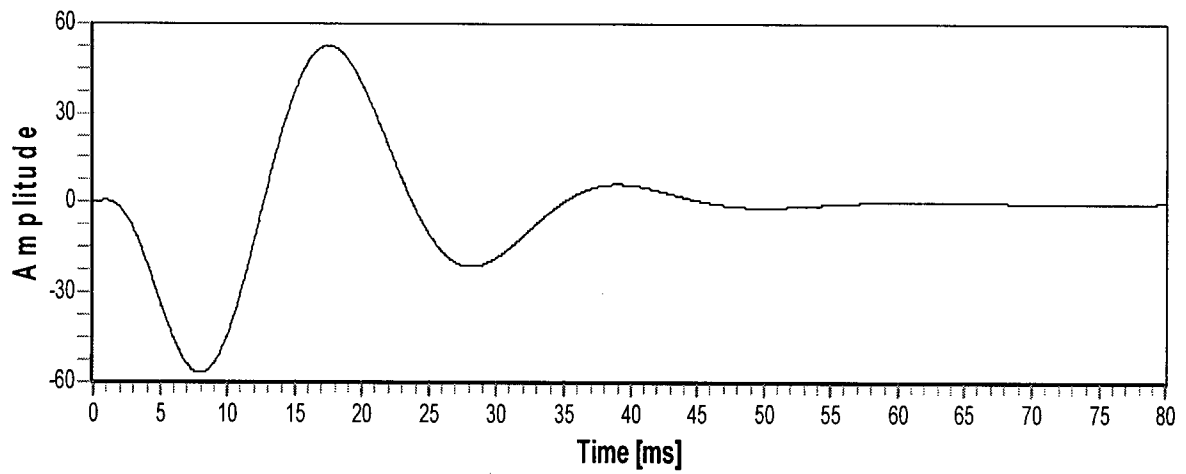


Figure 4.62. Illustration of BSW3 with parameters $f = 45 \text{ Hz}$, $n = 2$, $a = 170$ and $\phi = 60^\circ$ specified.

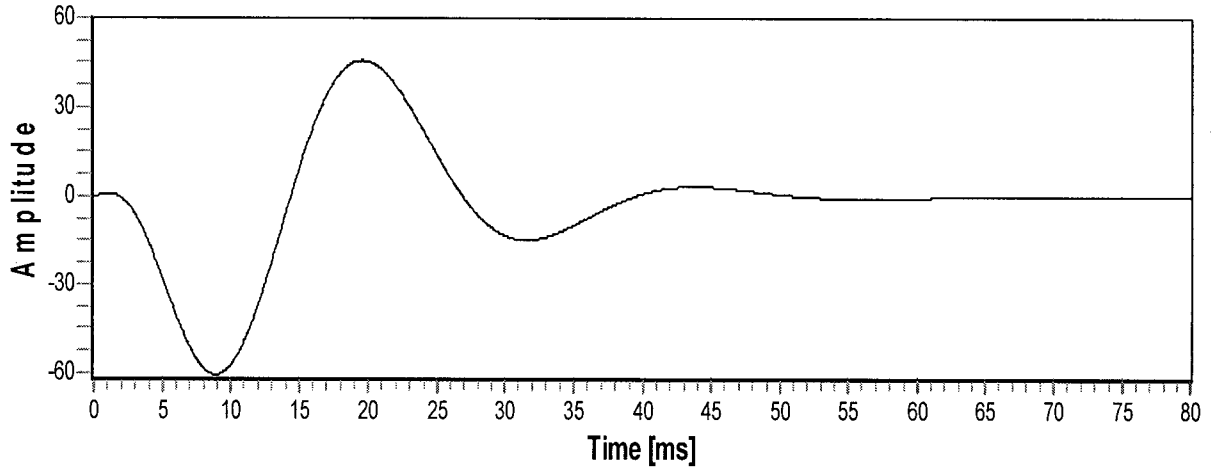


Figure 4.63. Illustration of BSW4 with parameters $f = 40$ Hz, $n = 2$, $a = 170$ and $\phi = 60^\circ$ specified.

The synthetic seismogram illustrated in Fig 4.64 was generated by convolving BSW1, BSW2, BSW3, and BSW4 with the first, second, third, and fourth reflection coefficients, respectively, shown in Fig. 4.65 and summing the results. The time series data illustrated in Fig. 4.64 has additive Gauss-Markov measurement noise with variance of 100 units² and a time constant of 0.01 ms. Figure 4.66 illustrates BSW1, BSW2, BSW3, and BSW4 after implementing the previously described convolution process.

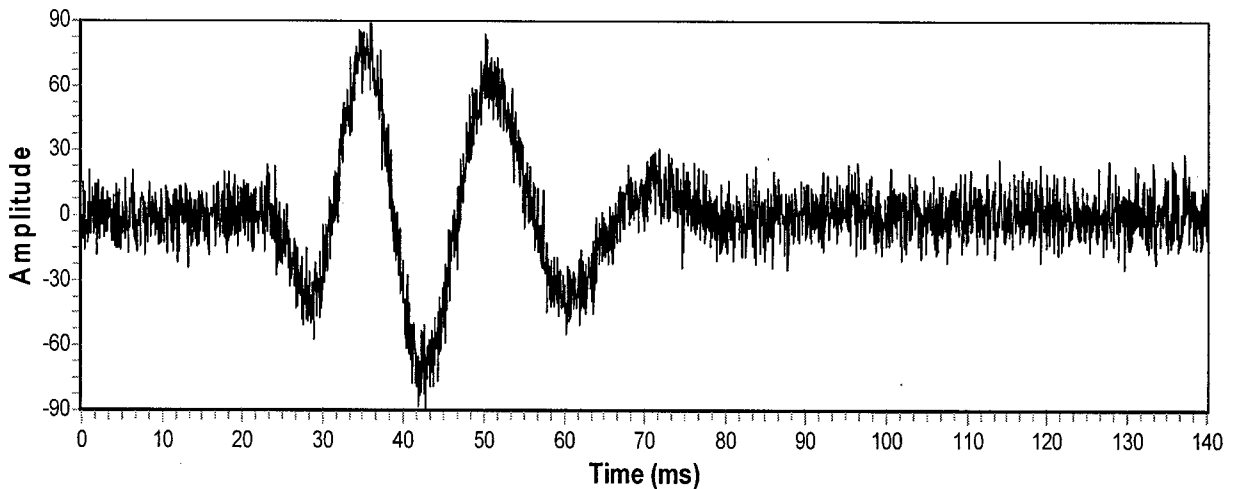


Figure 4.64. Synthetic seismogram generated by summing time variant source wavelets BSW1, BSW2, BSW3, and BSW4.

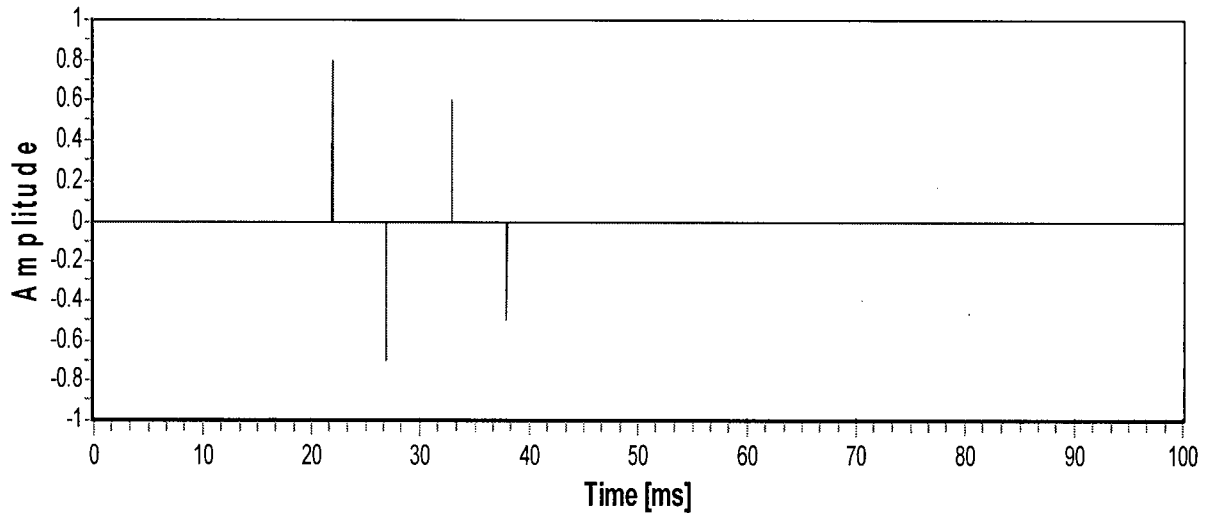


Figure 4.65. The reflection coefficients utilized to generated synthetic seismogram illustrated in Fig. 4.64.

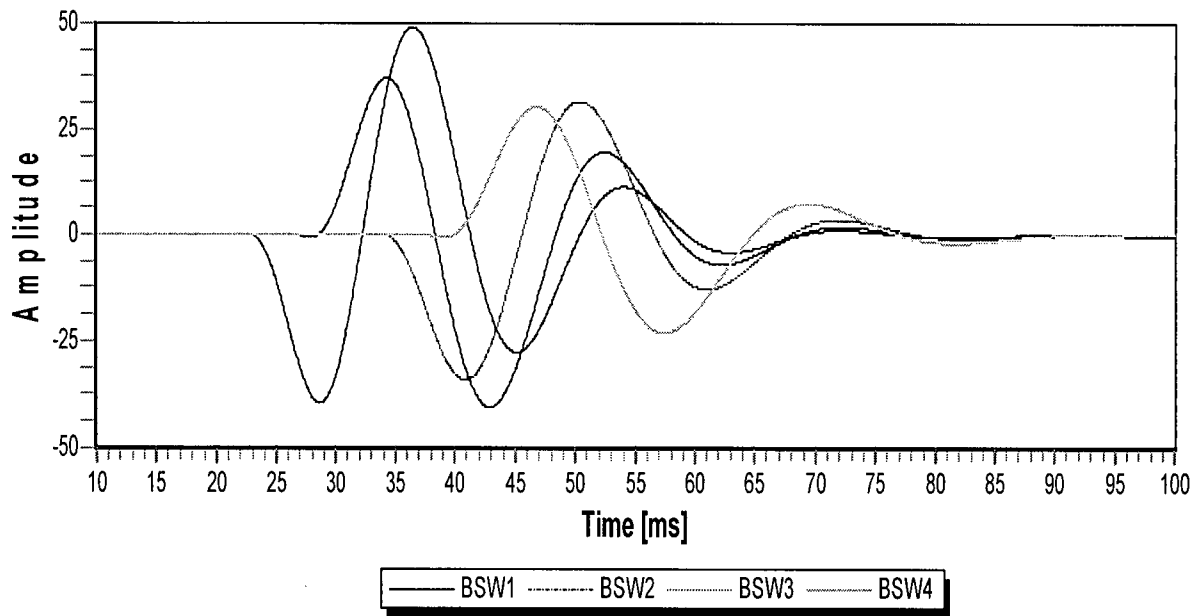


Figure 4.66. The output after convolving BSW1, BSW2, BSW3, and BSW4 with the first, second, third, and fourth reflection coefficients, respectively, shown in Fig. 4.65.

A 100 Hz, eighth order, zero-phase shift, low-pass Butterworth frequency filter is then applied to the synthetic seismogram shown in Fig 4.64 to give the output illustrated in Fig 4.67. Figure 4.67 shows the filtered time series data superimposed upon the raw synthetic seismogram illustrated in Fig 4.64 (with the initial 20 ms of the synthetic seismogram time series data being ignored). The time parameters t^* and t' were estimated to be 6 ms and 4.6 ms, respectively.

In the implementation of the HMM-FE an initial frequency range of 30 Hz to 58 Hz was specified with a increment resolution of 0.1 Hz. In the specification of the HMM-FE frequency range it is mandatory that the investigator does not specify frequency values which incorporate the seismogram's overall frequency components. For example, the synthetic seismogram in Fig. 4.67 has overall frequency components ranging from 60 Hz (e.g., peak 1 to peak 3 and peak 2 to peak 4) to 70 Hz (e.g., peak 1 to peak 2). If these frequencies are incorporated into the HMM-FE, then the PPD-WE will just track the seismogram response and not the principle phase components which comprise the seismogram.

Figure 4.68 shows the output of the HMM-FE filter after the first pass of the HMM-FE filter and an initial value of $\omega = 35 \text{ Hz}$ is specified. As is evident from Fig 4.68, the HMM-FE filter did an impressive job on locking onto the correct DF value of 55 Hz within a relatively short time frame.

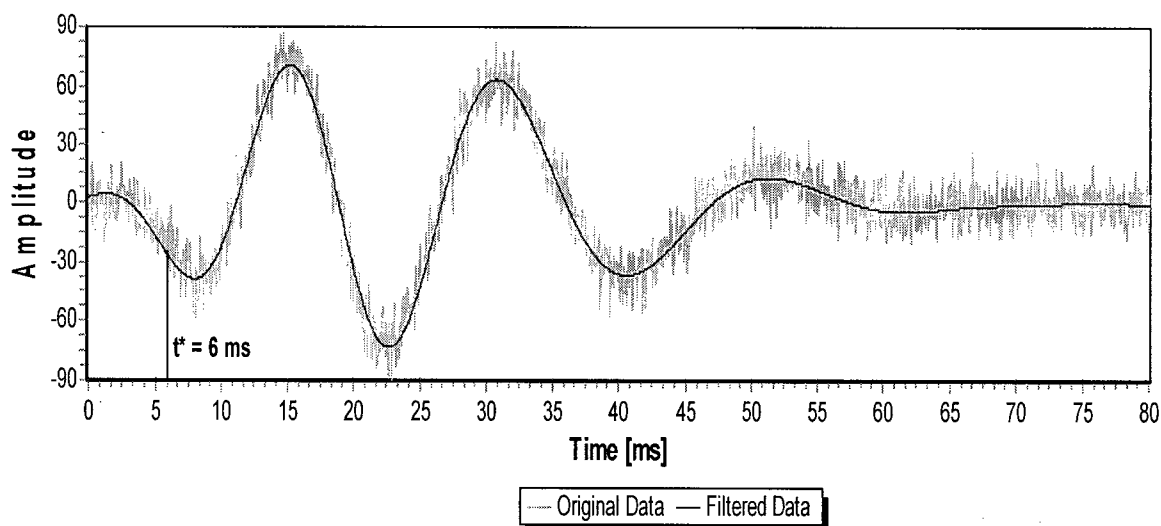


Figure 4.67. The output after applying a 100 Hz, eighth order, zero-phase shift, low-pass Butterworth frequency filter to the synthetic seismogram shown in Fig. 4.64.

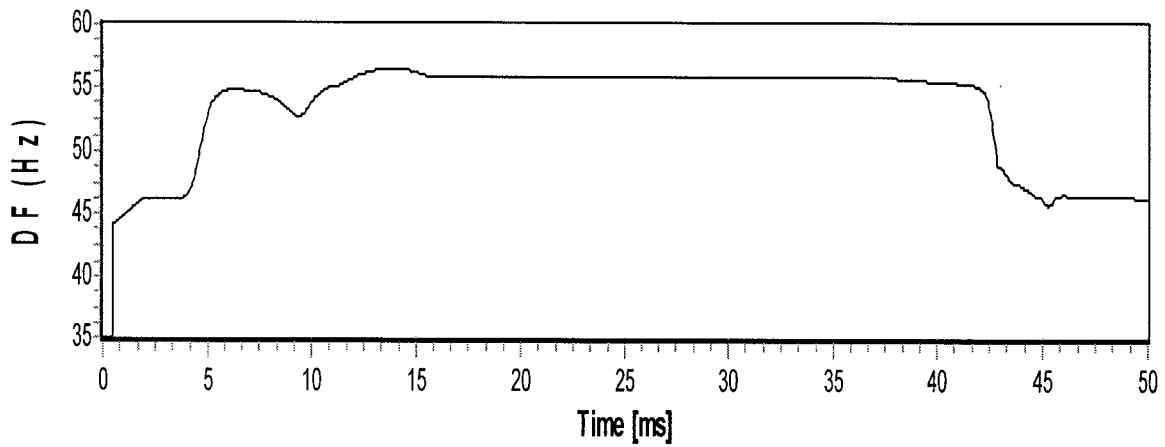


Figure 4.68. Illustration of the output of the HMM-FE filter after processing the synthetic seismogram shown in Fig. 4.64.

The PPD-WE algorithm provided for the AMS wavelet estimates illustrated in Figs. 4.69 and 4.71⁷. Figure 4.69 shows the estimated and true BSW1 source wavelet. Figure 4.70 illustrates the estimated residual wavelet and the actual residual wavelet (i.e., BSW1+BSW3+BSW4). As is evident from Figs. 4.69 and 4.70, there is very close agreement between the estimated and true time series responses.

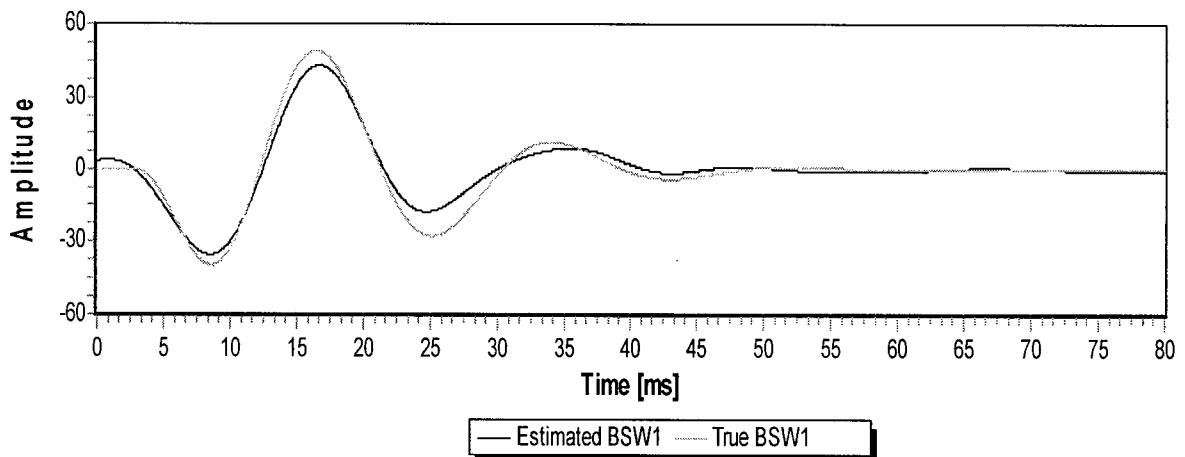


Figure 4.69. The estimated and true BSW1 source wavelets.

⁷ Please note that the PPD-WE output has a 100 Hz, eighth order, zero-phase shift, low-pass Butterworth frequency filter applied.

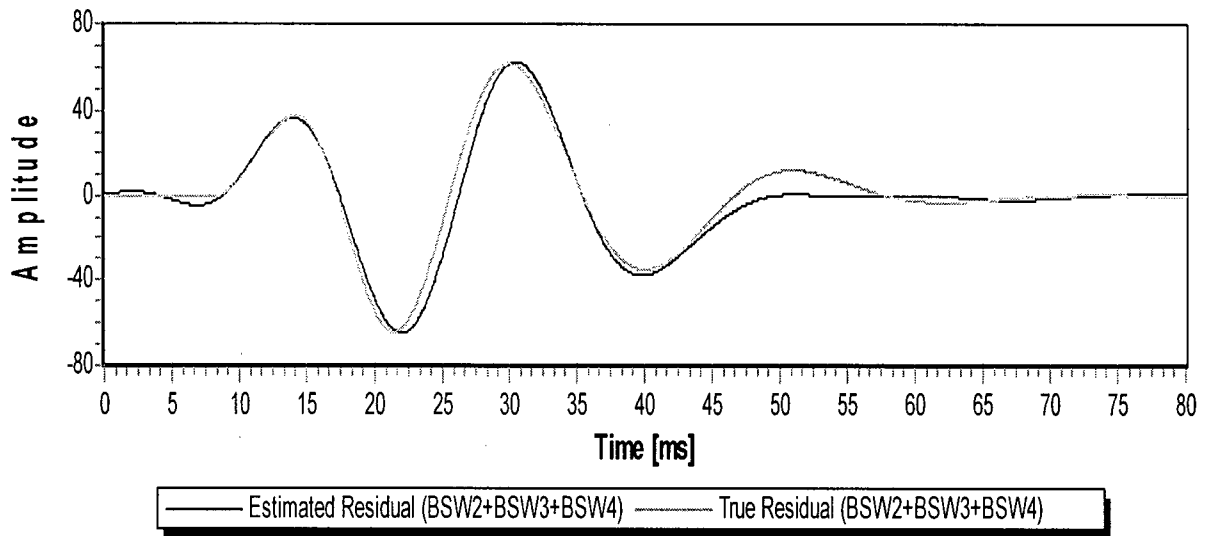


Figure 4.70. The estimated residual wavelet and the actual residual wavelet (i.e., BSW1 + BSW3 + BSW4).

Subsequent to the extraction of the first arriving Berlage source wavelet illustrated in Fig. 4.64, the PPD-WE algorithm is then applied to the estimated residual wavelet shown in Fig. 4.70. Figure 4.71 illustrates the estimated residual wavelet shown in Fig. 4.70 with the time parameters t^* and t' set to 11 ms and 8.96 ms, respectively.

In the implementation of the HMM-FE an initial frequency range of 30 Hz to 55 Hz (we know that the DF cannot be greater than the previous DF of 55 Hz) was specified with an increment resolution of 0.1 Hz. Figure 4.72 shows the output of the HMM-FE filter after the first pass of the HMM-FE filter and an initial value of $\omega = 40$ Hz specified. As is evident from Fig 4.72, the HMM-FE filter locked onto the correct DF value of 50 Hz within 23 ms.

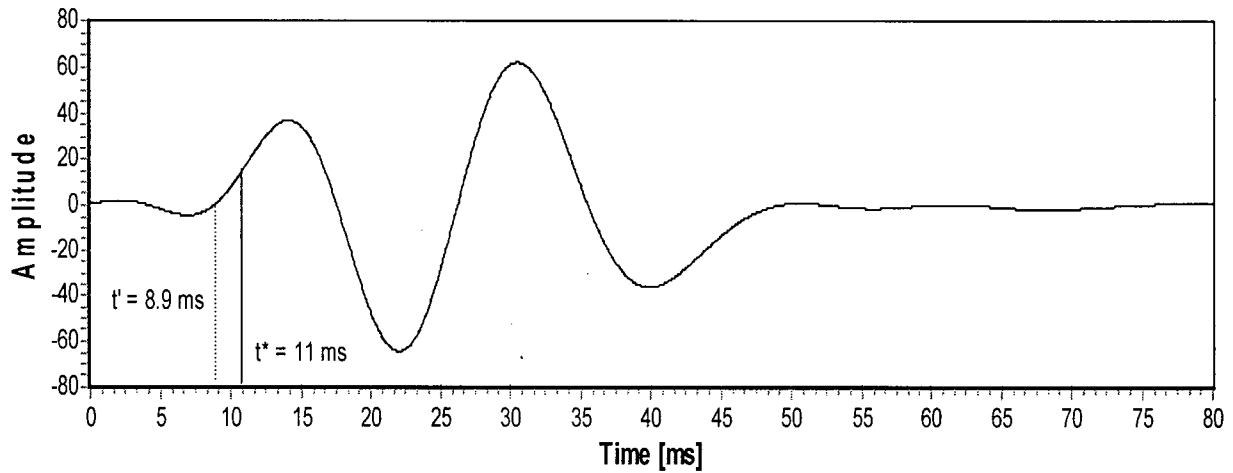


Figure 4.71. The estimated time series residual of Fig. 4.70 with the time parameters t^* and t' set to 11 ms and 8.96 ms, respectively.

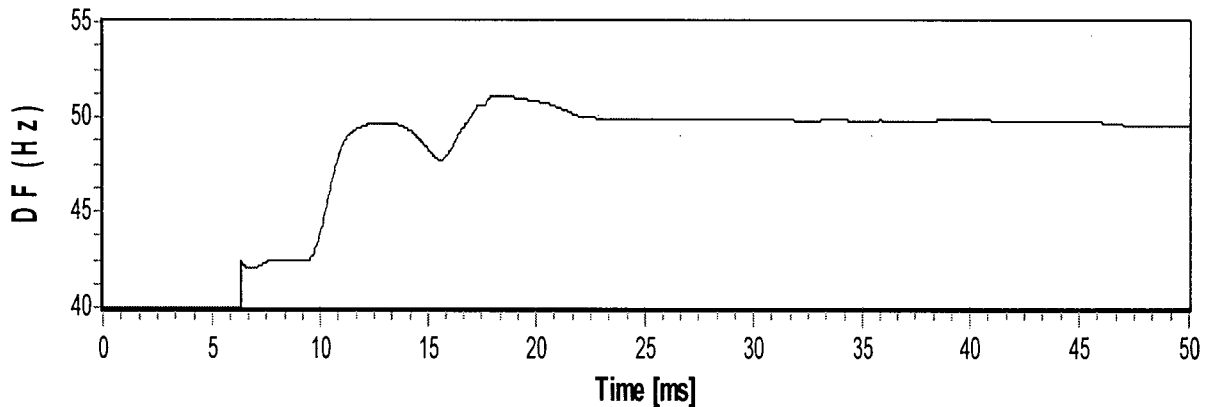


Figure 4.72. Illustration of the output of the HMM-FE filter after processing the synthetic seismogram shown in Fig. 4.71.

Implementation of the PPD-WE algorithm on the data shown in Fig. 4.71 resulted in the AMS wavelet estimates illustrated in Figs. 4.73 and 4.74. Figure 4.73 shows the estimated and true BSW2 source wavelets. Figure 4.74 illustrates the estimated residual wavelet and the actual residual wavelet (i.e., BSW3+BSW4). As is evident from Figs. 4.73 and 4.74, the estimated responses deviate from the true responses between approximately 17 ms to 27 ms.

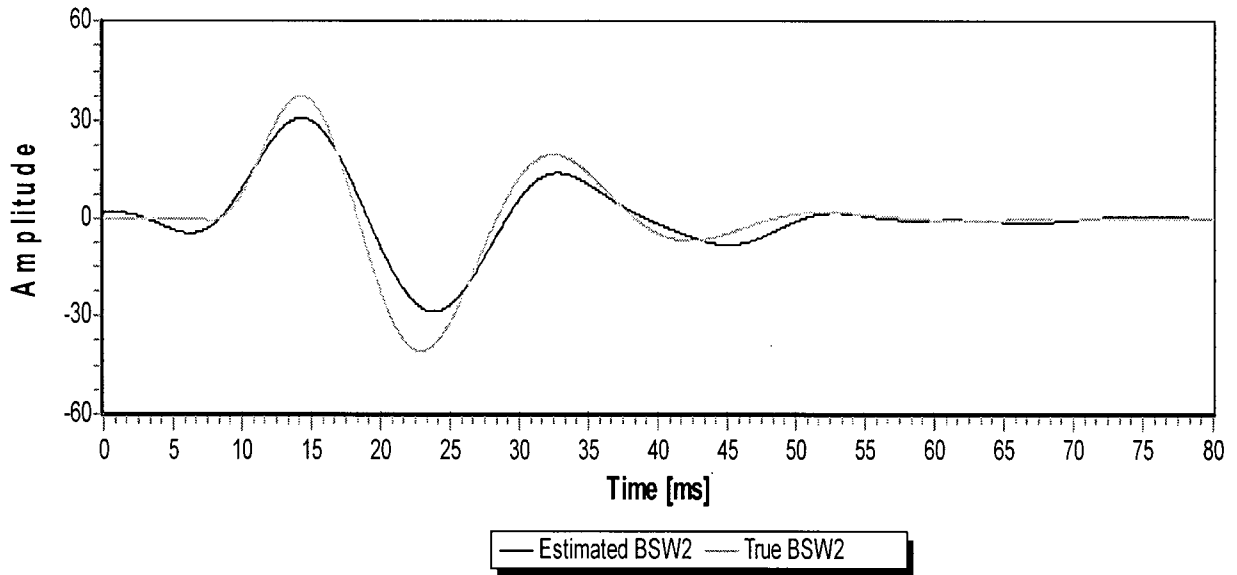


Figure 4.73. The estimated and true BSW2 source wavelets.

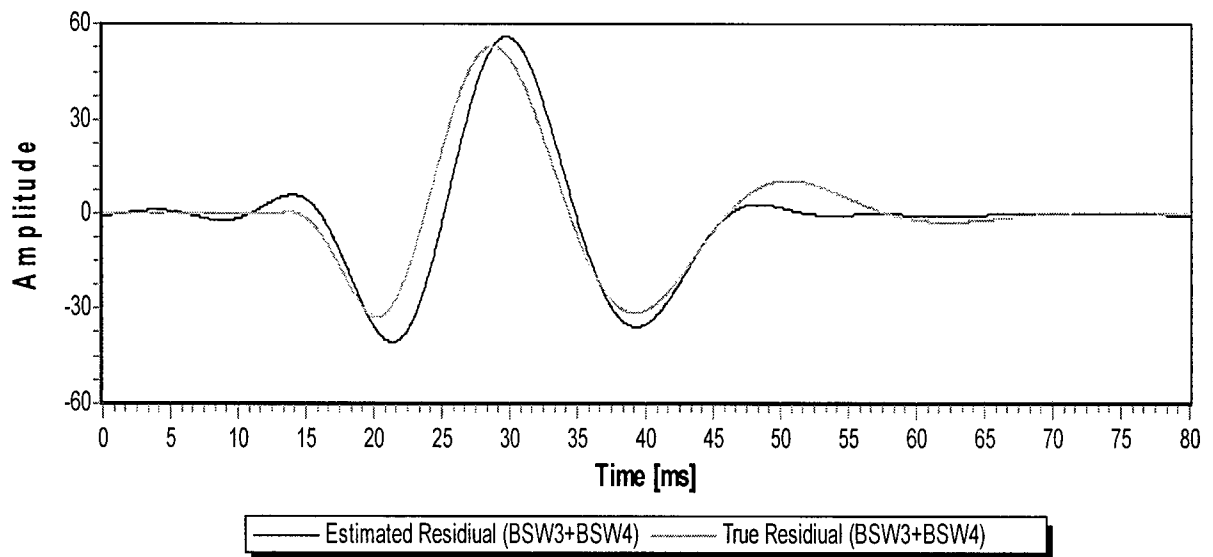


Figure 4.74. Estimated residual wavelet and the actual residual wavelet (i.e., BSW3+BSW4).

Subsequent to the extraction of Berlage source wavelets BSW1 and BSW2, the PPD-WE algorithm is then applied to the estimated residual wavelet shown in Fig. 4.74. Figure 4.75 illustrates the estimated residual wavelet shown in Fig. 4.74 with the time parameters t^* and t' set to 17 ms and 15 ms, respectively.

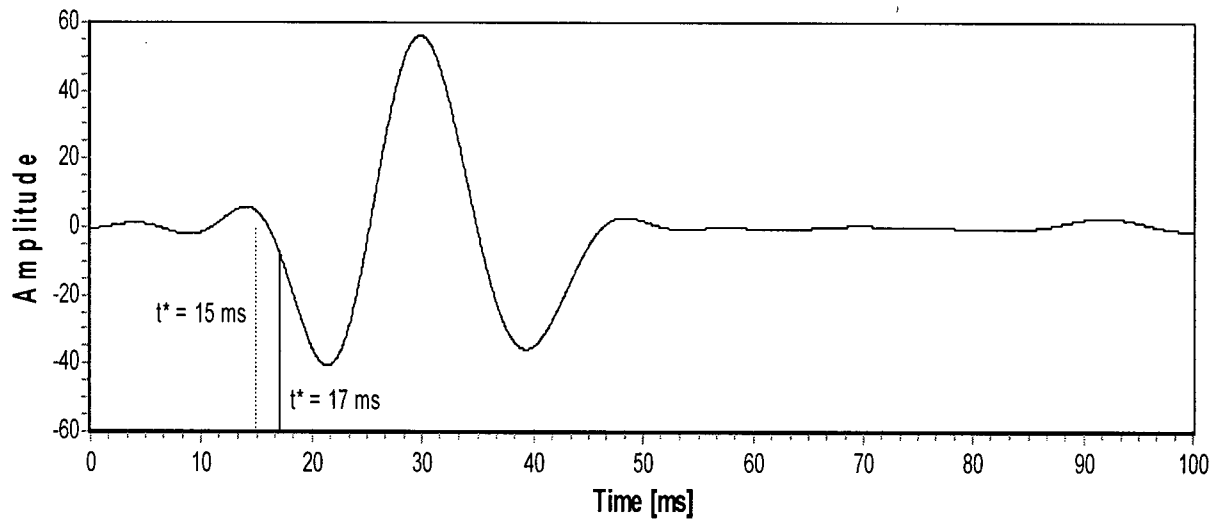


Figure 4.75. Estimated time series residual of Fig. 4.74 with the time parameters t^* and t' set to 17 ms and 15 ms, respectively.

An initial frequency range of 30 Hz to 47 Hz was specified with an increment resolution of 0.1 Hz within the HMM-FE filter. The 50 Hz frequency component was avoided due to the fact that the overall seismogram had a dominant frequency of approximately 50 Hz (peak 1 to peak 3). Figure 4.76 shows the output of the HMM-FE filter after the first pass of the HMM-FE filter and an initial value of $\omega = 40$ Hz specified. As is evident from Fig 4.77, the HMM-FE filter locked onto a DF value of approximately 44.5 Hz within 30 ms.

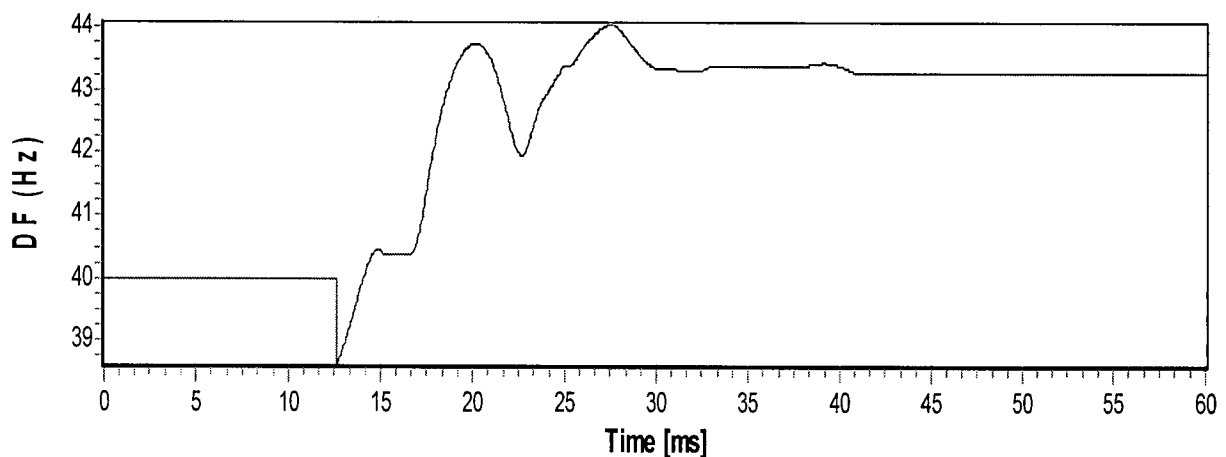


Figure 4.76. Illustration of the output of the HMM-FE filter after processing the synthetic seismogram shown in Fig. 4.75.

Implementation of the PPD-WE algorithm on the data shown in Fig. 4.76 resulted in the AMS wavelet estimates illustrated in Figs. 4.77 and 4.78. Figure 4.77 shows the estimated and true BSW3 source wavelets. Figure 4.74 illustrates the estimated and true BSW4 source wavelets. As is evident from Figs. 4.77 and 4.78, the PPD-WE algorithm but had some difficulty in estimating the AMTs. This is due to the fact that any errors generate during the wavelet extraction process will propagate as the seismogram is sequentially and chronologically processed.

To the best of my knowledge, the previously processed synthetic seismogram is the first example of the blind extraction of time variant overlapping source wavelets with closely spaced dipole reflection coefficients. The low signal-to-noise ratio synthetic seismogram contained two dipole reflection coefficients offset within 10 ms and time variant source

wavelets with an approximate duration of 40 ms. These results have significant implication for site characterization investigations (SCI) which utilize vertical seismic profiling (VSP). In many SCI there exists significant in-situ impedance contrast due to remediation efforts (e.g., insertion of stone columns utilizing vibro-compaction). This makes the post analysis of the VSP data appreciably difficult due to the closely spaced reflection coefficients and the time variant source wavelets. The PPD-WE algorithm could significantly mitigate the difficulty in separating the closely spaced overlapping source wavelets.

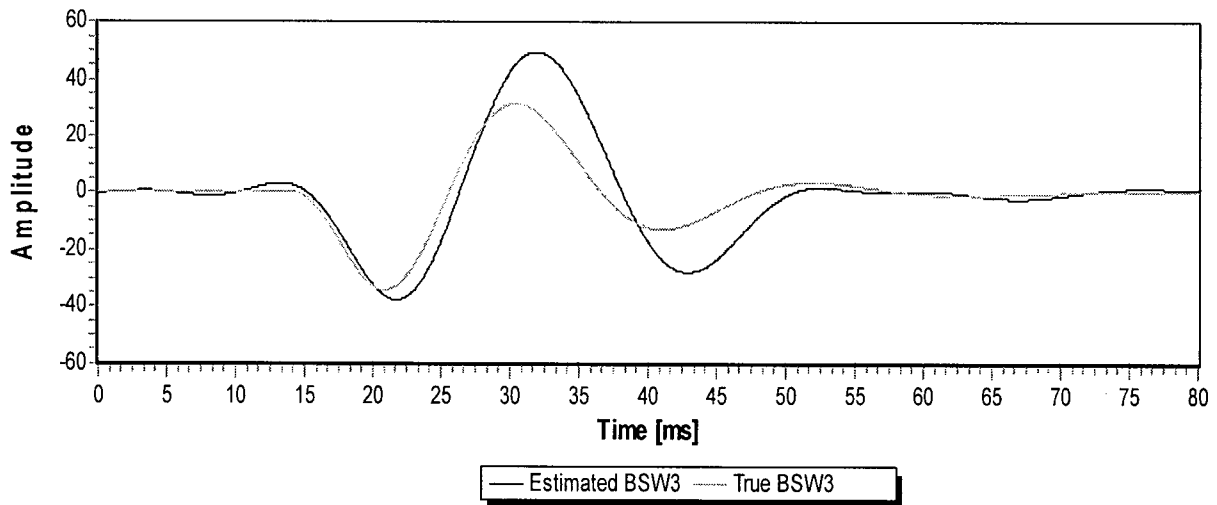


Figure 4.77. The estimated and true BSW3 source wavelets.

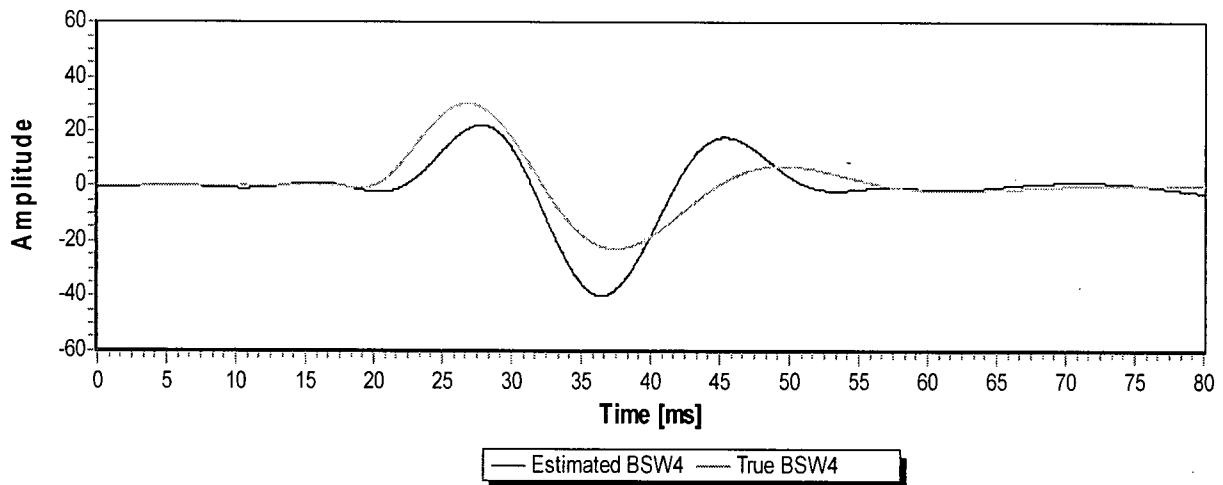


Figure 4.78. The estimated and true BSW4 source wavelets.

h) Utilization of the PPD-WE Algorithm within Standard Frequency Domain Deconvolution Techniques

A standard frequency domain methodology in estimating the reflection series, μ_k , is the water level technique (WLT) [51]. The WLT is outlined by considering (7), representing the Z transform by the Fourier transform (i.e., $z = e^{i\omega t}$) and rearranging terms as follows:

$$\Psi(\omega) = \frac{Z(\omega)}{S(\omega)} \quad (72)$$

where $\Psi(\omega)$ denotes the Fourier transform of the reflection series $\mu(t)$. Theoretically, for a known source wavelet, one could simply implement (72) and calculate $\Psi(\omega)$. The reflection series, μ_k , is then estimated by taking the inverse Fourier transform of $\Psi(\omega)$. Unfortunately, due to inaccuracies in the specification of the source wavelet, the bandlimited nature of the source wavelet and additive measurement noise, the implementation of (72) is highly unstable and inaccurate.

To mitigate the previously outlined limitations, (72) is modified by firstly multiplying the numerator and denominator by the complex conjugate of $S(\omega)$ (denoted as $S^*(\omega)$) and secondly, by introducing an additive scalar value to the denominator which is referred to as the *water level* (Δ) [51]. Implementation of these two modifications to (72) gives

$$\Psi(\omega) = \frac{Z(\omega)S^*(\omega)}{S(\omega)S^*(\omega) + \Delta} = \frac{Z(\omega)S^*(\omega)}{P_S(\omega) + \Delta} \quad (73)$$

where $P_S(\omega)$ denotes the power spectrum of the source wavelet (i.e., the Fourier transform of the autocorrelation of $S(t)$). In general terms, the setting of the water level is a trial and error approach. As $\Delta \rightarrow 0$, the resulting estimated reflection coefficients approach Dirac delta functions. When $\Delta \gg P(\omega)$ the resulting estimated reflection coefficients become significantly bandlimited and the result converges to the Fourier transform of the crosscorrelation between the recorded seismogram and the source wavelet (i.e., $Z(\omega)S^*(\omega)$).

The implementation of the WLT in conjunction with the PPD-WE technique is illustrated by considering the synthetic time series illustrated in Fig. 4.79. The simulated time series shown in this figure is a typical seismogram which one may encounter and it was generated without my prior knowledge of the source wavelet(s) or reflection series.

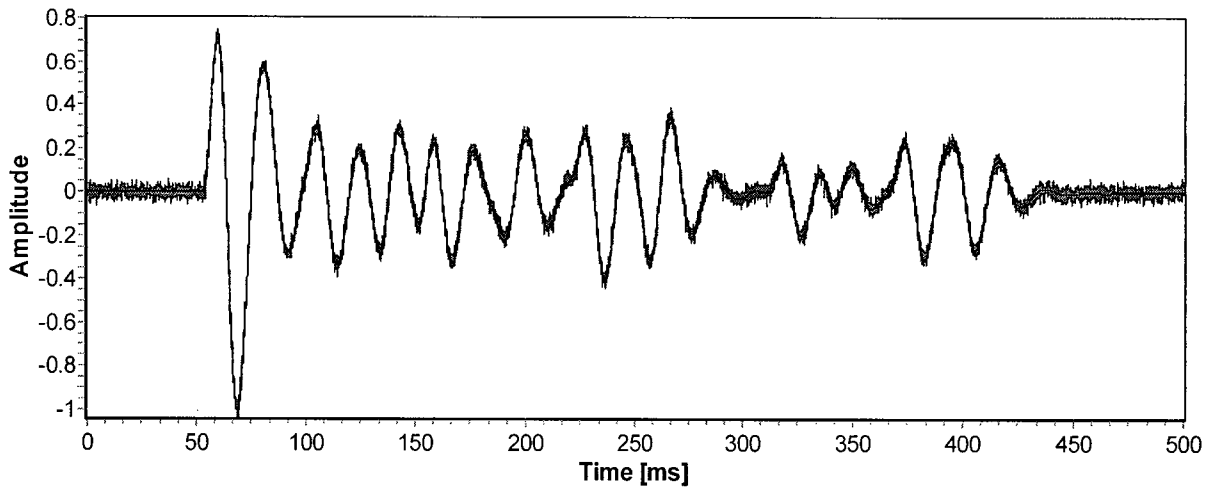


Figure 4.79. A typical synthetic seismogram.

The amplitude spectrum of the seismogram shown in Fig. 4.79 is illustrated in Fig. 4.80. As is evident from Fig. 4.80, the dominant seismic bandwidth resides between 40 Hz to 60 Hz.

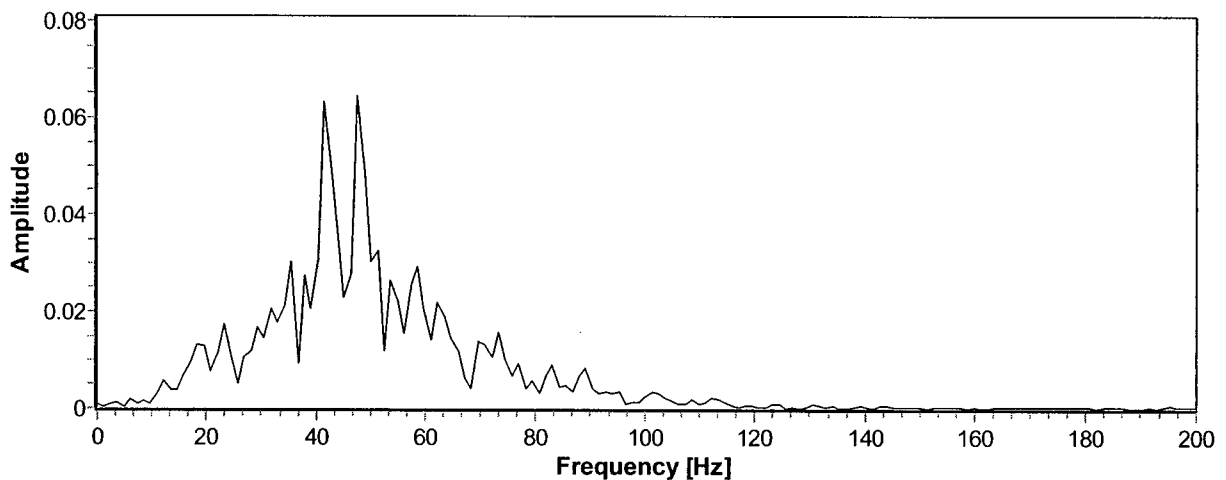


Figure 4.80. The amplitude spectrum of the seismogram illustrated in Fig. 4.79.

A 100 Hz low-pass Butterworth frequency filter was then applied to the seismogram of Fig. 4.79. Figure 4.81 illustrates the filtered seismogram (black line) superimposed upon the noisy seismogram (light grey plot) of Fig. 4.79.

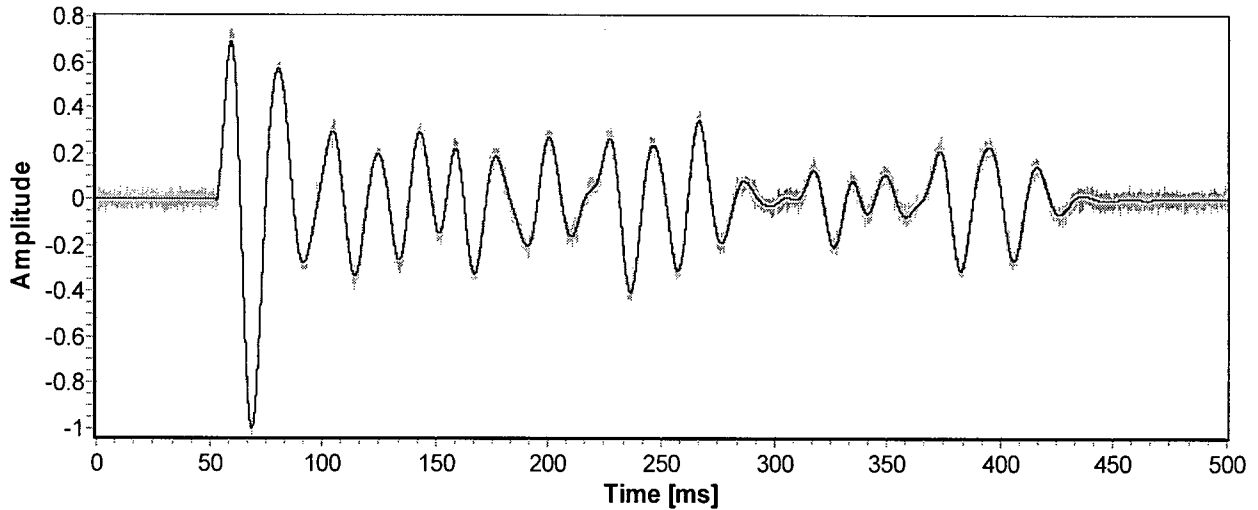


Figure 4.81. The superposition of filtered seismogram onto seismogram shown in Fig. 4.79.

The PPD-WE algorithm was then implemented on the filtered seismogram so that the first arriving source wavelet could be extracted and estimated. The first 45 ms of the filtered time series was ignored due to the fact no signal was present. As a result of the estimated frequency bandwidth of the seismogram (i.e., Fig. 4.80), the HMM-FE component of the PPD-WE algorithm had a frequency range of 40 Hz to 60 Hz specified. Figure 4.82 illustrates the estimated dominant frequency output of the HMM-FE. As is evident from Fig. 4.82, the HMM-FE locks onto a dominant frequency range of approximately 49 Hz to 51 Hz within 5 ms from the onset of the first arriving source wavelet.

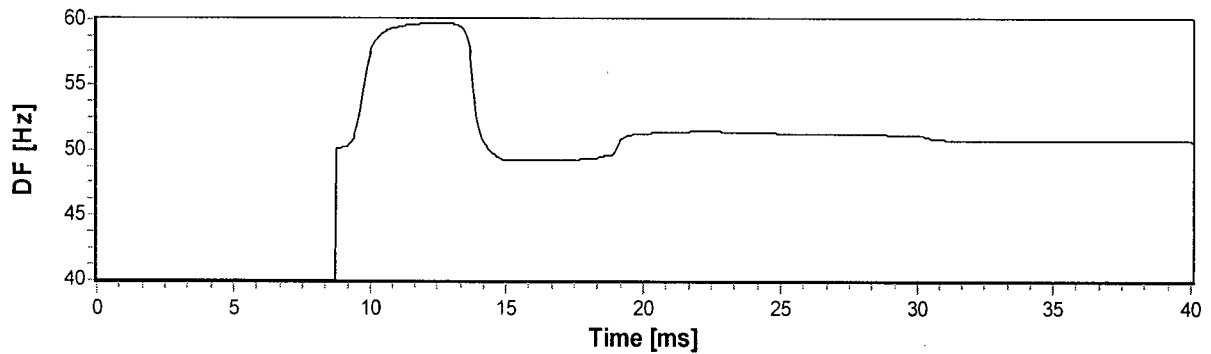


Figure 4.82. Illustration of the output of the HMM-FE filter after processing the filtered seismogram shown in Fig. 4.81.

Figure 4.83 shows the PPD-WE estimated first arriving source wavelet superimposed upon the true source wavelet. As is evident from Fig. 4.83, the PPD-WE algorithm estimated the correct dominant frequency of approximately 50 Hz and also did a very impressive job in estimating and extracting the first arriving source wavelet. The estimated responses after 105 ms are a PPD-WE filter residual where the algorithm is estimating overlapping source wavelet responses with a similar phase and dominant frequency to the currently estimated source wavelet. For this reason and due to the fact that the source wavelet will not likely, from a physics point of view, decay to zero and start up again, the estimated time series beyond 105 ms is set to zero. Fig. 4.84 illustrates the estimated source wavelet of Fig. 4.83 with the time series beyond 100 ms set to zero.

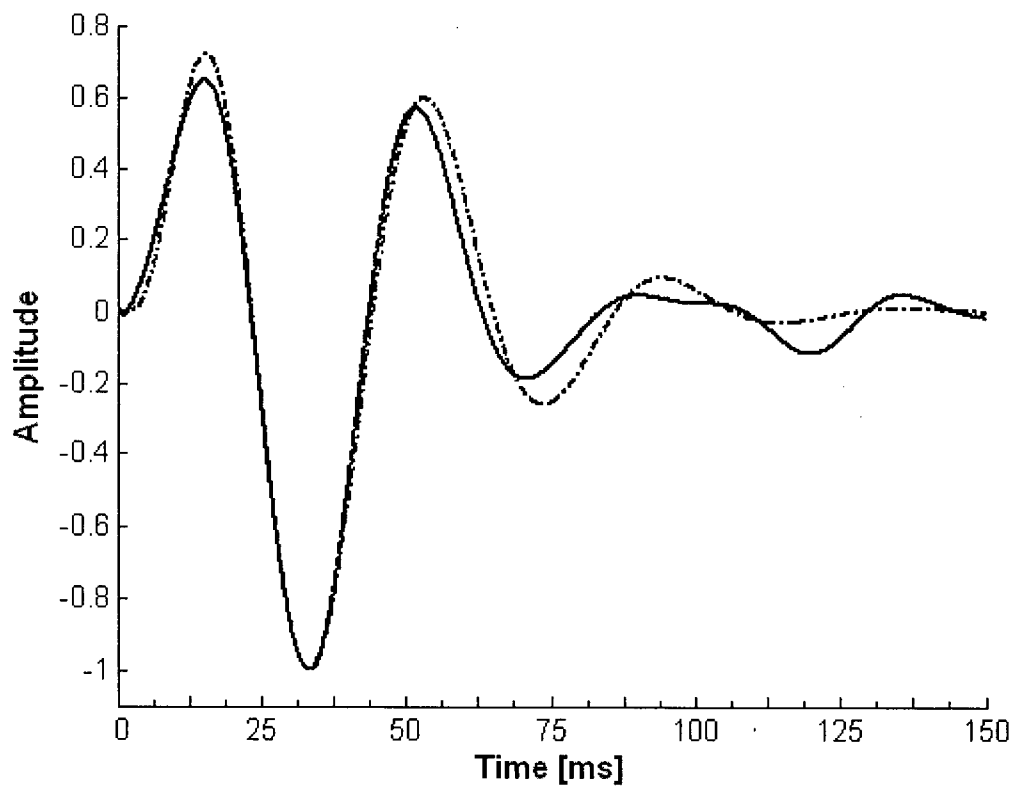


Figure 4.83. The estimated (solid black line) and true (dotted line) first arriving source wavelet.

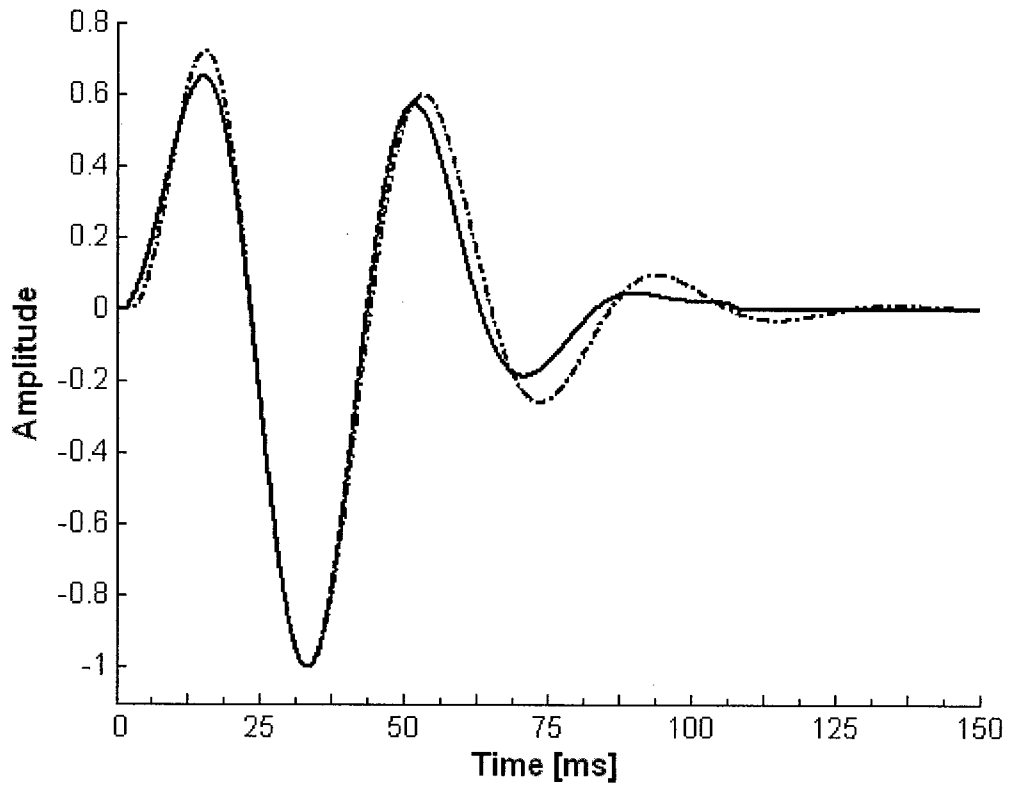


Figure 4.84. The estimated (solid black line) first arriving source wavelet of Fig. 4.83 with the time series beyond 105 ms set to zero.

As opposed to going through the lengthy process of separating all possible overlapping source wavelets, the first deconvolution attempt was performed using the estimated source wavelet of Fig. 4.84 and the WLT. If there is minimal source wavelet variation within the time series, the estimated reflection coefficients will be very similar in shape. Figure 4.85 illustrates the superimposition of the true reflection series onto the estimated reflection series for the synthetic seismogram shown in Fig. 4.79. For these results, an 8th order Butterworth low pass filter was applied to the noisy seismogram and the water level was set to 0.2% of the maximum value of the power spectrum of the seismogram. As is evident from Fig. 4.85, the WLT in conjunction with the PPD-WE algorithm did an excellent job in recovering the true reflection series. In addition, we can assume that a stationary source wavelet is present due to the nearly identical shape of the estimated reflection coefficients.

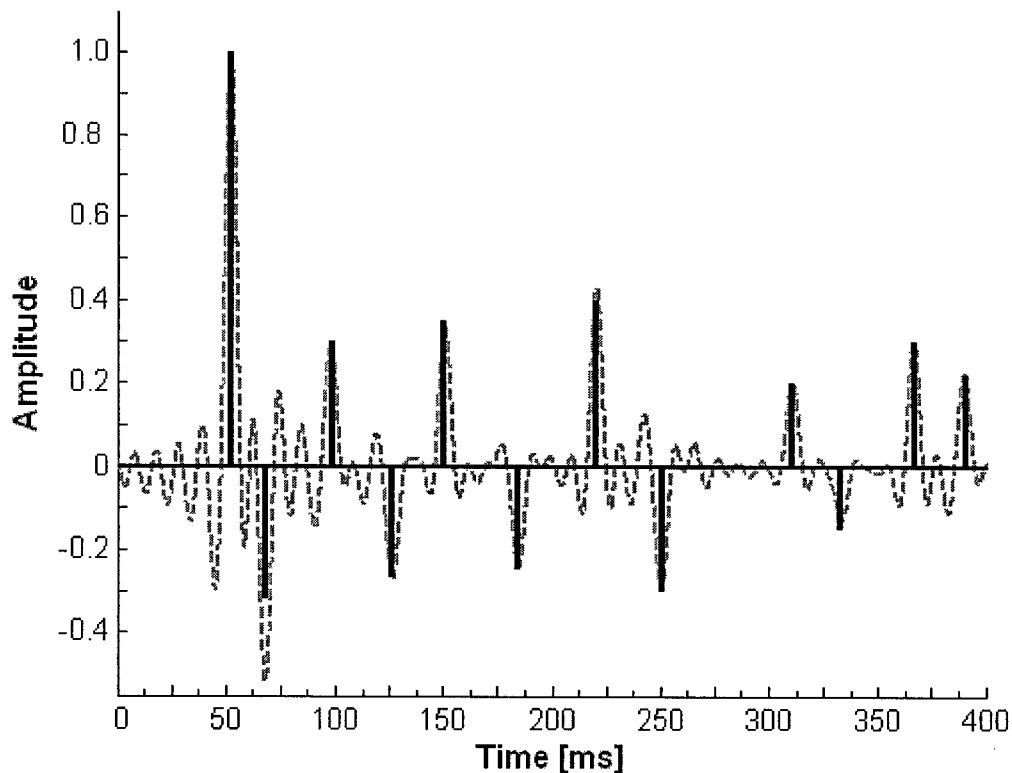


Figure 4.85. Superposition of the true reflection series (black line) onto the estimated reflection series (dotted line).

i) Monte Carlo Simulations

There two important Monte Carlo simulation (MCS) considerations in the implementation of the PPD-WE algorithm. 1) Step 4 of Table 4.4, where, if $y_k^i = y_k^3$, then states $x1_k$ and $x3_k$ are jittered by means of a random number generator. 2) The response of the algorithm to varying noise realizations. Figure 4.86 shows ten PPD-WE estimates for the noisy synthetic seismogram shown in Fig. 4.79. The response identified by the dotted line differs from the other nine estimates considerably and is, therefore, ignored. The remaining nine responses are averaged to give the source wavelet estimate.

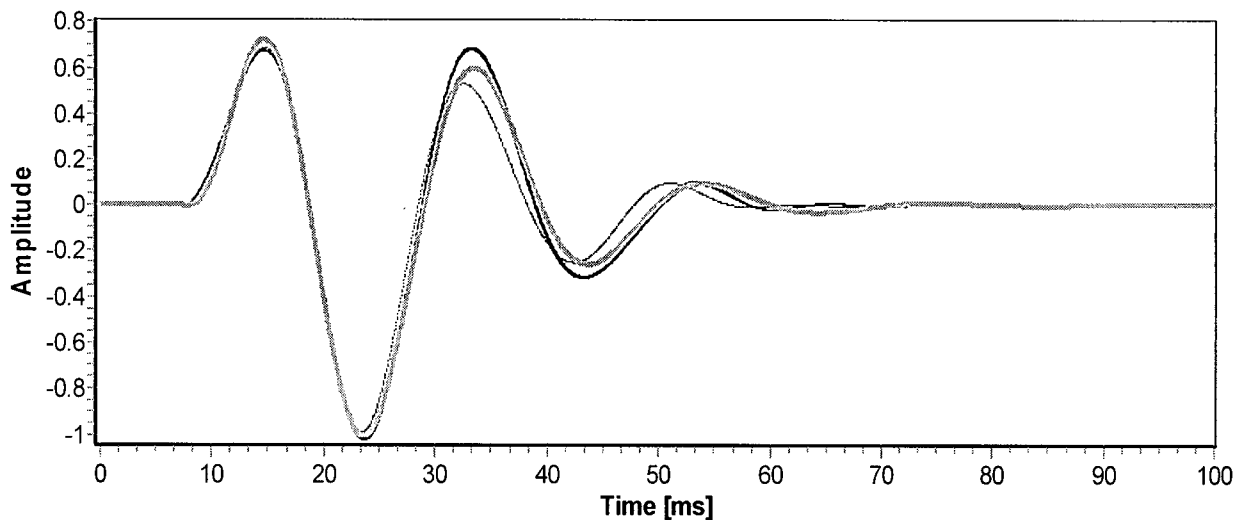


Figure 4.86. Ten PPD-WE estimates for noisy synthetic seismogram shown in Fig. 4.79. The estimate illustrated by the dotted line is explained in the text. The bold light grey line identifies the true source wavelet.

The ability of PPD-WE algorithm to respond to varying noise realizations is also of concern. Figure 4.87 illustrates an example of a synthetic seismogram where the noise free seismogram of Fig. 4.79 has additive Gauss-Markov noise with a time constant of 0.001 ms and a variance of 0.005 units².

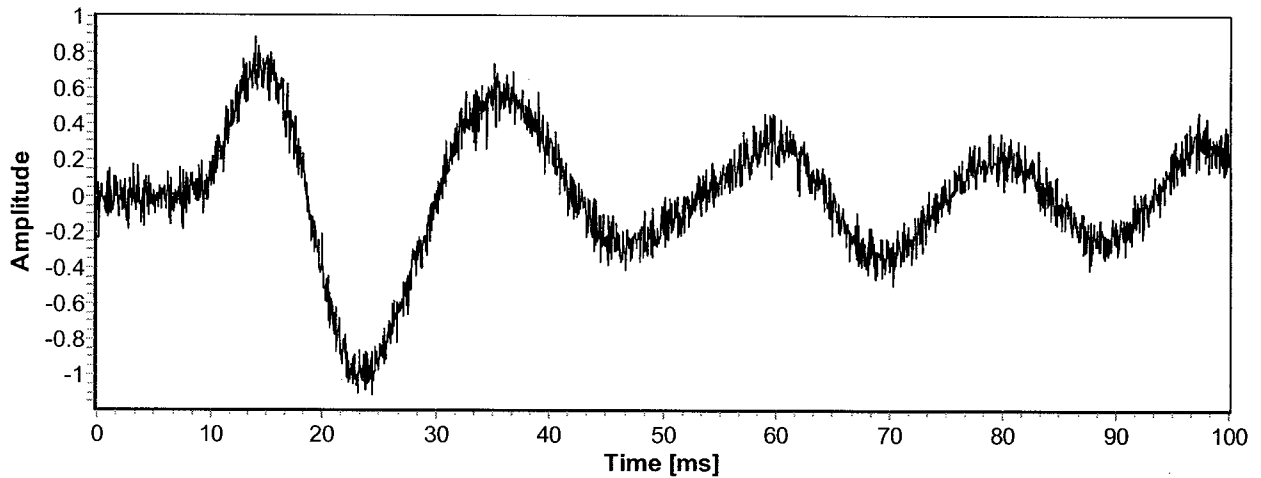


Figure 4.87. Synthetic seismogram where the noise free seismogram of Fig. 4.79 has additive Gauss-Markov noise with a time constant of 0.001 ms and a variance of 0.005 units².

Figure 4.88 illustrates the output of the PPD-WE algorithm for ten additive Gauss-Markov noise (time constant of 0.001 ms and a variance of 0.005 units²) realizations. As is evident from Fig. 4.88, the PPD-WE had high repeatability when processing the ten synthetic seismograms.

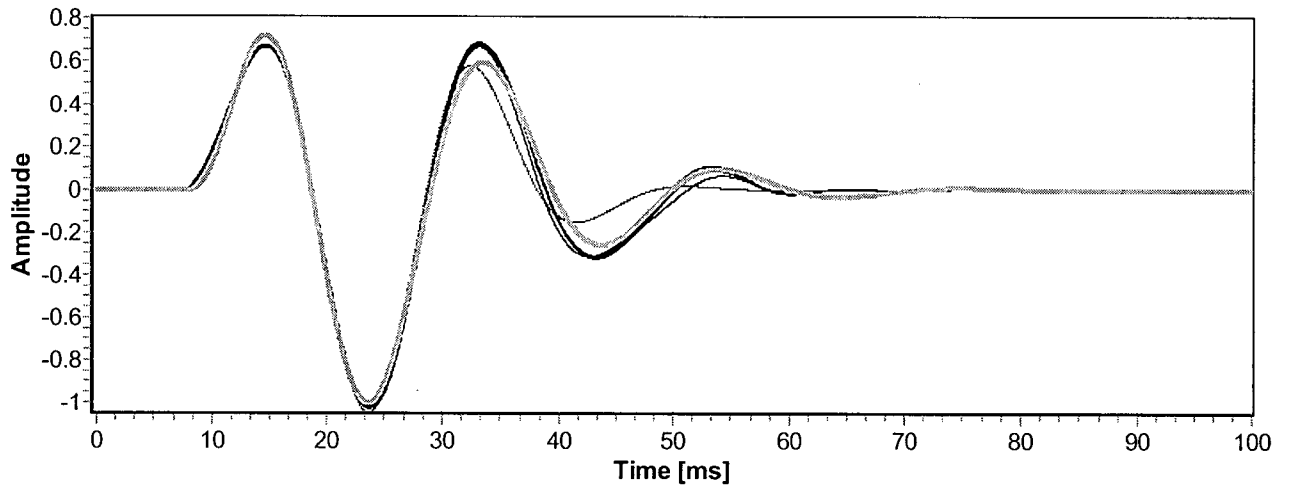


Figure 4.88. PPD-WE source wavelet estimates for ten additive Gauss-Markov noise (time constant of 0.001 ms and a variance of 0.005 units²) realizations. The bold light grey line identifies the true source wavelet.

j) Sensitivity Analysis

Due to the fact that the HMM filters are utilized to refine inaccurately specified initial phase estimates, the sensitivity limitation of the PPD and PPD-WE algorithms resides in their ability to separate source wavelets which have similar phases or have phase differences near 180° . Figure 4.89 illustrates two overlapping Berlage source wavelets where the first wavelet has an arrival time of 99 ms and the second Berlage wavelet has an arrival time of 108 ms. These two source wavelets have associated phases of 190° and 20° , respectively. This results in a phase difference of 170° that is 10° from the indiscernible value of 180° .

Figure 4.90 shows the output of the PPD algorithm where the algorithm was able to separate the two source wavelets, but has some difficulty in estimating the modulating amplitude term. This is highlighted in Figs. 4.91 and 4.92. In Fig. 4.91 the error residual between the estimated PPD Berlage wavelet and the true Berlage wavelet for the source wavelet with arrival time of 99 ms is shown. Figure 4.92 illustrates the error residual between the estimated PPD Berlage wavelet and the true Berlage wavelet for the source wavelet with an arrival time of 108 ms. Due to the nature of these and similar results, it is believed that the current formulation of the PPD and PPD-WE algorithms cannot sufficiently separate overlapping source wavelets which have phase difference less than 10° to 20° or between 160° to 180° .

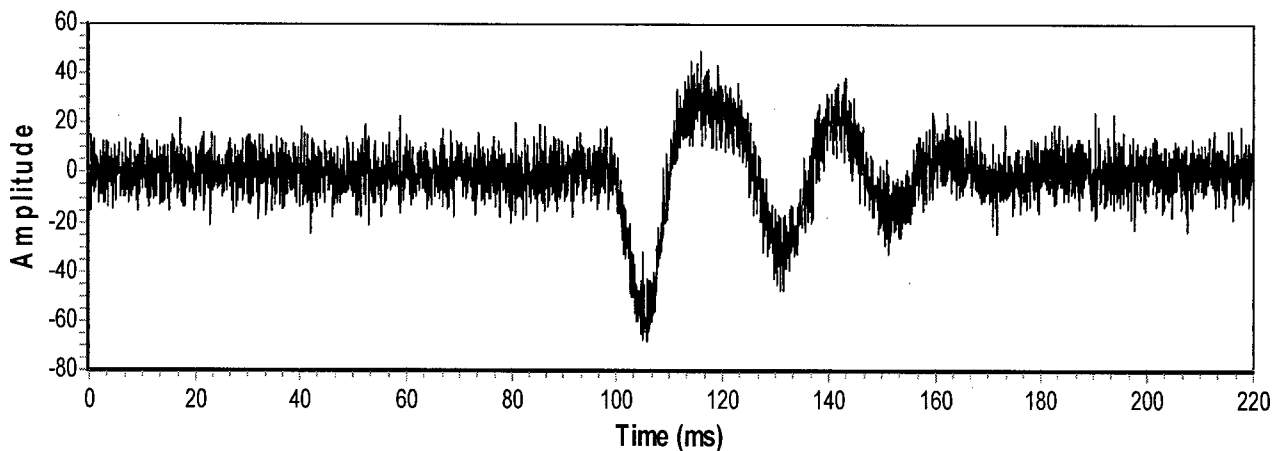


Figure 4.89. The output after overlapping two Berlage source wavelets with additive measurement noise. These two source wavelets have a phase difference of 170° .

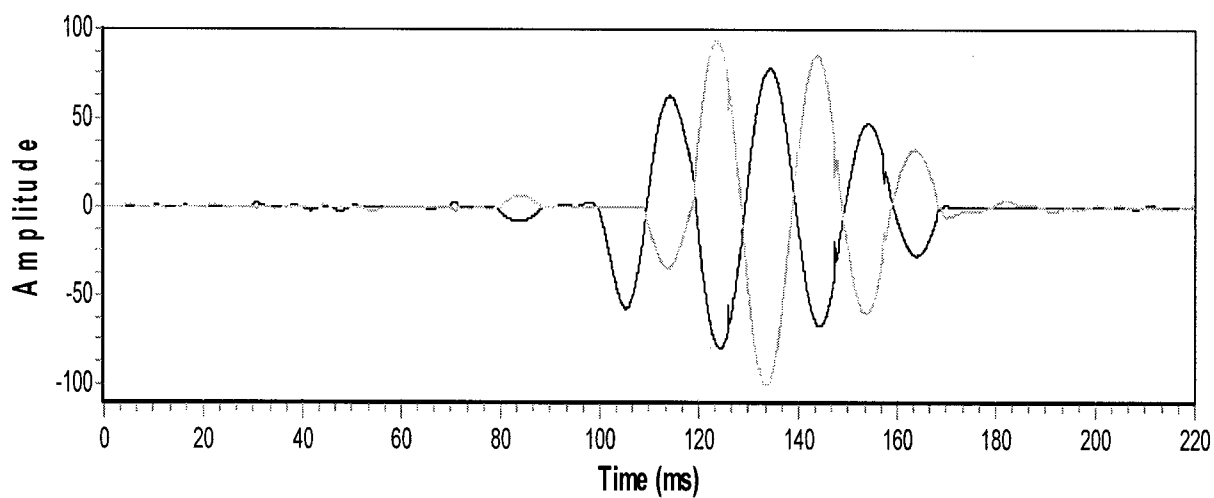


Figure 4.90. The output of the PPD algorithm, where the algorithm was able to separate the two source wavelets, but has some difficulty in estimating the modulating amplitude term.

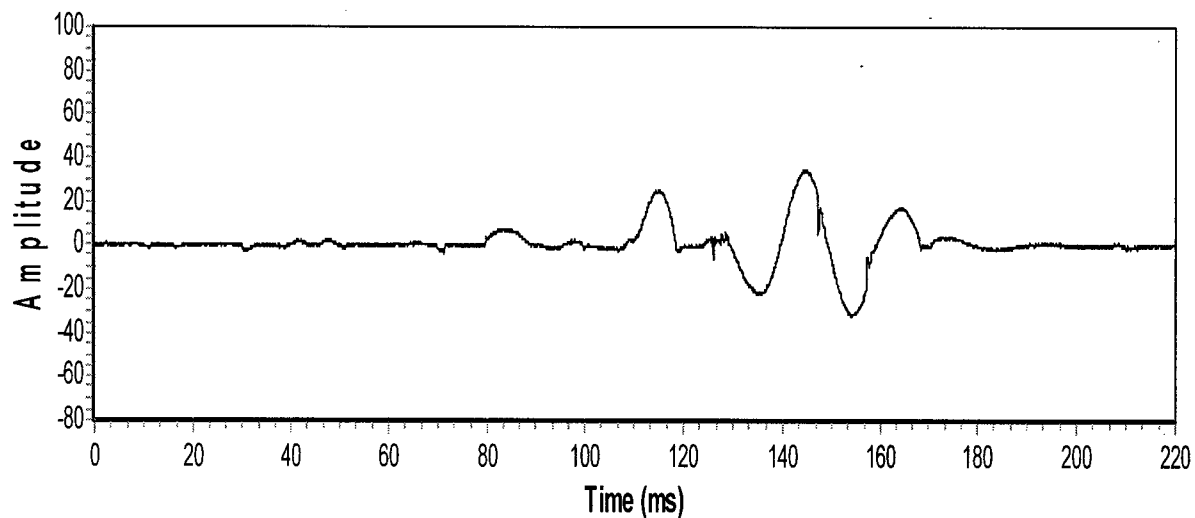


Figure 4.91. The error residual between the estimated PPD Berlage wavelet and the true Berlage wavelet with an arrival time of 99 ms.

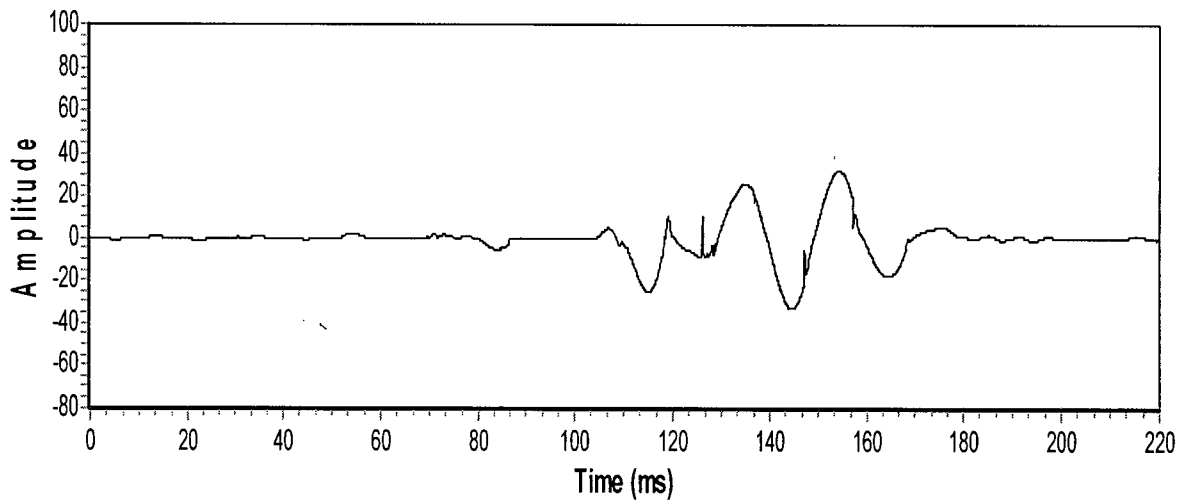


Figure 4.92. The error residual between the estimated PPD Beralge wavelet and the true Beralge wavelet with an arrival time of 108 ms.

The PPD and PPD-WE phase resolution limitation window is referred to as the null space. A $\pm 20^\circ$ resolution is equivalent to a theoretical reflection coefficient resolution of ± 1.1 ms for a source wavelet with a 50 Hz dominant frequency (i.e., it is possible to separate overlapping source wavelets which are separated by a minimum of 1.1 ms). Figure 4.93 illustrates the null spaces for a 50 Hz source wavelet ($T = 20$ ms) and null space resolution of $\pm 20^\circ$. In general terms, overlapping wavelets which arrive within the null spaces cannot be separated from the source wavelet to be extracted. An extracted source wavelet which has overlapping wavelets occupying the null spaces might be evident by a peculiar looking AMT and corresponding extracted source wavelet.

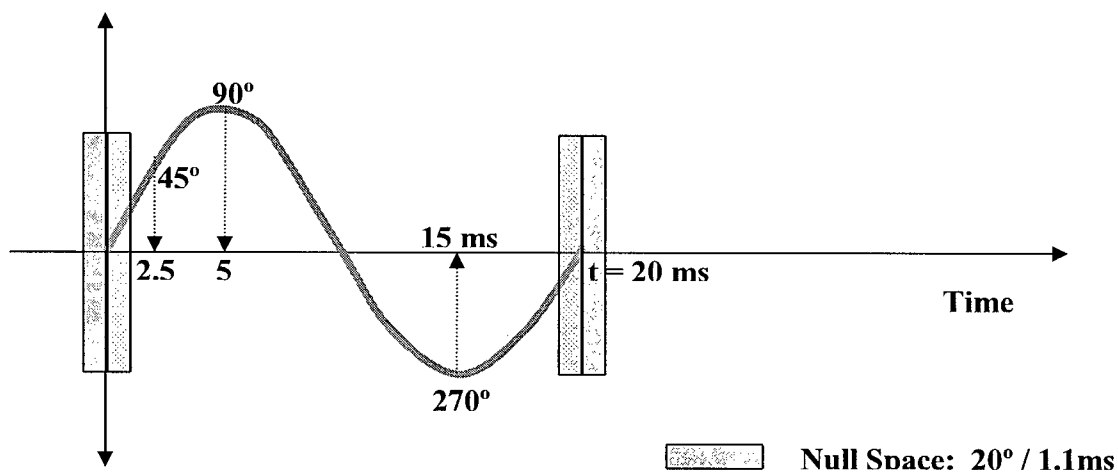


Figure 4.93. Illustration of the null spaces with a 50 Hz ($T = 20$ ms) source wavelet. Overlapping wavelets which arrive within the null spaces cannot be separated from the source wavelet to be extracted.

3) Implementation of the PPD-WE Algorithm on Real Data

The PPD-WE algorithm was implemented on real data acquired during a seismic cone penetration test (SCPT). The PPD-WE is a general purpose algorithm for blind deconvolution that is particularly well suited to wavelet estimation when no assumptions concerning the reflectivity can be made. For example, a minimal set of reflection coefficients is not conducive to assigning an associated pdf. Hence real data from a SCPT is analyzed due to the sparseness of the reflection coefficients (i.e., two to three reflection coefficients within the seismogram).

The SCPT has proven to be a very valuable geotechnical tool in facilitating the determination of low strain ($<10^{-6}$) in-situ compression (P) and shear (S) wave velocities. The P-wave velocities (V_p) and S-waves velocities (V_s) are directly related to the soil elastic constants of Poisson's ratio, shear modulus, bulk modulus, and Young's modulus. The estimation of elastic constants is essential in geotechnical foundation designs [30]. Another important use of estimated shear wave velocities in geotechnical design is in the liquefaction assessment of soils [5]. Details of the seismic cone, the downhole test procedures, and comparisons with the crosshole results at several sites have been described by Campanella et al. [20].

In general terms, the seismic cone is advanced to the depth of interest using a hydraulic reactionary pushing. The advance is halted at one meter (or other such increment) intervals. When the cone is at rest, a seismic event is caused at the surface using a hammer blow or explosive charge, causing seismic waves to propagate from the surface through the soil to be detected by seismic sensors installed in the cone penetrometer. This event is recorded and the penetrometer is advanced another increment and the process is repeated. By determining the relative seismic arrival times average velocities are calculated over the depth increment under study.

The relative arrival times are obtained by crosscorrelating the recorded source wavelets recorded at each depth increment [14]-[16]. The interval velocities are then calculated as the ratio between the relative arrival time differences and the corresponding relative travel path differences between successive depths (i.e., $v = \Delta d / \Delta T$, where ΔT is the relative arrival time

difference, Δd is the relative travel path difference and v is the corresponding SCPT interval velocity). It is of paramount importance to extract first arriving source wavelets from each trace so that crosscorrelation is meaningful when obtaining relative arrival times.

The data analyzed in this section was acquired with a triaxial system configuration. A triaxial sensor configuration is utilized so that full waveform analysis can be carried out and the possibility of rod rotation can easily be taken into account [17]. Details of the SC data acquisition system and seismic sensors utilized are given in [18]. For the SH wave analysis, the preprocessing of the seismic time series data captured on the X and Y axes is three-fold. 1) Apply bandpass frequency filter. 2) Rotate the X and Y axes responses onto the full waveform axis utilizing hodograms and polarization analysis [10], [17]. 3) Apply exponentially decaying windows to the front and end of the seismic responses on the recorded time series so that the S/N is increased.

Fig. 4.94 illustrates a typical SCPT configuration where a SH source is located at the outriggers of the in-situ testing vehicle. A triaxial SC sensor configuration is utilized and seismic source wavelets are acquired at constant depth intervals so that the in-situ SH wave interval velocities can be calculated. In Fig. 4.94 the interval velocity travel time ΔT_i is calculated by crosscorrelating the source wavelets captured at each depth increment.

The seismic cone data analysed in this section is referred to as *SC 64* and it was acquired in New Zealand on February 13th, 2006 near the Tauranga Eastern Motorway by Perry Drilling Ltd. of Tauranga New Zealand. The seismic source utilized was a horizontal shear (SH) hammer source. The (SH) source wavelets are generated at the outriggers which were positioned 2.3 metres from the centre of the rod strings. The source consists of a sledge hammer horizontally impacting point source steel beams located underneath the outriggers and an electrical contact trigger is utilized. Two stacked SH sources were generated for each depth increment.

Fig. 4.95 illustrates raw X axis time series data captured from SCPT test site *SC 64*. Fig. 4.96 illustrates raw Y axis time series data captured from SCPT test site *SC 64*. As is evident from Figs. 4.95 and 4.96, there are source multiples present within the captured time series data. The overlapping source wavelets present significant difficulties in implementing the crosscorrelation technique. To address this problem the PPD-WE algorithm is utilized to extract the first arriving source wavelet and subsequent to this the crosscorrelation

technique is implemented. Fig. 4.97 illustrates the vertical seismic profile (VSP) after processing the time series data shown in Figs. 4.95 and 4.96.

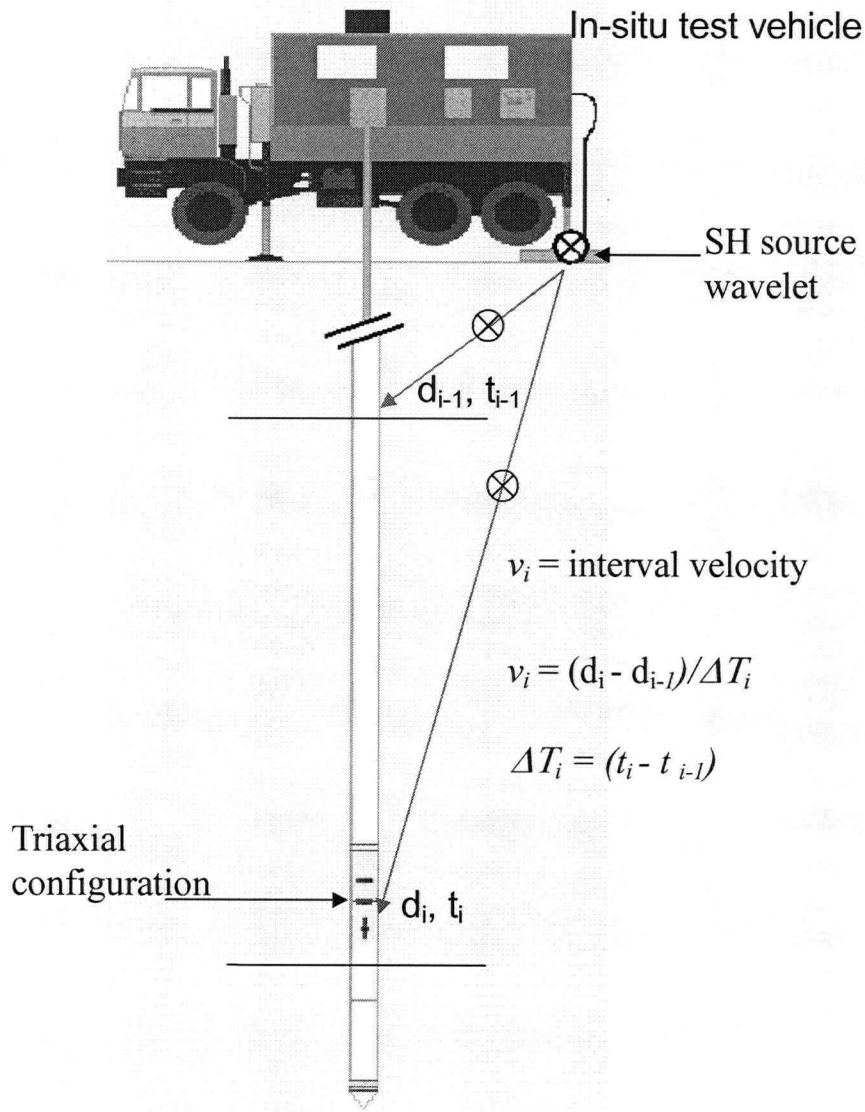


Figure 4.94. Typical SCPT configuration.

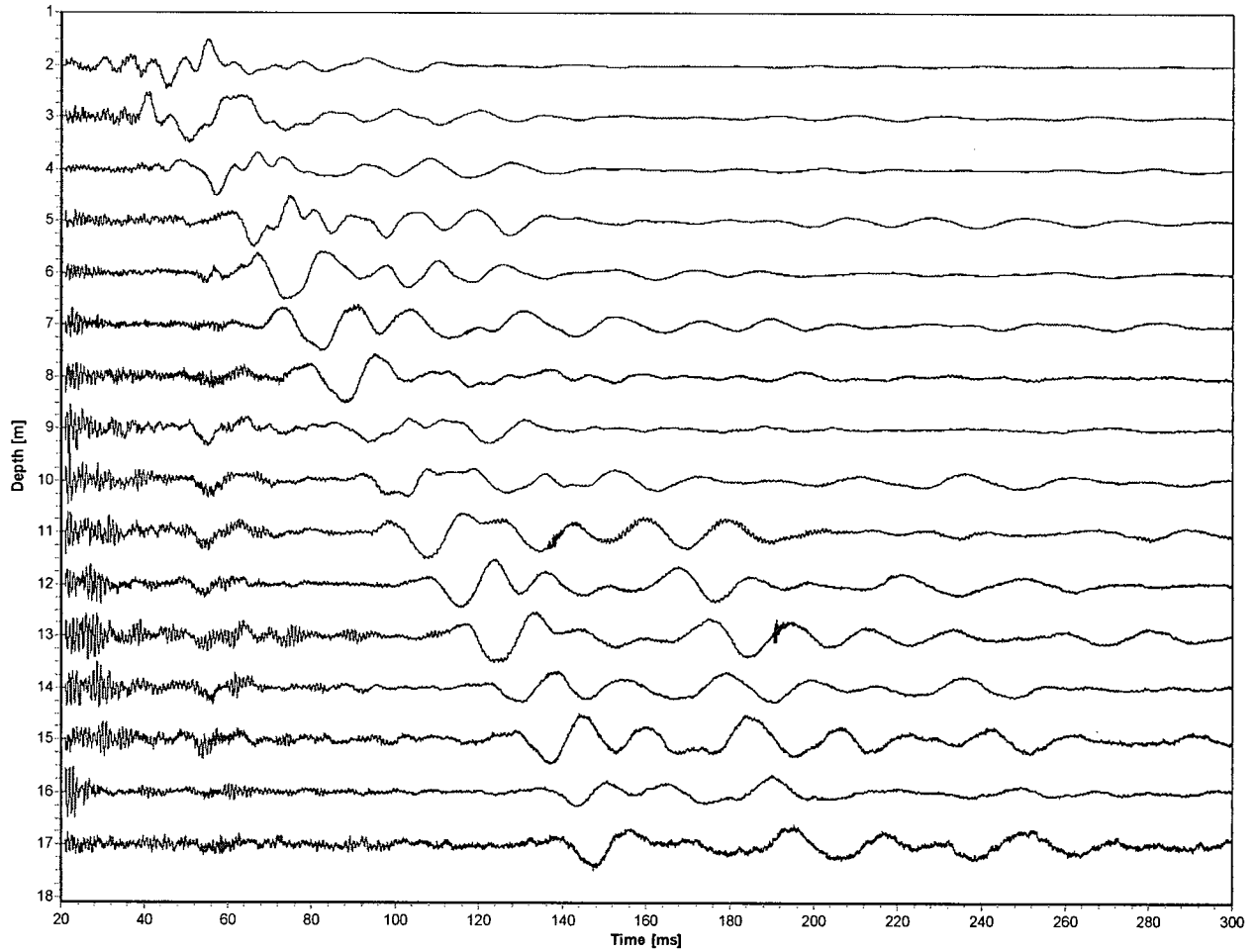


Figure 4.95. Raw X axis VSP from SCPT hole SC 64.

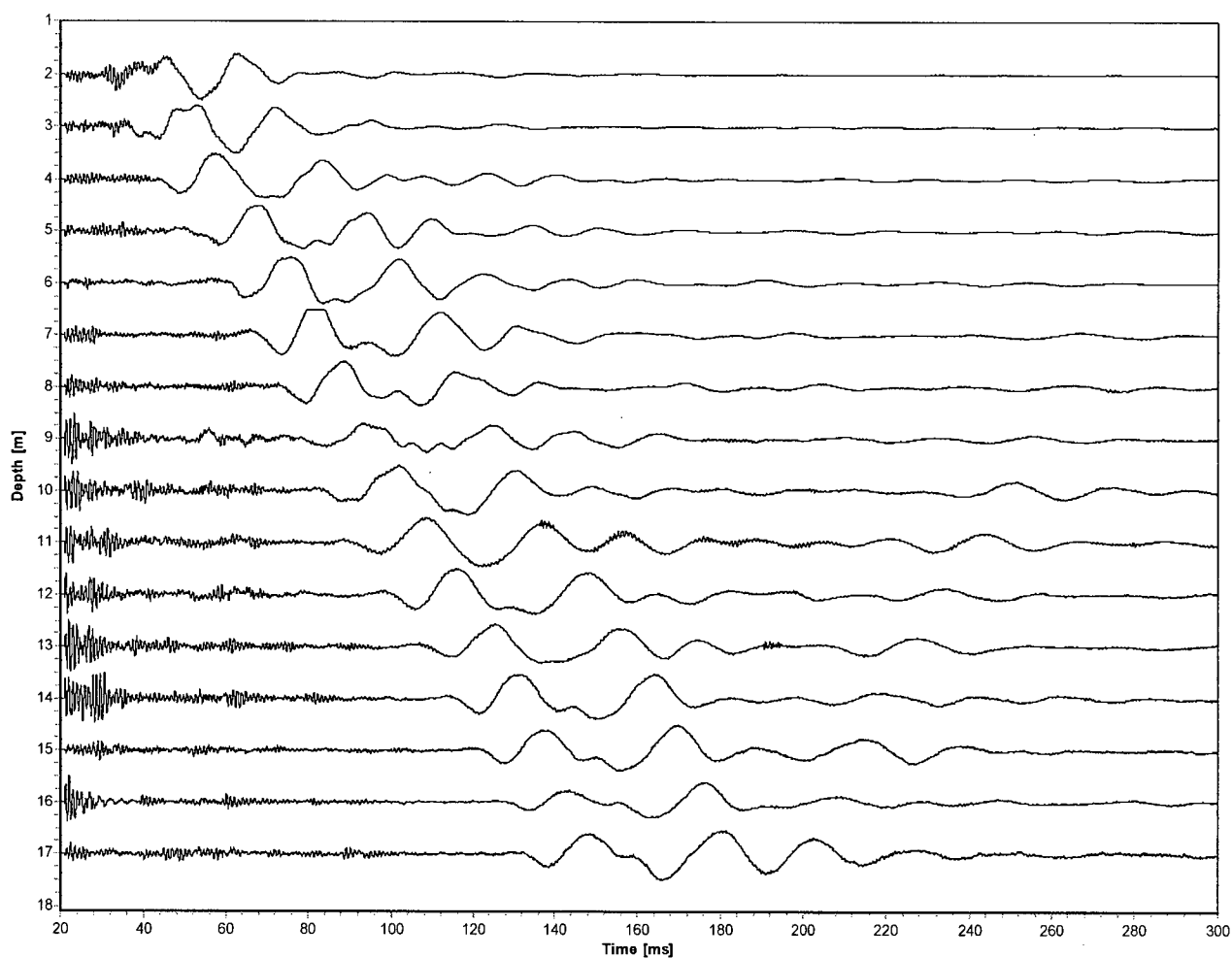


Figure 4.96. Raw Y axis VSP from SCPT hole SC 64.

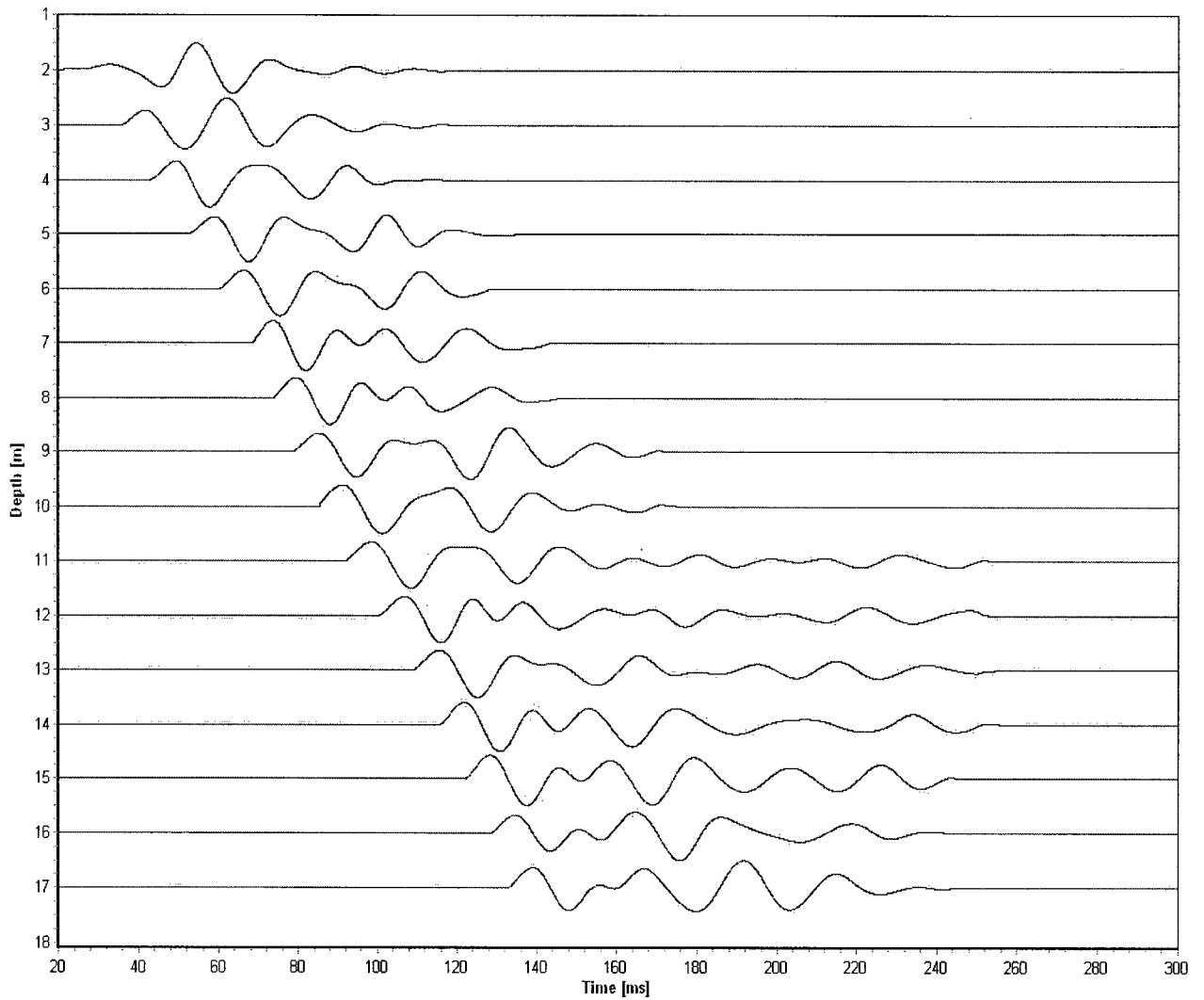


Figure 4.97. VSP for the processed seismic data captured at test site *SC 64* for depths 2 m to 17 m. There is clear evidence of overlapping source wavelets.

In the implementation of the PPD-WE technique there are slightly differing possible source wavelet estimation realizations depending upon the specification of the initial PPD-WE filter parameters of t' (zero crossing), t^* (time to source wavelet overlap), and R_k , (variance of measurement noise) and the utilization of Monte Carlo techniques to obtain realizations of $y_k^i \sim P(y_k^i | y_{k-1}^j)$ and jitter the particles (i.e., Step 4 of Table 4.4). For this reason, a Monte Carlo technique is utilized which allows the investigator to vary the input filter parameters and subsequently obtain many estimates of the source wavelet. The source wavelet is then derived by averaging the subsequent PPD-WE source wavelet estimates [13].

In this PPD-WE technique (PPD-WEMC) an additional time parameter, t_2 , is introduced. Unfortunately, there are some situations where the AMT of the source wavelet will slowly start to diverge from the true value due to the degeneracy check. To mitigate this effect, the degeneracy check is turned off after time t_2 which results in a noisier estimated source wavelet but the diversity of the particles is maintained.

In the PPD-WEMC algorithm the investigator initially specifies minimum t'_{min} (first seismogram zero crossing) and t_{2min} parameters. These parameters are modified within each iteration of the PPD-MEMC algorithm (source wavelet estimate) according to the following two equations:

$$t' = t'_{min} + abs(t'') \quad (74)$$

$$t_2 = t_{2min} + abs(t'_2) \quad (75)$$

where $t'' \sim N(0,0.4)$ and $t'_2 \sim N(0,225)$. In addition, the measurement noise variance is increased from an initial user specified minimum, R_{min} , according to a specified increment value, R_{inc} (i.e., $R = R_{min} + R_{inc}$).

The frequency window specified for the HMM-FE filter portion of PPD-WE algorithm was estimated based upon reviewing the amplitude spectrum of the acquired seismograms. For example, Fig. 4.98 shows the amplitude spectrum of the seismogram acquired at 2 m. As is evident from Fig. 4.98, the dominant seismic bandwidth resides between 45 Hz to 60 Hz.

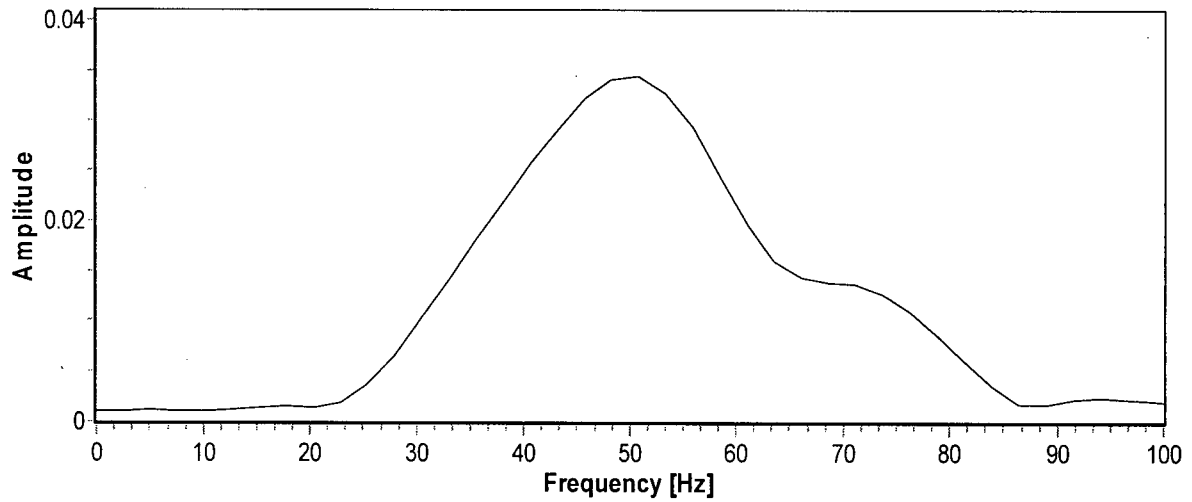


Figure 4.98. The amplitude spectrum of the seismogram captured at 2 m.

In the implementation of the PPD-WE algorithm on the SC data acquired at test site *SC 64*, the minimum zero crossing was readily available from the processed seismogram as is illustrated in Fig. 4.99. The HMM-FE frequency window was set to range from 45 Hz to 60 Hz. There were thirty five primary source wavelet estimates for each run of the PPD-WEMC algorithm and the minimum noise variance, R_{min} , was set to 0.1 with an increment increase of 0.1. This results in a measurement noise variance of 3.6 for the final run of the PPD-WEMC algorithm.

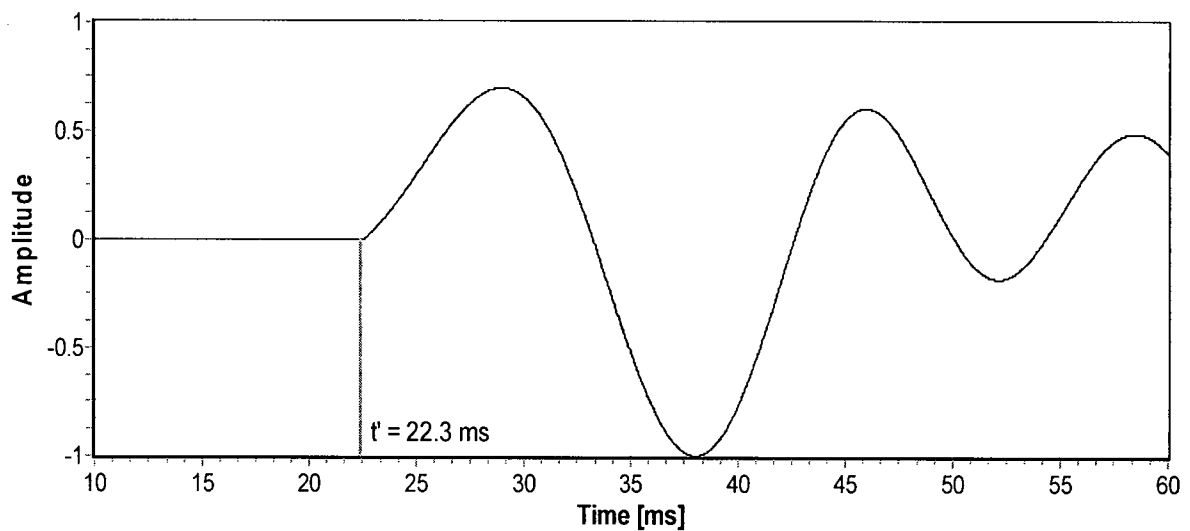


Figure 4.99. Estimating t'_{min} for the seismogram acquired at 12 m.

Fig. 4.100 illustrates the extracted (utilizing PPD-WE technique) primary source wavelets VSP for depths 2 m to 17 m of SCPT hole *SC 64*. The time series recorded at 2.0 m was assumed to contain no source multiples. Appendix H provides illustrations of the PPD-WE estimated source wavelets, averaged source wavelets and corresponding residual wavelets for test site *SC 64* and depths 3 m to 17 m. As is evident from Fig. 4.100, the PPD-WE technique did an impressive job in extracting the primary source wavelets. The crosscorrelation technique can now be implemented so that accurate interval SH wave velocities can be obtained.

The estimated interval velocities from the time series data given in Fig. 4.100 are outlined in Table 4.5. The traces shown in Fig. 4.100 have very high calculated interval correlation coefficients as shown in Table 4.5. Table 4.6 outlines the estimated interval velocities if the processed seismograms of Fig 4.97 are crosscorrelated when obtaining the interval arrival times. As is evident from Table 4.6, there are significant deviations from the estimated interval velocities of Table 4.5 and the calculated correlation coefficients are corresponding lower. It should be noted that the shear and compression wave velocities are squared in deriving the elastic constants; therefore, variations in the estimated velocities can cause appreciable errors in the calculation of the elastic constant. The crosscorrelation interval arrival times derived from the processed seismograms of Fig. 4.97 are also sensitive to the time window specified for the crosscorrelation function.

Fig. 4.101 illustrates the residual wavelets derived by subtracting the estimated primary source wavelets outlined in Fig. 4.100 from the processed seismograms shown in Fig. 4.97. As is evident from Fig. 4.101 and the residual wavelet plots shown in Appendix H, the majority of the seismograms have only one source multiple present. For the residuals at 16 m and 17 m there is evidence that there is more than two source wavelet multiples present in the acquired seismogram. For example, Fig. 4.102 shows the estimated reflection coefficients utilizing the WLT if the estimated source wavelet at 16 m is applied to the processed seismogram recorded at 16 m. Fig. 4.103 shows the estimated reflection coefficients utilizing the WLT if the estimated source wavelet at 17 m is applied to the processed seismogram recorded at 17 m.

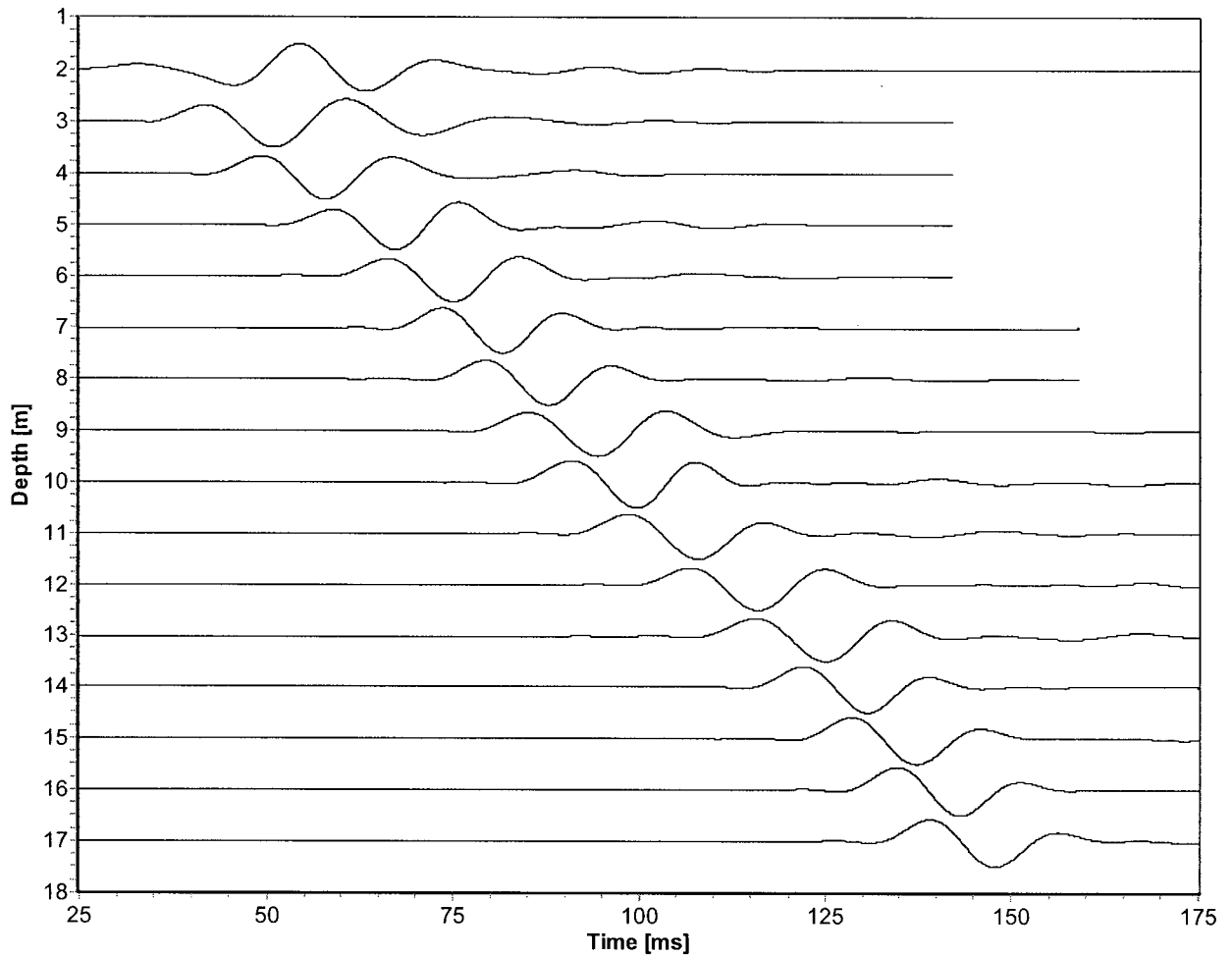


Figure 4.100. Extracted (utilizing PPD-WEMC technique) primary source wavelets VSP for depths 2 m to 17 m of SCPT hole SC 64.

TABLE 4.5
INTERVAL VELOCITIES (PPD-WE EXTRACTED SOURCE WAVELETS) FROM THE
CROSSCORRELATION TECHNIQUE FOR SCPT SC 64

<i>Interval Depth (m)</i>	<i>Crosscorrelation Interval Velocity Estimate (m/s)</i>	<i>Correlation Coefficient</i>
2.0-3.0	106	0.90
3.0-4.0	120	0.96
4.0-5.0	96	0.97
5.0-6.0	118	0.98
6.0-7.0	141	0.96
7.0-8.0	156	0.99
8.0-9.0	150	0.95
9.0-10.0	139	0.95
10.0-11.0	143	0.96
11.0-12.0	122	0.98
12.0-13.0	110	0.99
13.0-14.0	168	0.96
14.0-15.0	148	0.996
15.0-16.0	166	0.99
16.0-17.0	216	0.995

TABLE 4.6
INTERVAL VELOCITIES (PROCESSED SEISMOGRAMS) FROM THE CROSSCORRELATION
TECHNIQUE FOR SCPT SC 64

<i>Interval Depth (m)</i>	<i>Crosscorrelation Interval Velocity Estimate (m/s)</i>	<i>Correlation Coefficient</i>
2.0-3.0	93	0.90
3.0-4.0	104	0.86
4.0-5.0	92	0.93
5.0-6.0	114	0.97
6.0-7.0	121	0.81
7.0-8.0	164	0.97
8.0-9.0	152	0.84
9.0-10.0	167	0.94
10.0-11.0	144	0.97
11.0-12.0	118	0.77
12.0-13.0	108	0.91
13.0-14.0	154	0.80
14.0-15.0	167	0.96
15.0-16.0	148	0.85
16.0-17.0	287	0.79

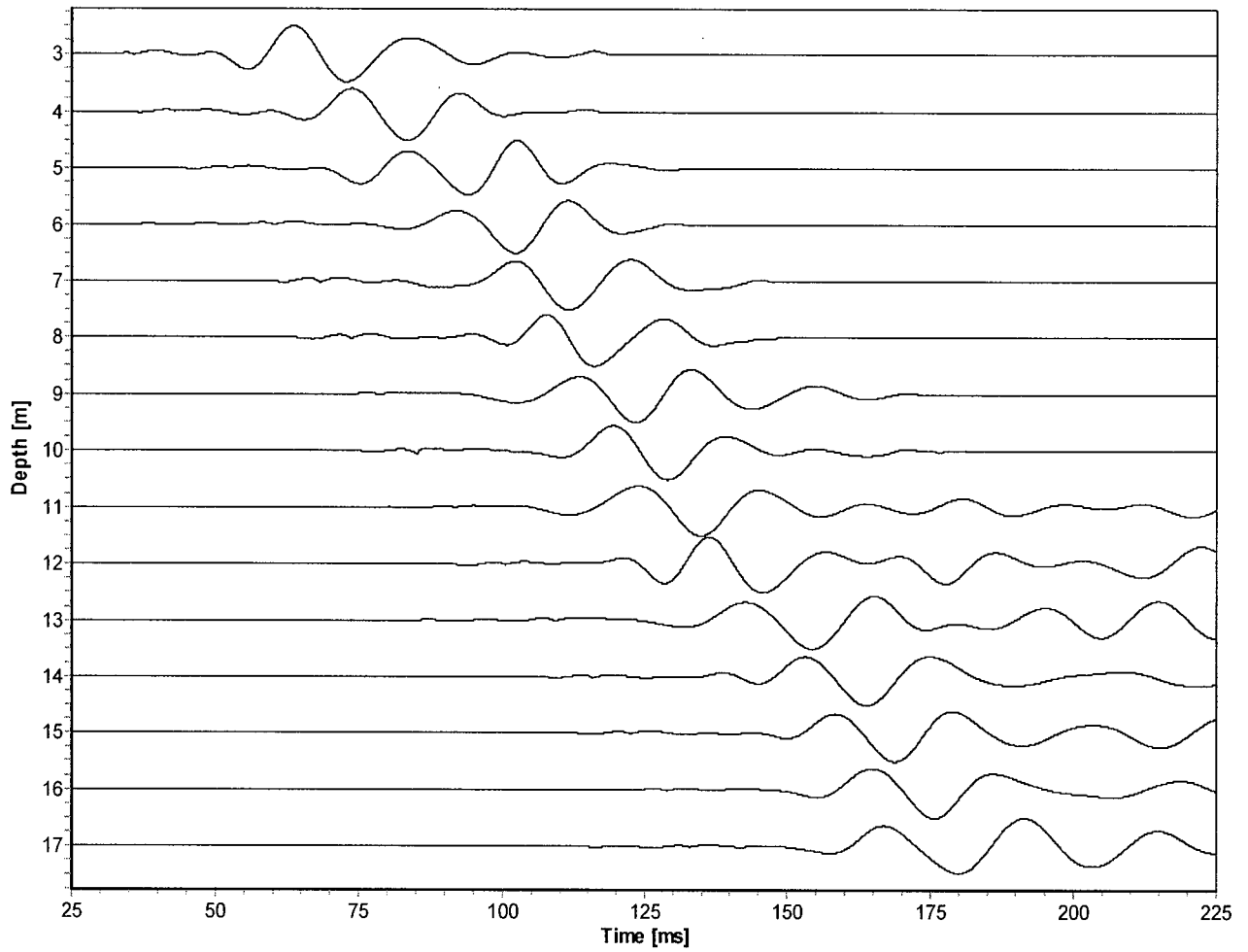


Figure 4.101. Residual wavelets VSP for depths 3 m to 17 m of SCPT hole SC 64.

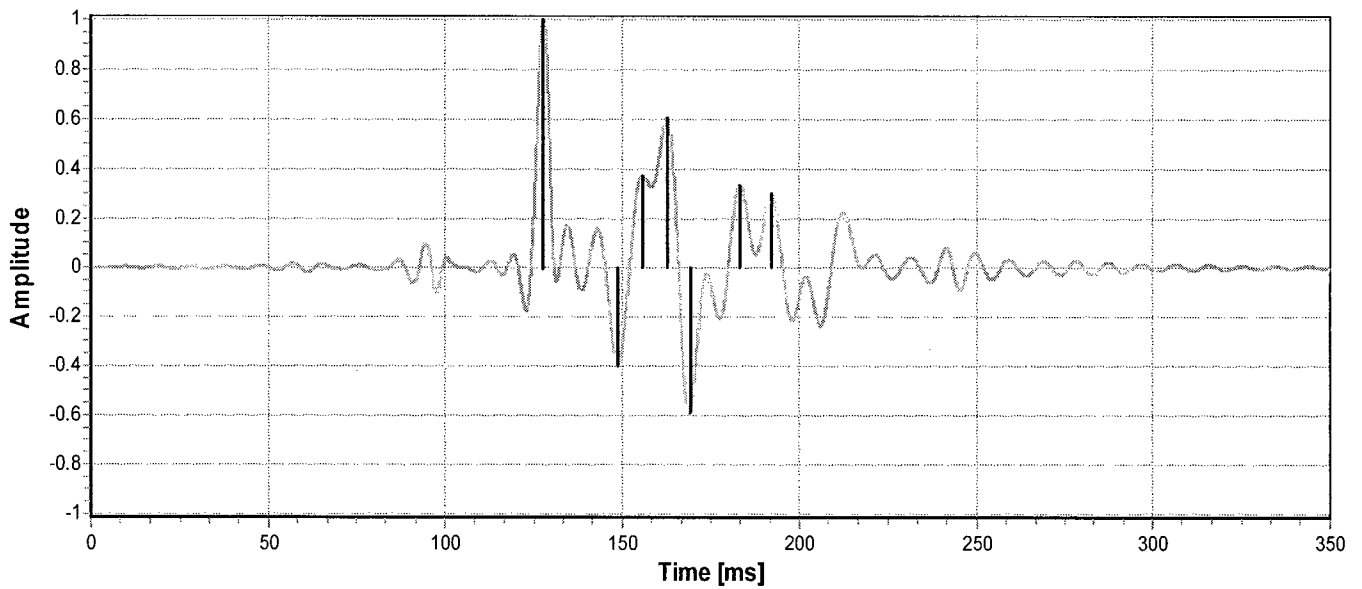


Figure 4.102. Estimated reflection coefficients for depth 16 m utilizing the WLT.

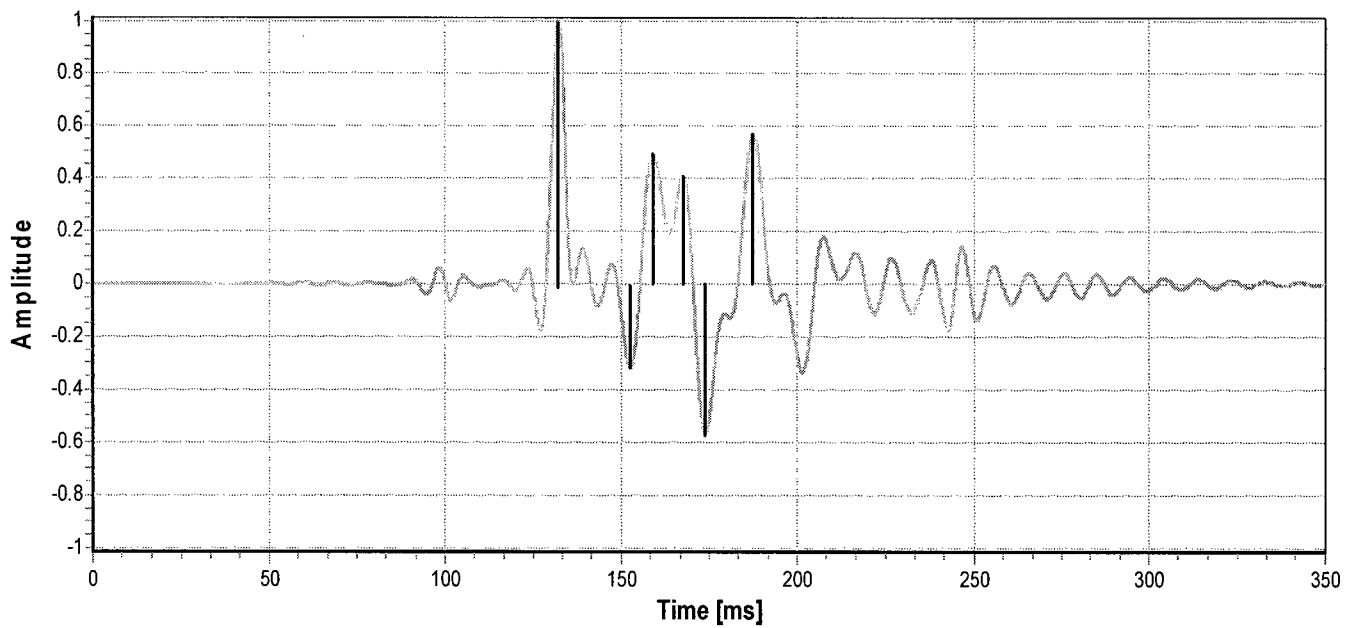


Figure 4.103. Estimated reflection coefficients for depth 17 m utilizing the WLT.

Fig. 4.104 shows the superposition of the PPD-WE estimated source wavelets outlined in Fig. 4.100 (depths 4 m to 17 m) and corrected zero time offset. Fig. 4.105 illustrates the source wavelet obtained by averaging the estimated source wavelets illustrated in Fig. 4.104. The estimated source wavelets outlined in Figs. 4.104 and 4.105 are scale to that of the central trough.

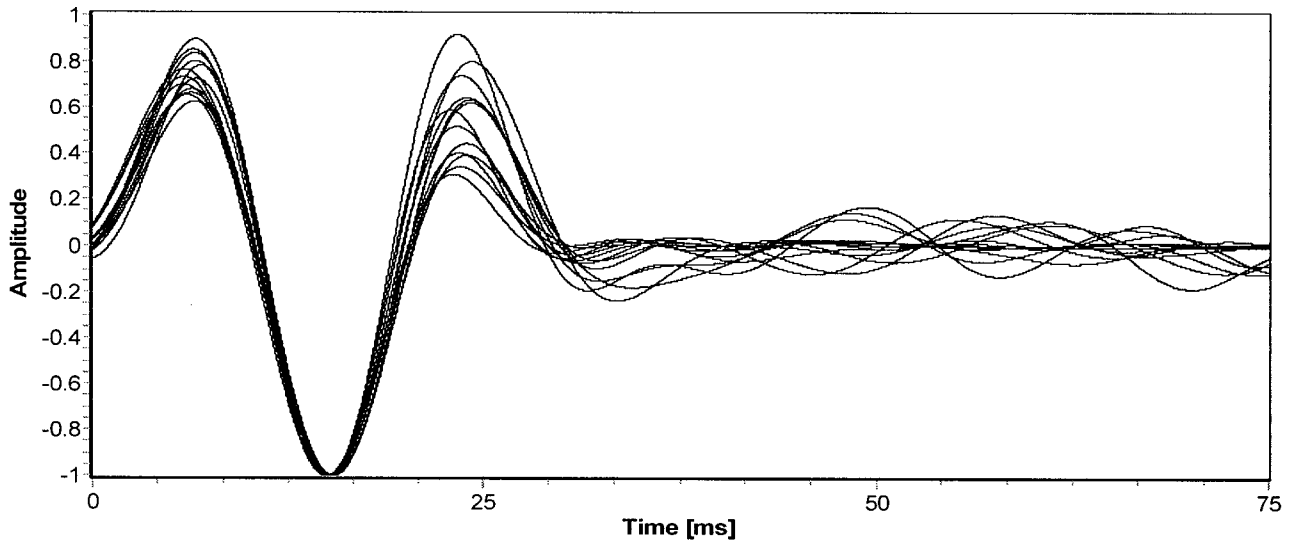


Figure 4.104. Superposition of estimated primary source wavelets for depths 4 m to 17 m.

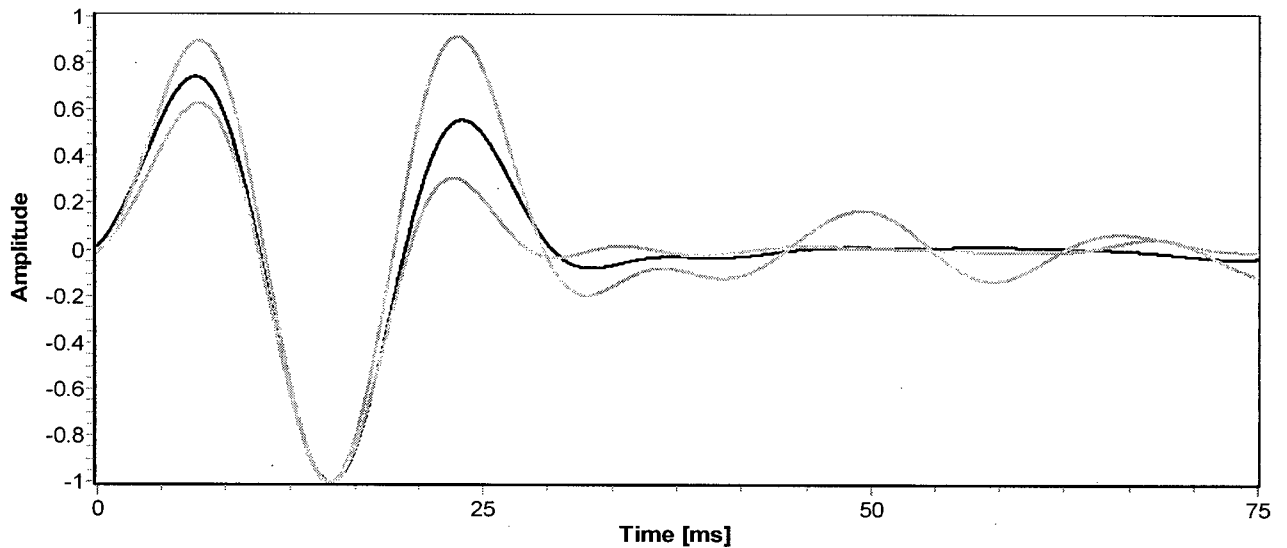


Figure 4.105. Estimated source wavelet (black line) obtained by averaging estimated PPD-WE source wavelets shown in Fig. 4.104. The light grey lines signify the maximum and minimum bounds based upon the response outlined in Fig. 4.104.

Test Site *SC 64* was located approximately 7 m to 9 m to the east of a pond that is 1 m to 2 m deep. The test was conducted 1 m below the bund surrounding the pond which is used as an access road. The bund is constructed of dense material and the SH source for SCPT *SC 64* was positioned approximately 4m from the bank of the bund. Table 4.7 outlines the estimated time offsets for the secondary arriving source wavelet for test site *SC 64*. These values were estimated visually by reviewing the figures in Appendix H which illustrate the estimated PPD-WE source wavelet superimposed upon the residual wavelet.

TABLE 4.7
ESTIMATED SECONDARY ARRIVING SOURCE WAVELET TIME OFFSET FOR SCPT SC 64

<i>Depth (m)</i>	<i>Estimated Offset of Secondary Arriving Source Wavelet (ms)</i>
3.0	22
4.0	25
5.0	25
6.0	26
7.0	28
8.0	28
9.0	28
10.0	28
11.0	27
12.0	29
13.0	27
14.0	31
15.0	30
16.0	30
17.0	29

The estimated time offsets outlined in Table 4.7 are consistent with the physics of a primary source wavelet traveling directly to the SC and a secondary source wavelet reflecting off the bund and then traveling directly to the SC. For example, the estimated arrival time of the primary arriving source wavelet at depth 17 m is 132 ms. This results in an estimated average velocity of 130 m/s (for a radial source offset of 2.3 m). The extra travel distance for the source wavelet to travel to the bund, reflect and then travel to the SC is approximately 3.8 m. This calculation is based upon a SH source bund offset of 4 m, average in-situ velocity of 130 m/s and a 2 m estimated depth of reflection off the bund. The associated

travel time offset for a 3.8 m travel distance is 29 ms (i.e., 3.8 m / 130 m/s) which is identical to the value estimated in Table 4.7.

As previously stated, the PPD-WE is a general purpose algorithm for blind deconvolution that is particularly well suited to wavelet estimation when no assumptions concerning the reflectivity can be made. In addition to the previously outlined ground breaking work of Mendel and his colleagues [42], there have been other researchers who have implemented BRE techniques such as SMC filtering in attempting to carry out blind seismic deconvolution. These techniques rely upon a priori assumptions about the reflection coefficients.

For example, in the work outlined by Cheng et. al. [23] the reflectivity sequence is modeled as a Bernoulli-Gaussian white sequence process. This statistical model was first introduced by Mendel [42]. Rosec and his colleagues [46] describe a blind marine seismic deconvolution technique where the reflectivity sequence is modeled as a Gaussian mixture depending upon three parameters (high and low reflector variances and reflector density), on the wavelet impulse response and on the observation noise variance. It is required to estimate these parameters from the recorded time series before the deconvolution can be carried out. Kaaresen & Taxt [39] give a thorough outline of the many different approaches for carrying out blind seismic deconvolution and their associated advantages and disadvantages. A major component of the outlined techniques is a priori assumptions about the reflection sequence. In the blind seismic deconvolution technique outlined by Kaaresen and Taxt the reflection sequence is again assumed to be a Bernoulli-Gaussian distribution. They also make additional assumptions about the reflectivity sequence such as it tends to be continuous in the horizontal direction and the wavelet is common to several traces.

V. Conclusions

This thesis has focused upon the application of the relatively new signal processing technique referred to as sequential Monte Carlo filtering or, more commonly, particle filtering to seismic problems. Particle filtering is a form of Bayesian recursive estimation, where it is required to solve optimal estimation problems of physical systems that are non-linear and/or non-stationary. In BRE, the posterior density function is estimated, so that the conditional mean estimates of desired parameters or states can be obtained. BRE has been referred to as a complete solution [33] to the estimation problem, since the posterior density function embodies all available statistical information (i.e., prior, likelihood and evidence).

In particle filtering, the required posterior density function is represented by a set of random samples with associated weights where state estimates are computed based on these samples and weights. Section II of this thesis outlined the mathematical background of BRE, where the requirement of modeling the physical problem in a state-space formulation was addressed and the fundamental Chapman-Komolgorov equation was outlined. Additional topics covered included the Kalman filter formulation, jump Markov-linear Gaussian systems, hidden Markov models, particle filtering, and Rao-Blackwellised particle filtering. Section III of this thesis addressed the two important seismic signal processing problems of real-time, non-linear, non-stationary passive seismic event detection and blind seismic deconvolution.

A passive seismic monitoring (PSM) system is designed to acquire and analyze, in real time, the acoustic signals collected by an array of appropriate seismic transducers. Seismic activity is often observed in the vicinity of underground excavations, deep open pits and quarries, around and below large reservoirs where fluids are being injected into, or removed from, permeable subsurface formations and adjacent to the sites of large underground explosions. Section IV(A) outlined a BRE algorithm (PS-SEED), which utilizes a hybrid RBPF and a HMM filter for the purpose of identifying events during passive seismic monitoring. The event- detection algorithm builds upon previous designs, where the major improvements consist of modeling the problem as a JMLGS and the implementation of a

HMM filter for quantifying the phase of the seismic events. Simulation results were presented where source wavelets with additive Gauss-Markov background noise were analyzed and the results evaluated in terms of the improvement in signal-to-noise ratio. There is up to an 80-fold improvement in signal-to-noise ratio after implementation of the PS-SEED algorithm. Although the described filter has been utilized for automating the identification of seismic events during passive seismic investigations, the filter could be applied to many other acoustic-emission problems requiring real-time event detection.

Seismic deconvolution is the most widely utilized signal enhancement technique in seismic signal processing. Ideally, by deconvolving the source wavelet from the recorded time series data, only the reflection coefficients remain. A very challenging problem in seismic deconvolution is blind deconvolution. In this case, both the source wavelet and reflection coefficients are assumed unknown. Section IV(C) of this thesis outlined two novel PF algorithms for solving the BSD problem. In these formulations, the source wavelet is again modeled as an amplitude modulated sinusoid and the deconvolution is carried out by determining the seismogram's principle phase components or by sequentially and chronologically extracting the overlapping source wavelets from the seismogram under analysis. These BSD algorithms are referred to as principle phase decomposition (PPD) and principle phase decomposition – wavelet extraction (PPD-WE), respectively. The PPD and PPD-WE algorithms are similar to that of the PS-SEED algorithm with the added complexity of modeling and reconstructing several overlapping source wavelets. The PPD and PPD-WE algorithms utilize RBPF, JMLGS, and HMM filter formulations in order to separate the overlapping wavelets according to their distinct phase components.

Some of the demonstrated advantages of the PPD and PPD-WE algorithms compared to other techniques are outlined as follows:

- Simple filter formulation with minimal parameter specification.
- Assumption of minimum phase source wavelet is not required.
- Avoids problems associated with band-limited source wavelets as in the case of frequency domain deconvolution. This is due to the fact the PPD algorithm is separating overlapping source wavelets and not estimating high bandwidth reflection coefficients.

- It is not required to incorporate applied frequency filters within the state-space formulation as would be necessary when implementing the KFSD algorithm.
- Easily handles non-stationary source wavelets.
- Provides for time-variant estimations of the source wavelet. This information can then be utilized within non-blind deconvolution techniques.
- The PPD-WE is a general purpose algorithm for blind deconvolution that is particularly well suited to wavelet estimation when no assumptions concerning the reflectivity can be made.
- A whiteness assumption governing the reflection coefficient series is not required.
- In general the PPD-WE algorithm does not like so many BSD techniques require assumptions concerning the character of the reflectivity.

There is much room for future enhancements for both the PS-SEED and PPD algorithms. For example, the PS-SEED algorithm could be updated, so that it not only gives real-time phase estimates but also quantifies the frequency content of the seismic events. A future possible enhancement to the PPD-WE algorithm is to address the limitation that any errors generated during the wavelet extraction process will propagate as the seismogram is sequentially and chronologically processed.

References

- 1) Aldridge, D.F. (1990) The Berlage wavelet. *Geophysics*. 55, No. 11, 1508-1511.
- 2) Allen, R.V. (1978) Automatic Earthquake Recognition and Timing from Single Traces. *Bulletin Seismic Society of America*, 1521-1532.
- 3) Arulampalam, M.S., Maskell, S., Gordon, N.J., & Clapp, T. (2002) A tutorial on particle filters for online nonlinear/non-Gaussian Bayesian tracking. *IEEE Transactions on Signal Processing*, 50, No. 2, 174-188.
- 4) Akashi, A. & Kumamoto, H. (1977). Random sampling approach to state estimation in switching environments. *Automatica*, 13, 429-434.
- 5) Andrus, R.D., Stokoe, K.H., & Chung, R.M. (1999). Draft guidelines for evaluating liquefaction resistance using shear wave velocity measurements and simplified procedures. NISTIR 6277. National Institute of Standards and Technology, Gaithersburg, Md.
- 6) Bayless, J.W. & Brigham, E.D. (1970) Application of the Kalman filter to continuous signal restoration. *Geophysics*, 35, 2-24.
- 7) Baziw, E. & Ulrych, T.J. (2006). Principle Phase Decomposition – A New Concept in Blind Seismic Deconvolution. *IEEE Transactions on Geoscience and Remote Sensing*, 2, No. 4, 418-422.
- 8) Baziw, E. (2005) Real-time seismic signal enhancement utilizing a hybrid Rao-Blackwellised particle filter and hidden Markov model filter. *IEEE Geoscience and Remote Sensing Letter*, 2, No. 4, 418-422.

- 9) Baziw, E. (2004) State-space seismic cone minimum variance deconvolution. *In Proceedings of the 2nd International Conference on Geotechnical Site Characterization (ISC-2):* Vol. 1. (pp. 835-84) Porto, Portugal: Millpress Science Publishers.
- 10) Baziw, E., Nedilko, B., & Weir-Jones, I. (2004) Microseismic event detection Kalman filter: derivation of the noise covariance matrix and automated first break determination for accurate source location estimation. *Pure Applied Geophysics*, 161, 303-329.
- 11) Baziw, E. & Weir-Jones, I. (2002) Application of Kalman filtering techniques for microseismic event detection. *Pure Applied Geophysics*, 159, 449-474.
- 12) Baziw, E. & Ulrych, T.J. (2004) A Rao-Blackwellised type algorithm for passive seismic event detection. *In Proceedings of the 8th Annual Consortium for the Development of Specialized Seismic Techniques Technical Meeting:* Vol. 1. (pp. 135-164) Vancouver, Canada: CDSST Publishing.
- 13) Baziw, E. (2007). Implementation of the Principle Phase Decomposition Algorithm. To appear in the 2007 June issue of *IEEE Transactions on Geoscience and Remote Sensing*.
- 14) Baziw, E. (1993). Digital filtering techniques for interpreting seismic cone data. *Journal of Geotechnical Engineering, ASCE*, 119(6), 98-1018.
- 15) Baziw, E., Campanella, R.G., & Sully, J.P. (1989). Interpretation of Seismic Cone Data Using Digital Filtering Techniques. *In Proceedings of the 12th International Conference on Soil Mechanics and Foundation Engineering*, Rio de Janeiro, 13-18 Aug. A.A. Balkema, Rotterdam.
- 16) Baziw, E. (2002). Derivation of Seismic Cone Interval Velocities Utilizing Forward Modeling and the Downhill Simplex Method. *Can. Geotech. J.* 39, 1-12.

- 17) Baziw, E. (2004). Two and three dimensional imaging utilizing the seismic cone penetrometer. *In Proceedings of the 2nd International Conference on Geotechnical Site Characterization (ISC-2)*, Porto, Portugal, 19-22 Sept. Millpress Science Publishers, pp. 1611-1618.
- 18) Baziw, E., Tichy, J., & de Caprona, G (2000). Data Acquisition in Seismic Cone Penetration Testing. *In Proceedings of the 3rd International Symposium on Integrated Technical Approaches to Site Characterization (ITASCE)*, Argonne, IL, 11-14 Sept. 2000. Argonne National Laboratory. pp. 69-72.
- 19) Box, G.E., Jenkins, G.M., & Reinsel, G.C. (1994) *Time series analysis: forecasting and control (3rd ed.)*. New Jersey: Prentice-Hall.
- 20) Campanella, R.G., Robertson, F.T.C., & Gillespie, D. (1986). Seismic cone penetration test. *In Proceedings of INSITU86. American Society of Civil Engineers (ASCE) Geotechnical Special Publication. No. 6*, pp. 116–130.
- 21) Casella, G, & Robert, C.P. (1996). Rao-Blackwellisation of sampling schemes. *Biometrika*, 83, No. 1, 81–94.
- 22) Crump, M.D. (1974) A Kalman filter approach to the deconvolution of seismic signals. *Geophysics*, 39, 1-14.
- 23) Cheng, Q., Rong C. & Li T.(1996). Simultaneous Wavelet Estimation and Deconvolution of Reflection Seismic Signals. *IEEE Transactions on Geoscience and Remote Sensing Letter*, 34, No. 4, 377-384.

- 24) de Freitas, N. (2002) Rao-Blackwellised particle filtering for fault diagnosis. *In the 2002 Proceedings of the IEEE Aerospace Conference: Vol. 4.* (pp. 1767-1772) Big Sky Montana, USA: IEEE Publishers.
- 25) Del Moral, P. (1998) Measure valued processes and interacting particle systems. Application to nonlinear filtering problems. *Ann. Appl. Probab.*, vol. 8, no. 2, 438–495.
- 26) Doucet, A., Godsill, S., & C Andrieu, C. (2000). On sequential Monte Carlo sampling methods for Bayesian filtering. *Statistics and Computing*, 10, No. 3, 197–208.
- 27) Doucet, A., de Freitas, N., & Gordon, N. (2001) editors. *Sequential Monte Carlo Methods in Practice*. Springer Verlag, 2001.
- 28) Doucet, A., Gordon, N.J., & Krishnamurthy, V. (2001) Particle filters for state estimation of jump Markov linear systems. *IEEE Transactions on Signal Processing*, 49, No. 3, 613-624.
- 29) Doucet, A., & Andrieu, C. (2001) Iterative algorithms for state estimation of jump Markov linear systems. *IEEE Transactions on Signal Processing*, 49, No. 6, 1216-1227.
- 30) Finn, W.D.L. (1984). *Dynamic response analysis of soils in engineering practice*. In *Mechanics of engineering materials*. John Wiley & Sons Ltd., New York. Chapter 13.
- 31) Frieden, B.R. (1983) *Probability, Statistical Optics, and Data Testing (1st ed)*. Berlin, Germany: Springer-Verlag Press.
- 32) Ge, M., & Kaiser, P.K. (1992) Interpretation of physical status of arrival picks for microseismic source location, *Bulletin Seismic Society of America*, 80, 1643-1660.
- 33) Gelb, A. (1974) *Applied Optimal Estimation (4th ed.)*. Cambridge, Mass: MIT Press.

- 34) Gibowicz, S.J. & Kijko, A. (1994) *An Introduction to Mining Seismology*, San Diego, CA: Academic Press.
- 35) Gustafsson, F., Gunnarsson, F., Bergman, N., Forssell, U., Jansson, J., Karlsson, R., & Nordlund, P. (2002) Particle filters for positioning, navigation, and tracking, *IEEE Transactions on Signal Processing*, 50, 425- 435.
- 36) Howie, J.A. & Amini, A. (2005). Numerical Simulation of Seismic Cone Signals. *Canadian Geotechnical Journal*. V. 42, No. 2, 574-586.
- 37) Hsueh, A.C. & Mendel, J.M. (1985) Minimum-variance and maximum-likelihood deconvolution for noncausal channel models. *IEEE Transactions On Geoscience and Remote Sensing*, 23, No. 6. 797-808.
- 38) Kanasewich, E.R. (1981) *Time Sequence Analysis* (3rd ed.) Edmonton, Alberta (Canada): University of Alberta Press.
- 39) Kaaresen, K.F. & Taxt, T. (1998). Multichannel Blind Deconvolution of Seismic Signals. *Geophysics*, 63, No. 6, 2093-2107.
- 40) Liu, J.S. & Chen, R. Blind (1995) Deconvolution via sequential imputations. *Journal of the American Statistical Association*, 90, No. 430, 567-576.
- 41) Mendel, J.M. (1995) *Lessons in Estimation Theory for Signal Processing, Communications, and Control*. Englewood Cliffs, N.J: Prentice Hall.
- 42) Mendel, J.M. (1983) *Optimal Seismic Deconvolution an Estimation-Based Approach*. New York, NY: Academic Press.

- 43) Mühlich, M. (2003, March). Particle filters: a tutorial. *Bucuresti Filter-Workshop, Institut für Angewandte Physik, J.W. Goethe-Universität Frankfurt* [online]. From www.uni-frankfurt.de/~muehlich/sci/TalkBucurestiMar2004.pdf
- 44) Ogata, J. (1987) *Discrete Process Control* (1st ed.) New Jersey: Prentice-Hall.
- 45) Papoulis, A. (1965) *Probability, Random Variables, and Stochastic Process* (1st ed.) New York, NY: McGraw-Hill.
- 46) Rosec O., Boucher J., Nsiri B. & Chonavel T. (2003). Blind Seismic Deconvolution Using Statistical MCMC Methods. *IEEE Journal of Oceanic Engineering*, 2, No. 4, 418-422.
- 47) Sheriff, R.E. & Geldart, L.P. (1982) *Exploration Seismology*, Vol. 1, (2nd ed.) Cambridge, UK: Cambridge University Press.
- 48) Sheriff, R.E. & Geldart, L.P. (1983) *Exploration Seismology*. Vol. 2. (2nd ed.) Cambridge, UK: Cambridge University Press.
- 49) Talebi, S. & Boone, T.J. (1998) Source parameters of injection-induced microseismicity. *Pure Applied Geophysics*, 153, 113-130.
- 50) Talebi, S., Ge, M., Rochon, P. & Mottahed, P. (1994) Analysis of induced seismicity in a hard-rock mine in the Sudbury basin. *In Proceedings of the first North American Rock Mechanics Symposium (NARMS): Vol. 1* (pp. 937-944) University of Texas at Austin, Rotterdam: Balkema Publishers.
- 51) Ulrych, T.J., and Sacchi, M.D. (2005) *Information-Based Inversion and Processing with Applications* (1st ed.) , Amsterdam, The Netherlands: Elsevier B.V.

Appendix

A. Derivation of Chapman-Kolmogorov Equation

The Chapman-Kolmogorov equation is derived based upon the transitional densities of a Markov sequence and the proof of (8) is outlined as follows [45]:

Proof

For any three random variables (r.v.) x_1, x_2, x_3 , we have the following:

$$p(x_1 | x_3) = \int_{-\infty}^{\infty} p(x_1 | x_2, x_3) p(x_2 | x_3) dx_2 \quad (\text{A1})$$

for a Markov sequence of order one we have the following:

$$p(x_1 | x_2, x_3) = p(x_1 | x_2) \quad (\text{A2})$$

Substituting $x_1 = x_k$, $x_2 = x_{k-1}$, and $x_3 = z_{1:k-1}$ into (A2) and then substituting this result in (A1) gives the (8).

B. Derivation of the BRE Update Equation

The derivation of (9) is outlined as follows:

Derivation

$$p(\mathbf{x}_k | z_{1:k}) = \frac{p(z_{1:k} | \mathbf{x}_k) p(\mathbf{x}_k)}{p(z_{1:k})} \quad (\text{A3})$$

Equation (A3) is from Bayes' rule. Separating the pdf $p(z_{1:k})$ into $p(z_k, z_{1:k-1})$ and utilizing

factorized joint probability² results in the following:

$$p(\mathbf{x}_k | \mathbf{z}_{1:k}) = \frac{p(\mathbf{z}_k, \mathbf{z}_{1:k-1} | \mathbf{x}_k) p(\mathbf{x}_k)}{p(\mathbf{z}_k, \mathbf{z}_{1:k-1})} = \frac{p(\mathbf{z}_k | \mathbf{z}_{1:k-1}, \mathbf{x}_k) p(\mathbf{z}_{1:k-1} | \mathbf{x}_k) p(\mathbf{x}_k)}{p(\mathbf{z}_k | \mathbf{z}_{1:k-1}) p(\mathbf{z}_{1:k-1})} \quad (\text{A4})$$

From Bayes' rule (A4) becomes as follows:

$$p(\mathbf{x}_k | \mathbf{z}_{1:k}) = \frac{p(\mathbf{z}_k | \mathbf{z}_{1:k-1}, \mathbf{x}_k) p(\mathbf{x}_k | \mathbf{z}_{1:k-1}) p(\mathbf{z}_{1:k-1}) p(\mathbf{x}_k)}{p(\mathbf{z}_k | \mathbf{z}_{1:k-1}) p(\mathbf{z}_{1:k-1}) p(\mathbf{x}_k)} \quad (\text{A5})$$

Canceling out terms in (A5) and using the assumption that we have independent measurements (white measurement noise)³ results in the update equation (9).

C. Derivation of the Recursive Weights Update Equation

The derivation of (30) is outlined as follows:

Derivation

From (28), we have the following:

$$\mathbf{w}_k^i = \frac{p^*(\mathbf{x}_{0:k}^i | \mathbf{z}_{1:k}^i)}{\sum_{i=1}^{N_s} \frac{p^*(\mathbf{x}_{0:k}^i | \mathbf{z}_{1:k}^i)}{q(\mathbf{x}_{0:k}^i | \mathbf{z}_{1:k}^i)}} = \frac{\tilde{\mathbf{w}}_k^i}{\sum_{i=1}^{N_s} \tilde{\mathbf{w}}_k^i}, \quad \text{where } \tilde{\mathbf{w}}_k^i = \frac{p^*(\mathbf{x}_{0:k}^i | \mathbf{z}_{1:k}^i)}{q(\mathbf{x}_{0:k}^i | \mathbf{z}_{1:k}^i)} \quad (\text{A6})$$

² $p(a,b|c) = p(a|b,c) \cdot p(b|c)$ and $p(a,b) = p(a|b) \cdot p(b)$

³ $p(\mathbf{z}_k | \mathbf{z}_{1:k-1}, \mathbf{x}_k) = p(\mathbf{z}_k | \mathbf{x}_k)$

Note:

$$\tilde{w}_k^i = \frac{p^*(\mathbf{x}_{0:k}^i | \mathbf{z}_{1:k}^i)}{q(\mathbf{x}_{0:k}^i | \mathbf{z}_{1:k}^i)} \propto \frac{p(\mathbf{x}_{0:k}^i | \mathbf{z}_{1:k}^i)}{q(\mathbf{x}_{0:k}^i | \mathbf{z}_{1:k}^i)} \quad (\text{A7})$$

If the importance density function is chosen to factorized such that:

$$q(\mathbf{x}_{0:k}^i | \mathbf{z}_{1:k}^i) = q(\mathbf{x}_k^i | \mathbf{x}_{0:k-1}^i, \mathbf{z}_{1:k}^i) q(\mathbf{x}_{0:k-1}^i | \mathbf{z}_{1:k}^i) \quad (\text{A8})$$

then one can augment old particles $\mathbf{x}_{0:k-1}^i$ by $\mathbf{x}_k^i \sim q(\mathbf{x}_k^i | \mathbf{x}_{0:k-1}^i, \mathbf{z}_{1:k}^i)$ to get new particles $\mathbf{x}_{0:k}^i$.

From (A5) we have the following:

$$p(\mathbf{x}_{0:k} | \mathbf{z}_{1:k}) = \frac{p(\mathbf{z}_k | \mathbf{z}_{1:k-1}, \mathbf{x}_{0:k}) p(\mathbf{x}_{0:k} | \mathbf{z}_{1:k-1}) p(\mathbf{z}_{1:k-1}) p(\mathbf{x}_{0:k})}{p(\mathbf{z}_k | \mathbf{z}_{1:k-1}) p(\mathbf{z}_{1:k-1}) p(\mathbf{x}_{0:k})} \quad (\text{A9})$$

Canceling out terms in and using the assumption that we have independent measurements results in the following:

$$p(\mathbf{x}_{0:k} | \mathbf{z}_{1:k}) = \frac{p(\mathbf{z}_k | \mathbf{x}_k, \mathbf{x}_{0:k-1}) p(\mathbf{x}_k, \mathbf{x}_{0:k-1} | \mathbf{z}_{1:k-1})}{p(\mathbf{z}_k | \mathbf{z}_{1:k-1})} \quad (\text{A10})$$

Utilizing factorized joint probability on (A10) gives the following:

$$p(\mathbf{x}_{0:k} | \mathbf{z}_{1:k}) = \frac{p(\mathbf{z}_k | \mathbf{x}_k, \mathbf{x}_{0:k-1}) p(\mathbf{x}_k | \mathbf{x}_{0:k-1}, \mathbf{z}_{1:k-1}) p(\mathbf{x}_{0:k-1} | \mathbf{z}_{1:k-1})}{p(\mathbf{z}_k | \mathbf{z}_{1:k-1})} \quad (\text{A11})$$

Using the fact that we have a first order Markov process results in the following:

$$p(\mathbf{x}_{0:k} | \mathbf{z}_{1:k}) = \frac{p(\mathbf{z}_k | \mathbf{x}_k)p(\mathbf{x}_k | \mathbf{x}_{k-1})}{p(\mathbf{z}_k | \mathbf{z}_{1:k-1})} p(\mathbf{x}_{0:k-1} | \mathbf{z}_{1:k-1}) \quad (\text{A12})$$

or

$$p(\mathbf{x}_{0:k} | \mathbf{z}_{1:k}) \propto p(\mathbf{z}_k | \mathbf{x}_k)p(\mathbf{x}_k | \mathbf{x}_{k-1})p(\mathbf{x}_{0:k-1} | \mathbf{z}_{1:k-1}) \quad (\text{A13})$$

Substituting (A13) and (A8) into (A7) gives the following:

$$\tilde{\mathbf{w}}_k^i = \tilde{\mathbf{w}}_{k-1}^i \frac{p(\mathbf{z}_k | \mathbf{x}_k^i)p(\mathbf{x}_k^i | \mathbf{x}_{k-1}^i)}{q(\mathbf{x}_k^i | \mathbf{x}_{0:k-1}^i, \mathbf{z}_{1:k-1}^i)} \quad (\text{A14})$$

Equation (A14) becomes (30) if it is assumed that $q(\mathbf{x}_k^i | \mathbf{x}_{0:k-1}^i, \mathbf{z}_{1:k}^i) = q(\mathbf{x}_k^i | \mathbf{x}_{k-1}^i, \mathbf{z}_k^i)$ (only dependent on last state and measurement).

D. Derivation of the ‘‘Likelihood’’ Formula

Derivation

Consider the stochastic processes $s(t)$ and $n(t)$ with the arbitrary probability laws $p_S(s)$ and $p_N(n)$ at t . Let $s(t)$ define the signal and $n(t)$ define a white noise process. Let $d(t)$ also be defined as a stochastic process which is the addition of $s(t)$ and $n(t)$

$$d(t) = s(t) + n(t) \quad (\text{A15})$$

The joint probability density of $d(t)$ and $s(t)$ is defined as follows:

$$p_{ds}(d, s) = p(d | s)p_s(s) \quad (\text{A16})$$

From the form of (A16) it is evident that if s is fixed, the fluctuations in d will follow those in n . This is stated probabilistically as follows:

$$p(d | s) = p(n | s) \quad (\text{A17})$$

Since the noise is white and independent of s we have the following [31]:

$$p(d | s) = p(n | s) = p_n(n) = p_n(d - s) \quad (\text{A18})$$

E. PS-SEED FSMCD and HMM Filter Implementation

As outlined in Table 4.1, the first step of the PS-SEED algorithm is to initialize a bank of KFs equal in number (N_S) to the particles pre-specified. The PS-SEED algorithm utilizes a FSMCD (within the JMGLS formulation) to sequentially update the set of KFs for each time increment as was outlined in Table 3.1. The two states of the FSMCD $y_k^i \sim P(y_k^i | y_{k-1}^j)$ are event ($p(y_k^1)$) and no-event ($p(y_k^2)$). A Markov chain is uniquely defined by the initial distribution and the transitional probabilities at time $k = 0$. For the simulations presented in Section IV.A.1.c, the initial distribution for the no-event and event states was set to $p(y_0^1) = 0.9$ and $p(y_0^2) = 0.1$, respectively. The initial transitional probabilities were specified as $p(y_k^1 | y_{k-1}^1) = 0.8$, $p(y_k^1 | y_{k-1}^2) = 0.8$, $p(y_k^2 | y_{k-1}^2) = 0.2$, and $p(y_k^2 | y_{k-1}^1) = 0.2$. In general terms, the probability of a source wavelet being present (“event”) at time index k is 20%, the transitional probability from moving from the event to no-event state is 80%, and the transitional probability from moving from the no-event to event state is 20%. The PS-SEED algorithm behaves robustly to the specification of the initial FSMCD probabilities as long as a sufficient number of particles are implemented. At each time increment k the FSMCD is updated according to the following equation:

$$\begin{bmatrix} p(y_k^1) \\ p(y_k^2) \end{bmatrix} = \begin{bmatrix} y_k^1 | y_{k-1}^1 & y_k^1 | y_{k-1}^2 \\ y_k^2 | y_{k-1}^1 & y_k^2 | y_{k-1}^2 \end{bmatrix} \begin{bmatrix} p(y_{k-1}^1) \\ p(y_{k-1}^2) \end{bmatrix} \quad (\text{A19})$$

In addition to updating the pdf of the FSMCD at each time increment k , a Monte Carlo technique is utilized to obtain realizations of the FSMCD equal to the number of event/no-event particles (N_S). In this step, a random number generator is utilized to obtain N_S samples of the uniform distribution $U^i[0,1]_k$ ($i = 1$ to N'_S). If $U^i[0,1]_k < p(y_k^1)$ then an

event has occurred otherwise no-event is present. In terms of the JMGLS, the system equation does not change but the measurement equation is updated based upon the event /no-event condition. For the no-event condition the measurement equation is equal to the background noise (e.g., $z_k^1 = x1_k + v_k$) as outlined in Step 1, Case 1 of Table 4.1. For the event condition, the measurement equation given as the addition of the background noise and source wavelet (e.g., $z_k^2 = x1_k + x2_k \sin(\omega k\Delta + \varphi_k) + v_k$) as outlined in Step 1, Case 2 of Table 4.1. is defined by the overlapping source wavelet combination (e.g., (22) for the case of three overlapping source wavelets). Based upon the output of the bank of KFs, the PS-SEED algorithm utilizes a RBPF to obtain asymptotically optimal estimate of the modulating amplitude term of the AMS source wavelet defined by the state vector (Steps 6 and 7 of Table 4.1).

From the output of the RBPF filter, a HMM filter is utilized to refine the initially specified phase component of the sinusoid within the user specified phase resolution window (Step 9 of Table 4.1). Once the PS-SEED algorithm obtains an optimal phase estimate at time index k , (18)-(20) of Table 3.1 are utilized to update the bank of KFs. The time index k is then incremented and the PS-SEED algorithm iterates to Step 4 of Table 4.1.

F. PPD FSMCD and HMM Filter Implementation

As outlined in Table 4.3, the first step of the PPD algorithm is to initialize a bank of KFs equal in number (N_S) to that defined by (65). The PPD algorithm utilizes a FSMCD (within the JMGLS formulation) to sequentially update the set of KFs for each time increment as was outlined in Table 3.1. The two states of the FSMCD $y_k^i \sim P(y_k^i | y_{k-1}^j)$ are event ($p(y_k^1)$) and no-event ($p(y_k^2)$). A Markov chain is uniquely defined by the initial distribution and the transitional probabilities at time $k = 0$. For the simulations presented in Section IV.B.2.e, the initial distribution for the event and no-event states was set to $p(y_0^1) = 0.4$ and $p(y_0^2) = 0.6$, respectively. The initial transitional probabilities were specified as $p(y_k^1 | y_{k-1}^1) = 0.4$, $p(y_k^1 | y_{k-1}^2) = 0.4$, $p(y_k^2 | y_{k-1}^1) = 0.6$, and $p(y_k^2 | y_{k-1}^2) = 0.6$. In general terms, the probability of an overlapping source wavelet being present (“event”) at time index k is 40%, the transitional probability from moving from the event to no-event state is 60%, and the transitional probability from moving from the no-event to event state is 40%. The PPD algorithm behaves robustly to the specification of the initial FSMCD probabilities as long as a sufficient number of particles are implemented. At each time increment k the FSMCD is updated according to (A19).

In addition to updating the pdf of the FSMCD at each time increment k , a Monte Carlo technique is utilized to obtain realizations of the FSMCD equal to the number of event/no-event particles (N'_S). In this step, a random number generator is utilized to obtain N'_S samples of the uniform distribution $U^i[0,1]_k$ ($i = 1$ to N'_S). If $U^i[0,1]_k < p(y_k^1)$ then an event has occurred otherwise no-event is present.

For the event condition the number of KFs sequentially updated is equal to the calculated number of combinations defined by (64). In terms of the JMGLS, the system equation (26) does not change but the measurement equation is updated based upon the event /no-event condition. For the no-event condition the measurement equation is equal to the

background noise ($z_k = x4_k$). For the event condition, the measurement equation is defined by the overlapping source wavelet combination (e.g., (63) for the case of three overlapping source wavelets). Based upon the output of the bank of KFs, the PPD algorithm utilizes a RBPF to obtain asymptotically optimal estimates of the modulating amplitude terms of the AMS source wavelets defined by the state vector (Steps 6 and 7 of Table 4.3). From the output of the RBPF filter, HMM filters are utilized to refine the initially specified phase components of the sinusoids within the user specified phase resolution window (Step 9 of Table 4.3). As previously stated, a HMM filter is implemented for each AMS source wavelet. For the simulations presented in Section IV.B.2.e, the initialization of the pdf of the AMS source wavelet phases was set to the uniform distribution, while the fixed-grid transitional pdf $p(\varphi_k^i | \varphi_{k-1}^i)$ was set quite high (e.g., 0.996) and the remaining values were set to have a uniform distribution. This is due to the fact that it is expected the AMS source wavelets have a constant phase value with the HMM filters utilized to obtain optimal phase estimates within the respective phase resolution windows. For the simulations presented in Section IV.B.2.e, each HMM filter formulation had 6 (N_p) phases specified for each phase resolution window to reflect the possible phase shifts of $\pm 3^\circ$ in 1° increments. Once the PPD obtains optimal phase estimates at time index k , (18)-(20) of Table 3.1 are utilized to update the bank of KFs. The time index k is then incremented and the PPD algorithm iterates to Step 4 of Table 4.1.

G. Implementation of the Three State FSMCD within the PPD-WE Algorithm

The three states of the PPD-WE FSMCD $y_k^i \sim P(y_k^i | y_{k-1}^j)$ are measurement noise present at time index k ($p(y_k^1)$), the source wavelet understudy plus measurement noise present at time index k ($p(y_k^2)$) and the source wavelet understudy is overlapped with other time series data plus measurement noise at time index k ($p(y_k^3)$). As previously stated, a Markov chain is uniquely defined by the initial distribution and the transitional probabilities at time $k = 0$. For the simulations presented in Section IVB.2.f, the initial distribution for the three state FSMCD was set to $p(y_0^1) = 0.5$, $p(y_0^2) = 0.4$, and $p(y_0^3) = 0.1$, respectively. This initial distribution is based upon the fact that at the start of the time series under analysis only measurement noise or the source wavelet understudy will be present (ability to window in on initial seismic wavelet recordings). The initial transitional probabilities were specified as

$$\begin{bmatrix} y_1^1 | y_0^1 & y_1^1 | y_0^2 & y_1^1 | y_0^3 \\ y_1^2 | y_0^1 & y_1^2 | y_0^2 & y_1^2 | y_0^3 \\ y_1^3 | y_0^1 & y_1^3 | y_0^2 & y_1^3 | y_0^3 \end{bmatrix} = \begin{bmatrix} 0.1429 & 0.0357 & 0.0909 \\ 0.5714 & 0.3214 & 0.0909 \\ 0.2857 & 0.6429 & 0.8182 \end{bmatrix} \quad (\text{A20})$$

These initial transitional probabilities were defined based upon the fact that the majority of the time series data under analysis would reflect the case where the source wavelet understudy is overlapped with other time series data plus measurement noise at time index k . It should also be noted that it is required that the columns of (A20) add up to 1.0 according to the law of total probability.

At each time increment k the pdf of the three state FSMCD is updated according to the following equation:

$$\begin{bmatrix} p(y_k^1) \\ p(y_k^2) \\ p(y_k^3) \end{bmatrix} = \begin{bmatrix} y_k^1 | y_{k-1}^1 & y_k^1 | y_{k-1}^2 & y_k^1 | y_{k-1}^3 \\ y_k^2 | y_{k-1}^1 & y_k^2 | y_{k-1}^2 & y_k^2 | y_{k-1}^3 \\ y_k^3 | y_{k-1}^1 & y_k^3 | y_{k-1}^2 & y_k^3 | y_{k-1}^3 \end{bmatrix} \begin{bmatrix} p(y_{k-1}^1) \\ p(y_{k-1}^2) \\ p(y_{k-1}^3) \end{bmatrix} \quad (\text{A21})$$

The calculated probabilities $p(y_k^i)$ of (A21) are sorted from lowest to highest. The Inverse Transform Method is then utilized to obtain realizations of the three state FSMCD equal to the number of particles, N_S , specified by the investigator. In this step, a random number generator is utilized to obtain N_S samples of the uniform distribution $U^i[0,1]_k$ ($i = 1$ to N_S). The realizations of the three state FSMCD are then calculated as follows:

$$y_k^i = \begin{cases} y_k^1 & \text{if } U^i[0,1]_k < p(y_k^1) \\ y_k^2 & \text{if } p(y_k^1) \leq U^i[0,1]_k < p(y_k^1) + p(y_k^2) \\ y_k^3 & \text{otherwise} \end{cases} \quad (\text{A22})$$

The realizations outlined in (A22) are based upon the assumption that $p(y_k^1) < p(y_k^2) < p(y_k^3)$. In terms of the JMGLS, the system equation (67) does not change but the measurement equation is updated based upon the estimated value of y_k^i . For the case $y_k^i = y_k^1$ the measurement equation is set equal to the background noise ($z_k = x5_k$). For the case $y_k^i = y_k^2$ the measurement equation is set as

$$z_k = x1_k \sin(\omega k \Delta + \phi 1_k) + x5_k \quad (\text{A23})$$

For the case $y_k^i = y_k^3$ the measurement equation is set to (68) and states $x1_k$ and $x3_k$ are jittered (i.e., add on $U[-1.5,+1.5]$) to facilitate a diversity of particles and minimize sample impoverishment [35].

H. PPD-WE Estimated Source and Residual Wavelets for SCPT Test Hole SC 64.

1) Estimated Source Wavelet at 3m

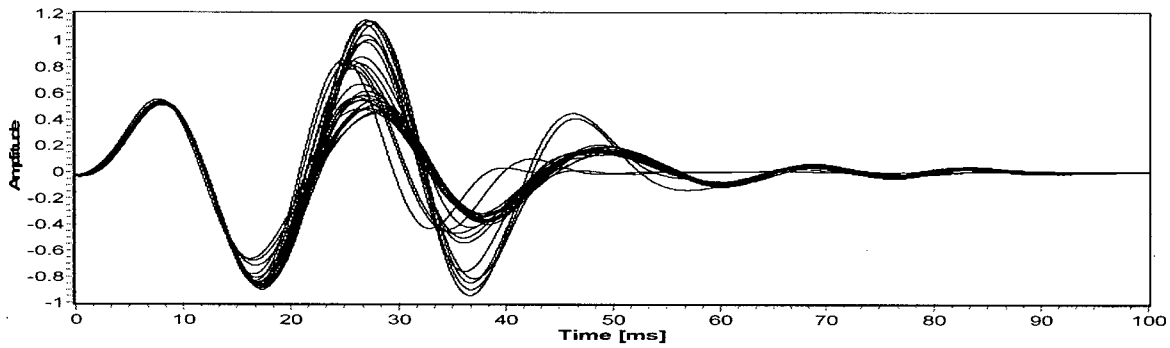


Figure H.1. Thirty five PPD-WE primary source wavelet estimations at depth of 3.0 m.

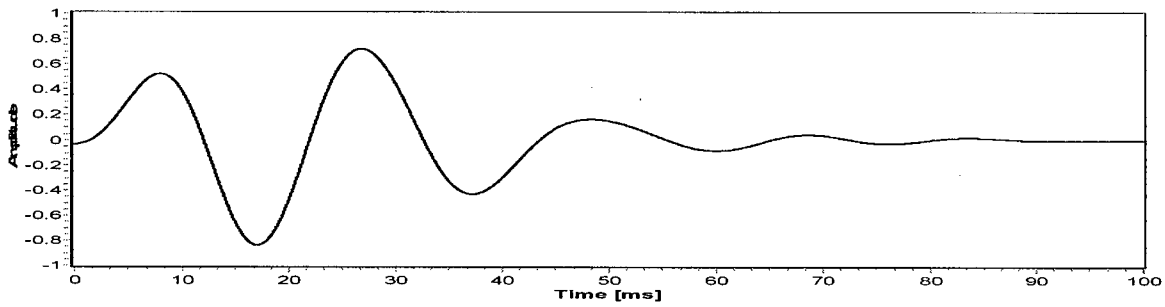


Figure H.2. The Averaged Estimated First Arriving Source Wavelet at 3.0m.

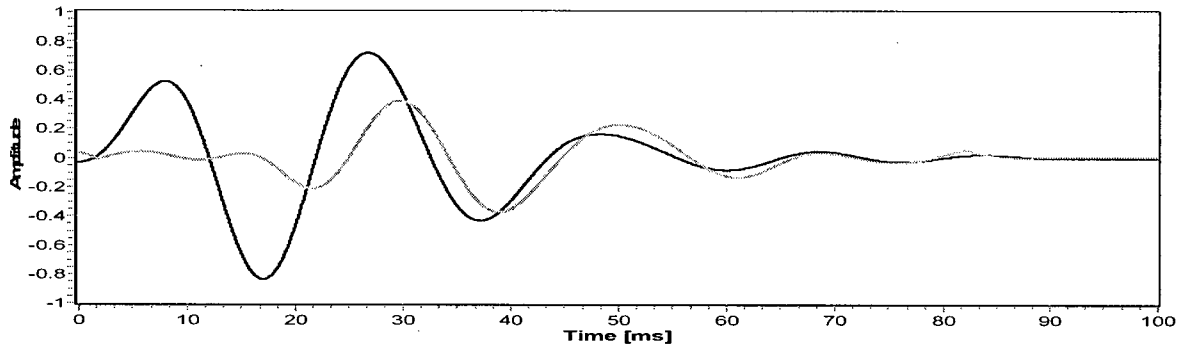


Figure H.3. The estimated first arriving source wavelet superimposed upon residual wavelet at 3.0 m.

2) Estimated Source Wavelet at 4m

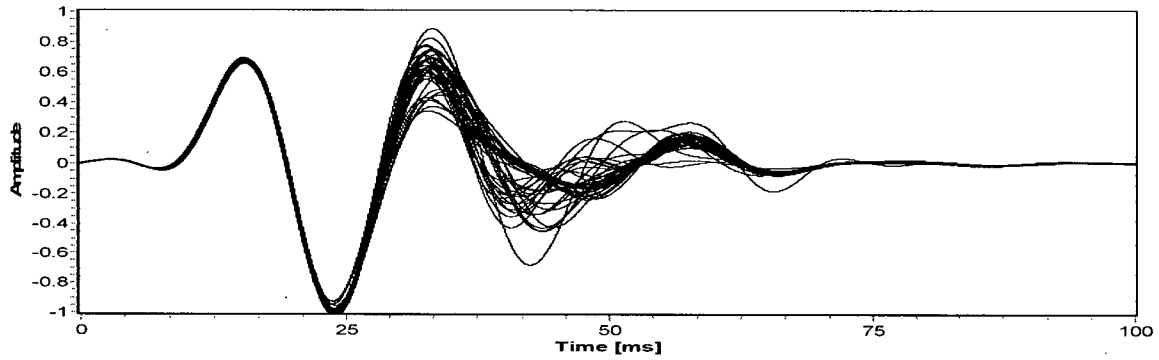


Figure H.4. Thirty five PPD-WE primary source wavelet estimations at depth of 4.0 m.

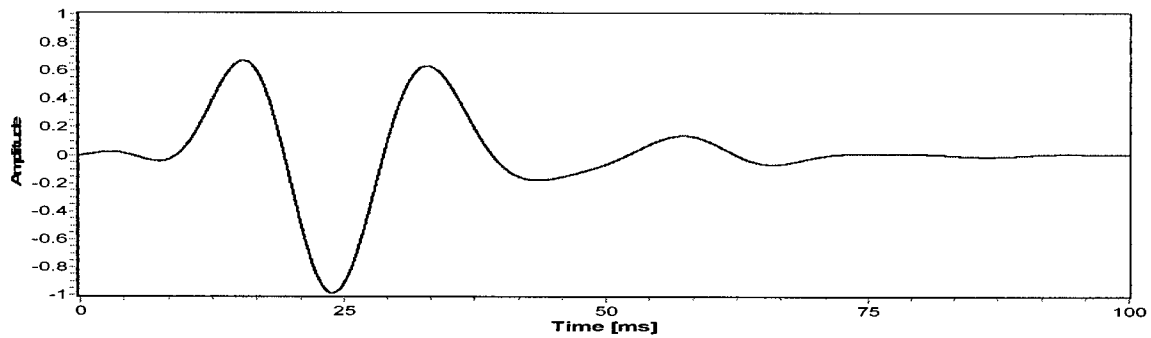


Figure H.5. The Averaged Estimated First Arriving Source Wavelet at 4.0m.

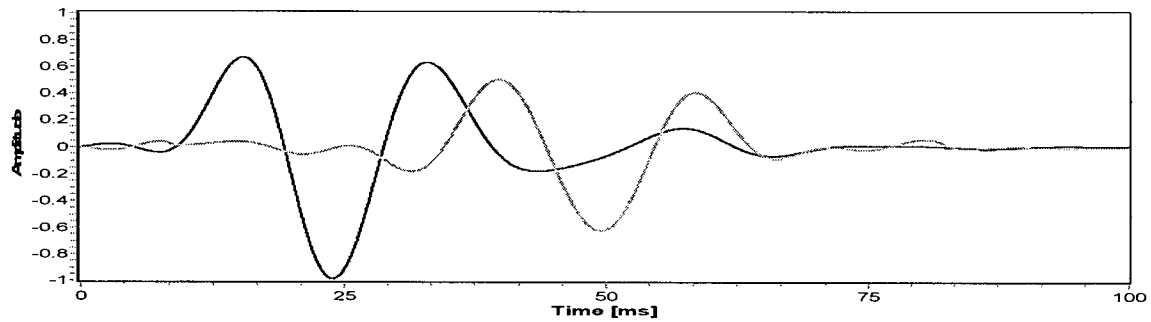


Figure H.6. The estimated first arriving source wavelet superimposed upon residual wavelet. One can have high confidence in the results due to the fact that the Primary and Secondary source wavelets are very similar in form.

3) Estimated Source Wavelet at 5m

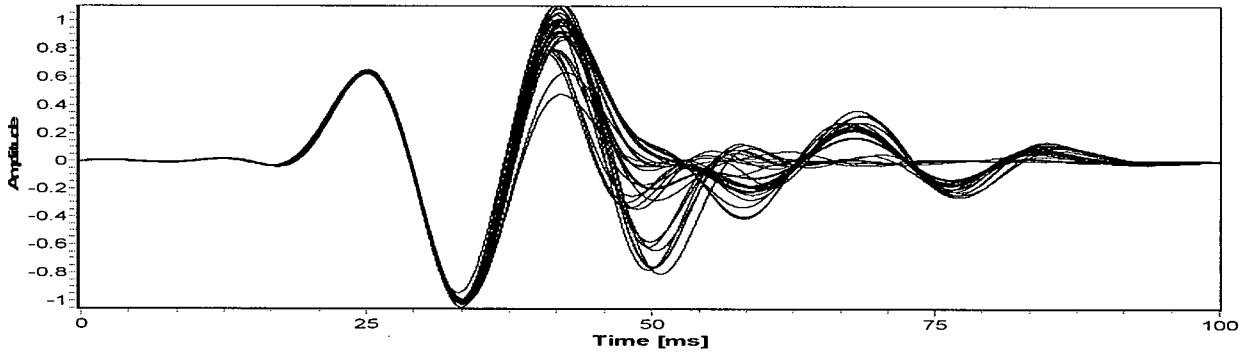


Figure H.7. Thirty five PPD-WE primary source wavelet estimations at depth of 5.0 m.

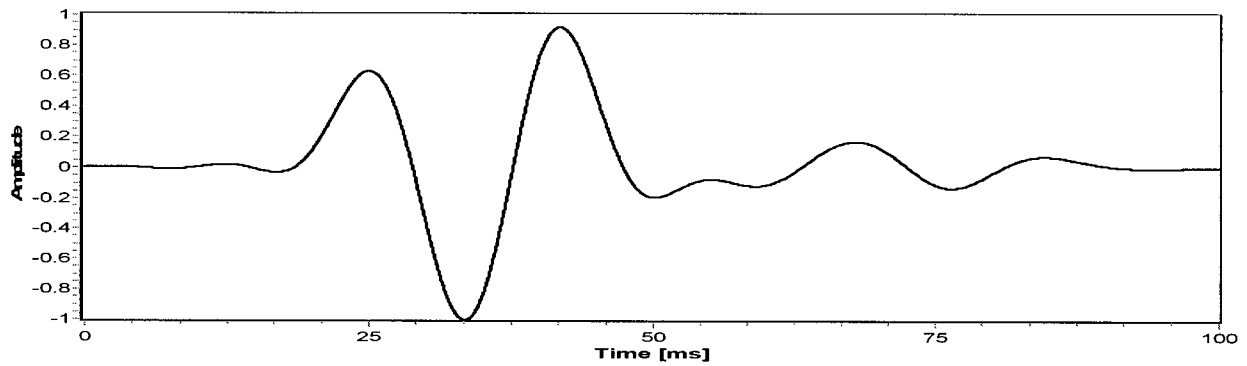


Figure H.8. The Averaged Estimated First Arriving Source Wavelet at 5.0m.

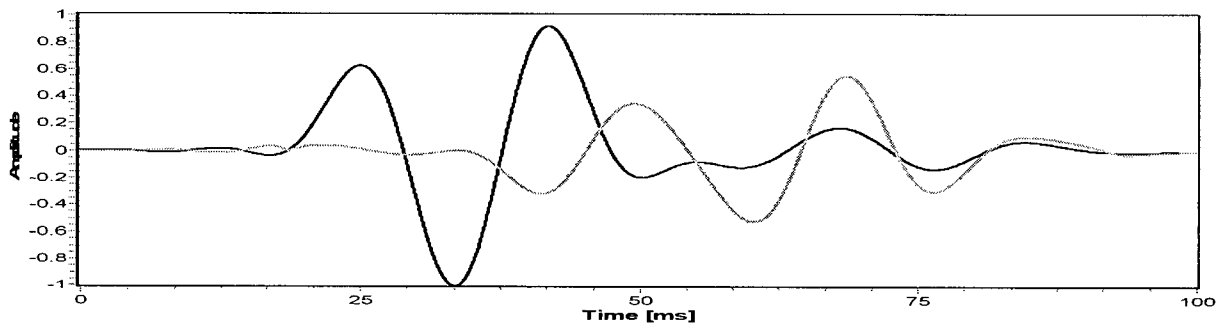


Figure H.9. The estimated first arriving source wavelet superimposed upon residual wavelet at 5.0 m.

4) Estimated Source Wavelet at 6m

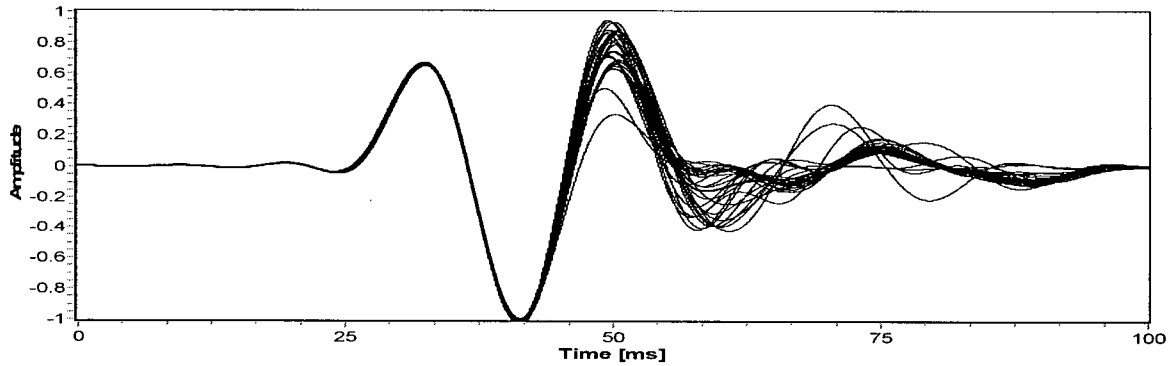


Figure H.10. Thirty five PPD-WE primary source wavelet estimations at depth of 6.0 m.

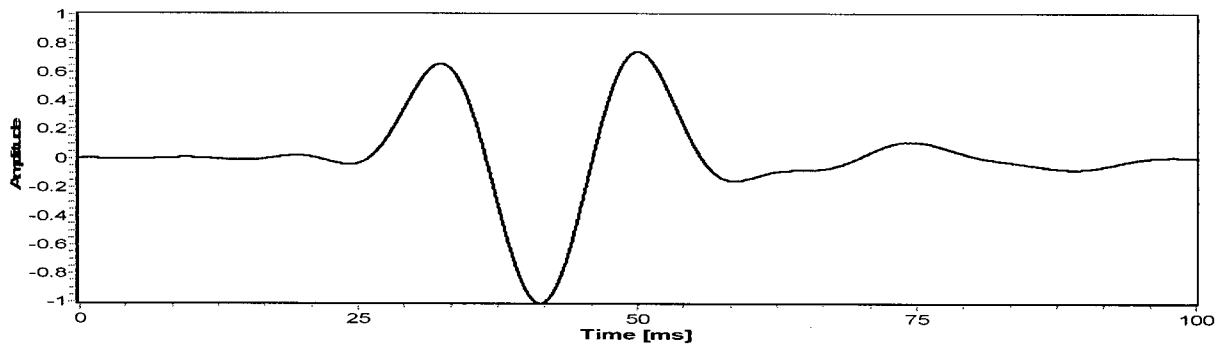


Figure H.11. The Averaged Estimated First Arriving Source Wavelet at 6.0m.

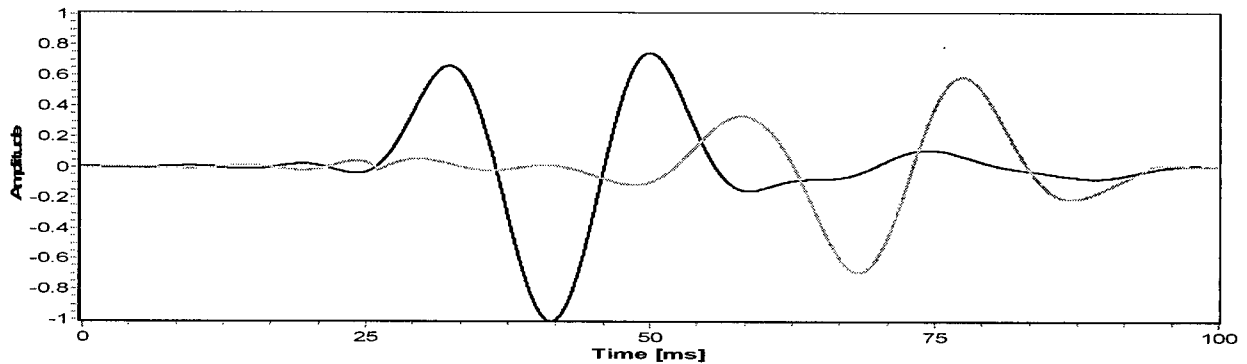


Figure H.12. The estimated first arriving source wavelet superimposed upon residual wavelet at 6.0 m.

5) Estimated Source Wavelet at 7m

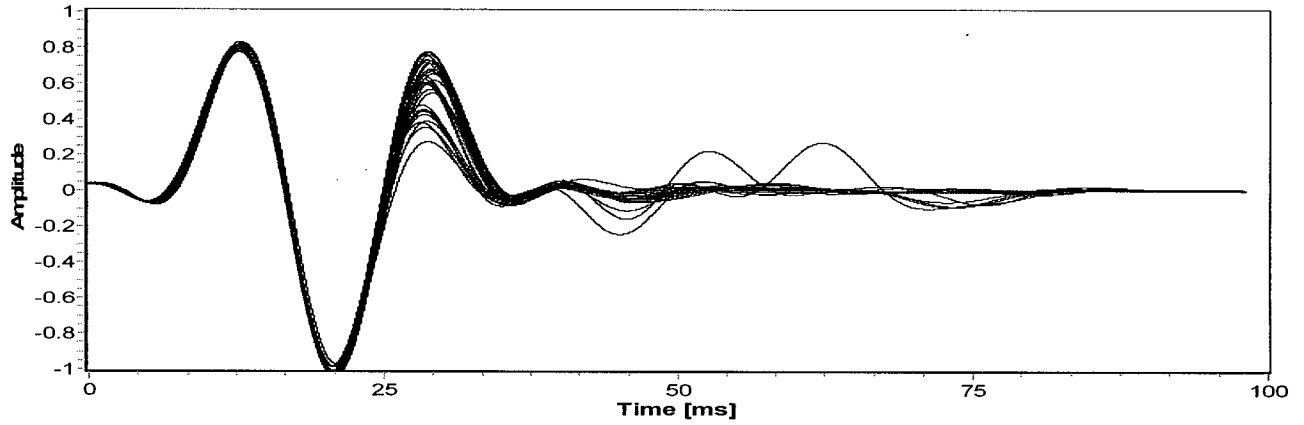


Figure H.13. Thirty five PPD-WE primary source wavelet estimations at depth of 7.0 m.

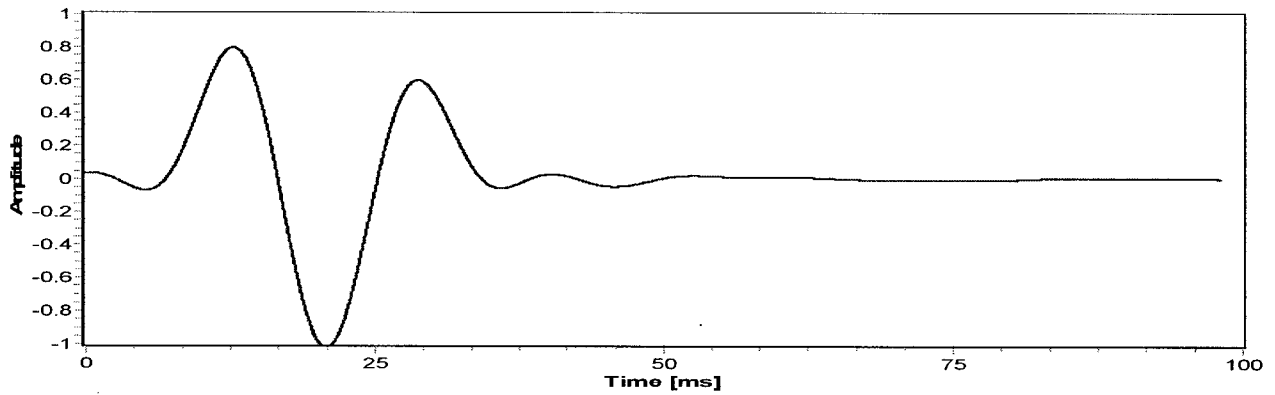


Figure H.14. The Averaged Estimated First Arriving Source Wavelet at 7.0m.

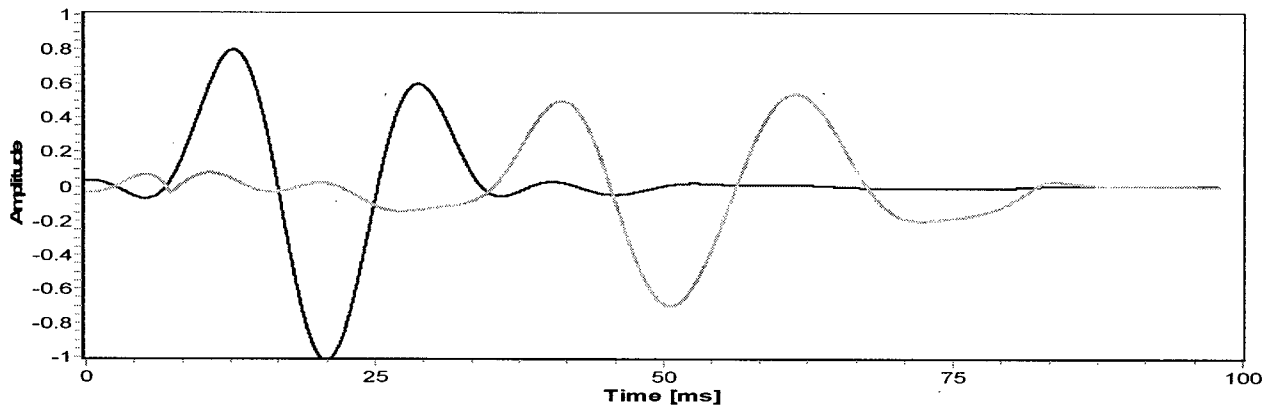


Figure H.15. The estimated first arriving source wavelet superimposed upon residual wavelet at 7.0 m.

6) Estimated Source Wavelet at 8m

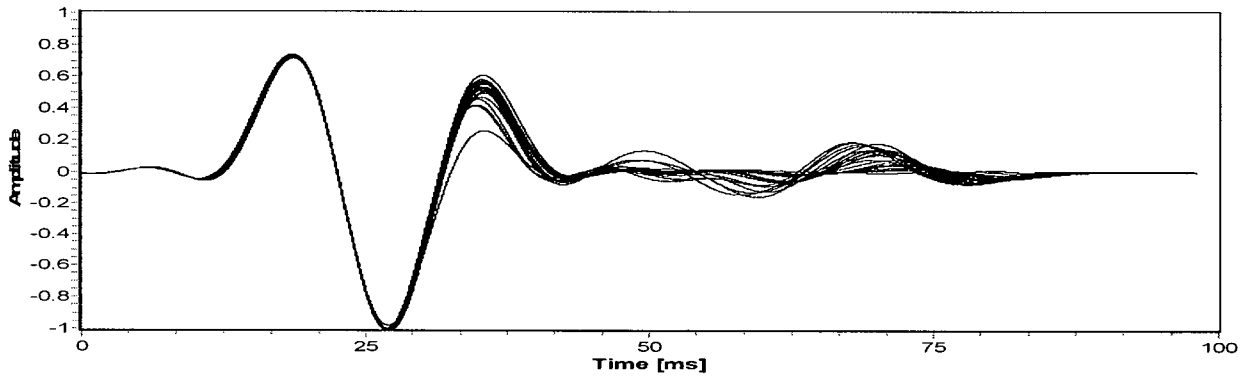


Figure H.16. Thirty five PPD-WE primary source wavelet estimations at depth of 8.0 m.

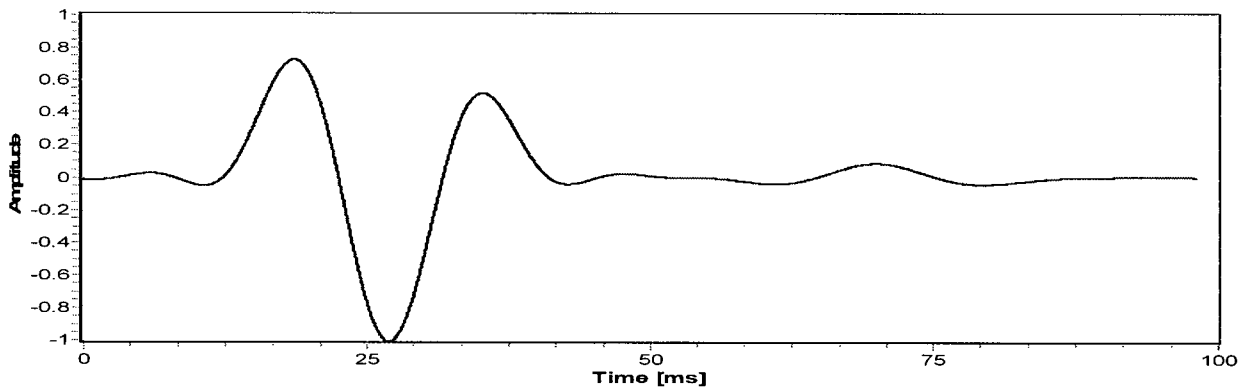


Figure H.17. The Averaged Estimated First Arriving Source Wavelet at 8.0m.

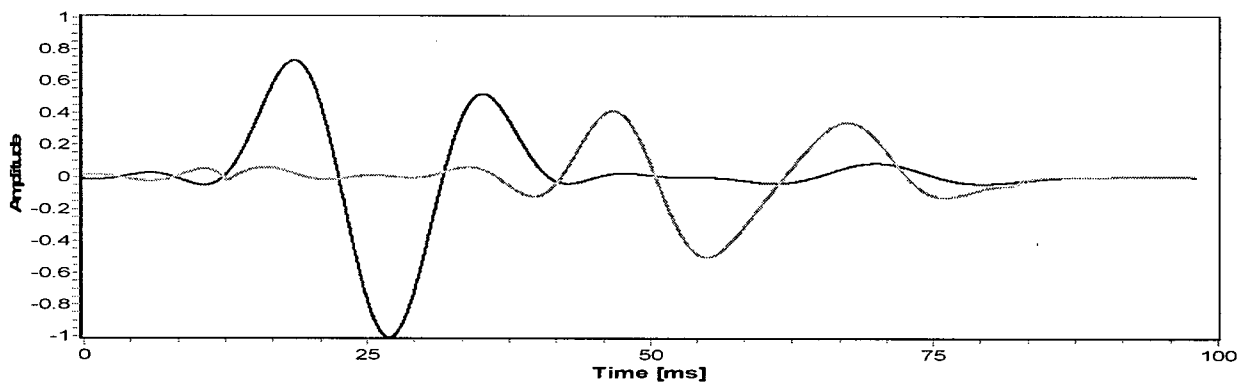


Figure H.18. The estimated first arriving source wavelet superimposed upon residual wavelet at 8.0 m.

7) Estimated Source Wavelet at 9m

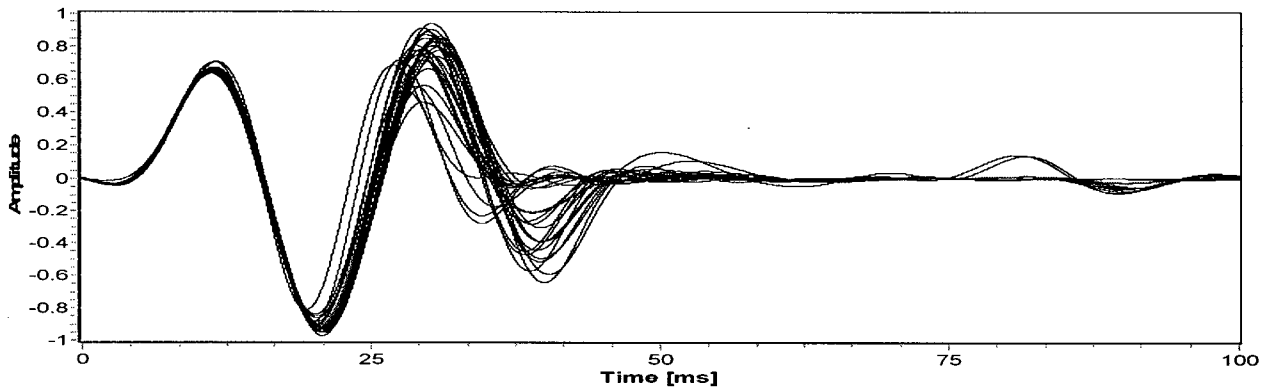


Figure H.19. Thirty five PPD-WE primary source wavelet estimations at depth of 9.0 m.

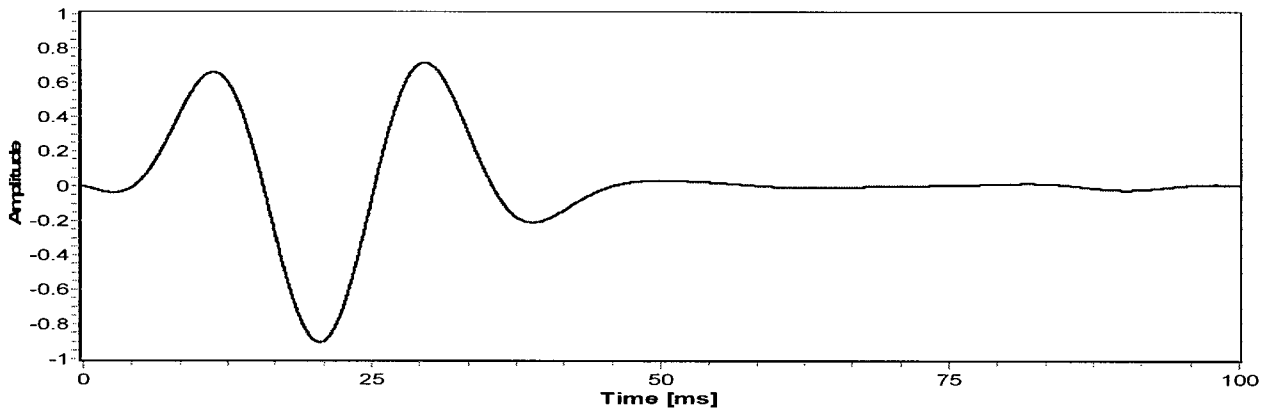


Figure H.20. The Averaged Estimated First Arriving Source Wavelet at 9.0m.

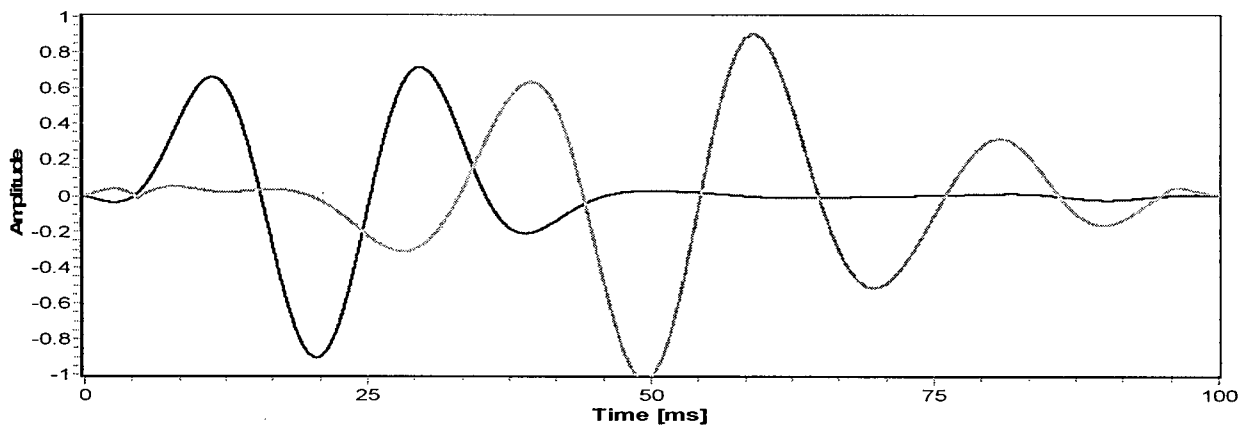


Figure H.21. The estimated first arriving source wavelet superimposed upon residual wavelet at 9.0 m.

8) Estimated Source Wavelet at 10m

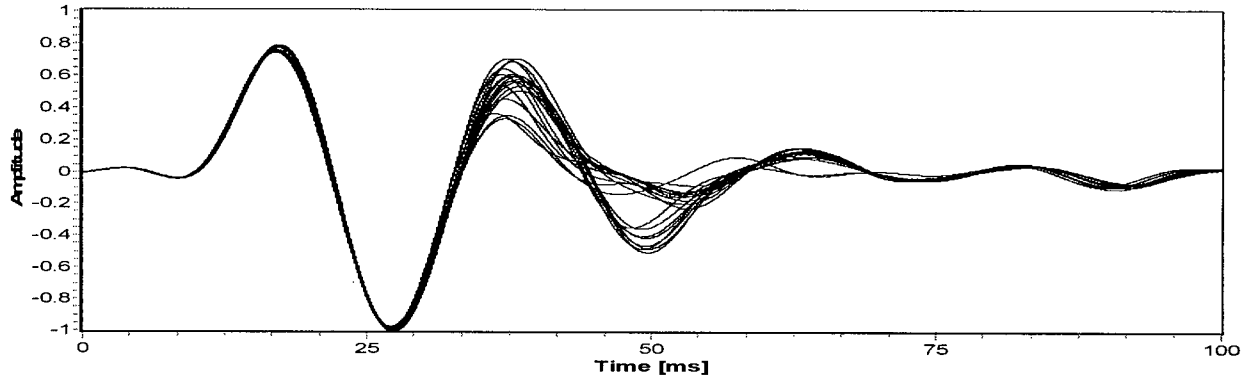


Figure H.22. Thirty five PPD-WE primary source wavelet estimations at depth of 10.0m.

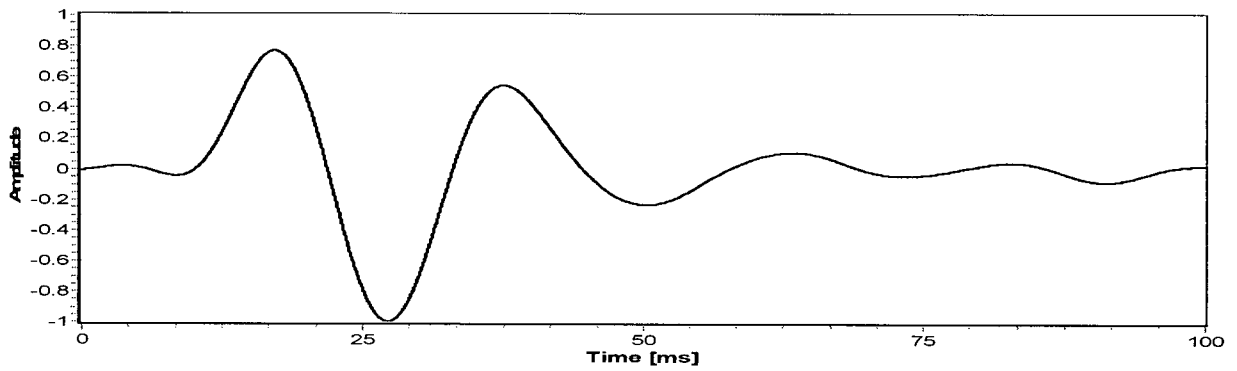


Figure H.23. The Averaged Estimated First Arriving Source Wavelet at 10.0m.

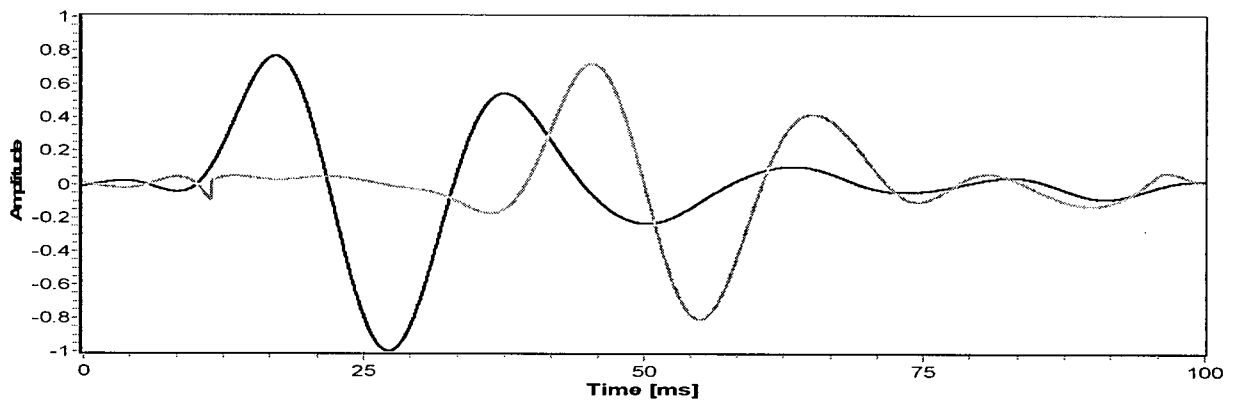


Figure H.24 The estimated first arriving source wavelet superimposed upon residual wavelet at 10.0 m.

9) Estimated Source Wavelet at 11m:

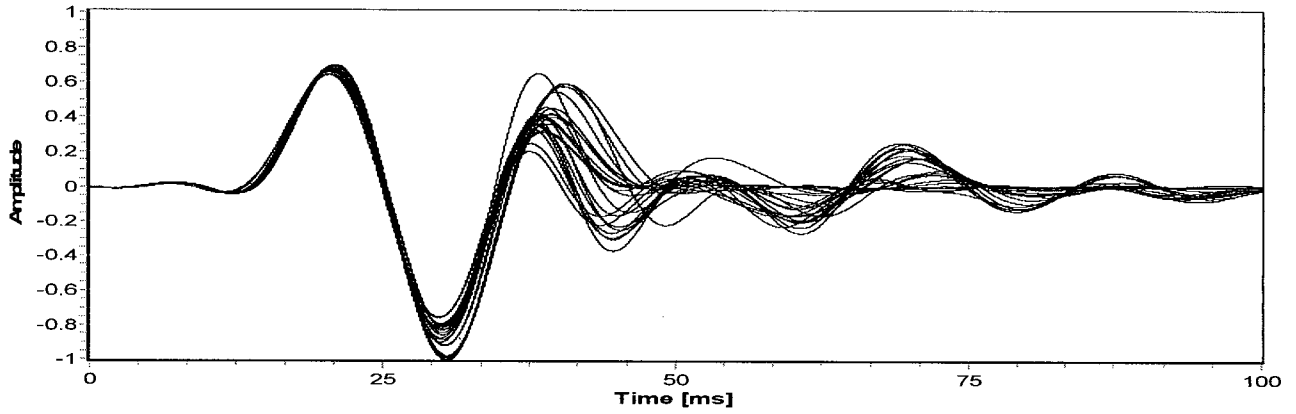


Figure H.25. Thirty five PPD-WE primary source wavelet estimations at depth of 11.0m.

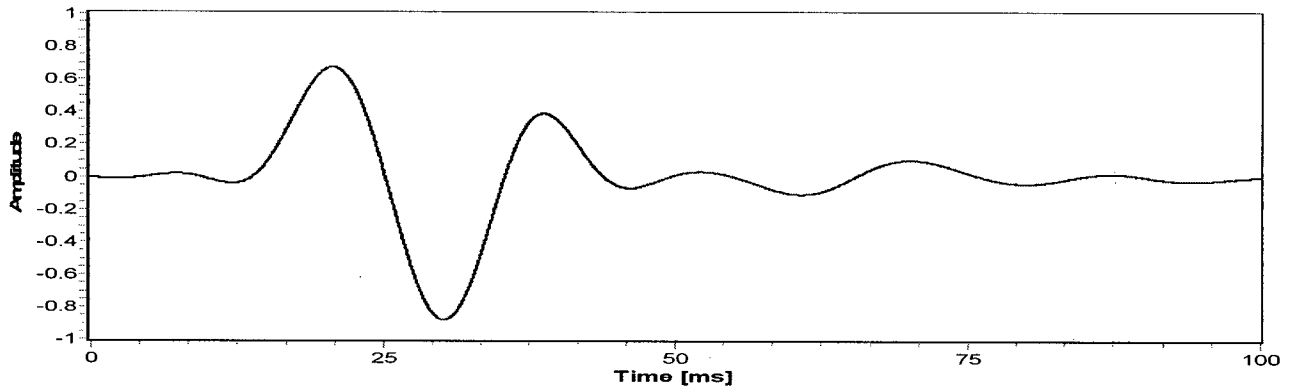


Figure H.26. The Averaged Estimated First Arriving Source Wavelet at 11.0m. yesian Recursive Estimation

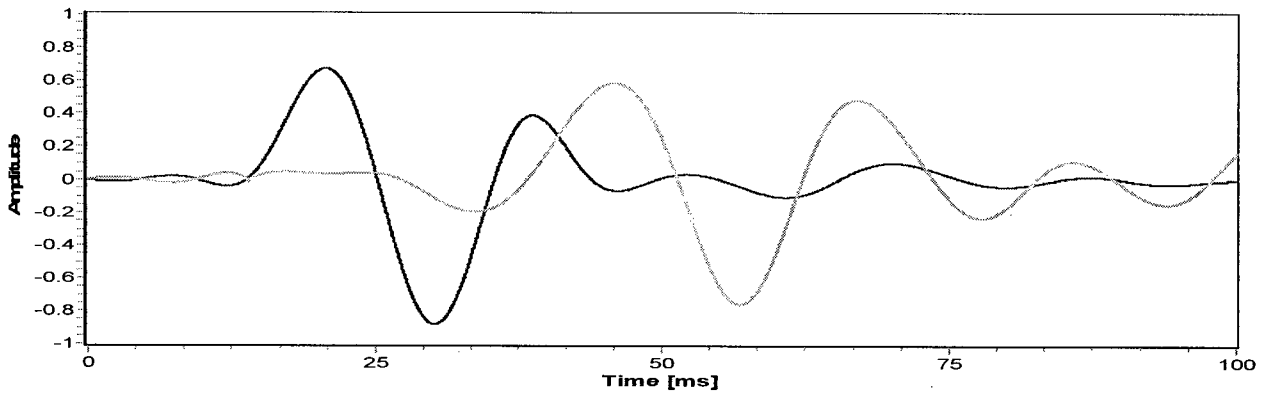


Figure H.27. The estimated first arriving source wavelet superimposed upon residual wavelet at 11.0 m.

10) Estimated Source Wavelet at 12m

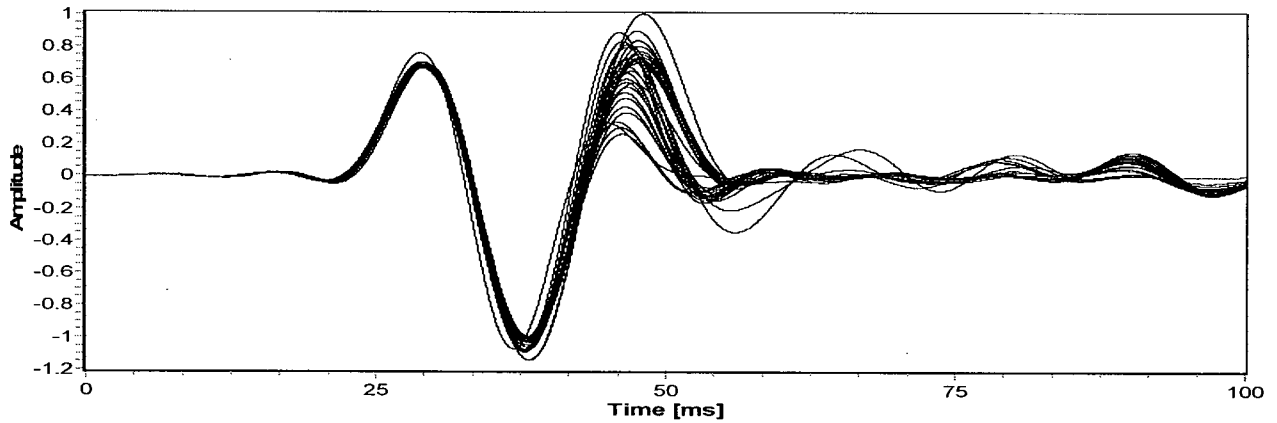


Figure H.28. Thirty five PPD-WE primary source wavelet estimations at depth of 12.0m.

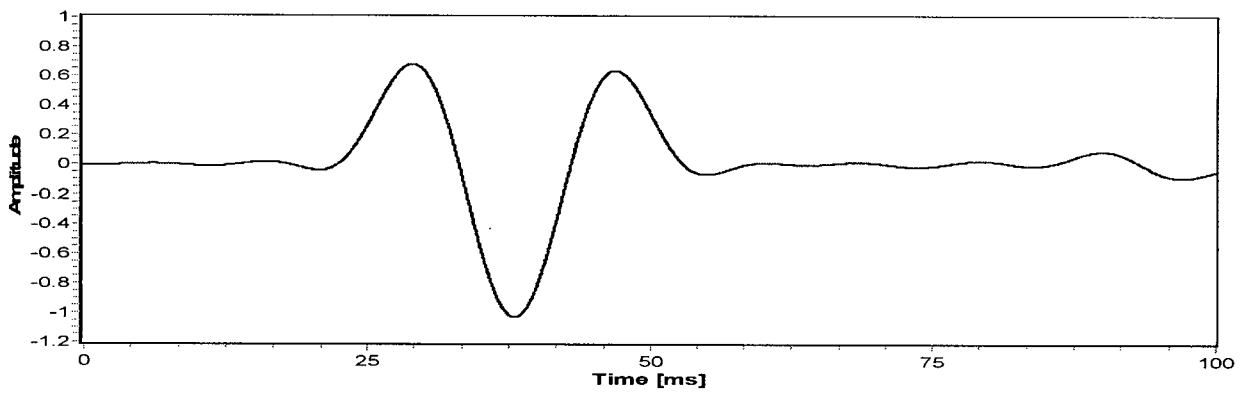


Figure H.29. The Averaged Estimated First Arriving Source Wavelet at 12.0m.

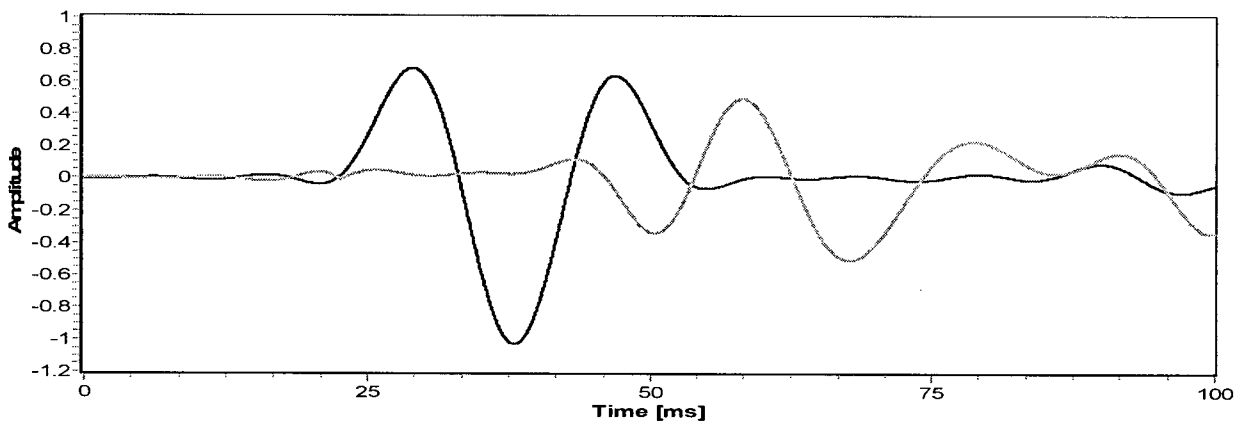


Figure H.30. The estimated first arriving source wavelet superimposed upon residual wavelet at 12.0 m.

11) Estimated Source Wavelet at 13m

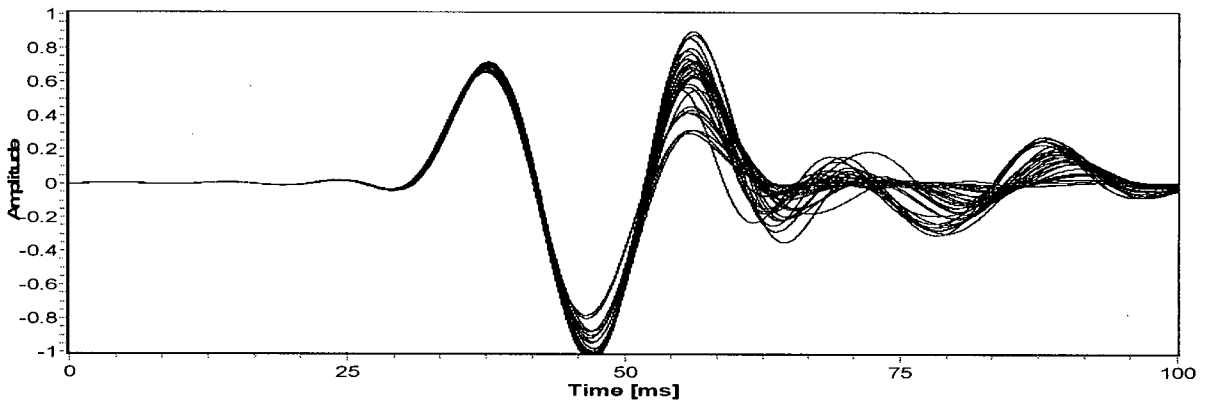


Figure H.31. Thirty five PPD-WE primary source wavelet estimations at depth of 13.0m.

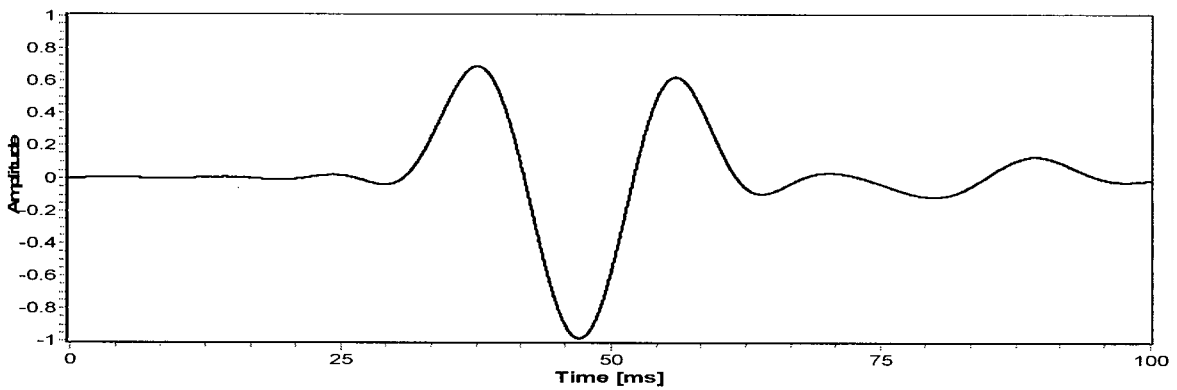


Figure H.32. The Averaged Estimated First Arriving Source Wavelet at 13.0m.

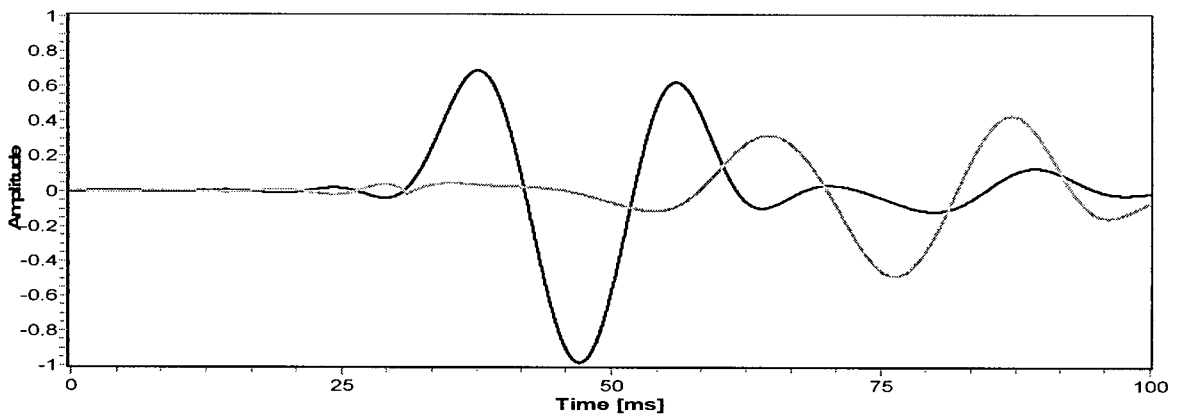


Figure H.33. The estimated first arriving source wavelet superimposed upon residual wavelet at 13.0 m.

12) Estimated Source Wavelet at 14m

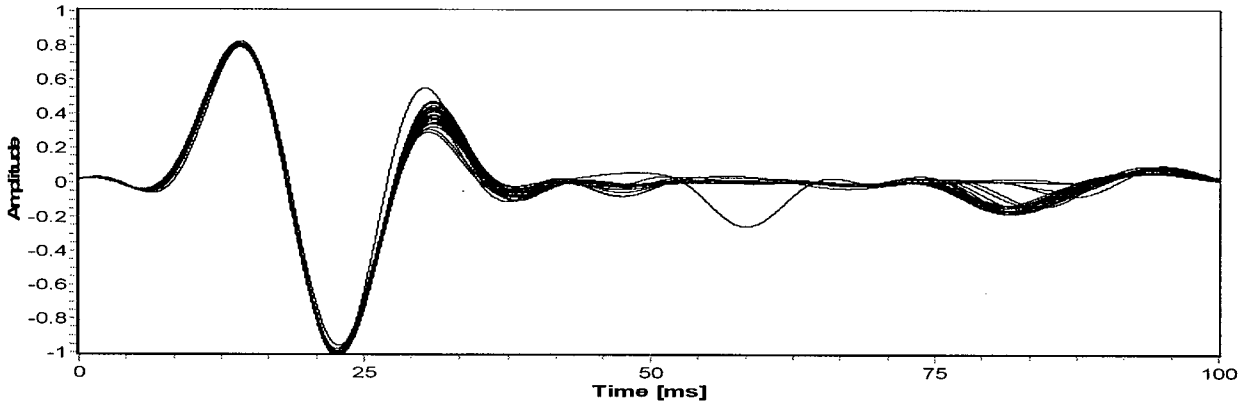


Figure H.34. Thirty five PPD-WE primary source wavelet estimations at depth of 14.0m

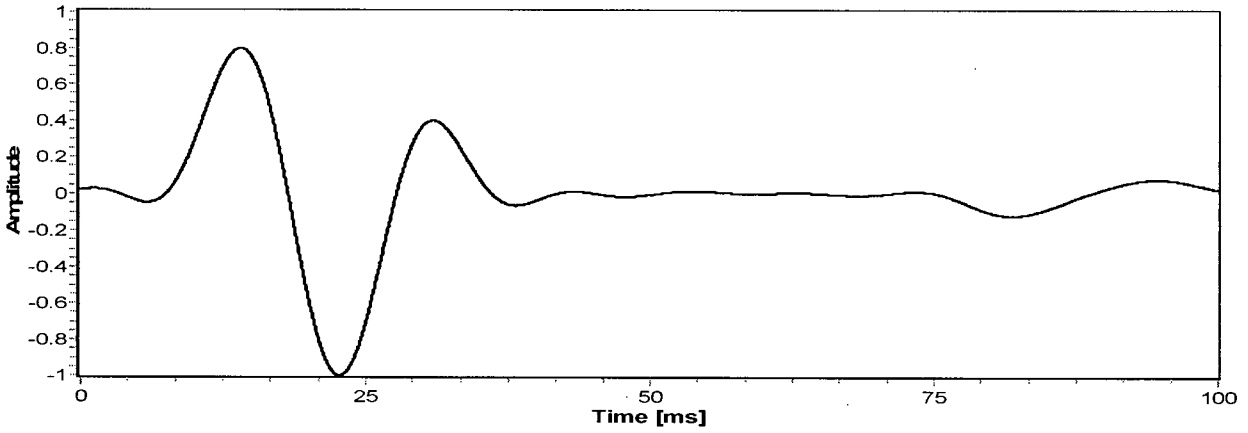


Figure H.35. The Averaged Estimated First Arriving Source Wavelet at 14.0m.

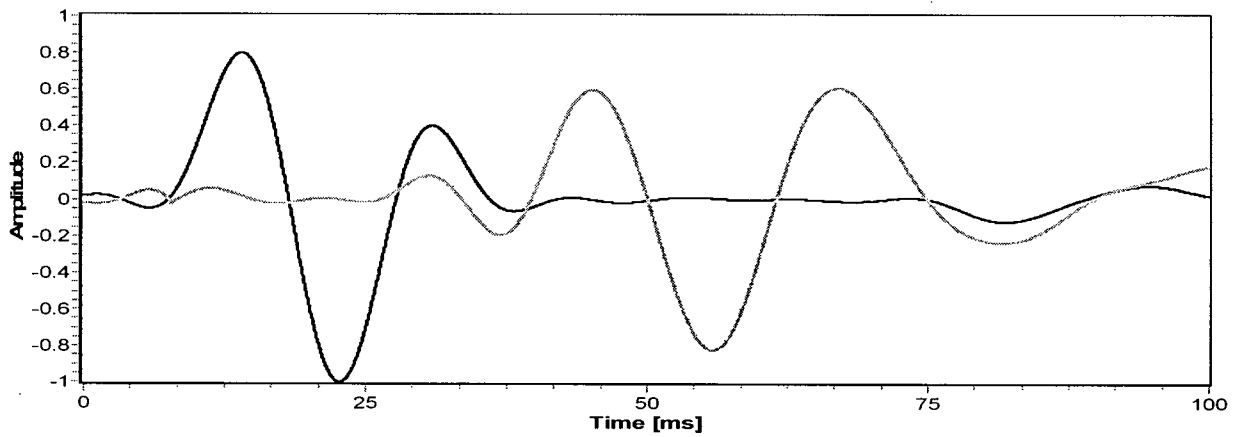


Figure H.36. The estimated first arriving source wavelet superimposed upon residual wavelet at 14.0 m.

13) Estimated Source Wavelet at 15m

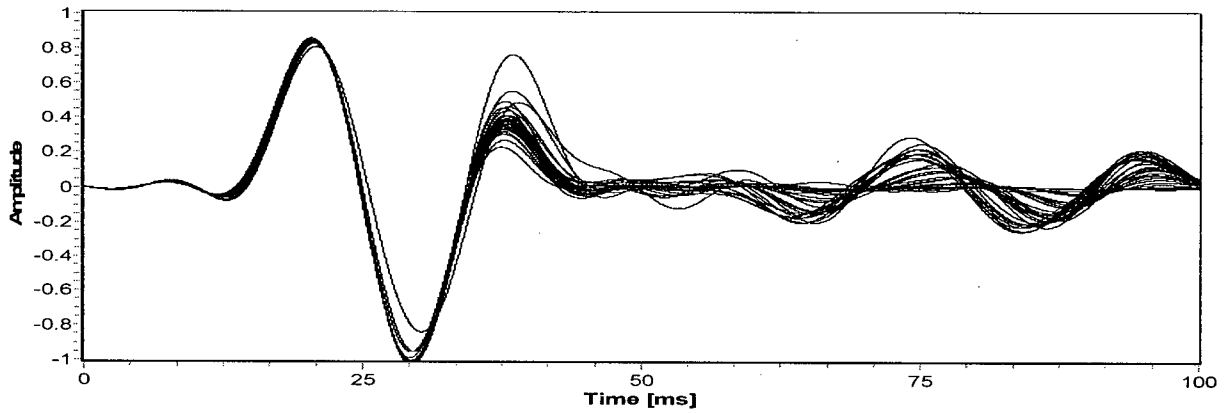


Figure H.37. Thirty five PPD-WE primary source wavelet estimations at depth of 15.0m.

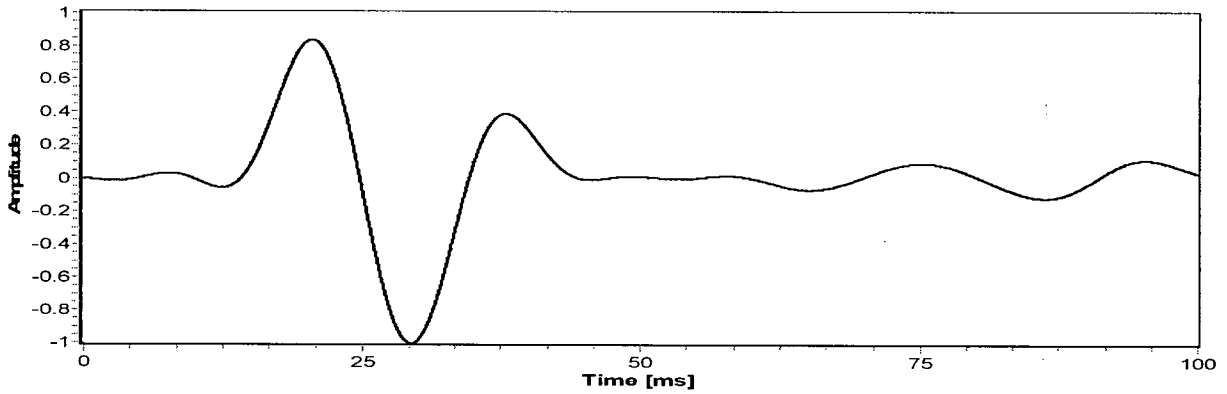


Figure H.38. The Averaged Estimated First Arriving Source Wavelet at 15.0m.

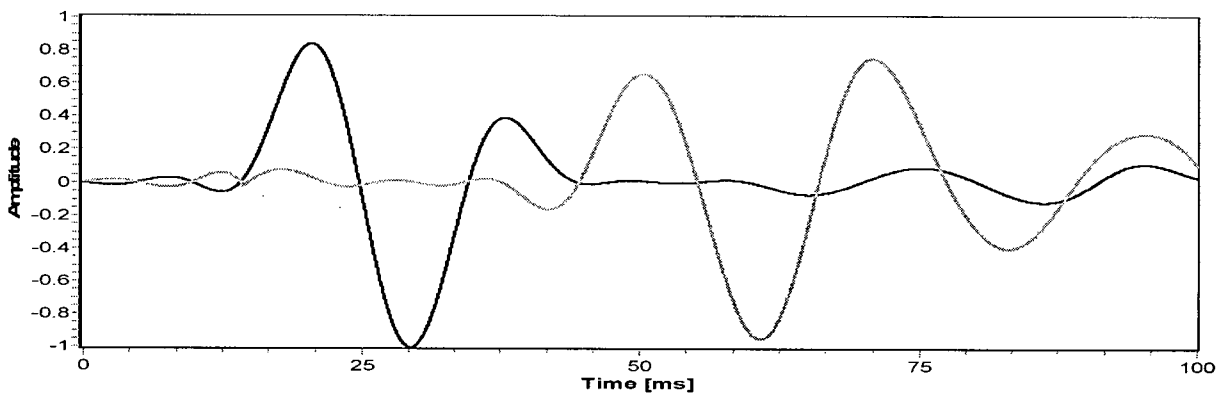


Figure H.39. The estimated first arriving source wavelet superimposed upon residual wavelet at 15.0 m.

14) Estimated Source Wavelet at 16m

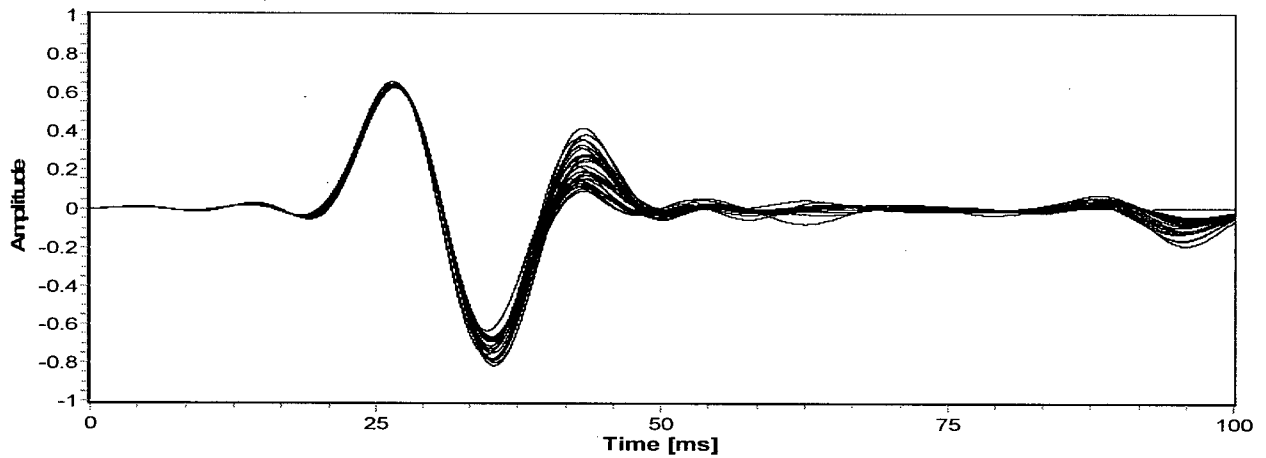


Figure H.40. Thirty five PPD-WE primary source wavelet estimations at depth of 16.0m.

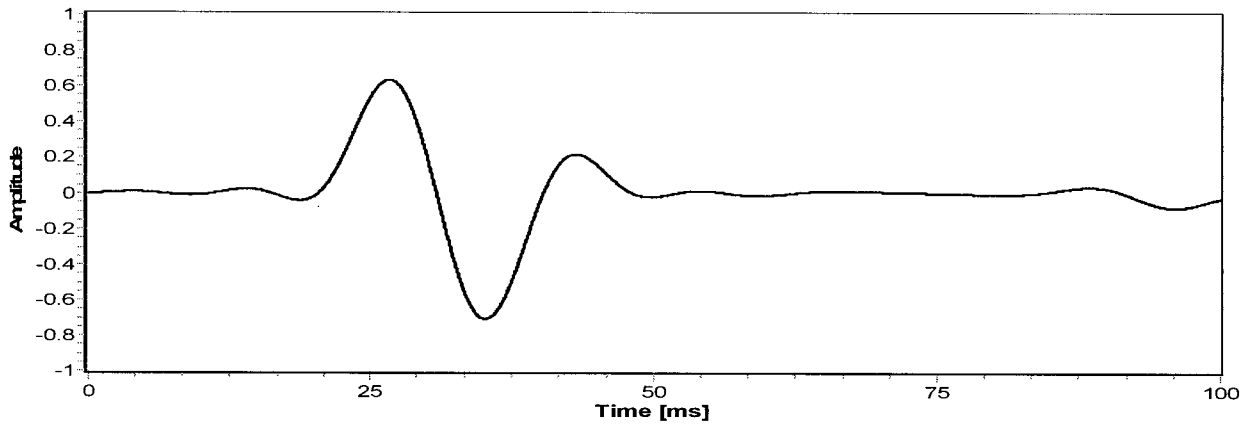


Figure H.41. The Averaged Estimated First Arriving Source Wavelet at 16.0m.

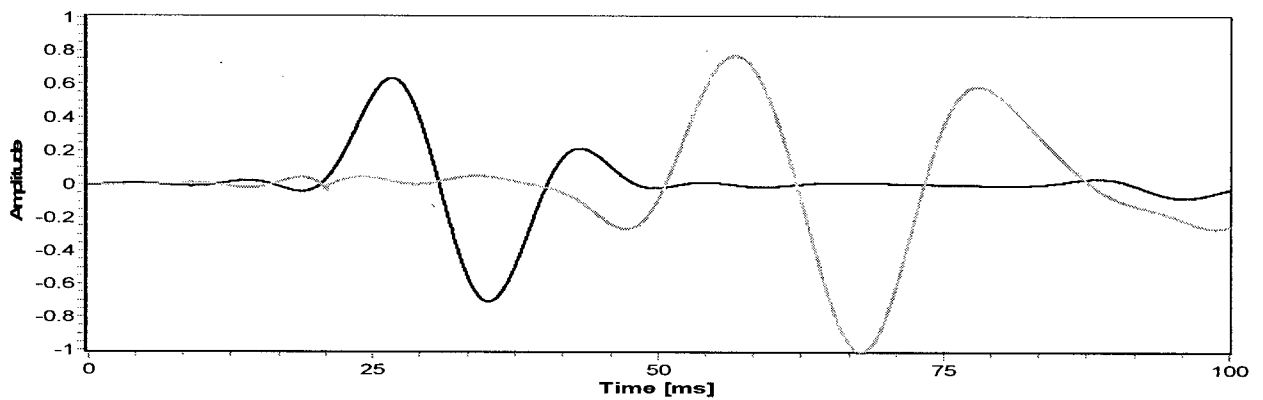


Figure H.42. The estimated first arriving source wavelet superimposed upon residual wavelet at 16.0 m.

15) Estimated Source Wavelet at 17m

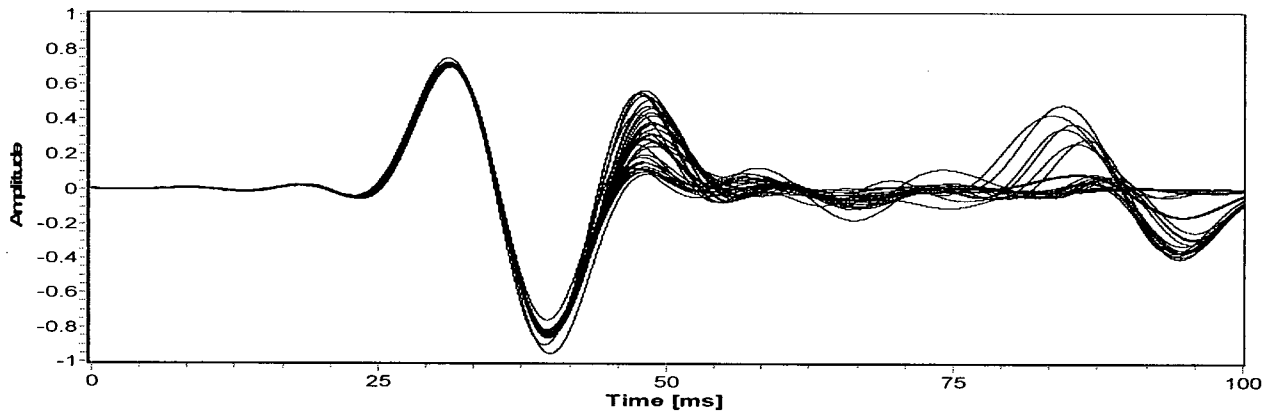


Figure H.43. Thirty five PPD-WE primary source wavelet estimations at depth of 17.0m.

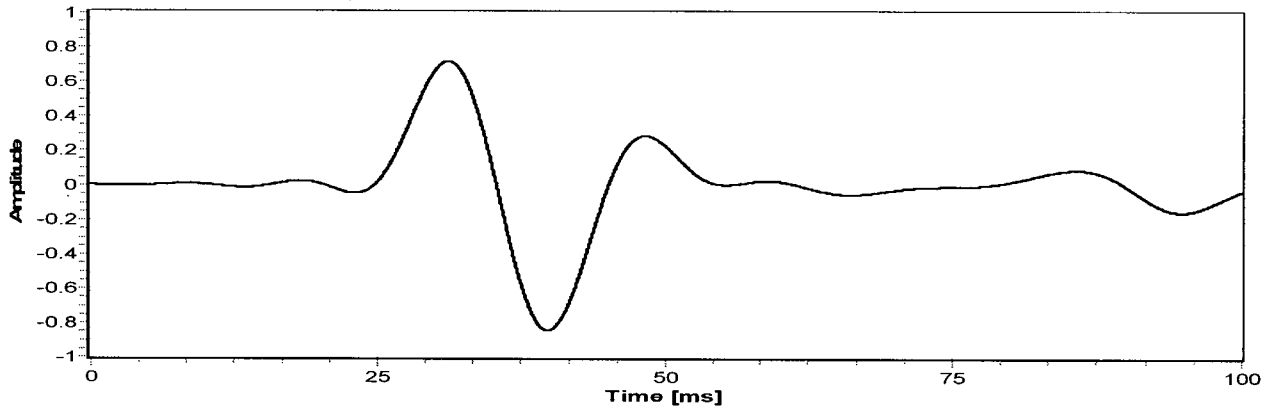


Figure H.44. The Averaged Estimated First Arriving Source Wavelet at 17.0m.

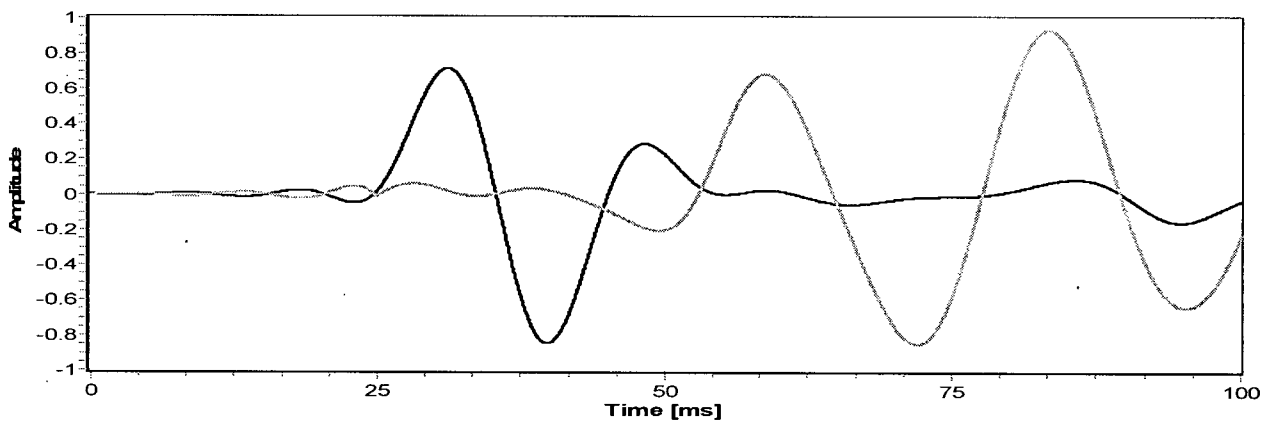


Figure H.45. The estimated first arriving source wavelet superimposed upon residual wavelet at 17.0 m.